ICFO-THE INSTITUTE OF PHOTONIC SCIENCES
&
UPC-UNIVERSITAT POLITÈCNICA DE CATALUNYA

Localized Surface Plasmon Resonance for Biosensing Lab-on-a-Chip Applications

Srdjan S. Aćimović

Advisor: Dr. Romain Quidant

Co-advisor: Dr. Mark P. Kreuzer

PhD Thesis-2012

To Marijana and Julija

Acknowledgments

The writing process of this document was very challenging due to various reasons. The data presented here are mostly of unpublished character, scattered around hard-drives of quite a few computers I have used this far. The additional difficulty originated from the fact that most of the work is not concluded yet, and as such, it required a lot of improvisation in order to make one coherent document. I started writing around March, 2011, and the first feedback about chapter 1 was strongly suggesting rewriting. The writing process was completely paused for 4-5 months, and finally, from "rewrite it" I managed to come to the "not bad" or "nicely done" comments for the last chapters. So, I guess, I improved substantially my writing skills during this period of time, thanks to Mark, Jan and Romain.

Scientific contributions

The whole thesis is supervised by Roman Quidant and co-supervised by Mark P. Kreuzer.

Chapter 1 resulted from numerous discussions with thesis advisers.

For Chapter 2, I have to mention Mark, María-Ujué Gonzáles and Jan Renger who helped me to master various nanofabrication techniques. A "magic" world of microfluidics was revealed to me by our project collaborators from EPFL (Switzerland) Jose Garcia-Cordero and Sebastian Maerkl. They managed to convince me that it is really possible to manufacture all of the complicated microfluidic chips reported in S. Quakes's SCIENCE papers, and I was left with no more excuses to avoid PDMS.

For chapters 3 and 4, I once again thank Mark and María.

Chapter 5 could not be possible without numerous discussions with Jan and Mark. Jan additionally, provided me with sputtered TiO_2 glass-substrates.

Finally, chapter 6 encompasses some data acquired also by Maria-Alejandra Ortega (Mariale). The experiments were discussed and agreed together with Mark and Mariale. Some microfluidic chips were acquired from EPFL collaborators. Jan built the optical setup.

I thank my supervisor Romain Quidant for guiding me through this dynamic field, to Mark P. Kreuzer who was working with me as co-supervisor from my earliest days at ICFO and to Gonçal Badenes with whom I started my PhD.

Since I have spent more hours in the clean-room than in my office, I owe gratitude to clean-room personnel, Luis Enrique and Javier Perez for showing great understanding and support. Also, there have been many people working near-by, sharing their expertise, such as: Mark, Jan, Sudhir, Petru, Stephanie, Danny, Davide, Domenico, Didit, Giorgio, Esteban, Johann O, Johann B, Sukanya, Guillaume…

I learned a lot from postdocs working in our group, such as Mathieu Juan, who was not mentioned earlier, apart from those already mentioned, like Mark, Jan, María, Guillaume, Johann B.

Other contributions

Manuscript was written in compliance with comments from Mark P. Kreuzer and Jan Renger, in addition to thesis supervisor Romain Quidant. Just before the submission act, the manuscript was proof-read by Johann Berthelot. A special thanks for abstract translation to Spanish to Esteban and Valeria.

I also would like to thank other group members which I collaborated with on various projects that stayed outside of this thesis's scope: Mariale, Giorgio, Jose, Valeria, Esteban, Sebastian, Chris, Jan G, Michael, Jon, Jean, Maurizio, and other ICFO people as well: Marta, Lars, Martin, Tim, Dan, Michela, Marko, Louis, Luis M, Miquel, COSINGO crew, Marcelo, Jeremié (Dijon), Phil, Ana, Dominik…

I cannot skip mentioning IT, mechanical and electric workshops, and HR department, especially Manuela for helping me in the everlasting struggle on an almost annual basis with Spanish embassy in Belgrade, who were really pushing the limits of my and Mariana's patience.

I owe big time to my parents and sister that supported me in every sense, Svetozar, Milka, Tijana, as well as Dragan, Mileva, Mirjana. Also, I thank to all of my university classmates scattered all over the world, among them especially to Marko Marinković and Vladimir D. Miljković, and to my friends in Serbia.

Finally, this thesis wouldn't be possible without endless support and understanding from my lovely wife Marijana and daughter Julija to whom I dedicate this manuscript.

In Castelldefels (Barcelona), May 2012,

Srdjan S. Aćimović

Abstract

In recent times, metallic nanoparticle plasmonics coupled with applications towards biosensing has gathered momentum to the point where commercial R&D are investing large resources in developing the so-called localized surface plasmon resonance (LSPR) biosensors. Having witnessed the rapid progress of metallic nanoparticle science in the last decade, many interesting LSPR systems have been proposed but rarely develop beyond a conceptual idea or proof-of-principle showing some biosensing potential. Scientific effort worldwide has significantly (but not entirely) switched from "pushing" sensitivity further (to single-molecule level) with emphasis more toward key aspects of LSPR sensing systems such as miniaturization, parallelization, easy operation and analyte handling, reusability, reproducibility, fabrication costs, read-out noise, just to mention a few.

Conceptually, the main motivation for the research presented within this thesis is achievement of fully-operational LSPR biosensor interfaced with the state-of-the-art microfluidics, allowing for very precise control of sample manipulation and stable read-out. LSPR sensors are specifficaly engineered by electron beam lithography nanofabrication technique, where nanoparticle interactions are optimized to exhibit increased sensitivity and higher signal-to-noise ratio. The near-field interaction among closely spaced nanoparticles (<40-50 nm) is shown to be very promising due to confined sensing volumes matching the characteristic dimensions of typical biomolecule. This optimization is referred as mode-analyte overlap engineering and it is proven to have a significant impact on achieved sensitivity. However, the overall performance of LSPR lab-on-a-chip (LOC) device depends critically on the biorecognition layer preparation in combination with surface passivation. Once surface-chemistry preparation protocols have been identified, in principle, adopting it for various analytes (disease markers, antibodies, etc.) should be relatively simple, requiring only the exchange of the receptor (typically, an antibody) used as biorecognition. The successful accomplishment certainly necessitates synergy and expertise in various fields such as nano- and micro-fabrication, nano-optics, surface chemistry and basic level of immunology. The most complex phase involved is certainly related to surface chemistry at the PDMS/glass/gold interfaces. The combination of the reaction parametres and its optimization has to be strongly balanced in order to achieve the strongest reaction product yields in terms of surface coverage and function, without jeopardizing the earlier stages in the chip development (previously functionalized surfaces or intrinsic chip functions). This general truth about surface-chemistry strongly shaped the context of this thesis, especially the concluding chapters.

As an introduction, the principles of plasmonic biosensing are identified encompassing both surface plasmon resonance (SPR) and localized SPR. Being successfully implemented into commercial product, the governing physics of SPR is compared to LSPR in chapter 1, together with advantages and disadvantages of both.

Chapter 2 describes methods necessary for LSPR biosensor development, beginning with nano-fabrication methods, where standard fabrication method based on positive tone resists and lift-off process is compared to negative resist in combination with Reactive Ion Etching, resulting in a higher quality of achieved nanoparticle parameters and improved optical properties. The modelling tool

(COMSOL Multiphisics) is discussed in the middle section, while the basics of micro-fabrication in microfluidics conclude this chapter, where passive and active microfluidics networks are discerned.

Particularly attractive optical properties are exhibited by closely-coupled nanoparticles (dimers), with the dielectric gap of below tens of nm, which were theoretically predicted to be very suitable as LSPR biosensing substrates. Chapter 3 is subjected to optical characterization (dependence on the size of the dielectric gap) of nanofabricated dimer arrays. The acquired data demonstrate the advantages of the nanofabrication methods presented in chapter 2, and the technique for fast and reliable determination of nanoparticle characteristic parameters (size and gaps) is introduced as spectral evolution method. This method is applied for various geometries based on close-coupling and compared with the results of modelling in Comsol.

The initial biosensing-like experiments presented in chapter 4 (no integration with microfluidics) proved for the first time, the theoretical predictions of higher sensitivity, yielding additionally the specific response as function of analyte size and dielectric gap between nanoparticles. The overall response of different dimer arrays (various gaps) provides information about adopted conformation of analyte protein once immobilized. At this point, the concept of static plasmon ruler was introduced. Additionally, it is estimated that the optimized dimer system can detect local binding of less than hundreds of bovine serum albumin proteins.

However, as the dimer resonance is strongly dependent on dielectric gap size (exponentially), the poly-dispersity of nanofabrication infers a broad dimer resonance as compared to individual structures. Broad resonances suffer a higher noise when employing them for the real-time LSPR biosensing. As a way to circumvent such problem, the feasibility of employing far-field interaction within the nanoparticle array to spectrally narrow resonance is investigated in chapter 5 by optimizing the array periodicity and introducing thin waveguiding layers.

Finally, the concluding chapter 6 is dedicated to a full assembly of a lab-on-a-chip LSPR biosensor, starting with interfacing plasmonic substrates with compatible active microfluidic networks, allowing the precise sample delivery and multiplexing. The prototype device consisting of 8 individual sensors is presented with typical modes of operation. The bulk refractive index determination of various samples demonstrates the working principle of such device. Finally, various strategies of biorecognition layer formation are discussed within the on-going research. The chapter concludes with the presentation of closed-box LSPR platform developed by our partner company.

List of Abbrevations

BF-Bright Field

BRIS-Bulk Refractive Index Sensitivity

BSA-Bovine Serum Albumin

CCD-Charged Coupled Device

CTP-Charge-Transfer Plasmon

CPU-Central Processing Unit

DDA-Dipole-dipole Approximation

DF-Dark Field

DNA-Deoxyribonucleic Acid

ECM-Exciton Coupling Model

EM-Electro Magnetic

FEM-Finite Element Method

FOM-Figure of Merit

FDTD-Finite-difference Time-domain

FWHM-Full Width at Half Maxima

HC-Honeycomb

HSP-Heat-Shcock Protein

LOC-Loab-On-a-Chip

LSI-Large Scale of Integration

LSPR-Locallized Surface Plasmon Resonance

MAO-Mode-analyte Overlap

MEMS-Microelectromechanical System

MMV-Micromechanical Valve

MUA-Mercapto-undecanoic Acid

PDMS-Polydimetylsiloxane

PEG-Polyethyleneglycol

PH-Plasmon Hibridization

QCM-Quartz Crystal Microbalance

RIE-Reactive Ion Etching

RUI-Refractive Index Units

SAM-Self-assembling Monolayer

SCF-Scattering Field

SEM-Scanning Electron Microscope

SERS-Surface Enhanced Raman Spectroscopy

SFP-Surface Functionalization Protocol

SPpr1-SPEDOC prototype 1

SPR-Surface Plasmon Resonance

TE-Transverse Electric

TF-Total Field

TIR-Total Interanl Reflection

TIRF-Total Internal Reflection Fluorescence

TM-transverse Magnetic

TPL-Two-photon Luminescence

Table of Contents

Introduction

Fundamental sciences deal with various phenomena and relations among them providing us with better understanding of world around us. Many of such phenomena, especially ones being subjects of physics and related fields, after being understood at least to some extent, are instantaneously being intended to apply to some sort of sensing device or detector. The very same idea was conveyed in the field of plasmonics. Owing to its sub-wavelength occurrence, the plasmonic effect was recognized as especially convenient in dealing with phenomena of the same spatial scale (<100nm). Consequently, considering that the size of important biomolecules (proteins, DNA) being similar to the spatial extent of plasmons occurance, a very successful implementation of fundamental understanding of plasmonics resulted in a biosensing device (Surface Plasmon Resonance biosensors, Biacore, GE Healthcare, USA).

A biosensor as such, can be defined as an analytical device that is composed of spatially coinciding biorecognition element and transducing mechanism. The transducing mechanism is in essence provided by the plasmonic effect manifested at plasmon supporting metal/dielectric interfaces, featured by high sensitivity to external refractive index perturbations. A biorecognition layer is formed at the metal surface providing the selectivity and specificity for a targeted analyte biomolecule. However, recently it was noticed that a slight size mismatch between SPR effect and typical molecules of interest can be surpassed by employing Localized SPR (occurring at 20-30nm range, commensurable to biomolecule size). Though LSPR properties for biosensing have been extensively investigated in last decades, only few finalized LSPR biosensing products have been offered today (for instance, Lambdagen Corporation, USA).

The main advantage of SPR and LSPR biosensors attribute to its label-free detection scheme that simplifies the operation of the device, however complicating its preparation. Other advantages are shared with optical biosensors in general, as detection through light modulation (fast, immune to EM interferences, compatible with optical fibers), high-sensitivity, miniaturization and parallel inspection, excellent compatibility with low-cost microfluidics, and massive production potential (economy of scales). Low volume sample consumption, together with all additional traits benefited the integration with microfluidics, make this technologies very attractive for various potential customers (research biotechnology centers, pharmaceutical companies, analytical laboratories, medical institutions, point-of care applications, and possible individual end-users in the future).

Beyond potential higher sensitivity to biomolecular detection, the intrinsic gain of LSPR systems in particular is related to multi-tasking lab-on-a-chip (LOC) operation. Beside the applications for label-free analyte detection, the LSPR effect is suitable for various types of bio-molecule interrogations and manipulation schemes, such as molecule identification (SERS), plasmon-assisted sorting and trapping, localized heating. The low cost of fabrication of integrated and miniaturized optical components (light sources, detectors) and compatibility with the nanofabrication technologies (plasmonics and fluidics), makes feasible the real lab-on-a-chip concept (not only the chip-in-the-lab), especially with foreseen improvements of parallel nanofabrication technologies (nano-imprint lithography, for instance). Although the subject of this thesis is mainly label-free LSPR biosensing and associated aspects, the work

conducted during my PhD was expanded to LOC SERS as well as LOC cell trapping and sorting. All of these working principles can be combined into single integrated LOC device. Conceptually, such LOC device for point-of-care application would certainly be highly valuable, especially in countries with poorly developed infrastructure (health-care, traffic, education). The level of expertise required to handle and operate such a device can be made low.

The outlook of the thesis is organized as follows. Chapter 1 briefly describes evanescent-wave based biosensors, extending the discussion to the plasmonic effects (SPR and LSPR). Chapter 2 introduces the methods used throughout this thesis in the development of LSPR devices. Namely, nanofabrication principles are introduced, followed by the description of modeling tools. The chapter concludes with the part devoted to relevant microfluidics technology. The basic physics of closely-interacting particles possessing particularly attractive LSPR properties is introduced in Chapter 3. The proof-of-principle experiments are presented in Chapter 4. Chapter 5 deals with the far-field interacting nanoparticles, and their potential impact in the future LSPR design of related biosensors. Finally, the last chapter (chapter 6) describes the development of LSPR LOC prototype, starting with an opto-fluidic device assembly, testing, and the status of the development of surface functionalization protocols that aim to complete the efficient biorecognition layer.

Chapter 1

Introduction to plasmonics and plasmonic sensing

This chapter introduces the basic terminology and physics underlying plasmonic sensing. Before describing a well-known surface plasmon resonance (SPR) sensing technique (Biacore), a wide class of biosensors based on evanescent fields will be covered. Although, exploiting similar type of evanescent field interaction with surrounding media as SPR sensors, this class generally employs detection schemes incorporating the use of labels. Typical representatives are evanescent based fiber optics sensors (not to be confused with fiber opt(r)odes where biorecognition elements are coupled to the fiber end [Israel et al. 2008]) and planar-wave guiding structures. After the introduction of SPR, localized surface plasmon resonances (LSPR) are discussed and compared to SPR. Finally, the end of this chapter is devoted to the assessment of the potential of LSPR that may lead to it becoming a major player in biosensing market share of today.

1.1. Introduction to evanescent waves

An evanescent (inhomogeneous) wave is an electromagnetic (EM) wave bound to an interface as opposed to free-propagating waves. This localization is associated to a purely imaginary component of the wave vector perpendicular to the interface, hence such an EM wave is not carrying energy in that direction. The corresponding EM field components are exponentially dampened away from the interface. One of the common situations where evanescent waves are generated is known as total internal reflection (TIR). This phenomenon occurs in a configuration where light is impinging from medium $n_1\,(z<0)$ onto the interface with material $n_2\,(z>0)$ and $(n_1>n_2)$ under an angle of incidence equal or exceeding the critical angle θ_c, defined as $\theta_c=\arcsin(\frac{n_2}{n_1})$. For a TE-polarized plane-wave incident from n_1, the electric field in n_2 is given by:

$$\mathbf{E_2}(z>0)=\mathbf{E_{2y}}=E_{0i}t_{S,TIR}\exp(-\delta z)\exp(-jk_0n_1\sin\theta_i x)\mathbf{e}_\mathbf{y} \qquad \text{(Eq.1.1)}$$

where the corresponding Fresnel transmission coefficient is given as: $t_{S,TIR}=\dfrac{2n_1\cos\theta_i}{n_1\cos\theta_i-jn_2\sqrt{(n_1/n_2)\sin^2\theta_i-1}}$. θ_i is angle of incidence ($\theta_i\geq\theta_c$), k_0 is wave vector in vacuum, $\mathbf{e}_\mathbf{y}$ unit vector and δ is evanescent field decay length, expressed as

$$\delta = k_0 n_2 \sqrt{\frac{n_1^2}{n_2^2}\sin^2\theta_i - 1}\,. \qquad \text{(Eq.1.2)}$$

The decay length δ is dependent on wavelength (through k_0) and incident angle. Similar expressions can be obtained for TM-polarization [Aćimović, 2011]. Penetration depth of evanescent wave defined as δ^{-1} is typically less than wavelength of light. Fig. 1.1 (a) displays field distribution for glass/water interface, where vacuum wavelength is set to 850nm, with incident angle equal to $\theta_c \approx 61^o$ for p-polarized illumination. The evanescent field normalized to the incident one is enhanced by a factor of 2.1. The theoretical maximum of the evanescent fields magnitude/intensity is expected for the critical angle illumination with the TM-polarization light, due to the induced surface polarization currents [Novotny and Hecht, 2006]. TIR condition is omnipresent for dielectric light waveguides (optical fibers, planar dielectric waveguides, etc). Beyond, evanescent fields find numerous applications in sensing [Marazuela and Moreno-Bondi, 2002], microscopy [Axelrod, 2001], trapping [Ganic et al. 2004], due to their sub-wavelength localization and field enhancement.

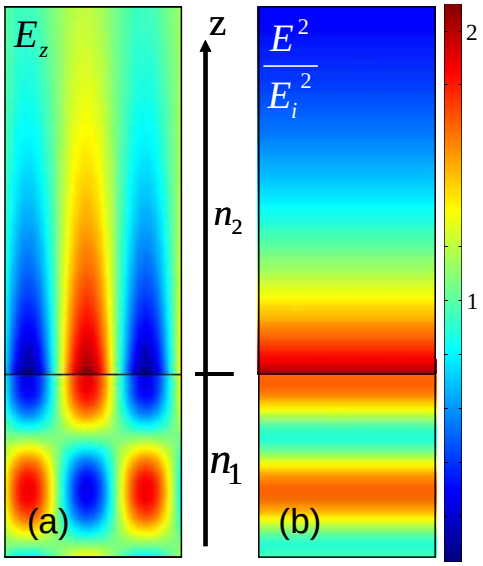

Figure 1.1-Total Internal Reflection at a glass(n_1=1.52)/water(n_2=1.33) interface. Incident wavelength is 850 nm with incident angle being equal to the critical (θ_i=61°). (a) Ez field components (b) Normalized electric field intensity $|\mathbf{E}|^2/|\mathbf{E}_i^2|$, with the maximum value of 2.1.

1.2. Dielectric waveguides as evanescent wave-based biosensors

Optical fibers or planar dielectric waveguides consist of a core and a cladding region. The core is the material having a higher refractive index than the surrounding cladding. Light can be efficiently guided through the core only if it rarely hits core-cladding interface under an angle that is smaller than the critical one. While the light travels inside the core it always produces a local evanescent field in the cladding area. The decay length of the evanescent field determines its interaction range within the cladding space. Due to its sub-wavelength nature, practical interaction zone is accessible only to species that are in close contact with the interface. This is basic principle of TIR flourescence (TIRF) microscopy, where labels are only excited if located within the evanescent field.

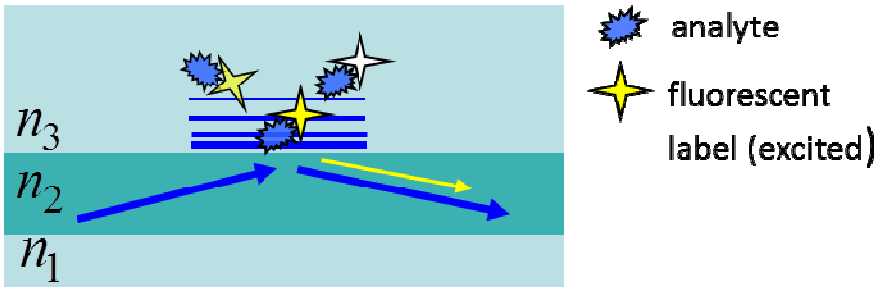

Figure 1.2-A typical bio-sensing transducing mechanism in dielectric waveguide platforms (Total Internal Reflection Fluorescence). Locally excited fluorescently labeled species emit more efficiently into waveguide core.

Fig. 1.2 depicts the basic principle behind TIRF microscopy or evanescent based biosensing (if the interface is coated with bio-recognition elements). Typical waveguiding structures employed as evanescent biosensors are planar waveguides [Ligler et al. 2008] or optical fibers [Anderson and Taitt, 2008]. Special modifications are introduced in order to increase light power carried in the cladding in the form of evanescent fields, for instance using nanofibers [Lou et al. 2010]. Biosensing platforms require source overlap with fluorophore's absorbing spectrum, filters for excitation-fluorescence separations and a detector. In TIRF Microscopy fluorescence coupled inside the core is preferentially detected at the waveguide output due to increased coupling of the fluorescence into the waveguide in comparison to freely propagating signal [Anderson and Taitt, 2008]. However, labeling strategy and limited mode sensitivity of most common waveguides to shallow refractive index changes, have promoted another technique, known as SPR, to become the gold standard of commercial biosensing techniques. The fundamental principle of SPR transducing mechanism owes to the features of the EM surface waves, called surface plasmon polaritons (SPPs).

1.3. Plasmonics and surface plasmon polaritons

The term plasmonics refers to systems that can support collective electron oscillations excited by light coupling or electron beams. Though bulk (volume) plasmons exist (metals at plasma frequency), the most interesting effects occur when these charge oscillations are confined to a surface (interface) that is readily approachable to some external objects (materials, bio-molecules, living organisms and environment in general). In the last two decades, one of the most attractive, promising and most studied plasmonic systems is the interface between a noble metal and a dielectric, supporting SPPs in visible/near IR spectral region.

SPPs are surface-confined coherent oscillations of conduction electrons at a metal/dielectric interface with characteristic fields, very similar to aforementioned evanescent waves in TIR. [Raether, 1988]. As shown in Appendix, "bound" solutions to Maxwell´s equations can exist at an interface between two materials if particular requirements are met. Primary characteristic that stands out is transverse magnetic (TM) nature of associated SPP´s EM fields. The dispersion relation for SPPs is given by:

$$\beta_{SPP} = \frac{\omega}{c}\sqrt{\frac{\varepsilon_+\varepsilon_-(\omega)}{\varepsilon_+ + \varepsilon_-(\omega)}} \qquad \text{(Eq.1.3)}$$

It describes relation between β_{SPP} (propagation constant of SPP) and angular frequency ω. ε_+ and $\varepsilon_-(\omega)$ are the dielectric and metal permittivity, respectively. The momentum mismatch between free-space propagating waves ($k = \sqrt{\varepsilon_+}\frac{\omega}{c}$) and SPP $\beta_{SPP} = \frac{\omega}{c}\sqrt{\varepsilon_+}\sqrt{(1+\frac{\varepsilon_+}{\varepsilon_-(\omega)})^{-1}}$ is sustained by the negative values of the permittivity of the involved metals $\varepsilon_-(\omega)$ (in visible/IR). Thus light cannot be coupled to SPPs when impinging directly onto a smooth metallic surface, and very little of the light energy will be absorbed by metal in the visible/near IR range. The metallic appearance of silver and aluminum owes to this strong specular reflection. To compensate for the momentum mismatch for SPP

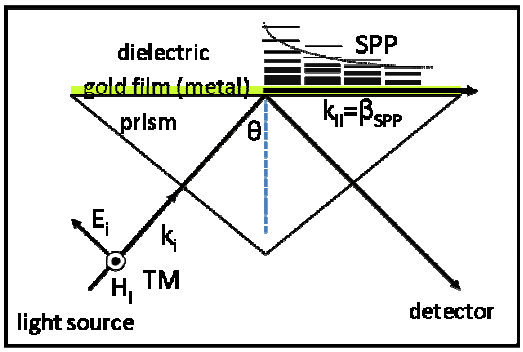

Figure 1.3-Surface plasmon coupling using the Kretschmann configuration. Evanescent waves generated at prism/metal interface penetrate through thin metalic layer and couple to SPP on the opposite side at angles satisfying $k_{II} = \beta_{SPP}$.

excitation, various optical configurations are available. The simplest excitation of SPPs is by light scattering from metallic surface sub-wavelength defects, but this method usually suffers low coupling efficiency. A very versatile configuration employs diffraction gratings, which are widely used for integrated and miniaturized SPP opto-electronic devices and biosensors [Homola, 2006]. Other methods rely on attenuated total internal reflection (ATIR), where evanescent fields generated by TIR penetrate a short distance before coupling to SPPs, at a near-by metallic-dielectric interface. As the range of interaction of evanescent wave is very limited, SPP supporting interface has to be within that range. One of these ATIR methods called Otto´s configuration employs the coupling prism and metallic interface being separated by a narrow air or dielectric gap, but more than that this is cumbersome for the majority of applications. An alternative, called Kretschmann´s configuration is widely accepted for SPP excitation, as sketched in Figure 1.3. It consists of a coupling glass prism covered by a thin metallic film. A detector is monitoring the light reflected out from the prism. The in-plane k-vector component can be large enough to match the SPP propagation constant on the opposite side of the metal. The supporting metallic film has to be thin enough for the incident evanescent field to penetrate through it [Reather, 1988]. The electric field profile is described by

$$E_x = \pm \frac{k_z^{\pm} H_0 e^{-j(\omega t - k_x x)} e^{\mp k_z^{\pm} z}}{j\omega \xi_0 \xi_{\pm}} \qquad \text{(Eq.1.4 a)},$$

$$E_z = \frac{j k_x H_0 e^{-j(\omega t - k_x x)} e^{\mp k_z^{\pm} z}}{j\omega \xi_0 \xi_{\pm}} \qquad \text{(Eq.1.4 b)},$$

where H_0 is the constant magnetic field amplitude (See Appendix). The fields decay exponentially in the direction normal to the interface. The decay length is different for the metal and the dielectric, and is expressed by Equation 1.5.

$$k_z^{\pm} = \sqrt{k_x^2 - k_0^2 \xi_{\pm}} \qquad \text{(Eq.1.5)}$$

k_x can be obtained from the dispersion relation (Eq. 1.3) (for the SPP excitation $k_x = \beta_{SPP}$). The decay length normal to the interface clearly depends on the metal and the dielectric permittivity and the angular frequency of the light. While the SPP field only penetrates tens of nanometers into the metal, the penetration depth into the dielectric is typically a few hundreds of nanometers. Additionally, metals intrinsically possess loss channels, thus limiting distances over which SPPs can propagate along the interface up to few tens of microns (non-radiative (Ohmic) damping on perfectly smooth surfaces).

The sub-wavelength confinement of SPP's EM fields finds similar applications as evanescent waves. Since evanescent waves don't carry energy in the direction normal to the supporting surface, direct observation of SPP propagating on smooth surface is impossible. However, indirect observation is feasible by monitoring light leaving the prism. The detector will detect a reflectivity nearly equal to 1, just before SPP excitation condition is met. For a particular angle and wavelength, when the coupling condition is satisfied, light is very efficiently converted into SPPs. The reflectance abruptly falls off thus

indicating SPP excitation. Typically if a monochromatic light source is used, the reflectivity as a function of the scanned angle displays a sharp dip. If broad spectral light source is used with a fixed angle, the dip in the spectrum can also be observed. Figure 1.4 (a) shows numerically calculated reflectivity as seen by a detector when monochromatic light (650 or 850 nm) is used and the incident angle is scanned above critical angle. The gold film thickness is 40 nm. Alternatively, reflectivity spectra are shown for two fixed angles (65 and 70 degrees, Fig. 1.4 (b)).

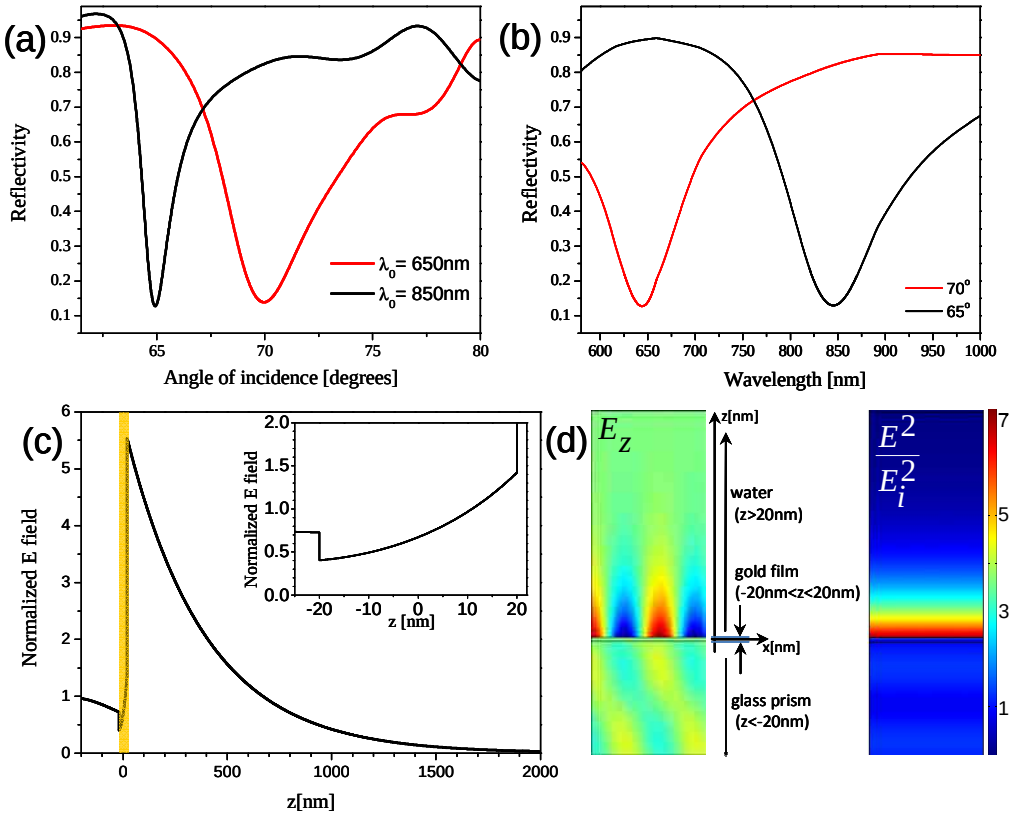

Figure 1.4-SPR: (a) Calculated Surface Plasmon signature for two fixed wavelengths, (b) wavelength-shift SPR detection for two fixed angles, (c) SPP E-field profile on the gold-water interface (normalized to the incident field), Inset: SPP E-field profile inside the gold film (highlighted in orange in main figure (c)), (d) SPP E-field distribution and intensity profile corresponding to (c) (FEM model)

The maximum of SPP associated electric-field is occurs at the interface. This field can exceed the incident one by an order of magnitude. Figure 1.4 (c) plots field enhancement profile with corresponding decay lengths. The enhancement reaches almost 6, for λ_0=850 nm at the angle of maximum coupling (see Figure 1.4 (a)). The decay length in the metal is ca. 20 nm, while the field extends ca. 380 nm into the dielectric (water in this case). Figure 1.4 (d) shows the normal electric field component map (left) and the corresponding intensity enhancement profile (right). The sub-wavelength confinement and the field enhancement are the basis for a variety of SPP applications. Since many nonlinear effects strongly depend on the field intensity, better said on its 2nd (or 3rd or 4th and so on) power, the SPPs can feature

orders of magnitude stronger nonlinear effects. For instance, Raman signals from molecules immobilized onto metallic surface can be amplified significantly due to fourth power dependency on local-electromagnetic radiation, with decreased contribution from background, similarly in case of local and efficient excitation of fluorophores. The ability of SPP to confine light at the sub-wavelength scale and its relatively decent propagation distances, make SPPs very promising candidates for next generation of fast electo-optical circuits [Ju et al. 2007].

In practice, the implementation of SPPs into any kind of functional devices involves the miniaturization from an infinite metallic film into a metallic patch that supports SPPs. The degree of integration goes side-by-side with the possibility of parallel operation (e.g. SPR imaging). While the minimum metallic area that supports extended SPPs depends on wavelength of light, illumination optics and the losses in the metal, it falls typically within the 5-10 μm range. It has been shown that as small as 5 μm gold disks posses the dispersion relation almost identical to the one of SPPs supported by the extended gold film [Righini, 2010]. However, in such case SPPs suffer multiple reflections from disk's edges and the associated evanescent field is no longer uniform. The field profile of the aforementioned disks exhibit a potential well, deep enough for micron-sized dielectric bead or cell optical trapping [Righini et al. 2007]. When the supporting metal gets sufficiently small (of the order of tens to hundreds of nm radius), the dispersion relation changes upon the effect of boundaries – in that case one referrers to localized surface plasmon resonance (LSPR) phenomena .

1.4. Localized Surface Plasmon Resonance

Extraordinary color effects are displayed by objects made of glass enriched with metallic nanoparticles. Besides its intensive color, the color varies complementary if observed in reflection or transmission. The addition of metallic salts during glass manufacture is responsible for the colors of the Lycurgus cup, dating back from 4th century AD, or for the colorful vitrages in many medieval cathedrals, like the Notre-Dame cathedral in Paris. The first analytical description of nanoparticle interaction with light was attributed to Gustav Mie in 1908. Mie's theory accurately predicts optical properties of spherical metallic objects, independently of its diameter. His approach is based on incident plane wave decomposition into spherical harmonics and their interaction with the sphere. After his theory, plasmonics of metallic nanoparticles was constantly occupying attention of world's scientific community, with periodical tides triggered by some groundbreaking discoveries in the field (fundamental physics, or nanoparticle synthesis or spectroscopy techniques). Intentionally not presenting them in the historical order, many modeling approaches were developed and available today: Gans-Mie theory, T-matrix method, Green-dyadic approach, Discrete dipole approximation (DDA) and many more [Bohren and Huffman, 1998]. All of these techniques suffer some lack of generality (for instance, restrictions in the modeling geometry design). More flexible commercial (with graphic user interface control), but yet more CPU and memory demanding numerical methods are recently extensively employed in modeling of nano-phenomena, such as the finite difference time domain (FDTD) and finite element method (FEM) [Zhao et al. 2008]. Rapid progress in the theory was followed by the

development of many ways of nanoparticle synthesis. Wet chemical synthesis of noble nanoparticles has come a long way to reach exclusive possibility of manufacturing almost any imaginable nanoparticle shape. By reduction of metal salts in the presence of metallic seeds and various surfactant compounds, and by careful process control (reagents concentration and reaction conditions), nanoparticles in the shapes of spheres, rods, triangles, prisms, cubes, stars are readily attainable. The processes of the chemical synthesis are adopted for many metallic materials, with focus on noble metals. Additionally, composite nano-objects, commonly referred as nanoshells [Prodan et al. 2003], or stable biomolecule-nanoparticle complexes are available today. Beside wet synthesis, numerous planar nanofabrication techniques have been recently proposed, most of them adopted from micro-electronic technology [Cui, 2005]. The experimental characterization of fabricated nanoparticle relies essentially on spectroscopic techniques, involving a broad-band light source, collecting optics, and a spectrometer. Since nanoparticle extinction cross-section (sum of absorption and scattering coefficients) are too low for the direct observation of low density nanoparticle containing specimens (bright-field detection), dark-field microscopy provides improved signal-to-noise ratio, sufficient for even single-particle detection of subwavelength sized particles [Ament et al. 2012]. Other more complicated techniques based on scanning confocal-microscope configuration can retrieve more information about investigated nanoparticles. Among them, let's mention two-photon luminescence (TPL) microscopy [Ghenuche et al. 2008, Huang et al. 2010], or lock-in amplified single-particle spectroscopy for detection in bright-field transmission [Mahaba et al. 2009]. Finally, the most common non-optical characterization schemes are scanning electron microscopy (SEM) or transmission electron microscopy (TEM). In the following chapter 2, more details can be found about fabrication, microscopy and modeling techniques that were utilized by the thesis author.

LSPR can be understood as confined collective oscillation of the quasi-free electron cloud against fixed ionic background in metallic nanostructures. Due to the finite geometry of the nanoparticles, direct coupling of the light to LSPR is not forbidden, thus rendering the dispersion relation of LSPR rather flat. Localized plasmons decay both radiatively (by light scattering) and non-radiatively (by conversion into heat). The scattering and absorbing efficiency of the nanoparticles is expressed by the corresponding cross-sections that are a couple of times larger than the geometrical cross-sections. Typically, metallic particles support multiple resonances such as dipolar, quadrupolar or multipolar. The spectral position of the LSPR strongly depends on: the material composition, particle size, and shape (Fig. 1.5), dielectric environment, presence and arrangement of other nearby particles (far-field and near-field coupling), illumination conditions (polarization and angle of illumination) [Liz-Marzán, 2005]. Any of these parameters can be exploited to tailor resonant response, to match particular need in the vast area of nanoparticle applications, spanning from optics and chemistry to biology and medicine. More about tuning of LSPR can be found throughout the thesis, especially in chapters 3 and 5. Figure 1.5 illustrates simulated scattering spectra of different isolated gold particles with different geometries upon unpolarized illumination.

Enhanced scattering and absorption at resonance allows relatively easy detection and tracking of the metallic nanoparticles in comparison to other non-resonant objects of the same sizes. Enhanced near-fields confined to nano-volume find applications in sub-diffraction optics, material sciences [Renger et

al. 2010], plasmon-assisted optical trapping [Righini et al. 2009], emission enhancement [Bek et al. 2008, Zhang et al. 2007] and tailoring the directivity of fluorescent entities (optical antennas) [Curto et al. 2010] and surface enhanced Raman scattering (SERS). Efficient resonant generation of heat on the nanoscale also converts nanoparticles into punctual thermal sources for cancer therapy [Gobin et al. 2007]. A variety of nanoparticles can be used as imaging tags or contrast agents, with benefits of long term-stability (noble metals) and low toxicity (gold) in vivo. The research in solar cells was recently boosted by possibility of increased light-harvesting efficiency by using nanoparticles [Atwater and Polman, 2010].

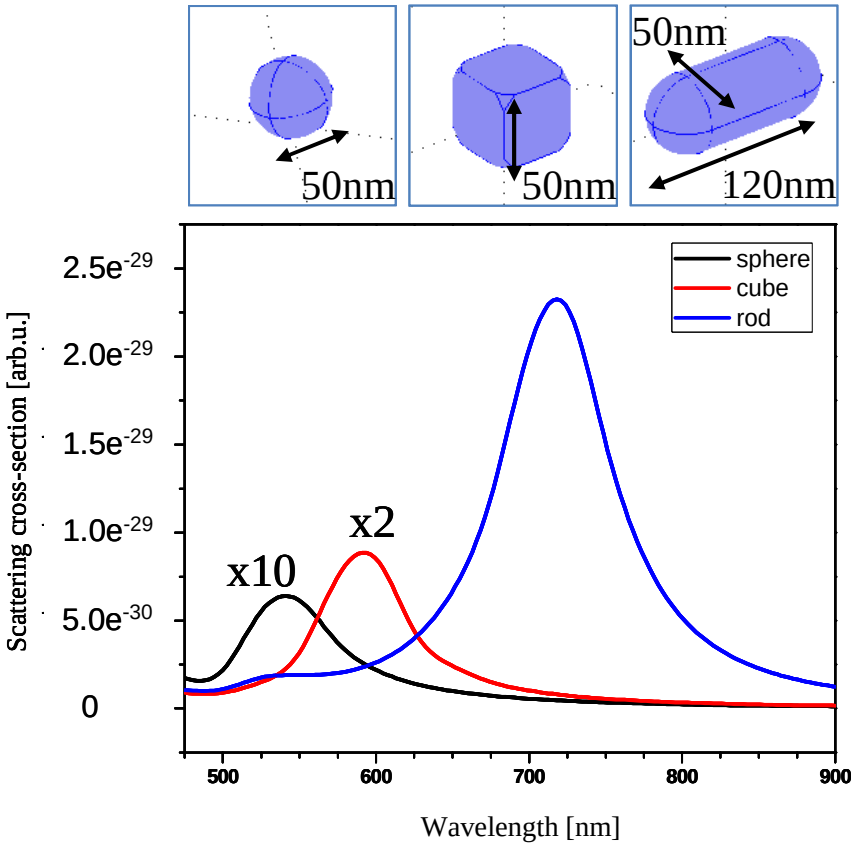

Figure 1.5-Spectral response of individual gold nanoparticles in water calculated using COMSOL: 50nm in diameter sphere (black), 50 nm sized cube (rounded apexes-5nm radius of curvature) (red), 120nm long and 50nm wide cylindrical rod (blue). Graph shows scattering-cross sections in water calculated with FEM (scattering formalism).

1.5. Plasmonic sensing: SPR vs. LSPR

By far, the most successful contemporary application of plasmonics is in the field of biosensing. Over the last 2 decades, SPR can be considered the established benchmark for label-free biosensing [Mukhopadhyay, 2005]. Rapid and decisive biosensing market breakthrough was undertaken by Biacore, (Sweden) and has recently been taken over by GE Healthcare (USA). Founders of Biacore, initially Pharmacia Biosensor AB, recognized the huge potential and possible impact of label-free biosensing platform based on SPR. Today, beside GE Healthcare, which is considered as the main player, many other companies x are actively present on the market with specific SPR-based products. Just recently, some 25-30 years after SPR industry foundation, LSPR bio-sensing systems are becoming very popular and widely used by biologists and medical doctors [Gerion and Day, 2010].

1.5.1. Transducing mechanism and read-out

Plasmonic resonances exhibit a very strong dependence upon any refractive index change inside the sensing region defined by the range of extension of evanescent fields. The addition of any material within this region, with different refractive index from the background environment, will induce a resonance shift to lower or higher energies depending on the relative sign of refractive index change. Two types of perturbations will be discriminated from now on: one is bulk change, where the complete sensing volume is uniformly perturbed, and the other one is the local perturbation provoked by molecule adsorption, thin film deposition, etc. that occupies only a portion of the sensing volume In an ideal case, a perfect biosensor should be very sensitive to local perturbations. More detailed discussion on this matter can be found in the following chapters. Since bio-molecules have in general a higher refractive index than typical background matrix (water, serum, buffers), their presence within the sensing volume will red shift the deep in the reflectivity of SPR or the peak in the case of LSPR. The magnitude of this shift is directly related to the relative bulk refractive index change or the number of adsorbed molecules (or both). Thus the sensor can be calibrated and later used for determination of an unknown quantity. Figure 1.6 (a) shows the calculated shift of the SPR peak for 5e-3 bulk change of the refractive index of water (n_0 = 1.33), while (b) shows the LSPR peak shift of a gold cylinder due to the adsorption of 1 nm thick dielectric layer of refractive index 1.4863 in an aqueous background.

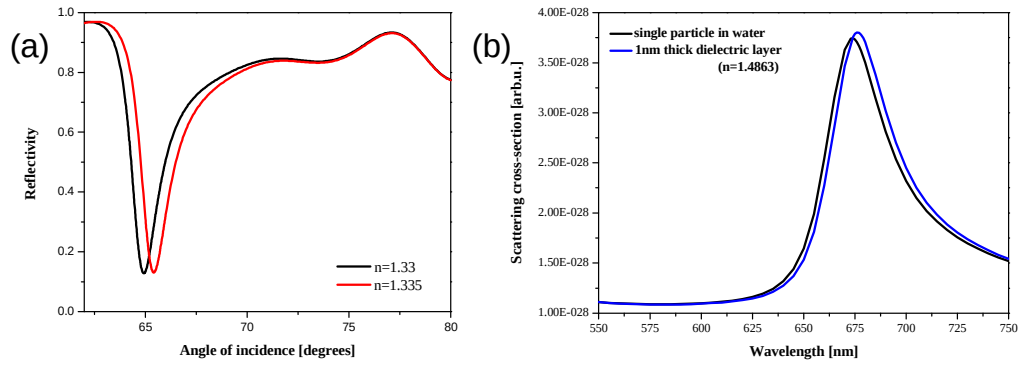

Figure 1.6-SPR versus LSPR sensing (Calculated). (a) SPR dip shifts upon averaged bulk refractive index change toward lower energies. (b) LSPR peak change upon molecular binding (black-before, blue-after binding)

In practice, free moving molecules are not staying sufficiently long inside the sensing region and/or their contribution can just increase the average bulk index felt by sensor. Other very important issues are related to the sensor specificity and nonspecific binding. As a consequence of the inertness of noble metals, bio-molecules show very low affinity toward noble metallic surface. Apart from electrostatic interactions and physisorption of some proteins to metallic surfaces, only thiol functionality (-SH) exhibits a strong affinity to gold via complex-coordinate bonds. Typically, short molecules consisting of a carbon backbone are "equipped" with thiol ending that binds to the metals. The opposite extremity of these molecules can be any other functional group(s) that can bind to the different moieties of the required bio-molecules, thus bridging intrinsic inertness of gold. This class of molecules is referred to as self-assembling monolayers (SAM), since they tend to rearrange themselves into uniform coatings on flat metallic surfaces via sideways inter-chain interactions. Figure 1.7 (1) sketches a typical SAM formation. Once the SAM is formed, bio-recognition molecules (antibodies [Anker et al. 2008], peptides [Rérole et al. 2011], proteins, natural receptors [Subrahmanyam et al. 2002]) are anchored to provide a selectivity and specificity toward particular targeted analyte/s (2). Analyte-biorecognition reaction is then transduced into resonant shift dependent on the occupation of total binding sites, which is in specific conditions related to the analyte concentrations in the sample matrix (3). This is only a very simplified biosensing protocol. This subject will be discussed in more details in Chapter 5.

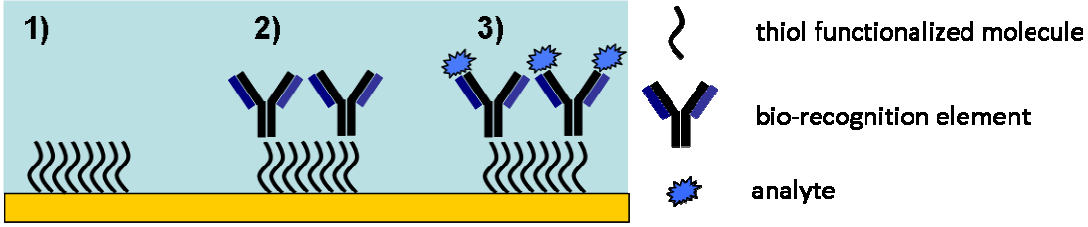

Figure 1.6-Typical biosensing strategy with metallic plasmonic sensors. 1) Surface functionalization with thiol self-assembling monolayers, 2) Bio-recognition anchoring, 3) Capturing of specific analyte

1.5.2. SPR vs LSPR

SPR systems are commonly classified in two groups: SPR spectroscopy and SPR imaging. In SPR spectroscopy, the probing area is determined by laser spot size. Detection principle is based on angle scanning (fixed wavelength), wavelength scanning (fixed angle), or more recently phase, polarization and intensity detection [Homola, 2008]. The need for in-parallel monitoring of large number of reactions, especially in the pharmaceutical industry or in genomics, can be satisfied by SPR imaging systems. In this configuration, an extended beam is uniformly illuminating a large area consisting of many distinct probing locations within. The reflectivity is monitored in real time by a 2-dimensional CCD array, where each or groups of few pixels are recording a particular sub-area. The angle and the wavelength are fixed to "near resonance" condition, and any local refractive index change will provoke change of light intensity reaching corresponding pixel(s) of the CCD. Besides the optics required for parallel inspection, the biggest challenge here represents the spatially distinct surface functionalization with different probes. The density of probing locations should be high and without cross-contamination during substrate preparation. The main techniques used for accomplishing this are microspotting [Shumaker-Parry et al. 2004] (as in case of DNA micro-arrays) or smartly designed microfluidic networks [Hu et al. 2010], that can provide a couple hundreds of micrometers resolution. There are numerous SPR platforms proposed and offered for various applications such as in food safety control, environmental monitoring, medical diagnostics, pharmaceuticals, and home-land security [Homola, 2008]. The highest sensitivities reported go as high as 10^{-8} RIU for bulk changes, while standard systems reach 10^{-5} -10^{-6} RIU. Usually, sensitivity and resolution of these systems is inversely proportional to the degree of miniaturization, parallelization, simplicity and cost [Homola, 2006].

What was initially thought of as the main advantage of LSPR, was its extreme miniaturization down to the level of a single particle biosensor [Dondapati, 2010]. Single particle sensors with attomolar sensitivities have been demonstrated recently [McFarland and Van Duyne, 2003], as well as high-throughput LSPR, where tracking just a few particles at the same time was demonstrated [Bingham et al. 2009]. Still, there are very serious issues related to single particle sensors. The first one is a direct consequence of the relatively complicated detection schemes requiring complex and expensive optics. Typically, detection is performed in dark-field configuration, where collection time can be in the best case on the order of ten of seconds. In an ideal case, this is background-free detection, but when monitoring real-time reactions in complex matrices (whole blood, serum,) many other interferents (cells, agglomerates of different kind) can cross light path and seriously perturb the measurement. What is rarely mentioned is the low reproducibility of the sensing characteristics of single nanoparticles, regardless if they originate from the same batch or appearing homogenous under TEM. Considering cumbersome selection and discrimination between particles with very low repeatability (even considering only one particle and repeated sensing events) have made the concept of single-particle LSPR sensor less likely to become widely and routinely used. Thus, when talking about LSPR sensors, as a rule the sensing area consists of random or regular collection of nanoparticles. In this thesis, the nanoparticle arrays are 25×25 μm^2 or 50×50 μm^2 in size (the further miniaturization is not restricted (for instance, 5x5 μm^2)) . They can consist of more than 10^4 nanoparticles and the benefits of signal

collection from a larger number of nanoparticles are multiple. (It is widely accepted that the minimum SPR gold pads are around 10x10 μm^2).The collective response features a much better signal to noise ratio compared to single particle response. Supporting optics is thus simpler, and size and shape fluctuations are averaged. Commonly, extinction measurements are employed, where transmitted light is measured in zero order transmission [Dahlin et al, 2009]. Since the transmitted light saturates CCD fast, temporal resolution can be as high as 1ms, allowing temporal averaging for further noise reduction. Besides temporal averaging, spatial averaging of individual nanoparticle response is highly desirable for statistical approaches that are valuable in biology. Throughout this thesis, all of the sensing experiments are performed on regular arrays of gold nanoparticles if not stated differently.

Direct comparisons of SPR and LSPR systems are rarely reported in the literature. One direct comparison was conducted in the group of Van Duyne in 2004 [Yonzon et al. 2004]. The target analyte was Concanavalin A (ConA) that was specifically recognized by a mannose terminated self-assembled-monolayer. In this set-up a commercial angle-dependent SPR system on a gold film was compared with specific triangular arrangement of silver nanoparticles. The real-time responses showed the same dynamics of the ConA association phase (binding), while the dissociation phase (where non-specifically or loosely bound ConA molecules were rinsed off) showed a signal drop of 60% for SPR and 14% for the LSPR systems. Without comparing the sensitivity of both systems but rather directing the discussion towards the difference of associated molecule kinetics, the authors focused on developing models for the analyte dissociation and loosely bound molecule removal. With all specificity of surface chemistry on planar film and nanoparticles, the discrepancy in the signal can be attributed mainly to the bulk refractive index sensitivity difference between SPR and LSPR. The supreme bulk sensitivity of SPR detects the difference between solution of ConA in a buffer and a plain buffer during the washing step.

Another more comprehensive study by Svedendahl et al. presents a comparison in a more elaborative way in attempt to use identical components and methods wherever possible [Svedendahl et al. 2009]. By keeping similar experimental conditions for real-time SPR and LSPR sensing, conclusions are meant to be more general. The authors used the same light source and a similar illumination conditions, same material (gold) engineered to support similar resonances of LSPR (random nanodisk arrays) and SPR (50nm thick film) at λ_0 =700 nm, same data processing algorithm. Beside the verification that bulk sensitivity of SPR exceeds LSPR by 20 times, the resonant shift upon streptavidin binding to biotinylated-BSA non-covalently functionalized gold are almost coinciding, where binding dynamics was a bit faster for LSPR. Although this experiment compares very similar SPR and LSPR systems, the question about the absolute winner still remains open. The most sensitive SPR systems utilize angle scanning due to sharper peaks and higher dispersion of SPR as function of coupling angle, and not wavelength tracking. On the other hand, determining the most sensitive LSPR system is also still an open question as the sensitivity strongly depends, as it is going to be demonstrated in this thesis, on the actual nanoparticle geometry.

The main differences between SPR and LSPR systems can be summarized as follows:

- The most obvious difference is in the complexity of the supporting optics. SPR requires a coupling mechanism (prism, grating or waveguide coupler) which is not necessary for LSPR systems.

- Intrinsic difference between extended and localized surface plasmons is the field confinement which defines the sensing volume. SPPs extend much further into an analyte matrix. LSPR evanescent fields are more confined with a decay length being typically 1 order of magnitude smaller. As a direct consequence, SPR systems are much more sensitive to bulk refractive index changes (a couple orders of magnitude). This advantage of SPR in bulk sensing, is not advantageous over LSPR for bio-molecular detection. First, the sensing volume of the LSPR can be as small as the analyte molecule, thus increasing the detection volume-analyte overlap there by decreasing the influence of bulk matrix background in real-time measurement (chapter 4). Additionally, the large sensitivity to the bulk refractive index, as in the SPR case, requires cumbersome active temperature control and feed-back that adds complexity to the experimental setup.

- Surface chemistry and assay protocols for different applications are already developed for SPR. Most of the protocols will also work for LSPR due to same materials employed, with the difference being in passivation of the substrate, which consists largely of glass. Also, due to the smaller sensing surface, kinetics are faster for LSPR.

- Nowadays, SPR substrates are generally much cheaper, but with alternative parallel nanofabrication (colloidal lithographies, nano-imprint, etc.) the cost of LSPR substrates can be reduced significantly.

On the other hand, both systems share common advantages. One of the most important is the compatibility with microfluidics, and with integrated photonics components [Wong et al. 2011]. Plasmonic sensing can be combined with other techniques that can provide complementary information such as SERS [Margueritat et al. 2011], electrochemistry and plasmonic trapping.

1.6. Conclusions

Since the SPR field is now very mature one, further development goes in line with commercial market demands, while the additional advances in the sensitivity levels are not obvious. The common approaches involve different labelling strategies, employing typical mass labels (sandwich assays or metallic nanoparticle labels). This actually cancels the inherent advantage of SPR or LSPR over other sensors based on labelling (for instance ELISA). Enzyme reactions for increased sensitivity (known in SPR) have been recently demonstrated in LSPR [Lee et al. 2011, Chen et al. 2011]. Nevertheless the sensitivity limit of nanoparticle systems can be pushed in many ways, and one of them, based on squeezing of sensing volume is among the subjects of this thesis. Another advantage of LSPR is the faster dynamics due to smaller sensor surfaces. However, LSPR sensors require substrate passivation schemes, contrary to SPR. Special care must be taken when designing LSPR sensing protocols, due to the very fast decaying EM fields (very small sensing range), thus keeping analyte of interest as close to the nanoparticle surface as possible. This problem gets more

pronounced with a decrease of the sensing volume, as in the case of close-coupling between adjacent nanoparticles.

The commercialization of LSPR technology has already started, but whether the LSPR sensors will survive the competition, it is yet not certain. Expectantly, this thesis will provide more insights into the future of LSPR sensors as parts of lab-on-a-chip devices.

Chapter 2

Methods for plasmonic lab-on-a-chip devices

The development and practical realization of an opto-fluidic LOC device requires a variety of know-how from different fields: plasmonics, nanofabrication, microfluidics and chemistry. Before fabricating a prototype, it is highly desirable to be able to model the device, understand the underlying physics and to choose the optimum fabrication protocols. Additionally, to adapt LOC platform toward a particular function such as in the case of LSPR immunosensing device, expertise in surface chemistry is a must while even moderate familiarity with immunology is advantageous.

Manufacturing a LSPR sensing platform (also SERS, plasmon assisted trapping, etc) starts with the fabrication of plasmonic-metallic nanostructured substrates. Once plasmonic nanostructures have been fabricated and characterized (optically, Scanning Electron Microscopy, Atomic Force Microscopy, etc.), a microfluidic network of channels has to be precisely aligned over the patterned substrate, before the final bonding step between them. The device assembly is covered in detail in chapter 6. Assembled plasmon-microfluidic device (henceforth called chip) has to be adequately functionalized with specific bio-recognition elements prior to any particular analyte detection. Every fabrication procedure toward a functional device is important, and special care must be taken for achieving full compatibility (physical and chemical) of the various steps involved.

The first part of the chapter deals with novel nano-fabrication techniques developed to fabricated nanostructures. The second part provides information about modeling tools used to predict/understand the optical properties of referring plasmonic systems. Finally, the basics of microfluidic fabrication are covered, highlighting the active control of the flow via crossed channels by using so called Quake's valves.

2.1. Nanofabrication

The most typical metallic nanoparticle fabrication methods can be classified into bottom-up (wet chemical synthesis) and top-down (lithography) processes. The advantages of wet chemical synthesis are numerous: low cost, fast, large-scale production feasibility, variable shapes (spheres, rod, stars, cubes, shells, prisms) and sizes (from a few hundreds down to few nm), mono-crystalinity, and when not bound to a substrate, they can be used for in-vivo applications (drug-delivery, photo-thermal therapy [Huang et al. 2008]), etc. The disadvantages associated originate from poly-dispersion of shapes and sizes after synthesis, and the difficulty in the precise arrangement and positioning on a substrate. Immobilization of colloids to substrates can be done via surface chemistry among others [Kreuzer et al. 2008], but the arrangement is generally random. A more precise organization of colloidal nanoparticles was recently demonstrated using electron beam lithography (EBL) made template [Malaquin et al. 2007]. The possibility of self-organization of colloids has been investigated for different nanoparticle systems to varying degrees of success [Tong et al. 2009].

Lithography processes are generally resolution limited. Standard optical lithography is a diffraction limited process and standard UV writers provide a resolution of about 0.5-1 μm that is not sufficient for nanoparticle fabrication. Among the available techniques with sufficiently high resolution are the EBL and focused ion beam (FIB) milling. The FIB milling is a serial (scanning) technique where an accelerated ion beam removes material. The resolution is below 50 nm, but the method can be limited by problems related to heavy ion implantation and milling depth control. The larger nanostructure fabrication by FIB is rarely used, because it is a very time consuming and costly process (too much of the metallic substrate has to be removed). To relax time necessary for FIB processes, typically a substrate preparation by optical lithography or EBL is carried out before, where the smaller metallic areas are pre-patterned with sizes optimized for more time efficient FIB milling.

As we have already seen, top-down nanofabrication approaches are generally cost-ineffective and slow. The new classes of bottom-up techniques offers cost reduction, parallel and large-scale fabrication. These methods are based on the widely utilized microspheres that tend to self-assemble on substrates, prior to or after the material evaporation. It is worth mentioning that nanosphere lithography can produce triangular structures in the special arrangement [Haynes and Van Duyne, 2001], nanoholes [Jonsson et al. 2010], nanodisks and nanorings [Aizpurua et al. 2003], and many more. The disadvantage is reflected in a limited size and shape flexibility and the arrangement control of such structures. One very promising technique is nano-imprint lithography (NIL), where a large stamp, premade by EBL is transferred under pressure and heat to the substrate covered by appropriate resist [Chou et al. 1996,1997]. The drawback of NIL is that resolution is limited by EBL, and usually is deteriorated further due to mask transfer steps.

The fabrication of plasmonic nanostructures with nanometric control over size, shape and spatial arrangement is most often performed by what is considered as one of the most flexible technique at the research laboratory level, i.e., EBL. In this thesis, the patterning of the plasmonic systems is exclusively made by EBL. EBL is based on precise scanning and exposure of electron-sensitive polymer resist by a focused electron beam. By the absorption of the electron energy, polymer molecules can undergo structural changes [Cui, 2005]. If the locally exposed polymer can be easily dissolved in a developer solution it is called positive and in the opposite case when the unexposed polymer can be dissolved, then is called negative resist. The resolution of typical EBL resists is currently around 10 nm. However resolution of the process is determined by beam spot size, accelerating voltage of the system and by chemistry. Apart from the cost and time inefficiency, EBL enables high-accuracy especially in positioning.

2.1.1. Positive electron beam process in combination with lift-off

Within the framework of plasmon optics, most EBL applications employ procedures based on a positive resist. In a standard procedure a thin layer (10 nm) of indium tin oxide (ITO) is deposited on top of a glass substrate prior to the polymer resist spin coating. After short heating, ITO becomes transparent and conductive. Positive resist, such as PMMA, is spin coated and typically baked 3h at 160^{o}C in order to remove solvent. The resist exposed by EBL (Fig. 2.1 A), is developed for certain time and exposed areas are dissolved (Fig. 2.1 B). The following step can be descum process with reactive ion etching (RIE), where a gentle oxygen plasma etches homogeneously the resist with the aim of removing the resist debris inside exposed regions. The developed polymer template is ready for the material deposition (Fig. 2.1 C). Additionally, thin conductive layers (1-2 nm) of titanium (Ti) or chromium (Cr) are deposited below the metal to assure good particle adhesion to glass substrate. The following step is called lift-off, where the underlying resist is dissolved, leaving the gold pattern on substrate (Fig. 2.1 D).

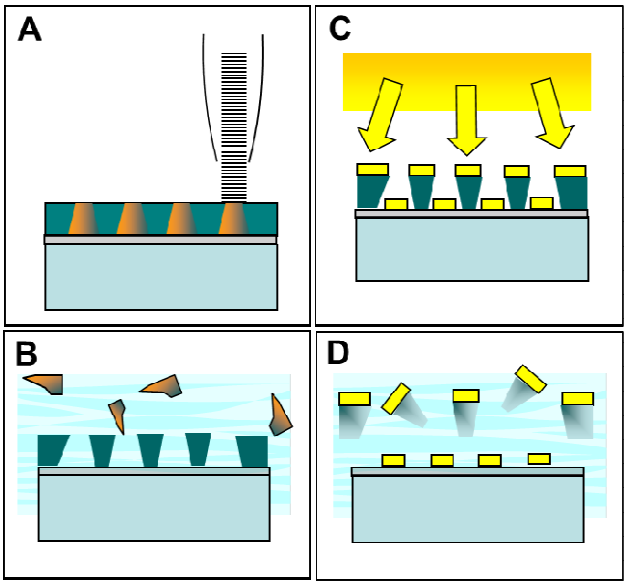

Figure 2.1- Preparation of metallic nanostructures by EBL based on positive electron beam resist. (A) Patterning of the spin coated resist over conductive ITO. (B) Resist development (exposed areas are dissolved). (C) Gold evaporation. (D) Lift-off process (dissolving remaining resist).

It is worth noting that, samples used for scanning electron microscopy (SEM) and/or EBL lithography need to be conductive, in order to discharge the accumulated charges of the beam. A thin ITO layer (10 nm) allows for such charge evacuation. However, since its absorption, it represents an additional loss channel for the plasmon decay. In other words, it dampens and broadens the resonances. Additionally, the relatively high refractive index of the ITO (around n=1.9 in visible spectrum) red-shifts the resonance of the nanoparticles due to the increased refractive index in comparison to glass substrate (n=1.52). This might be critical when it is necessary to tune the plasmon resonance to shorter wavelengths (< 600 nm in water). Alternative process relies on the deposition of a thin gold film over the resist layer. The

subsequent exposure is done through this metallic film. In a later step, the gold film is selectively removed with KOH before the resist is developed [Jain, Huang & El-Sayed, 2007]. Nonetheless, this process requires EBL system with high acceleration voltage (100 kV), in order to ensure maximum resolution. On the other hand the descum process can be avoided, but it might improve adhesion of particles. Thin layers of chromium (Cr) or titanium (Ti) induce losses as well as ITO [Otte et al. 2011], with the additional risk of molecular non-specific binding if used for biosensing [Haes et al. 2005]. The resist thickness is generally recommended to be 3 times the thickness of evaporated gold for successful lift-off. To improve lift-off, two layers of different electron sensitive polymers (different molecular

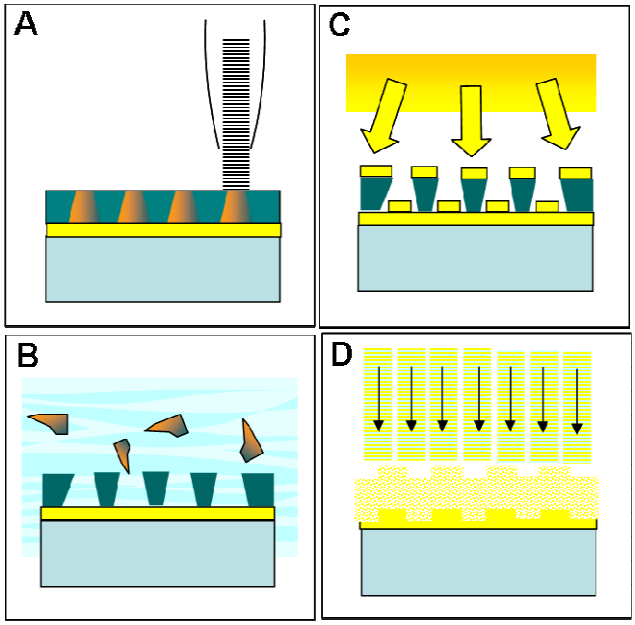

Figure 2.2-Nanofabrication with a positive electron beam resist in combination with lift-off and reactive ion etching (RIE). (A) Patterning the spin-coated resist over gold film. (B) Resist development (exposed areas are dissolved). (C) Gold evaporation. (D) After lift-off process, the gold pattern is transferred to underlying gold film by the RIE process

weights) are spin coated on top of each other. This combination produces better undercut profile that facilitates lift-off [Zhang et al. 2009]. Lift-off optimization is a crucial step, since it typically determines the overall process quality. Generally, the remaining resist is dissolved in acetone or di-chloro-methane under specific conditions (temperature, stirring, sonication, time duration).

To probe the adhesion and feasibility of the nanoparticle fabrication without any ITO layer, sticking Cr or Ti layer, the following fabrication process was adopted. Instead of ITO, a gold film of the same thickness as intended nanoparticle's height was evaporated on the previously cleaned glass substrate. PMMA resist is spin coated, and the pattern is exposed (Fig. 2.2 A). The exposed resist is developed (Fig. 2.2 B), and a descum process followed by a second gold evaporation is performed (Fig. 2. 2 C). After the lift-off a gold pattern on top of gold film is created. This pattern is transferred to the continuous film below by anisotropic (directional) argon plasma etching (Fig. 2.2 D). Nanoparticles fabricated in this way show better adhesion to glass, than nanoparticles made by direct evaporation through patterned positive resist without Cr/Ti (Fig. 2.1). They can generally withstand moderate ultrasounds for minutes.

Sonication resistance is appreciated, because it is widely used for removal of loosely bound or physisorbed molecules from sensing areas. The comparison of spectra between nanoparticles (disks of ca. 100 nm in diameter, 40nm height, arranged in rectangular periodic array of 200x400nm) fabricated via both processes, reveals that absence of ITO and Ti increases the magnitude of the resonance peak (Fig. 2.3). The full-width-at-half-maximum (FWHM) of both peaks is similar (ca. 100 nm), while the central peak position is slightly blue shifted for nanoparticles directly located on glass (due to the absence of ITO). Beside the different magnitude (which is important for noise reduction in real-time LSPR sensing [Dahlin et al. 2006]), the FWHM generally improved slightly when not using any absorbing layer. Additional advantage was noticed when attempting the fabrication of closely coupled nanoparticles. In line with Chapter 3 (Fig. 3.11), the absence of additional layers improved the smallest obtainable gap.

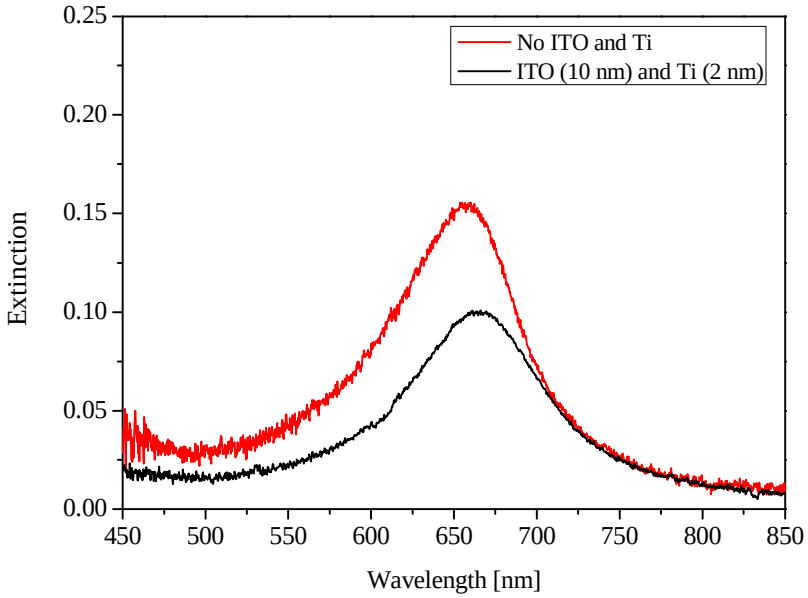

Figure 2.3-Influence of ITO (10nm) and Ti (1nm) adhesive layers. Extinction spectra of similar nanoparticle array fabricated with two different methods, as outlined in Fig. 3.1 and Fig. 3.2.

2.1.2. Electron Beam Lithography with negative resist combined with Reactive Ion Etching

While the fabrication process based on PMMA and RIE showed some improvement, still it suffered few limitations. First one is related to the lift-off step itself, which determines the quality of the samples. The somewhat uncontrolled nature of the lift-off process restricts the level of reproducibility, particularly when attempting patterns in which gaps between adjacent structures are smaller than 15 nm. The other issue is related to the evaporation step. If the sample cannot be evaporated with material at normal

incidence, the nanoparticles obtained will be distorted and the final result will depend on the orientation of the sample inside the evaporator. Non-vertical evaporation is in some cases very useful, and by controlling the angle between source and sample many interesting nanoparticle shapes can be fabricated [Zhao et al. 2011]. However, exposed circular nanodisks can end up being ellipsoids. The effect is very pronounced when exposing closely-coupled nanoparticles aimed at being symmetrical (for instance, honey comb geometry; see Chapter 4.).The rotation of a sample during the material deposition can make structures perfectly symmetrical but with that comes a further increase of the slope of the vertical metal walls of the exposed patterns. Intrinsically, even during vertical material deposition, the upper opening in the PMMA template is shrinking while depositing the material. Thus instead of cylinders, nanoparticles usually resemble to "tip-less cones" with slope characteristic to particular process parameters (Fig. 3.5. A) All this combined with unavoidable slope produced by RIE make that the nanoparticle shape can deviate very much from perfect cylinder.

To circumvent problems related to lift-off and rotation during evaporation, negative tone electron beam resists can be used. Traditionally, it was believed that negative resist suffer low resolution. However, new families of negative electron beam resists with improved properties became commercially available. Negative resists of choice were AR-N 7500.08 and AR-N 7520.073 (Allresist, Germany). The fabrication procedure is sketched in Figure 2.4. The patterned negative resist functions as mask that protects the gold underneath during the subsequent plasma etching (Fig. 2.4 C). The finishing step is selective removal of remaining mask by mild oxygen plasma (Fig. 2.4 D). The described method is very advantageous, since resolution is then only limited by the resolution of the EBL and its stability. As we will see in Chapter 4, fabricated structures are more uniform and smaller gaps are achievable.

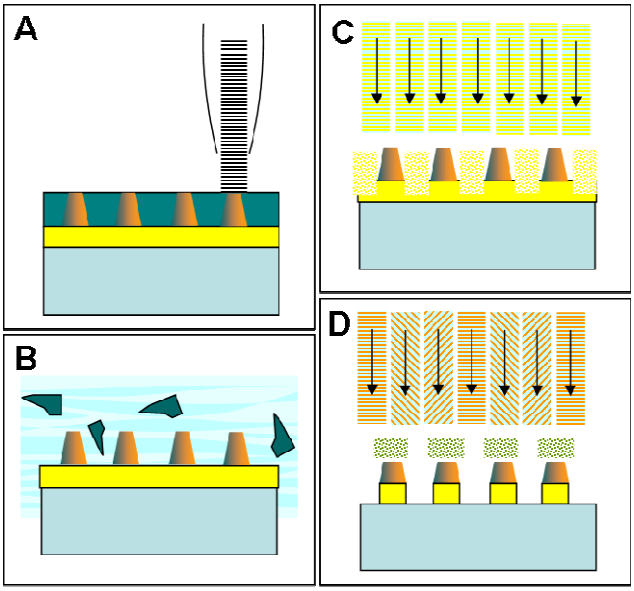

Figure 2.4-Electron Beam Lithography with negative resist in combination with RIE. (A) Resist patterning. (B) Resist development. (C) Selective gold etching. (D) Mask stripping.

To inspect the fabricated nanostructures by SEM, the samples have to be covered with a conductive polymer (e.g. Aquasave, Mitsubishi) or by a thin metal layer (5-8 nm of Cr or Ti). Aquasave provides poor resolution for imaging of nano objects, but can be easily removed in water. Metallic layer gives better resolution, but after imaging the sample is generally wasted (in case sample needs to be used further for molecular binding studies, etc). If the imaging is necessary during some multi-step procedure, thin ITO layer can be buried 50nm deep inside glass substrate prior to nanoparticle fabrication. However, for proper periodicity of nanoparticle arrays the ITO layer can guide light and the spectra can become complicated due to LSPR-guided mode coupling [Linden et al. 2001]. Figure 2.5 shows the direct comparison between the two fabrication processes for the nanoparticles disk dimer arrays. The standard lift-off process with underneath ITO layer allows higher resolution SEM imaging (Fig. 2.5 A). The image shown in the Fig. 2.5 B is obtained through a thin Cr layer deposited, revealing a higher degree of homogeneity but with lower image resolution. Though this type of comparison is already quite explicit, the discussion in chapter 3 evidences further into the favor of the negative resist/RIE method.

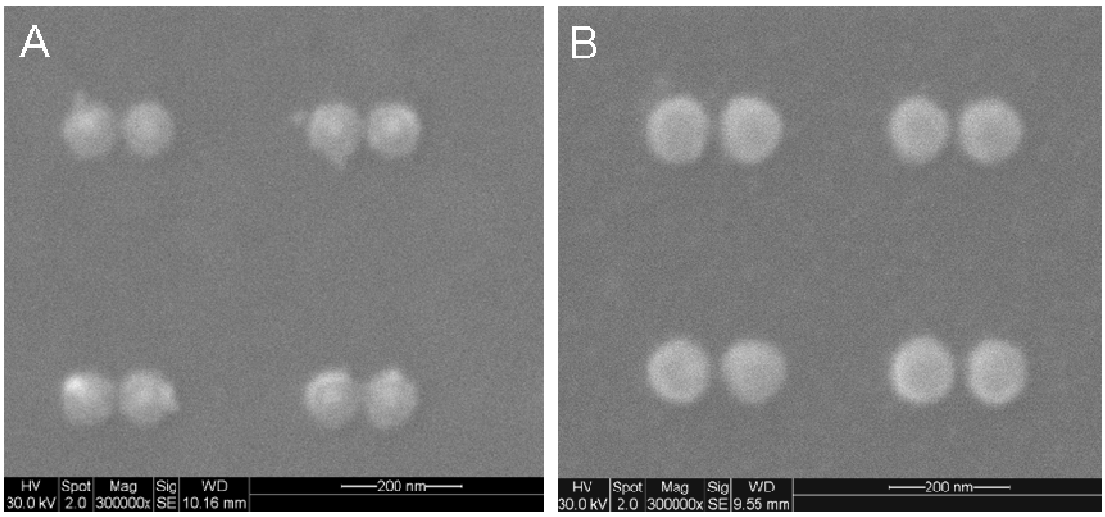

Figure 2.5-SEM images comparing dimer structures obtained by A) positive resist (PMMA) and lift-off B) negative resist and RIE fabrication procedures. Image A) clearly suggests the conical shape of nanoparticles, while in image B) such details are lost due to thin overlaying Cr layer

2.1.3. Multi-step lithography techniques

More complicated planar nanostructures can be achieved through multiple lithography steps. With properly designed aligning marks, it is possible to employ different processes and different resist in the fabrication sequence. Recently, double layer EBL was employ for fabrication of nano-size Yagi-Uda antenna coupled to a quantum dot [Curto et al. 2010]. Additionally, vertically emitting Yagi-Uda nano-antennas were also reported, where the fabrication procedure consists of multiple EBL steps [Dregely et al. 2011]. As an example, we have fabricated special array of TiO_2 nano-pillars in front of a semi-infinite gold film by a combination of negative and positive resists processes (Fig. 2.6). On top of a continuous gold film, 200nm thick layer of TiO_2 was sputtered, followed by 100 nm of gold. The pillars were patterned using a negative resist, which served for preparation of gold mask. After RIE of the gold, the

remaining gold pillars (100nm height) were used as masking material for selective TiO_2 etching (etching rate TiO_2:Au was 2:1) with mixture of Ar/SF_6 in the plasma. Figure 2.6 (A) shows SEM image after first fabrication step. Subsequent semi-infinite gold carpet was fabricated with standard PMMA/lift-off process with precise alignment (Fig. 2.6 (B)). These types of structures were used to demonstrate SPP cloaking at visible frequencies [Renger et al. 2010].

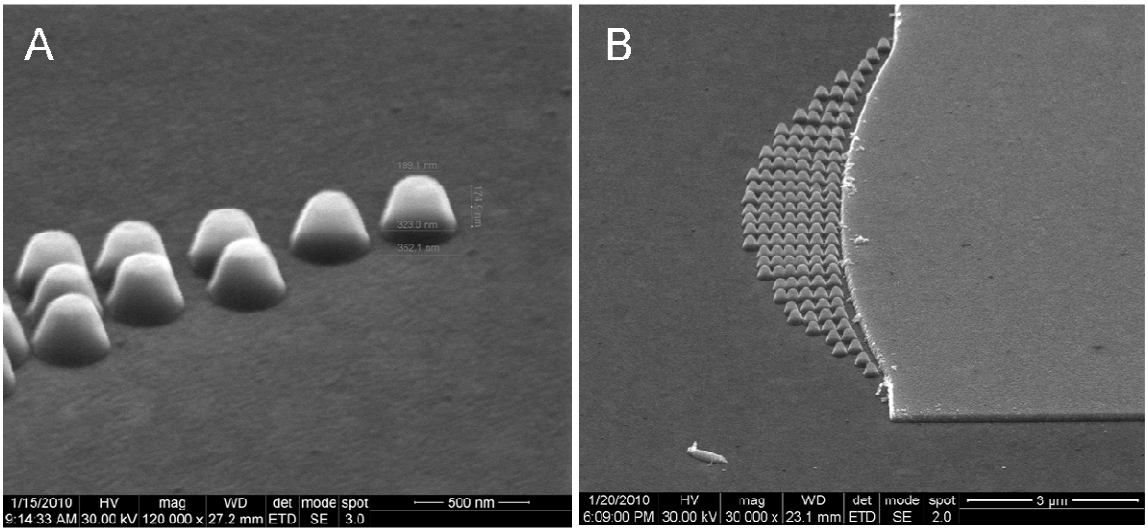

Figure 2.6-SEM images of the combined EBL processes. A) The TiO_2 nano-pillars are fabricated with negative resist and RIE. B)The semi-infinite gold film is added by a second lithography step using a positive resist and lift-off. The positive resist debris at the border of the film can be removed by a mild oxygen plasma treatment.

2.2. Modeling tool - Finite Element Method (FEM)

Finite Element Methods are well suited for solving partial differential equations (PDE). Briefly, it is based on an appropriate truncation and discretization (meshing) of the space. Solutions of the problem are generally computed in the nodes of the discretization units (meshing elements), and interpolated everywhere else inside each other element, accordingly [Jin, 2002].

The FEM based software package COMSOL Multiphysics 3.4 and later version 3.5a were used throughout this thesis. COMSOL comes with different graphic user interfaces (GUI) organized in modules (AC/DC, Heat-transfer, Acoustics, Fluid mechanics, etc.) that are adopted for various classes of problems in physics described by PDEs. I used exclusively the radio-frequency (RF) module. The availability of GUI in COMSOL might lead to conclusion that it is very easy to use. Surprisingly, it is sometimes tricky, since very important information about "syntax of the programming codes" is hidden behind the GUI while the manuals are of limited value. It is worth mentioning a serious software bug of erroneous perfectly matching layers (PMLs) implementation in versions 3.5 or older, which gives intense reflections instead of being perfectly absorbing. Many users (including me) were not aware of the problem for a long period of time until the company released a patch for COMSOL 3.5a that fixed this problem.

Altogether, COMSOL is a very young software package, with the lack of a proper and detailed manual for beginners and with frequent software bugs. However, its potential is significant, due to unrestricted

modeling flexibility, and its ability to respond to the majority of problems that a physicist may encounter. Additionally, COMSOL is compatible with Matlab, hence it is possible to perform full parameterization of any model built initially in COMSOL (variables, geometry, meshing density, etc.). Also, subsequent manipulation of solved variables can be implemented by MATLAB (for instance, near-to-far field transformations [Miljković, 2011]). "Multiphysics" feature of COMSOL allows solving of coupled physical phenomena that take place in same (or overlapping) geometry space by combining multiple modules, for instance fluid dynamics, RF and Heat-transfer modules [Donner et al. 2011] .
The following paragraph gives a short overview of the RF module with explanation of how to set a model in a proper way. The difference between solving model in harmonic propagation module (total field) and scattering harmonic propagation (scattered field) is discussed. Throughout this thesis, results of the modeling of very complex structures will be presented. More details about RF module are available in a online manual for beginners that was written over this thesis [Aćimović, 2011].

2.2.1. Basic EM theory used in COMSOL RF module

COMSOL solves numerically a very general Helmholtz's equation derived from the set of Maxwell´s equations:

$$\nabla \times \mathbf{E} = -\frac{\partial \mathbf{B}}{\partial t} \qquad \text{(Eq. 2.1)}$$

$$\nabla \times \mathbf{H} = \mathbf{j} + \frac{\partial \mathbf{D}}{\partial t} \qquad \text{(Eq. 2.2)}$$

$$\nabla \cdot \mathbf{D} = \rho \qquad \text{(Eq. 2.3)}$$

$$\nabla \cdot \mathbf{B} = 0 \qquad \text{(Eq. 2.4)}$$

An additional set of constitutive relations is necessary for the description of any classical EM problem: $\mathbf{D} = \varepsilon_0 \varepsilon_r \mathbf{E}$, $\mathbf{B} = \mu_0 \mu_r \mathbf{H}$ and $\mathbf{j} = \sigma \mathbf{E}$. Here $\mathbf{E}$, $\mathbf{H}$, $\mathbf{D}$, $\mathbf{B}$ and $\mathbf{j}$ are the electric field, the magnetic field, the electric displacement, the magnetic flux density and the current density vectors respectively. The scalar ρ is the electric charge density, while ε_0 and μ_0 are permittivity and permeability of vacuum whereas, ε_r, μ_r and σ are the relative permittivity, relative permeability and electric conductivity, describing EM properties of materials.

Substituting the constitutive relation $\mathbf{B} = \mu_0 \mu_r \mathbf{H}$ into (Eq. 2.1), and the application of the curl operator yields to:

$$\nabla \times (\mu_r^{-1} \nabla \times \mathbf{E}) = -\mu_0 \frac{\partial}{\partial t} (\nabla \times \mathbf{H}) \qquad \text{(Eq. 2.5),}$$

Substitution of equation (Eq. 2.2) and constitutive relations into (Eq. 2.5) yields

$$\nabla\times(\mu_r^{-1}\nabla\times\mathbf{E}) = -\mu_0\frac{\partial}{\partial t}(\sigma\mathbf{E} + \varepsilon_0\varepsilon_r\frac{\partial\mathbf{E}}{\partial t}) \qquad \text{(Eq. 2.6)}$$

COMSOL employs $e^{(j\omega t)}$ time dependence convention, thus taking derivates in (Eq. 2.6) with respect to the time, we end up with the general equation for the electric field that is solved by COMSOL, as

$$\nabla\times(\mu_r^{-1}\nabla\times\mathbf{E}) - \mathbf{k}_0^2(\varepsilon_r - \frac{j\sigma}{\omega\varepsilon_0})\mathbf{E} = 0 \quad \text{(Eq. 2.7)}$$

In (Eq. 2.7) j is the imaginary unit, $k_0 = \frac{\omega}{(\sqrt{\mu_0\varepsilon_0})^{-1}} = \frac{\omega}{c}$ is wave-vector in vacuum (c is speed of light in vacuum). Similarly, COMSOL can also solve the magnetic field as the independent variable, the corresponding equation (obtained in similar manner as (Eq. 2.7)) is

$$\nabla\times((\varepsilon_r - \frac{j\sigma}{\omega\varepsilon_0})^{-1}\nabla\times\mathbf{H}) - \mathbf{k}_0^2\mu_r\mathbf{H} = 0 \qquad \text{(Eq. 2.8)}$$

The materials are described by setting ε_r, μ_r and σ, or alternatively by the refractive index n. The latter definition assumes in (2.7) or (2.8) that $\varepsilon_r = n^2$ and $\sigma = 0$, allowing n to be complex for absorbing or gain media.

2.2.2. Boundary conditions and Perfectly Matched Layers (PMLs)

To complete the description of the EM problem, boundary conditions (BC) need to be imposed on all external and internal boundaries or interfaces in the model. Typically, BCs in/of nanoparticles are:

1) Continuity

Continuity BC imposes continuity of tangential components of the fields across boundary.

2) Scattering BC

Scattering (SC) BC allows scattered waves with precisely defined k-vector to pass the boundary without reflections. They work well for guided modes (similar to absorbing BC), but for scattered or radiated waves from antennas, SC BC can produce reflections. Thus, in scattering problems they are used in combination with PMLs.

3) Port BC

Port BC can be used to define the incident wave by setting mode numbers (e.g. for boundaries that are inlets of wave-guiding structures) or by setting mathematical representation. Simultaneously, Port absorbs well all waves reflected back with the same propagation constant as excitation. The "propagation constant" for the propagating waves in COMSOL is considered to be longitudinal

component of k-vector. If no excitation is defined, it is merely absorbing boundary condition and corresponding propagation constant has to be provided additionally.

4) Periodic BC

Periodic BC imposes equality of the fields on the source and the destination boundaries. The source and the destination boundaries are characterized by the same index numbers.

5) Floquet periodic BC

Floquet BC ensures periodicity with proper phase shifts in propagation direction on the source and the destination boundaries. The source and the destination boundaries are characterized by the same index numbers. Typically, Floquet BCs find application in total field formulation when modeling oblique incidence [Yang and Altermatt, 2008].

6) Perfect Electric Conductor (PEC)

The tangential components of the electric fields are equal to zero. It is generally used when exploiting symmetry of modeled space or modeling perfect conductors.

7) Perfect Magnetic Conductor (PMC)

The tangential components of magnetic fields are equal to zero. It finds application when exploiting symmetry of modeled space.

PMLs are domains that absorb all waves passing through them [Johnson, 2007]. In COMSOL it is important to set the refractive index of the PML to be the same as the adjoining media, in order to avoid abrupt change of refractive index that would provoke reflection. Versions older than the patched 3.5a have a serious bug in PML implementation, resulting in strong reflections inside the modeled space. It is possible to define PML analytically via refractive index edit dialog (for instance, see [Polycarpou and Balanis, 1998]), but in the new versions the default implementation works perfectly. However, when dealing with an interface problems, the boundary between different PMLs induces inevitable reflections [Knight et al. 2009]. These reflections can only be neglected, if PML is set up far away from the scattering entities (nanoparticles).
By default, COMSOL creates a single unified geometry with the BCs set on the external boundaries. However, for some problems the unified geometry cannot yield exact solution. If one wants to use total field formalism (see below), where there are efficient scatterers inside the geometry, PORT BC or SC BC cannot handle efficiently with scattered or reflected waves with longitudinal k-vector components that differ from the incident wave. The only way around is the use of PMLs, more specifically the excitation passes first through a PML where it gets strongly dampened and continues propagating thought the rest of the geometry (PORT cannot be defined at an internal boundary). Although this type of model setting can be used [Liu et al. 2008, Lee and Wu, 2010], it is not recommended because PML can change the k-vector after a wave initially passes through the layer. I compared these settings with more accurate ones (see below) for the case of honey-comb structures (see chapter 3). Both methods provide qualitatively similar extinction spectral shape, although with slightly displaced features (ca. 50 nm). However, it is

quite likely that the observed similarity comes from the fact that models were solved for normal incidence, while oblique incidence might yield more significant differences. To circumvent this problem, the geometry can be decomposed into two separate geometries (source and destination) using "assembly" option, which we link via Identity Pair condition. The boundary that just appears common to both geometries is actually considered being two boundaries that are physically separated. One is defined as the source and other one as the destination. The Identity Pair condition only ensures continuity of reflected waves when passing in the source-destination direction. If we set PORT BC on Identity Pair, it will launch a plane wave into the source geometry, while reflected waves will pass from one part of the geometry into the other. In this way, both geometries can include PMLs that will absorb all reflected waves. The meshing of both boundaries linked by Identity Pair condition is recommended to be identical to avoid any errors due to the discretization and uneven meshing of the boundary.

2.2.3. Meshing (Volume discretization)

Flexibility of the FEM is greatly enhanced if uneven mesh element distribution with mesh elements of various shapes (tetrahedral or prisms in 3D) and sizes can be used. Areas with small radius of curvature have to be truly represented with very fine meshing based on tetrahedral elements. Thus tetrahedral mesh can represent curved objects better than uniform quadratic mesh employed by other methods (DDA for instance). Additionally, where strong field gradients are expected, finer meshing can help to nicely resolve the strong field variations in the solution. Other regions can be coarsely meshed. The number of the meshing elements determines the CPU and memory demand. Thus, one should always go for a compromise – a minimum number of meshing elements that gives a sufficiently accurate solution.
Special attention must be paid to the way the geometries are meshed, not only the density of the mesh matters alone. A symmetrical object should be symmetrically meshed. This is done by meshing the edges of the objects, and then copying them to the identical boundaries. After, subdomains (distinct regions of the geometrical space) are meshed by COMSOL's built-in meshing algorithm, which is now constrained to mesh corresponding object symmetrically. Boundaries that are defined with periodic conditions should be also meshed identically. Any deviation of the symmetrical meshing of objects and/or identical boundaries can produce erroneous results even if the meshing is highly refined. As a consequence, careful meshing can reduce significantly the mesh density used by the free built-in meshing algorithm, thus optimizing the solving time necessary to find a correct and accurate solution.

2.2.4. Total field vs. Scattered field formulation

In the FEM representation every computational domain has to be limited. Outer boundaries are typically enclosed by absorbing boundary condition for scattered and reflected waves. When solving for total electric field (TF) (Eq. (2.7)), scattered field ($\mathbf{E}_{sc}$) can be expressed as $\mathbf{E}_{sc} = \mathbf{E} - \mathbf{E}_{inc}$ (difference between total and incident field). As shown in [Jin and Riley, 2009], substituting this into an absorbing boundary condition for scattered waves yields that the incident field is then directly imposed on the same boundary if $\mathbf{E}_{inc} \neq 0$ (PORT BC or SC BC with excitation can be used for this purpose). The excitation is thus defined on the truncation boundary only, and there should be no other sources inside the domain.

On the other hand, when solving for the scattered field (SCF) equation (Eq. 2.7) becomes

$$\nabla\times(\mu_r^{-1}\nabla\times\mathbf{E}_{sc})-\mathbf{k}_0^2(\varepsilon_r-\frac{j\sigma}{\omega\varepsilon_0})\mathbf{E}_{sc}=-\nabla\times(\mu_r^{-1}\nabla\times\mathbf{E}_{inc})-\mathbf{k}_0^2(\varepsilon_r-\frac{j\sigma}{\omega\varepsilon_0})\mathbf{E}_{inc}\,.$$

If the excitation is described analytically in the background space (geometry without scattering objects), then the right hand side equals to 0 in every domain, except at the border and inside the scattering domains.

The user can choose the field formulation before solving the geometry. These formulations generally deal with similar EM problems, but in COMSOL both formalisms possess distinct characteristics. For instance:

a) Setting up excitation in TF is a light problem (see example below). It is done just by setting mathematical description of entering plane wave on the truncation boundary (PORT BC, SC BC, etc). Normally, in the TF formulation, the definition of the incident field is independent from the complexity of the modeled system, and hence, the presence of many scatterers, numerous dielectric domains and waveguides will not change the definition. However, complexity of the model will influence number and difficulty in setting boundary conditions on the remaining truncation boundaries. In the SCF formulation, as mentioned, the excitation has to be described analytically in the whole background space. This seems easy for an uniform media where the incident field is expressed by $\mathbf{E}_{inc}=\mathbf{E}_o\exp(-j\mathbf{kr})$ [Knight and Halas, 2008], but can be more complicated, such as in the case of a substrate, where the mathematical definition has to include the Fresnel coefficients [Aćimović, 2011]. For the increasing number of dielectric layers, analytical expressions get more and more complicated.

b) In the SCF formulation, the boundary is usually truncated by a SC BC in combination with PML. In TF formulation the choice of BCs can be complicated depending of the complexity of the model. In the case of strong scattering, PORT BC cannot deal with scattered waves (only with the speculary reflected ones), thus the incorporation of PMLs is necessary. This enforces the use of assemblies and identity pairs, which increase the model complexity.

c) Since the accuracy of the solution depends on meshing density, in the TF formulation, the propagation of the excitation has to be solved numerically. This induces a loss of accuracy, because of the accumulation of numerical errors, and very often wave-front bending of plane waves is observed [Kappeler, 2006]. In the SCF formulation, these problems are circumvented by itself, since the excitation is analytically expressed, and not solved numerically.

d) The meshing density of the background in the TF formulation has to be sufficiently fine in order to decrease the accumulated numerical errors during the excitation propagation. In the SCF formulation, the background meshing can be kept coarse. In both cases, the mesh should be refined near the scatterer (where field gradients are expected to be high).

e) The TF formulation is very suitable for infinite periodic arrays, while for single particle calculation on the substrate modeling gets very cumbersome.

f) The TF formulation is suitable for all general problems in optics and photonics (e.g. multilayered films, waveguides, gratings), while application of the SCF is exclusively limited to scattering problems only.

2.2.5. Example: plane wave excitation in TF and SCF

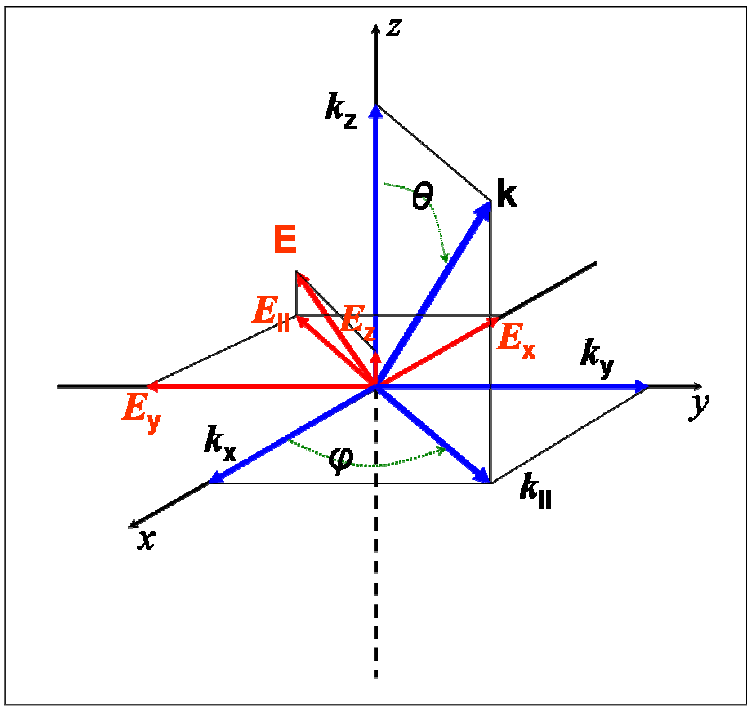

Figure 2.7-Arbitrary free-space propagating plane wave. Electric field vector components are shown in red, while k-vector components are in blue

An EM plane wave can be represented in Cartesian coordinate system with the following set of expressions (Fig.2.7), where time dependences can be disregarded, as:

$\mathbf{E} = (E_x, E_y, E_z)$ where

$$E_x = -E_o \cos\varphi \sin(\frac{\pi}{2} - \theta) e^{j(k_X x + k_Y y + k_Z z)},$$

$$E_y = -E_o \sin\varphi \sin(\frac{\pi}{2} - \theta) e^{j(k_X x + k_Y y + k_Z z)},$$

$$E_z = E_o \sin\theta e^{j(k_X x + k_Y y + k_Z z)}$$

The components of the $\mathbf{k}$-vector are $k_x = k\cos\varphi\sin\theta$, $k_y = k\sin\varphi\sin\theta$, $k_z = k\cos\theta$.

a) Defining plane wave excitation in TF formulation via PORT BC

For the definition of such a plane wave excitation COMSOL offers a dialog to enter E_{ox}, E_{oy}, E_{oz} and the port power level P_{IN}. The port power level is defined as $P_{IN} = \frac{n\cos\theta|E|^2}{2Z_0}S$, where n is refractive index of medium, $Z_0 = \sqrt{\frac{\mu_0}{\varepsilon_0}}$ is free-space impedance and S is PORT area. Since E is determined by port power level, COMSOL needs information about θ, φ, and k vector components only. Thus in the remaining dialog box one needs to put

$$E_{ox} = -\cos\varphi\sin(\frac{\pi}{2}-\theta)e^{j(k_x x+k_y y+k_z z)},$$

$$E_{0y} = -\sin\varphi\sin(\frac{\pi}{2}-\theta)e^{j(k_x x+k_y y+k_z z)},$$

$$E_{0z} = \sin\theta e^{j(k_x x+k_y y+k_z z)}$$

In case of erroneous inputs or by omitting exponential parts, COMSOL makes some assumptions that might confuse the user. If one doesn't define exponential parts of the all k-vector components, COMSOL will assume propagation in the normal direction to the boundary.

b) Defining a plane wave excitation in SCF formulation

The situation gets more complicated in the case of the SCF formalism. The typical example is a scatterer (nanoparticles) in an inhomogeneous environment, e.g. substrate case. Since one has to define the exact solution of the background space in an analytical form, the interface problem has to be solved manually. The solution to this brings us to Fresnel´s coefficient calculation. In the general case (Fig. 2.8) the z axis and the k-vector mark the plane of incidence and one should decompose the plane wave into TM (p-) and TE (s-) polarization. To do that one needs to rotate coordinate system in xy plane by an angle φ, where the new axes are marked as x' and y'. The transformation that links the old and the new coordinate system are $x' = x\cos\varphi + y\sin\varphi$, $y' = y\cos\varphi - x\sin\varphi$ while $z' = z$. In the new coordinate system one can decompose the plane wave into TM polarization where we have $E_x^{'}$, $E_z^{'}$ and $H_y^{'}$, while the other components are equal to 0. For TE polarization the non-zero are $E_y^{'}$, $H_x^{'}$ and $H_z^{'}$. Note that in the new system $k_y^{'} = 0$.

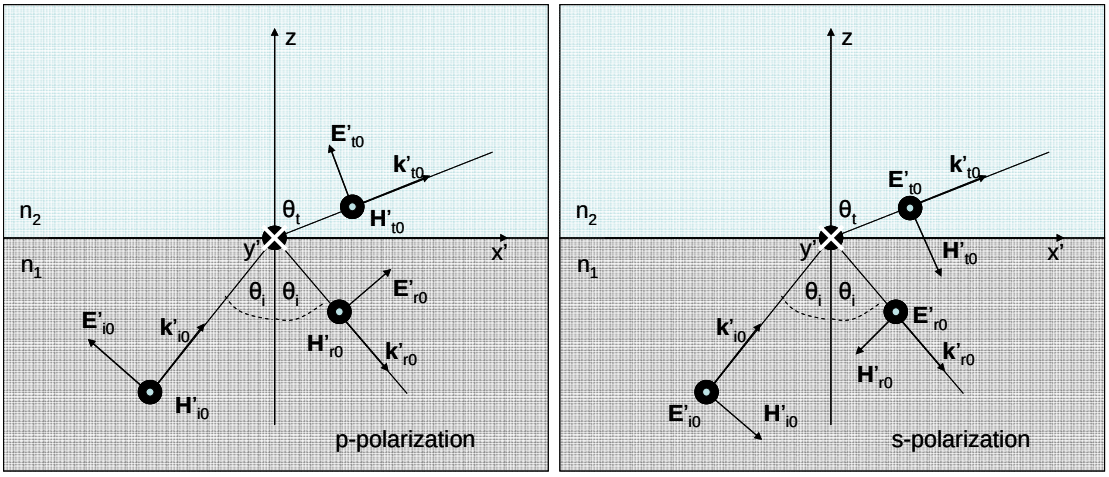

Figure 2.8-Variables used in the Fresnel's equations for TM (p-) polarization (left) and TE (s-) polarization (right)

Thus, for TM polarization (Fig. 2.8, left):

$$E_{x'}^{'} = (z<0)(-E_{op}\cos\theta_1 e^{j(k_{x1}^{'}x^{'}+k_{z1}z)} + r_p E_{op}\cos\theta_1 e^{j(k_{x1}x^{'}-k_{z1}z)}) + \\ + (z>0)(-t_p E_{op}\cos\theta_2 e^{j(k_{x1}^{'}x^{'}+k_{z2}z)}) \quad \text{(Eq. 2.9)}$$

$$E_{z}^{'} = (z<0)(E_{o}\sin\theta_1 e^{j(k_{x1}^{'}x+k_{z1}z)} + r_p E_{o}\sin\theta_1 e^{j(k_{x1}x-k_{z1}z)}) + \\ + (z>0)(-t_p E_{o}\sin\theta_2 e^{j(k_{x1}^{'}x+k_{z2}z)}) \quad \text{(Eq. 2.10)}$$

where $r_p = \dfrac{n_2\cos\theta_1 - n_1\cos\theta_2}{n_2\cos\theta_1 + n_1\cos\theta_2}$, $t_p = \dfrac{2n_1\cos\theta_1}{n_2\cos\theta_1 + n_1\cos\theta_2}$ are the Fresnel's coefficients for TM polarization.

For TE polarization (Fig. 2.8, right):

$$E_{y'}^{'} = (z<0)(-E_{os}e^{j(k_{x1}^{'}x^{'}+k_{z1}z)} + r_s E_{os}e^{j(k_{x1}x^{'}-k_{z1}z)}) + \\ + (z>0)(t_s E_{os}e^{j(k_{x1}^{'}x^{'}+k_{z2}z)}) \quad \text{(Eq. 2.11)}$$

$r_s = \dfrac{n_1\cos\theta_1 - n_2\cos\theta_2}{n_1\cos\theta_1 + n_2\cos\theta_2}, t_s = \dfrac{2n_1\cos\theta_1}{n_1\cos\theta_1 + n_2\cos\theta_2}$ are the Fresnel's coefficients for TE polarization.

Additionally, $\sin\theta_2 = \dfrac{n_1}{n_2}\sin\theta_1$ (Snell's law), $E_{op}^2 = (E_{x'}^{'})^2 + (E_z^{'})^2$ and $E_{os}^2 = (E_{y'}^{'})^2$.

Equations (Eq. 2.9), (Eq. 2.10) and (Eq. 2.11) are the expressions that describe accurately the background field (the solution of the scatterer-free geometry).

This looks rather cumbersome and is very prone to typo errors. If one can reduce the problem to TM polarization or TE polarization only, the complexity is reduced. However it depends on nature of the problem. If there are multiple interfaces inside geometry, defining excitation in SCF formulation gets even more complicated. As mentioned before, the simplicity of the definition of the excitation in the TF formulation is paid by denser mesh everywhere in the model for the calculations of incident field propagation. That can affect the accuracy and demands more powerful hardware.

If the incident angle (θ_1) is equal or larger than the critical angle of the total internal reflection at substrate/superstrate interface, 100% of the light intensity is reflected. The definition of the incident field for SCF in the case of TIR has to be modified once again [Aćimović, 2011], while in the case of the TF the definition stays unchanged.

2.2.6. Detecting coarse meshing and errors in the model settings

One of the inherent problems in FEM originates from the fact that the software will come up with a solution even for models set up in an erroneous way. Typically, the results are compared with other methods, at least for simple models. To detect errors in parameter settings and to determine overall mesh quality the following procedure can be adopted for every model:

a) SCF formulation

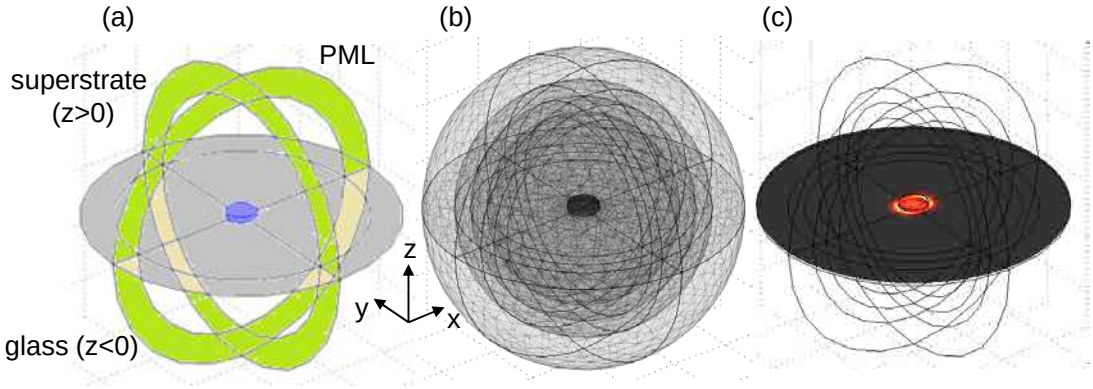

Figure 2.9-Model adopted for SCF formalism. (a) Schematic of the typical simulation domain, consisting of the PMLs, substrate, superstrate, and the nanodisk scatterer. The excitation is defined via analytical formulae (Equations (9), (10) and (11)). (b) Typical mesh density is the highest for the scatterer representation (c) Solution: plot of the scattered field intensity

Before solving the full model, the scattering domains should be turned “invisible”, ie. it’s refractive index should be changed to the refractive index of the surrounding background media so they can blend in. If the PML and the incident field expressions are set properly everywhere, the calculated scattered field amplitude should be very small in comparison to the incident field. (Typically 4-5 orders of magnitude). If a further refinement of the background meshing does not decrease the scattered field amplitude drastically, the background meshing and all parameters are set correctly. On the contrary, very high field amplitude of the scattered field anywhere inside the background model would point out to two possible causes. Firstly, a wrong definition of the propagating excitation may induce reflections (not being the

exact solution of the background model). Secondly, a bad PML implementation (older versions of COMSOL) or bad parameter settings (refractive index of PMLs, thickness, number of meshed layers, etc.) could be the case.
After the previous step is successfully completed, the full model with scatterer can be solved once, and then solved again with a refined mesh of scatterers. If the solution (nanoparticle spectra for instance) does not change considerably with a mesh refinement, the initial (lower) meshing density will do just fine.

b) TF formulation

In the TF formulation, the background meshing and the BCs have to be checked in slightly different manner. After initially solving scatterer-free background model, the transmittance and the reflectance can be retrieved. These can be compared with the results of the T-matrix method. If the difference is too big, the COMSOL model has to be further refined and/or the parameters have to be double checked. Later, the same procedure as in the SCF can be followed in order to determine the minimum mesh density of nanoparticle that gives good accuracy. For each wavelength, the model has to be solved twice, first for the background, and second for the scatterer, in order to retrieve the reflectance, transmittance, and from them absorbance and extinction.

Typical examples of models are shown in Fig.2.9. (SCF) and Fig.2.10. (TF).

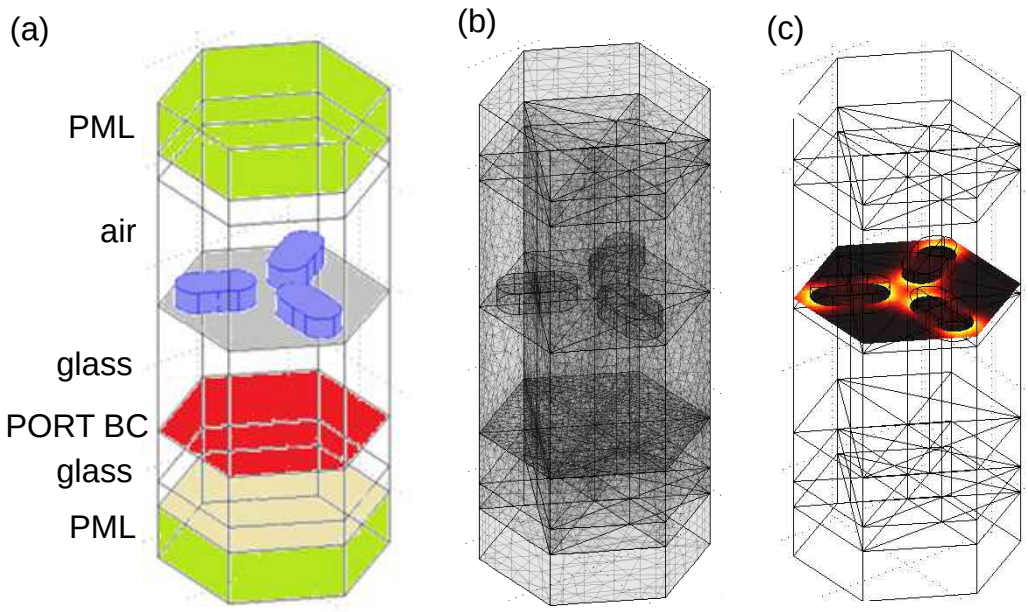

Figure 2.10-Model adopted for TF formalism. (a) Schematic of the typical simulation domain, consisting of PML, substrate, superstrate, scatterer and PML. The excitation is defined via PORT BC inside simulation domains. The two interior boundaries close to the PMLs are used for the boundary integration to obtain reflected and transmitted power (b) Typical mesh density is the highest for the scatterers and the Identity Pair Boundary (c) Calculated intensity of total field .

COMSOL allows linking of the different models and/or geometries. For instance, it is possible to solve the background model in TF formalism with adopted meshing, and then to insert the calculated field as incident field for the SCF model, with a more refined meshing of the scatterer. In this way, by solving the model twice, the computational resources are distributed
in a more optimal way. Also, sometimes it is difficult to analytically express the excitation field for a multilayer background in SCF, and hence, this approach can become very handy.
Throughout this thesis, both formalisms were used. The SCF was used mainly for qualitative resonance prediction and biosensing modeling, due to more flexible memory usage for meshing of thin layers. The TF formulation was used for quantitative prediction of the resonant response of infinite arrays of nanoparticles.

2.3. Microfluidics

Operating miniaturized and parallel plasmonic sensors requires interface with liquid that provides each sensor to be individually addressable without sample cross-contamination or sensor's cross-talk. The properties (mechanical, chemical, optical, etc.) of liquid control interfaces are the most important among the limiting factors that determine the extent of sensor miniaturization for parallel inspection (critical surface density of probing areas). As such, neither the optical detection apparatus, nor the fabrication impose the miniaturization limits, but rather the technology that enables us to control and deliver molecule to the sensors in an efficient manner. Consequently, the liquid flows on micron scale are perfectly matching the practical requirements for the individual plasmonic probes (SPR patches or nanoparticle arrays) [Dahlin, 2012], and the way of controlling the liquid flow is subject of microfluidics.
The field of microfluidics deals the manipulation of fluids at nanoliter scales and below [Squires and Quake, 2005]. Such low volumes are transported through micro-channels with the dimensions of 10-100 μm that are commensurate with plasmonic active areas. A class of biosensors is intended for the detection of biomolecules (proteins, DNA sequences, biomarkers, etc.) that are in the body fluids (blood, saliva, urine, etc.). These liquids can be considered scarce and valuable, imposing the restriction about low volume consumption. Still, reduced consumption requires a very precise control of sample delivery to the sensor (loading, directing the flow, flow velocity, etc.) Fast switching and delivery increases the sensing throughput and additionally enables the precise control of the microenvironment, especially important in cell biology. As a result of its typical micrometer dimensions, the physics and the properties of liquids on micro and nano scales are drastically different from what occurs at the macro scale.
Contrary to everyday experience of turbulent flows, in miniaturized flow systems, flow features are not directed by inertial forces. The inertial forces become overruled by viscous forces and surface effects owing to small volume-to-surface ratio of microfluidics channels. The nature of the flow inside microfluidic channel can be assessed by inertial to viscosity contributions ratio known as Reynolds' number [Squires and Quake, 2005], where its low value designate laminar flows. These types of flow exhibit parabolic cross-section velocity profile. The mixing of laminar flows is not of convective type. Instead, in a simple Y-channel, after merging, two stream lines flow parallel to each other, while the mixing is governed by diffusion of molecules across the interface [Psaltis et al. 2006].

Early microfluidic materials considered were of silicon and glass. Nowadays, materials that find applications are also metals (stainless steel, titanium), various hardened polymers, Teflon, etc. Nevertheless, the dominant role (so far) has been reserved to poly-dimethylsiloxane (PDMS). Among the advantages of PDMS microfluidics let's mention:

- optical transparency in visible and near-IR
- non-toxicity and biocompatibility
- parallel, rapid and cheap fabrication
- elasticity allowing realization of micromechanical valves
- good adhesion to many substrates
- gas permeability
- simple miniature inlet connectors (glue-less)
- surface chemistry modifications

However, there are issues related to the incompatibility to many solvents (especially, organics) and hydrophobicity of PDMS that provokes elevated nonspecific adsorption of proteins and cells.

2.3.1. Passive microfluidics

The passive microfluidics in this thesis denotes flow-through channel networks where fluid is driven only by an external pumping system (syringe, peristaltic or pressure pumps) without any on-the-chip active components that can direct or influence the liquid flow. Normally these systems can perform rather simple operations (Y-shaped channels or H mixers), although interesting functionalities have been reported, for instance 'lymph' valves and 3D networks [McDonald and Whitesides, 2002, Wu et al. 2002]. PDMS microfluidic chips are made by replica molding, as one of the subgroup of a technique known as soft-lithography [Xia and Whitesides, 1998].

The fabrication of passive microfluidic chip consists of the following steps:

1) Optical lithography mask design (and fabrication)
2) Mold fabrication
3) PDMS casting
4) Inlet/outlet hole punching
5) Bonding to the substrate

1) Mask fabrication

A typical optical lithographic mask for cheap and rapid prototyping of microfluidic networks is made by a high-resolution printing on transparent plastic foil, at the expense of reduced pattern quality and resolution. Usually, printed plastic masks are not 100% opaque (transparent), difficult to clean (producing a lot of defects), while sometimes insufficient printing resolution results in ripples at channel walls due to printing pixels. A more sophisticated mask (high-resolution, full transparency/opacity, smooth borders) for optical lithography can be done by EBL patterning with chromium lift-off process (see Section 2.1.1.). An alternative is also a direct laser pattern writing onto photo resist. The author used exclusively transparent foils as optical lithographic masks, with exception of SPEDOC LSPR sensing

chip-prototype 1, where molds were fabricated by direct laser writing by external collaborators (EPFL, Lausanne, Switzerland).

2) Mold fabrication

A silicon wafer is prepared by standard optical lithography, where obtained pattern represents replica of the inverted microfluidic network (trenches correspond to channels). Initially, the wafer coated with photo resist is exposed to UV light through optical mask that contains negative or the positive pattern of microfluidic network depending on the nature of selected photo resist (see Section 2.1.1). Developing reagent leaves only network pattern on the wafer. More particularly, in passive microfluidic processes a relatively thick layer of very viscous SU8 photo resist (SU8 25, Microchem, USA) is spin coated on the wafer. The thickness of the SU8 depends on the spinning parameters and once exposed determines the channel height. All other in-plane dimensions are determined by the mask design. Channel aspect ratio (width/height) in PDMS is recommended not to exceed 20:1, due to otherwise possible channel collapsing (sagging) [Xia and Whitesides, 1998]. Subsequent to UV exposure and development, wafer is baked to ensure hardness of residual pattern, for multiple casting procedures.

3) PDMS casting

Prepolymer PDMS (Sylgard 184 silicone elastomer kit, Dow Corning, USA) 10:1 mixture (oligomer : curing agent) is thoroughly stirred until the mass is homogenized. Resist pattern on the silicon wafer (mold) has to be specially treated to facilitate easy PDMS removal from its surface. Due to strong adhesion of PDMS to glass and silicon surface, a passivation layer has to be pre-formed on the silicon mold, before PDMS casting. One method is based on chemical vapor passivation of trimethylchlorosilane (TMCS) (Sigma Aldrich, Germany) during 15-45 min. TMCS formation is of a temporal character and has to be repeated prior to any subsequent use of the mold. Molds can be permanently passivated by CF_4 deposition in the RIE process (5 min at 80^{o}C). Viscous PDMS residing on the mold gets thermally cross-linked (solidified), thus the pattern is transferred in the polymer. The frame around patterned areas is manually cut out and peeled off carefully.

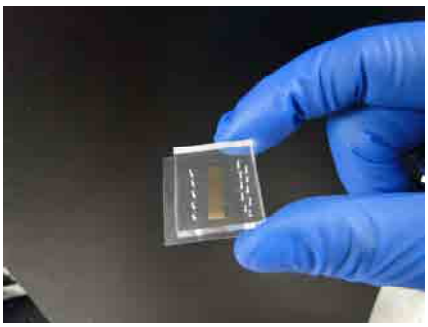

Figure 2.7-An all passive micro-fluidic chip with five individual Y-channels aligned over 50 nm thick, 5 mm wide gold stripe.

4) Inlets and outlets

Instead of bulky plastic connectors that occupy a lot of space on the chip surface (a few mm^2), stainless-steel pins slightly wider than holes perforated in the PDMS can be used [Andrew, 2005]. Elastic PDMS strongly seals to the inserted pins, withstanding very high operating pressures and making these connectors suitable for large scale integration microfluidics [Melin and Quake, 2007, Thorsen et al. 2002].

5) Bonding to substrate

PDMS chip can be bonded to glass substrates reversibly (possible separation without damaging neither the substrate nor microfluidic chip) or irreversibly. Reversible is thermal bonding, but it can withstand moderate operating pressures. Much stronger (irreversible) bond occurs when activated PDMS and glass surfaces are brought into contact and then thermally treated.

As a simple example, a passive microfluidic chip consisting of five isolated Y-channels is shown in Fig.2.11. A 5 mm wide gold stripe is crossing all 5 channels. This system found application for the determination of specific/nonspecific antibody adsorption to different substrates by confocal fluorescence microscopy.
Apart from the limited functionality and the minimum level of automation of the assays interfaced with passive microfluidic networks, an additional nuisance might represent air bubbles, especially critical in real-time LSPR sensing devices. Numerous solutions for 'bubble traps' are devised for different applications and proposed in the literature [Cheng and Jiang, 2009, Edward et al. 2010, Tan and Takeuchi, 2007]. However, the range of microfluidic networks compatible with a majority of the proposed traps is very limited or its implementation raises the fabrication complexity to very high levels [Skelley and Voldman, 2008].

2.3.2. Active microfluidics

Inspired by the rapid miniaturization in the large and very large scale of integration semi-conductor circuits (LSI and VLSI), where millions of transistors and components are integrated into a single functional component (CPU chip, memories, etc), the LOC concept grew very popular in the last few decades in biology and chemistry fields. The LOC vision is a single integrated device capable of performing numerous bio-lab procedures (parallel bio-assays, cell and molecule sorting, etc). In order to achieve such functionality integration, the very precise delivery and control of minute liquid volumes (nanoliters) is a must, thus development of miniaturized and parallel microfluidic system with automation operation, represent a huge step toward making high-end user's LOC possible. A crucial component of such system is certainly the micro-valve. "Traditional" MEMS valves are bulky, complicating successful implementation and miniaturization, while other micro-valves are not flexible and its function might depend strongly on fluid properties [Van Dam, 2006]. Reduction of the number of inlets and outlets without losing functionality of the microfluidic system is also essential for successful LOC miniaturization, since in general, inlet/outlet connectors occupy much more space than the integrated microfluidic network itself, with all functionalities within (chambers, reactors, mixers, etc).

The milestone in LOC R&D was certainly the invention of integrated micro-mechanical valve (MMV) by S. Quake's research laboratory [Thorsen et al. 2002].

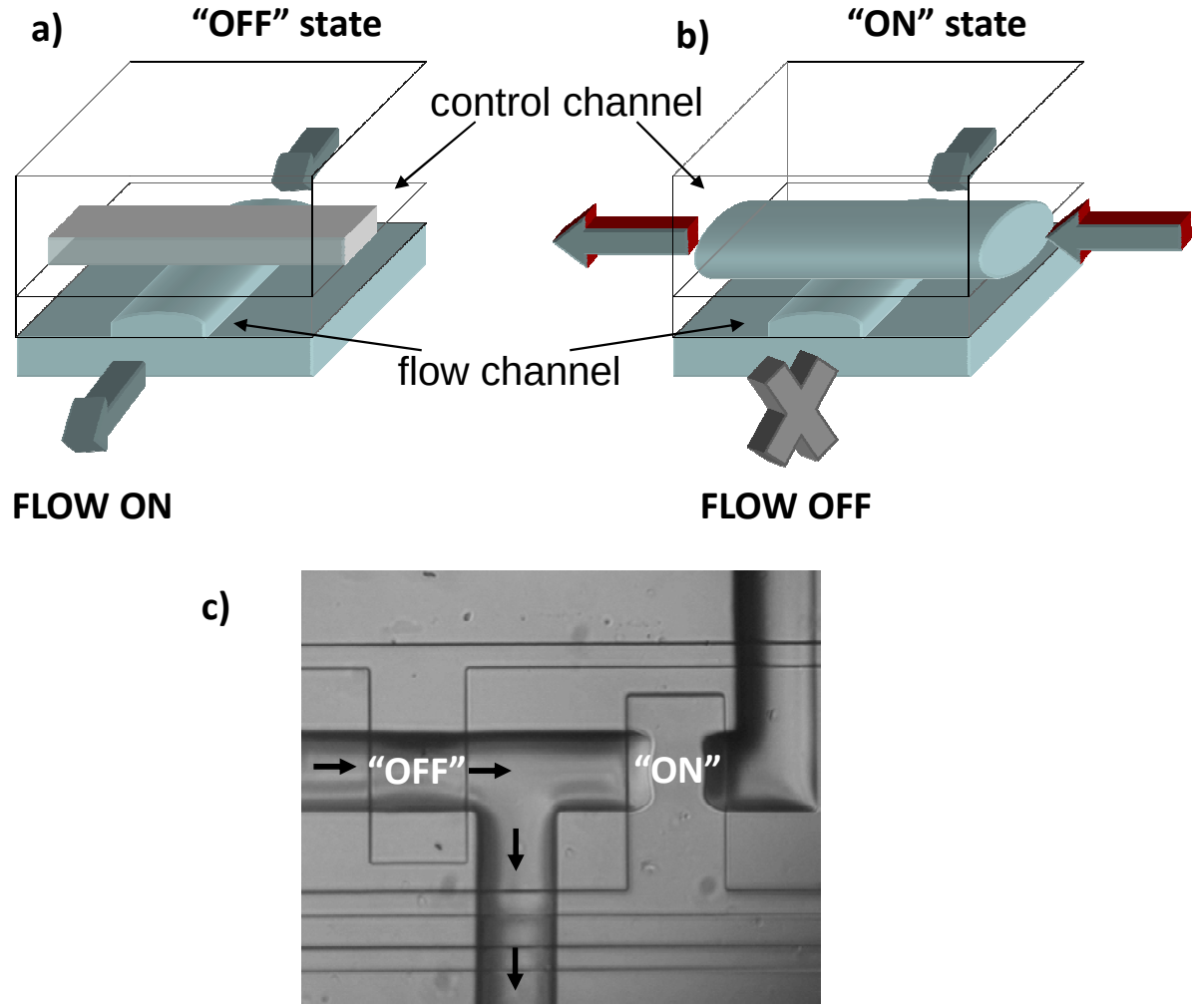

Figure 2.8-Schematic of micro-mechanical valve operation. a) ON state b) OFF state (pressurized upper channel expands and blocks the flow below) c) Photo of ON (left) and OFF (right) state of MMV

Two crossing microfluidic channels vertically displaced by 10-30 µm can form such a MMV, also known as Quake valve [Unger et al. 2000]. One channel is flow channel, while the other is control channel. (Fig. 2.12 (a)). Due to PDMS elasticity, channels expand in transversal direction upon increased driving pressure in the flow. If the pressure in the control channel is large enough to overcome elasticity of the PDMS membrane of the crossing area and the pressure drop inside the flow channel, membrane collapses and blocks the liquid circulation (Fig. 2.12 (b)). Once the pressure of control channel is released, PDMS elasticity (and the flow channel pressure) deflects the membrane back that restores the flow. Therefore, by driving pressure levels in the control channel, flow can be blocked or undisturbed. These functional crossings between two channels are referred as MMVs. Actuating pressure of MMV depends on the membrane thickness and crossing-area (the actuating pressure grows with thickness and falls off with crossing-area). The latter property enables efficient channel multiplexing (see below). The maximum operating pressure is mainly determined by bonding strength of PDMS layers, thus

actuating and operating pressures must be within some safe range to prevent chip de-lamination. To allow MMV function, flow channel should have hemispherical [Thorsen et al. 2002] or bell-shaped cross-section [Futai et al. 2004]. Rectangular flow channels cannot be completely sealed but can be utilized as sieves or size exclusion filters. Fig. 2.12 shows sketch and image of "ON" and "OFF" states of MMV in "push down" architecture, where flow channel is sandwiched between glass substrate and control channel. Other architectures as "push up" or multilayered designs with its benefits are covered elsewhere [Unger et al. 2000]. The invention of MMV opened the way for microfluidic large scale integration (LSI) and the applications in pharmaceutical and genomics [Einav et al. 2008, Fidalgo and Maerkl, 2011]. As mentioned, the important requisite for viable LSI (large-scale of integration) is the maximized reduction of control lines, similar to the electronic integrated circuits. In electronic industry, multiplexing and demultiplexing enables addressing of an individual location (line, register, etc.) among n others, with just $c = \log_2 n$ addressing lines (bits) on the bus. The address of each location represents a one combination of c bits long array of 1 and 0 bits. The integrated electronic circuits can employ "high impedance" state as idle line status, while in the microfluidic architecture idle status is naturally released control line state. As consequence, every microfluidic addressing bit has to be represented by two control channels, making n locations addressable by $c = 2\log_2 n$ control lines [Thorsen et al. 2002].

Another possible issue represents viability of the non-functional crossings between flow and control lines, in analogy to isolated wire crossings in electronic circuits. However, that problem is circumvented by the fact that the actuating pressure depends on the crossing area, thus actuating pressure for larger crossing area will not be sufficient for the actuation of smaller crossings. Fig. 2.13 shows part of integrated microfluidic chip, with MMVs and unfunctional channel crossings. More details and different functionalities built by MMV architecture, such as peristaltic pumps, mixers, sorters, etc. can be found elsewhere [McDonald and Whitesides, 2002, Melin and Quake, 2007, Thorsen et al. 2002, Fidalgo and Maerkl, 2011, Whitesides, 2006].

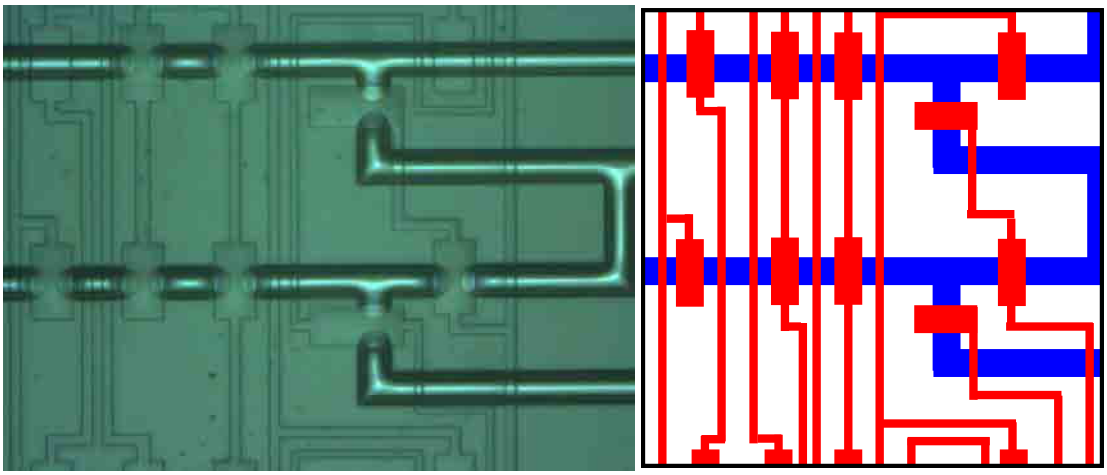

Figure 2.13-Photo and corresponding design of complex active microfluidic network. MMV function exhibit only larger area crossings, while narrow crossings very slightly disturb the flow. Photo shows part of multiplexing network.

The active-microfluidics (with integrated MMVs) fabrication procedure is considerably more complicated than for passive networks. Each functional layer (control and flow) have distinct architecture, thus two corresponding molds are necessary. Control layer molds are fabricated identically to the section 2.3.1. Flow layer molds are made in positive photoresist AZ 9260 (Microchem, USA). When the pattern in AZ is prepared, the mold is thermally treated at 160^{o}C for the resist reshaping of the rectangular into hemispherical cross-sections of the channels. Figure 2.14 shows part of the patterned mold, before and after resist annealing.

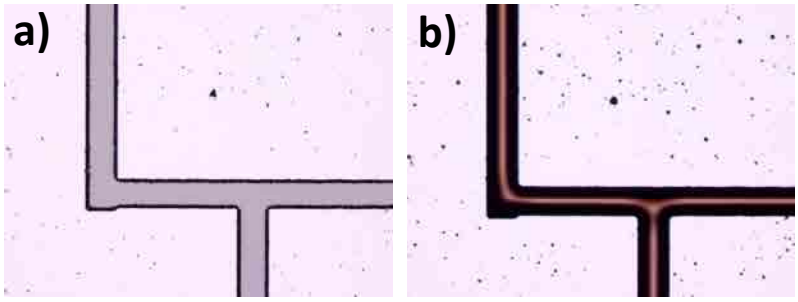

Figure 2.94-The part of flow layer mold a) before and b) after thermal treatment, clearly indicating channel cross-section.

In this work the "push down" architecture was used, where flow layer is embedded into thin PDMS layer (30-40 μm), while control layer is embedded into thick PDMS (4-6 mm). To ensure a strong bond between PDMS layers, different PDMS solutions are prepared [14]. Thinner PDMS is 20:1 mixture, while thicker layer is made of 5:1 (elastomer: curing agent) ratio. The uniform thin layer is formed by spin coating PDMS over flow-layer mold. After a short baking (cross-linking only partially done), the control layer network frame is cut and peeled-off from the mold, inlet holes are punched and features are aligned over flow-layer network. This process has to be performed within 30min, in order to decrease chances of the later chip de-lamination during chip operation. Flow layer mold with the thin PDMS layer and aligned thick PDMS control layer in contact, is returned in the oven for cross-linking to be finished. A strong bond between layers is formed due to diffusion of curing agent across PDMS interfaces. An alternative method exists where two PDMS surfaces are activated by O_2 plasma or UV/Ozone before aligning process. Aligning process can be facilitated in this case by sliding thicker chip part onto a thin methanol film that is inert toward silanol groups formed on the surface of PDMS during activation [Van Dam, 2006]. This method is similar to the plasmonic-microfluidic aligning procedure described in chapter 6. A complete process of integrated plasmonic-microfluidic device fabrication from scratch can be found in chapter 6.

2.3.3. Ultra-thin microfluidic devices

Certain optical configurations limit the total thickness of a chip to below 300 μm , for instance when using immersion oil objectives on both sides of the chip. With zero thickness glass substrate (80 μm), the thickness of the PDMS layer is limited up to ca. 200 μm. The assembly of ultra-thin PDMS membranes into functional microfluidic devices requires a considerable effort. The biggest issues are the handling of the thin membranes (removing them from the mold) and subsequent aligning onto a very thin and

fragile glass substrate. All of these difficulties generate relatively low fabrication yield, at least in a typical manual fabrication process.

We developed a fabrication process for such ultra-thin microfluidic devices, in Figure 2.15 (a)-(c). It resembles the active-microfluidics building-up techniques, where the thin PDMS layer is spin-coated over patterned mold. Thick PDMS parts on the sides have multiple functions, as inletting area for the pins, and as the auxiliary parts for easier handling of the thin PDMS (peeling off from the mold, and alignment control). The bonding of the auxiliary parts is identical to active microfluidics procedure (5:1 and 20:1 PDMS). Example in Fig. 2.15 represents a passive device of 270 µm total thickness (120 µm PDMS membrane) where the auxiliary parts don't possess any control features. After the bond is formed (Fig. 2.15(a)), chip frame is cut, and the membrane is carefully removed from the mold by holding and peeling it off in the direction from the extremities towards the middle (Fig. 2.15 (b)).

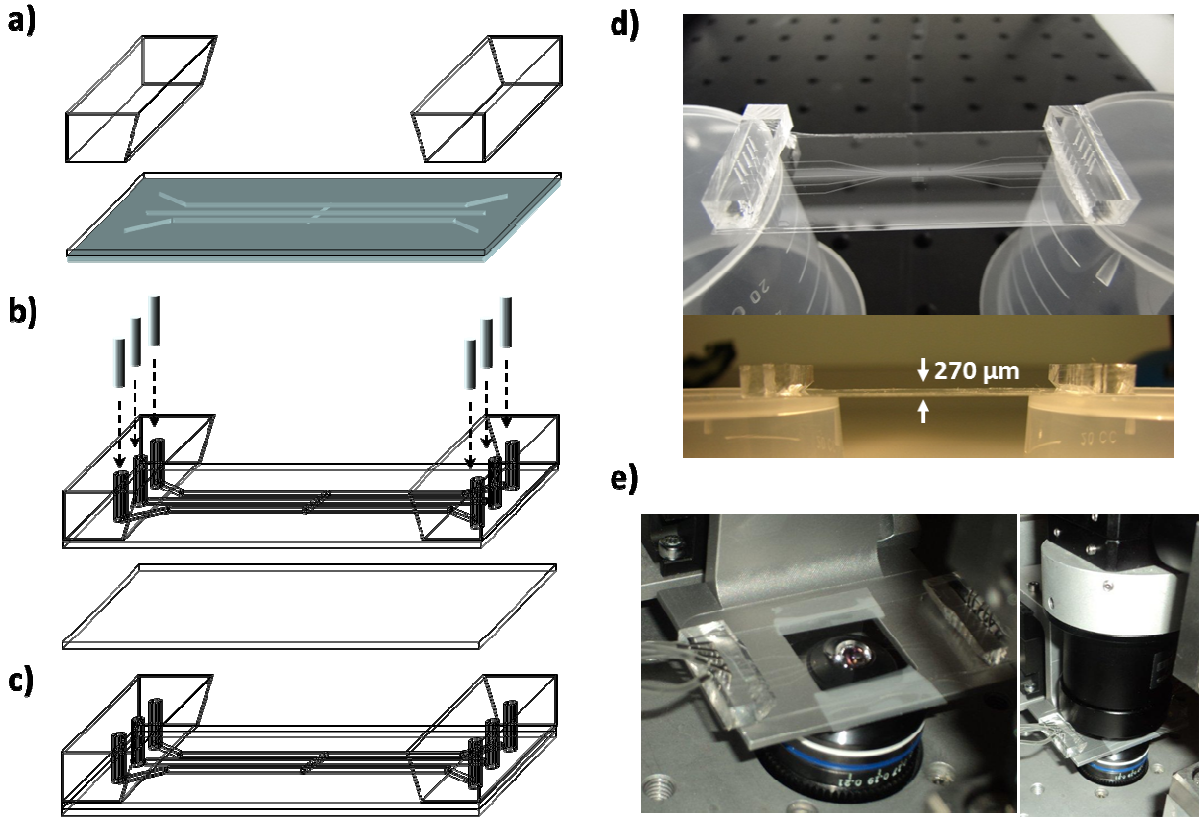

Figure 2.15-Ultra-thin microfluidic cell. Fabrication steps: a) auxiliary parts bonded to thin PDMS membrane b) the removal of the PDMS from the mold and aligning to the glass substrate c) thermal bonding of microfluidic cell d) ultra-thin microfluidic cell (glass thickness 150 µm; PDMS membrane thickness 120 µm) d) thin cell in contact with immersion oil objective from bottom side, and immersion-oil dark-field condenser from the top side.

The membrane tends to crumple if not stretched. After inlet punching, membrane can be carefully placed over the glass substrate, and thermally treated for 12h (Fig. 2.15 (c)). If microfluidic features need to be aligned over the patterned substrate, a thin layer of liquid inert to PDMS can be placed between

them (methanol). The PDMS can be adjusted until alignment is completed. However, a contrary to the thick microfluidics (see chapter 6 about chip assembly), the membrane tends to distort due to randomly formed vapor bubbles. If these deformed regions overlap with the channel network, it will render the chip partially or fully dysfunctional. In the example shown in Fig. 2.15, due to very long distance between inlets and outlets (more than 6 cm to fit immersion oil dark-field condenser), defects are usually produced in the middle of the chip. One of the options is to press membrane with Teflon-like material to prevent membrane distortion during baking, with slow temperature ramping. The second alternative is to perforate glass at safe distance from microfluidic channels, and to incorporate dummy channels connected to the holes in the glass, creating low resistance evacuation path for the liquid vapor. The third alternative employed in this work is based on a syringe pump working in the sucking regime that extracts liquids and vapors during the initial layers bonding on the hot-plate.
Fig. 2.15 (d) and (e) also compares side-by-side low-yield, old thin microfluidic cell manufactured a few years ago in the group, with recent fabrication method developed. These particular designs are used for the detection of Raman active species in the optical trap [Tong et al. 2009].
The active control can be embedded with the ultra-thin microfluidics, via structuring control network in the auxiliary parts, or by application of very challenging multi-layered architecture with extremely thin PDMS layers.

2.4. Conclusions

The methods and techniques presented in this chapter are main ingredients for the realization of LOC devices. Nanofabrication of plasmonic substrates is accomplished with combination of EBL and RIE, yielding highly homogeneous and reproducible patterned substrates. The optical response can be predicted to certain level with 3D modeling, which is in our case done by commercial FEM package-COMSOL. Apart of EM (optical) modeling, COMSOL can be used in the flow pattern prediction (not covered here), thus yielding the design rules for microfluidic networks used for interfacing purposes. PDMS as microfluidic material gains in importance additionally, due to easy implementation of MMVs, which enable multiplexing and precise liquid delivery, as being crucial requirements for successive LOC implementation. More detailed description of LSPR device fabrication and assembly is represented in the final chapters.

Chapter 3

Engineering of plasmonic nanostructures for sensing applications

The resonance change of plasmonic nanostructures to a small variation of the shallow refractive index as induced by the binding of molecules to the metal surface determines the sensitivity of plasmonic sensors. The magnitude of this change is strongly determined by a number of factors including dielectric constant of the metal at the working wavelengths, refractive indices of analyte and surroundings [Miller and Lazarides, 2005], but also the spatial overlap between the region of local refractive index change and the plasmon mode. It turns out that mode-analyte overlap (MAO) is a very important parameter in sensor optimization. Superior and tunable MAO is the intrinsic advantage of nanoparticle systems over conventional SPR.

Throughout this chapter, a brief introduction to the state-of-the-art modeling of LSPR biosensing is presented. This is followed by a discussion about the recent break-through in the low noise resonance peak shift detection that enabled resolutions down to few picometers. Such a low noise is directly related to the way of optical detection, where the nanoparticle ensemble measurement dominates low density or single particle plasmonic sensors. General trends in spectral and spatial LSPR tuning, are followed by the historical development of plasmonic near-field coupling (theory and experiment) and the contribution of this thesis to the field is presented. The experimental section is devoted to optical characterization of nanodisk dimer arrays, and to a new and advantageous spectral evolution method for the averaged nanodisk dimer gap assessment. Additional geometries based on near-field coupling are presented, such as gap nanoantennas arrays (nanorod dimers), honey-comb geometry, and bow-ties. The applicability of the spectral evolution method is demonstrated.

3.1. Modeling nanoparticle systems for sensing applications

The resonance shift of a plasmonic sensor upon binding of molecules is determined by various parameters related to the sensor itself, its surrounding medium and the target molecule. It has been established that such dependence can be formalized into the following equation, adopted from exact theory of planar surface plasmon resonance sensors [Jung et al. 1998], and accepted to some extent as a valid approximation for LSPR:

$$\Delta\lambda \propto m(n_{analyte} - n_{medium})(1 - e^{(-2d/L_d)}) \qquad \text{(Eq. 3.1)}$$

where m is the bulk refractive index sensitivity (BRIS) in RIU/nm (refractive index units), $n_{analyte}$ and n_{medium} are refractive indices of the adsorbing molecules and medium surrounding the system respectively, d is the thickness of the adsorbed layer and L_d is the EM field decay length. Equation 3.1 suggests that there are quite a number of parameters that influence the change in the resonance position. Considering a system that is adopted for any particular analyte ($n_{analyte}$ and d are fixed), to increase resonance shift one can tune m, n_{medium} and L_d. The only parameter independent of the plasmonic sensor is n_{medium}, and its decrease benefits the sensitivity. However, the refractive index of the medium surrounding the nanoparticle is a very rigid parameter and as a rule, is mostly governed by the analyte's nature. For instance, when employing free colloidal nanoparticles in solutions as sensors, n_{medium} usually falls in the small range around 1.33 (refractive index of water), and may be adjusted for analyte requirements, such as solubility, pH, stability, etc. [Lee et al. 2003]. In the case of nanoparticles fixed on a substrate, the medium in principle can be varied depending on sensing protocols and resistance of the delivery system [Lee et al. 2003]. In the limiting case, the medium refractive index can be reduced to 1 (air), but it is not favorable for real-time tracking and kinetic studies, thus imposing restrictions to only applications for molecular concentration detection in equilibrium [Malinsky et al. 2001, Barbillon et al. 2007] or for the detection of gases [Kreno et al. 2010]. The natural environment of biomolecules (proteins, antibodies) is considered an aqueous medium (blood and other body fluids). Drying or removing this medium after binding increases the shift induced by molecular binding [Malinsky et al. 2001], but for the accurate concentration determination it complicates detection procedures and protocols. Frequent drying also brings issues of molecule stability when exposed to air, poor reproducibility of measurements due to instability of nanoparticles when exposed to different media (see solvent annealing paragraph), and uncertainty on whether the solvent has been completely removed (residue problems) [Grigorenko et al. 2006]. One thus rather prefers working in a microfluidic environment (see chapter 6). Note though, that in PDMS microfluidics, glass/air/PDMS (1.52/1/1.4 refractive indices) acts as a dielectric multilayer inducing significant transmittance modulation as function of air channel thickness, and modifying the extinction calculated according to:

$$E = \log(1-T) = \log\left(\frac{reference - background}{signal - background}\right) \qquad \text{(Eq. 3.2)}$$

where T is the transmitted signal, $reference$ is the collected transmitted spectrum outside of nanoparticle arrays, $signal$ stands for transmitted spectrum from nanoparticles and $background$ accounts for the CCDs dark current spectrum. In the case of hemi-spherical channels, any difference between transmittance for the $reference$ and the $signal$ modulates the Lorentzian peak of LSPR, by superimposing faster oscillating function in the frequency domain (due to Fabry-Pérot effect). Apart from the increased noise due to fast oscillating envelope of LSPR peak, this effect might be amplified in case of any mechanical instability and/or background matrix change, compromising senor readout.

Water however, makes total refractive index modulation smaller (1.52/1.33/1.4), thus inducing weaker transmittance modulation (for instance, see Fig. 6.13 (b)).

The remaining two parameters, the bulk refractive index sensitivity m and the EM field decay L_d, are strongly correlated, accounting for the near-field enhancement and modal distribution. In a SPR configuration using a flat metallic film, m is related to the maximum field value on the dielectric-metal interface, while L_d accounts for out-of-plane field decay and depends on the normal component of the incident wave vector [Reather, 1988].

While being simple and intuitive, the 2D model of Eq.3.1 fails in accounting for the inhomogeneous spatial 3D distribution of the near-field in LSPR sensing as well as the non-uniform distribution of molecules onto the sensor consisted of closely-coupled nanoparticles. It supposes indeed an uniform molecular coverage (thin layers) [Haes and Van Duyne, 2002, Chen et al. 2009, Barbillon et al. 2008], and consequently does not apply to single or few molecule binding events [Aćimović et al. 2009].

One of the more rigorous approaches based on perturbation theory, attempting to address the important differences between LSPR and SPP, yields a complicated expression. Derived, initially for dielectric non-lossy resonators, Eq. 3.3 gives more insight into the contributions of spatial near-field distribution around 3D particles and the location and magnitude of the perturbation. In Eq. 3.3 C stands for the MAO. More details about the derivation, approximations and viability of this equation can be found in the work of Unger et al. [Unger and Kreiter, 2009].

$$\Delta\lambda \approx \lambda \frac{(n_{analyte} - n_{medium}) \int\limits_{Vanalyte} \varepsilon_{medium} \left|\vec{E}^2\right| dV}{n_{medium} \int\limits_{Vnearfield} \varepsilon_{metal} \left|\vec{E}^2\right| dV} = \lambda \frac{\Delta n}{n_{medium}} C \qquad \text{(Eq. 3.3)}$$

Although emphasizing the role of spatial MAO, Equation 3.3 still remains inappropriate to many LSPR sensing regimes. For instance, it gives that if one matches the resonance of a single metallic nano-cylinder with the resonance of nano-cylinder dimer formed by slightly smaller disks, both systems feature the same bulk refractive sensitivity. This statement is not valid and such false conclusion is the consequence of the initial approximation of infinitesimal perturbation. Indeed, Unger et al. show that this expression gains in validity for small perturbation (smaller molecules with refractive index close to the medium) while it fails for infinite perturbation case (bulk refractive index sensing). Worth noting is the difficulty in calculating the MAO value, where excessive numerical calculations are required. Thus, by convenience, majority of the LSPR community utilizes Eq. 3.1 although the meaning of the parameter L_d can be physically misleading for non-uniform modal distribution, as discussed later.

3.2. Tracking resonance change upon sensor perturbation

Until recently, the generally accepted way of describing the applicability of considered plasmonic system for biosensing was the figure of merit (FOM). The FOM of a particular resonance (curve) is defined as sensitivity/full-width-at-half-maximum ratio. Further on, the sensitivity is defined as resonance shift as a function of bulk refractive index change (bulk refractive index sensitivity-BRIS), and thus optimum systems would possess infinitesimally small FWHM with maximum possible sensitivity. This definition of FOM is rather incomplete when considering plasmonic biosensing and becomes slowly obsolete (However it is used in Ch.5). Different elaboration of the FOM definition have been proposed and everything points out that nanoparticle systems can be compared strictly for, in advance, a given molecular binding sequence [Becker et al. 2010, Nusz et al. 2009]. Thus, BRIS of LSPR systems is of a very limited value. As described previously, it has significantly lower values than its SPR counterpart. Actually, very high BRIS is usually correlated with evanescent fields expanding considerably into sample volume, thus increasing mismatch between bio-molecules and sensing volume [Kabashin et al. 2009]. In other words, the majority of available sensing volume of SPR is unoccupied after molecular analyte binding, making the sensor very sensitive to background fluctuations, noise due to thermal effects, non-specifically bound or non-targeted species in the sample matrix. Additionally, MAO is not and cannot be included into the FOM as usually defined. For instance, different resonance modes of the same structure are probing different sample volumes [Bocchio et al. 2008], and as a rule, such defined FOM is usually directly proportional to the active sensing volume. As we will see, the mode localization that typically increases MAO, as a rule, induces FOM reduction due to resonance broadening [Aćimović et al, in press].

The sensitivity/noise ratio for a particular nanoparticle-analyte system is more valuable, however it lacks generality as defined as such. It will be usually very dependent on the particular analyte, and also on the particular surface chemistry protocol employed. One of the very attractive methods for sensitivity increase is near-field coupling, which is among the main topics of this thesis. But first, I will present data processing algorithms that are particularly useful for LSPR sensors.

Conventional LSPR sensing readout relies on the position detection of the resonance peak. The maximum extinction or scattering wavelength is located and taken as a monitoring quantity. This method is known as the “minimum-hunt” procedure in SPR, which becomes the “maximum-hunt” in LSPR [Johnston et al. 1999]. Typically, polynomial fit or smoothing algorithms are applied over the spectral range corresponding to roughly 2xFWHM of related resonance curve. The zero of the first derivate is located, and taken as output value. Smoothing and especially polynomial fitting reduces the output noise levels. Although a wider spatial range of spectrometer’s CCD is employed for fitting, only one or a few particular CCD pixels are contributing to the output value.

Further noise reduction is thus achieved by accounting for a larger spectral range (larger portion of CCD array) when deriving the output value. Alternatively, centroid tracking method, normally employed in SPR [Garet et al. 2002], was adopted and discussed into detail by Dahlin et al. in [Dahlin et al. 2006; Dahlin et al. 2009]. Namely, instead of taking the first derivate, this procedure finds the geometrical mean value of the spectral data corresponding to smoothed or fitted 2xFWHM range. As more CCD

pixels are contributing to the output value, noise is considerably reduced, in correspondence to "maximum-hunt" method. Additionally, LSPR curve, beside resonance shift upon mass perturbation, displays also extinction magnitude change, which is "picked-up" by the centroid method (Fig. 1. 6. (b)). Temporal averaging further reduces noise at the expense of real-time tracking resolution. (This is one of the key points why bright-field extinction is superior against dark-field scattering method). Single accumulation CCD cycle in the bright-field configuration is on the millisecond order, at least two or the three orders of magnitude faster than the typical scattering photons collection cycle in the dark-field configuration (DF). As the noise decreases as $\sqrt{N}$ where N is number of averaged acquisitions, extinction measurements are at least with 10x less noise. Other problem in dark-field is the difficulty in controlling incident light polarization, due to oblique incidence. The oblique incidence excites LSPR out-of plane oscillations that might overlap (partially) with in-plane LSPR modes, giving rise to broader peaks and MAO delocalization. The solution to this problem is polarizer-slit crossed configuration [Knight et al. 2009], but it diminishes the incident light power interacting with nanoparticles. This in turn reduces further possibility of temporal averaging. Extra details about signal to noise management in LSPR can be found in above mentioned publications by Dahlin et al. Beside the centroid, there are more algorithms proposed by Chinowsky et al [1999]. In the case of multiple peaks present in the sensor spectum, each peak can be simultaneously centroid tracked, or full range can be integrated in the centroid algorithm, or alternatively multispectral integration method can also be employed [Lee and Wei, 2010].

3.3. Spectral and spatial LSPR mode engineering

Over the last decade, intensive research in plasmon optics has shown the huge potential of metallic nanostructures to concentrate light into nanoscale volumes in which the field amplitude can be enhanced by several orders of magnitude over the incident field. From the early stage of research in Surface Enhanced Raman Scattering (SERS), the so-called *hot spots* were found partially responsible for the enhancement of the Raman cross-section [Xu et al. 2000, Ringler et al. 2007, 2008]. *Hot spots* generally arise from a surface charge accumulation that preferentially occurs at sharp metallic tips [Stockman, 2004, De Angelis et al. 2008] and across dielectric gaps between adjacent metallic structures [Li et al. 2003, Romero et al. 2006] as explained below. The resulting strong charge gradients oscillating with the driving electromagnetic field lead to a large field magnitude within highly localized regions.

While intense *hot spots* appear in random ensembles of metallic nanoclusters, either prepared by annealing of thin metallic films or agglomeration of colloidal metal particles, their location and density can rarely be controlled. In that sense, a very attractive aspect of lithographically prepared plasmonic nanostructures is in the possibility of accurately controlling the location and density of *hot spots* within a well-defined region of the surface (chapter 3.1). Moreover, top-down approaches also enable to control the shape of each individual particle that directly affects the plasmonic mode distribution. All these advantages need to be balanced though by the limitations of state-of-the-art lithography techniques in the definition of sharp edges or dielectric gaps between adjacent particles that limits the magnitude and volume of *hot spots*.

While the mode confinement has a direct influence on the magnitude of the resonance shift, the accuracy in resolving a tiny change of the LSP resonance is influenced by the signal strength and FWHM of the resonant peak as mentioned above. Although the absorption of metals in the optical range is responsible for rather broad resonances, great emphasis has recently been placed on identifying systems that can give a tunable plasmonic peak with a narrow linewidth. For the majority of colloids, linewidth has been a problem due to polydispersity of the synthetic approach rendering a wide distribution of sizes and thus a broadening of the plasmonic peak. It is worth commenting however that as more effort is being invested in fully understanding the chemical pathways in making said colloidal nanoparticles, improvements are already seen towards monodispersed systems [Pérez-Juste et al. 2005] as well as in controlled arranged positioning of colloidal nanoparticles [Malaquin et al. 2007]. Coupled with the current optical capability of performing single-particle spectroscopy [Biswas et al. 2010], it is now possible to perform binding study experiments on a dispersion of colloids and selecting the particle with the optimum spectral peak width [Nehl et al. 2006, Sannomiya et al. 2008]. In fact these single experiments can now be multiplexed in what is known as HT-LSPR (High Throughput) and more quantitative information can be harnessed where otherwise was very time consuming [Becker et al. 2007, Bingham et al. 2009].

Nevertheless, the nanoparticle toolbox for colloidal chemists, whilst vast, is somewhat more difficult to exploit as each synthesis relies on some fine-tuning and experience to prepare mono-dispersions of one size, material or shape. As an alternative, lithographic methods offer here a great potential to accurately control the shape and size parameters with nanometric precision and manage areas of thousands of identical particles. Nevertheless, this gain in the control on the resonance linewidth has to be balanced by the intrinsically larger absorption losses associated to the amorphous metal, usually used in lithography that leads to broader plasmon resonances as compared to colloidal particles (see chapter 3). On the other hand, several works have lately pointed out configurations of electromagnetically coupled metal nanoparticles that enable the achievement of sharp spectral features [Hicks et al. 2005, Kravets et al. 2008, Auguié and Barnes, 2008]. I will discuss some of these systems within chapter 5.

3.4. Nanoparticle near-field coupling

Enhancement of Raman signals mediated by metallic colloid agglomerates attracted the attention of wide scientific community and the first questions raised were about the origins and mechanisms responsible for such amplification [Fleischmann et al. 1974]. Immediately, two different paths were identified that may contribute to the Raman signal enhancement, one being chemical in nature (charge-transfer effect) [Albrecht and Creighton, 1977] and the other electromagnetic effect [Jeanmarie and Van Duyne, 1977]. Since the Raman signal was absent from individual colloidal particles, it suggested that the agglomeration is the key factor in such a process. Soon after the “hot-spot” term was established, EM enhancement of Raman signal prevailed as the more dominant Raman enhancing mechanism, making possible single molecule sensitivity.

More systematic studies of the "hot-spot" effect was prevented due to difficulties in the colloidal agglomerates control and manipulation, thus alluding to the fixed two-particles as the most simple hot-spot system, commonly known as a *dimer* (Fig. 3.1). Dimer consists of two metallic nanoparticles that are brought into very close proximity. By close proximity, we usually mean at sub-wavelength distances, which is short enough to invoke dimer's properties distinctly different from the isolated nanoparticles alone. The nanoparticle interaction within the dimer is mediated by the nanoparticle's near-fields which decay as r^{-3}.Therefore, for the efficient near-field coupling, inter-particle separations should be smaller than the particles themselves.

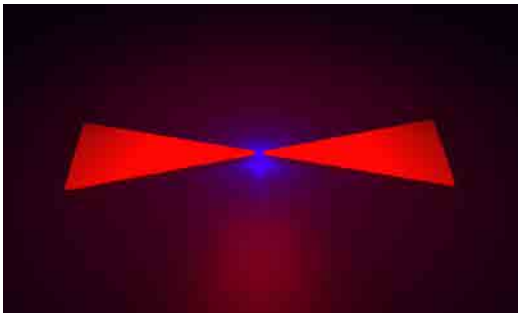

Figure 3.1-Artistic view of the near-field coupling between two metallic nanoparticles (bow-tie dimer)

Nanoparticle arrays with separations of the order of wavelength were an ideal system for the studies on the influence of nanoparticles' spacing on collective spectra [Schider, 2001, Lamprecht et al. 2000]. A simple bright field or dark field microscopy collects enough "absorbed" or scattered photons within short acquisition times from the arrays consisting of thousands of particles, making the optical characterization straightforward. The two regimes of NPs interactions were identified, that depend on the separations between them. It was established that the radiative (dipole) coupling (diffractive coupling or long-range coupling) exhibits d^{-1} dependence, while near-field coupling (short-range) d^{-3} [Zhao et al. 2003]. Experimental findings of Hayes et al. verified these dependencies, showing a blue-shift with the decrease of the array lattice (square and hexagonal 2D array), while at some point (typically 200nm) near-field interactions red-shift resonance with separation further decreasing [Haynes et al. 2003]. This provided a roadmap for the investigation of arrays made of dimers, as reported by Rechberger et al. in 2003. The sufficient distance between individual dimers allowed them to experience of near-field coupling, with the advantage of summing up signals of non-interacting dimers via linear bright-field spectroscopy. The main finding was the polarization anisotropy of the dimer spectra. For a light polarization parallel to the interparticle axis, they observed strong resonance shift to the larger wavelength with gap decrease, while transversal polarization provoked negligible blue shift. This work shined light onto nanoparticle close coupling that has been in focus since then. The resonance dimer behavior was simply explained through the interaction of free-electron charges in metals when driven by the oscillating electric field. If the driving field is parallel to the interparticle axis, the repulsive forces felt by both particles weaken, thus lowering the resonance frequency of such system in comparison to isolated particle [Rechberger et al. 2001]. Charge distributions associated with transversal light polarization remain almost unaffected, very closely resembling to an individual particle case. Weekly

dependence of transversal resonances on the interaction distance renders them quite uninteresting, and from now on, the term 'dimer response' accounts only longitudinal resonance, if not stated differently. Figure 3.2 shows experimental extinction of 5 nm gap dimer array made by EBL (nanodisk diameter 100 nm, out-of-plane height 40 nm) for two orthogonal polarizations of incident light. Dimers are arranged in 2D square arrays with 400x400 nm periodicities. Mode splitting is slightly above 100 nm between transversal (red) and longitudinal (black) resonances. Blue curve represents response of 100 nm gap dimer (quasi-isolated nanoparticles).

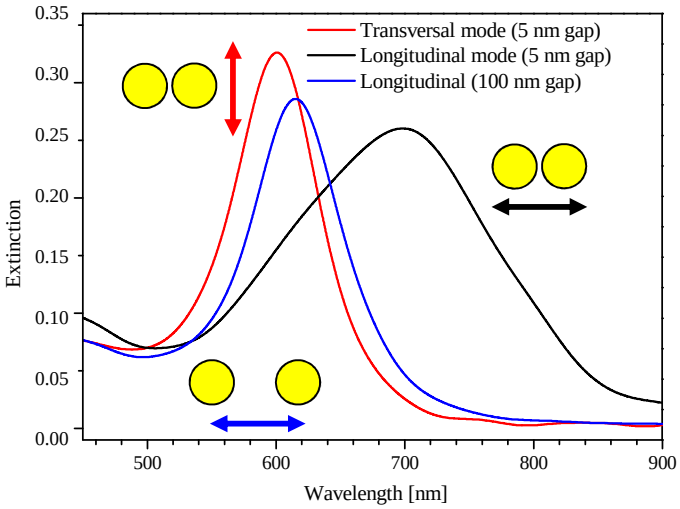

Figure 3.2- Extinction spectra of arrays of gold nanodisks (100/40 nm) arranged in 2D square grating: quasi-isolated nanoparticles (gap 100 nm-blue), 5 nm gap longitudinal (black) and transversal (red) resonance.

Sue et al. further investigated dimer near-field coupling, and observed near-exponential dependence of resonance as gap function [Su et al. 2003]. Our experimental data is shown in Fig. 3.3, where black squares correspond to resonance position of various arrays with different nominal gaps. Note that achievable gaps reach 0 nm, or so called "the touching regime". Accessibility of such small gaps in a large nanoparticle EBL array will be discussed later, but it is worth noting that they are clear outcome of advanced EBL processing described in previous chapter. Blue line corresponds to least-squares fit to a single exponential function $y = y_0 + a\exp(-xl^{-1})$ with decay length l =17.24±0.08 nm and corresponding correlation of R^2=0.995. The decay length marks region of gap sizes exhibiting intense near-field coupling.

Moreover, Sue et al. also noticed that a general rule exists that can describe this interactions. Namely, the coupling strength is an exponential function of gap to particle diameter ratio, where the coupling strength is defined as $\Delta\lambda/\lambda_0$. λ_0 is the resonance of the individual nanoparticle forming the dimer, while $\Delta\lambda$ is difference between dimer and single particle resonance. The coupling strength $\Delta\lambda/\lambda_0$ as function of gap/diameter ratio (x) was modeled as:

$$\frac{\Delta\lambda}{\lambda_0} = A \cdot e^{-\frac{x}{\tau}} \quad \text{(Eq. 3.4)}$$

where A and τ being fitting parameters. The universal scaling trend is characterized by the universal decay constant τ .

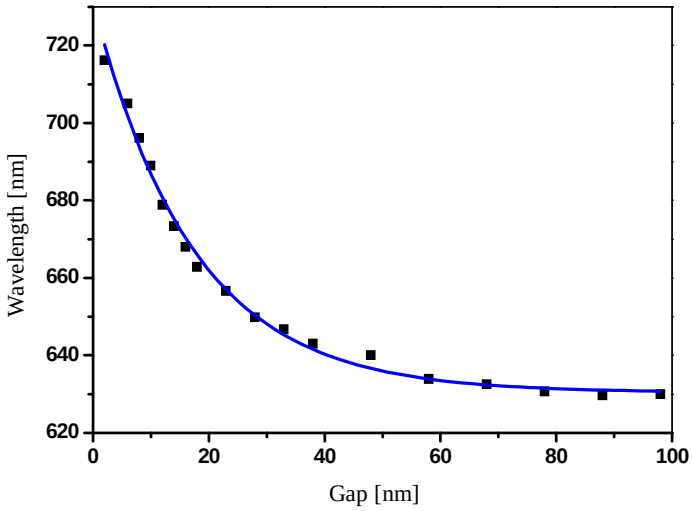

Figure 3.3- Extinction maximum as function of dimer gap exhibits a clear exponential trend (blue). Black squares are experimental values.

This universal scaling behavior was thoroughly investigated by the group of El-Sayed (Georgia Institute of technology, Atlanta, USA). In 2007 Jain et al. reported high-quality arrays of disk dimers fabricated by standard PMMA lift-off process [Jain, Huang & El-Sayed, 2007]. The extracted LSPRs confirmed observation of Sue et al. and further established the exponential fit through experimental as well as theoretical (DDA) data.

A characteristic experimental universal scaling curve is displayed in Fig. 3.4 for nanocylinders of 105nm in diameter, and 40 nm high, arranged in 2D array with spacing of 400x400 nm. The obtained decay constant is 0.179±0.016, with correlation of R^2=0.989±0.011 (N=6). These values are almost identical to Jain's values 0.18±0.02, as to our knowledge, the best lithography samples reported anywhere. Again, I will stress the fact that samples here are fabricated with "obsolete" thermal-emission 30 kV EBL system, which cannot be compared to performances of 100 kV field-emission systems. This almost perfect matching is an evidence of the power of EBL/RIE process that we developed, as well as of the reliability of our gap-assessment method that is introduced later.

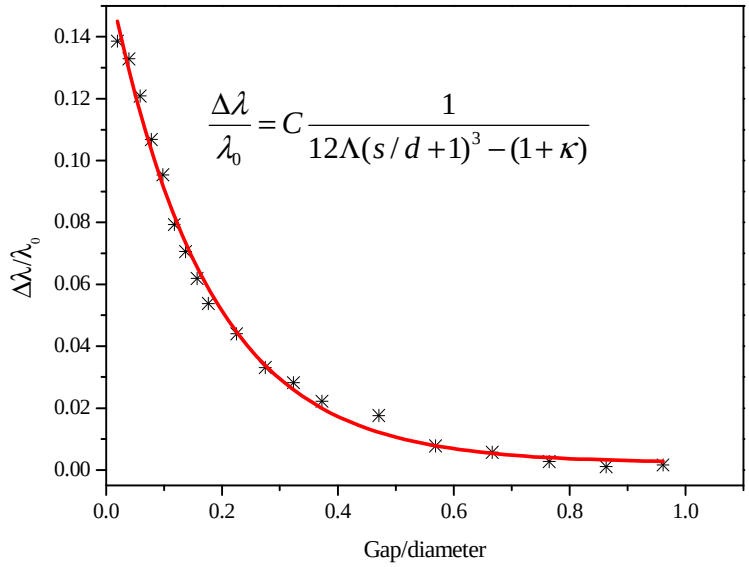

Figure 3.4-Universal scalling behavior of nanofabricated godl disk dimers

El-Sayed's group used semi-analytical model known as Dipolar-Coupling Model, to describe observed behavior [Tabor et al. 2008]. Taking into account only near-field interactions between two dipoles, the derived analytical expression yields:

$$\frac{\Delta\lambda}{\lambda_0} = C\frac{1}{12\Lambda(s/d+1)^3-(1+\kappa)} \qquad \text{(Eq. 3.5)}$$

where s is gap, d is particle diameter, and Λ and κ shape factors. As such, $(s/d)^{-3}$ dependence can be approximated well by the exponential decay. In other words, the near-field interactions exhibit d^{-3} dependence, while the polarizability of individual particle is proportional to nanoparticle volume according to the Clausius-Mossotti dipole polarizability expression [Jain, 2008]. Equation 3.5 gives no dependence on metal permittivity, dielectric permittivity, and very weakly dependence on shape factors exists. However, these parameters will influence the total plasmon shift due to near-field coupling, reflected as higher values of fitting parameter A in Eq. 3.4. Gunnarsson et al. observed a very similar decay constant τ for silver nanodisks [Gunnarsson et al. 2004]. Equation 3.4 is known as "plasmon ruler" equation. Explicitly, Alivisatos group (University of California, Berkley, USA) showed the application of colloidal dimers as real time optical ruler, where two metallic nanoparticles were attached to opposite extremities of molecule. Under conformational change, distance between colloids changes, inducing the resonance shift whose magnitude is directly related to the distance change [Sonnichsen et al. 2005]. This work emphasized the importance of the plasmon ruler calibration for any applications. The exponential dependence is sensitive enough to result in a relatively large spectral shift for small distance alteration. Note that the state-of-the-art technique for small distance changes is based on FRET (Förester Resonance Energy Transfer), with d^{-6} dependence on the distance (between donor and acceptor dyes). Owing to the fluorescent labeling, the associated drawbacks are label photostability (photo-bleaching and blinking), as well as very small dynamic range (<10 nm). On the contrary, plasmonic ruler is less sensitive to distance change ($d^{-3} \propto \exp(-d)$), but with larger range that depends on nanoparticle sizes

and provides very stable output signals. Recently, Jain et al. reported advances in plasmon ruler equation, where the simple exponential fit is replaced by more complicated expressions that describe dimer plasmonic effects in a more accurate way [Jain, 2008; Jain & El-Sayed, 2010]. I will introduce a new idea of "static" plasmon ruler at the end of this chapter, the system which can measure analyte sizes instead of distance variations.

Recently the Norlander's group developed a theoretical approach for modeling plasmonic behavior of complex and coupled plasmonic systems [Prodan et al. 2003]. The model is known as Plasmon Hybridization (PH) in analogy to molecular orbital theory. While rigorous approach of plasmon hybridization is valid only for quasi-static limit, this model allows for versatile and easy qualitative prediction of very complex systems, among which are nanoshells, coupled particles, nano-matryushkas, etc. The attractiveness of PH lays in the decomposition of a complex system into more elementary structures with easy predictable plasmonic modes, called "primitive" modes. Near-field interaction leads to hybridization of primitive modes, resulting in new hybrid modes of so formed complex system. The method also detects "dark-modes", with zero net dipole moment which cannot be coupled to light and thus experimentally verified with conventional light spectroscopies.

Figure 3.5 is a graphic diagram illustrating the PH analysis for the nanodisk dimer configuration. A nanoparticle homodimer consists of two identical nanodisks that supports a dipole resonant mode called "the primitive" plasmon resonance. The dimer is excited by a linearly polarized EM field, with the E-field component represented as double edge red arrow. One can discern two coupling configurations, when the electric field polarization is parallel to the interparticle axis (longitudinal) or perpendicular to it (transversal). Upon longitudinal polarization, the two different alignments of individual particle's dipoles are possible: parallel orientation that refers to symmetric or bonding, and anti-parallel that refers to anti-symmetric or antibonding mode. The parallel alignment increases total dipole moment of homodimer and red-shifts bonding mode in relation to primitive plasmons. Antiparallel orientation generally induces mode that is blue-shifted due to net dipole moment reduction. In the case of homo-dimer, the total net dipole moment of antibonding mode is equal to zero, rendering it "dark". The transversal configuration analysis is analogous, where mode splitting is much lower due to lower interaction of associated charge distributions. Thus, light excited homo dimers can support longitudinal (Fig 3.2 black) and transversal bonding (Fig 3.2 red).

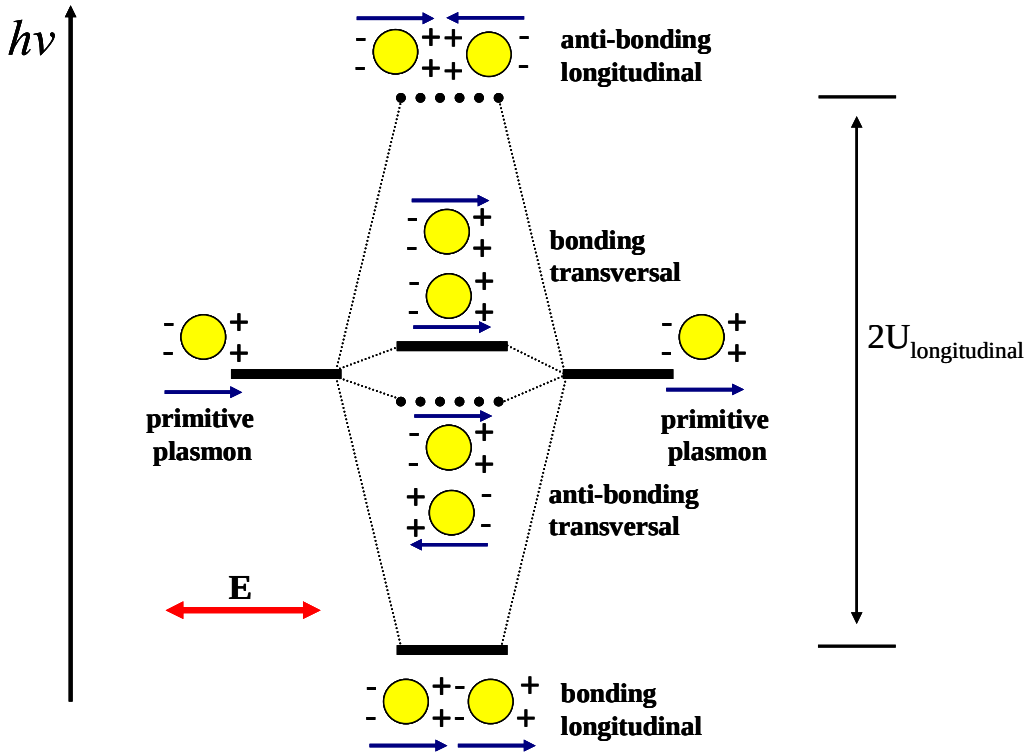

Figure 3.5–Plasmon hybridization model for a nanodisk (homo) dimer. Optically allowed bright model are marked by solid bands, while dark-modes are marked by dotted bands.

Similar conclusions are brought up by Exciton-Coupling Model (ECM) applied to plasmonic interaction by the El-Sayed's group [Jain et al. 2006]. While the same schematic results from application of ECM, the simple analytical formula allows qualitative assessment of the energy splitting between hybridized modes according to:

$$U = \frac{1}{4\pi\varepsilon_0}\frac{|\mu|^2}{n_m^2 R^3}\kappa \qquad \text{(Eq. 3.6)}$$

where μ is transition dipole moment, n_m is refractive index of environment, R is center to center spacing, and κ is shape factor. When referring to interacting nanoparticles, the coupling strength (U) increases with separation decrease and with dipole moment strength. Since the dipole moment in quasi-static limit is given as $\mu = n_m^2 \alpha \mathrm{E}$, it is clear that the mode splitting depends as the inverse cubic power of gap (center-to-center). The influence of n_m is not obvious, since the polarizability α (or resonance condition) depends on permittivity of the plasmonic material as:

$$\alpha = \frac{\varepsilon_0 V}{L^2}\left(\frac{\varepsilon - \varepsilon_m(\omega)}{\varepsilon + \left(\frac{1-L}{L}\right)\varepsilon_m(\omega)}\right) \qquad \text{(Eq.3.7)}$$

where L is depolarization factor (depends on shape), ε and $\varepsilon_m = n_m^2$ are permittivities of metal and surroundings [Jain and El-Sayed, 2007].

As mentioned earlier, both hybridization models are valid for nanoparticles in quasi-static limit, i.e. for very small nanoparticles in comparison to resonant wavelength. Under such condition incident electric field can be approximated as uniform across metallic volume. Naturally, these models qualitatively fail for nanoparticle sizes relevant for biosensing. Ordinary resolution of EBL is also exceeding quasi-static limit. Thus, the typical nanoparticles are subdued to retardation effects, which are responsible for broadening and red-shifting of primitive modes. Moreover, there is a clear distinction between nanoparticles and point dipoles in ECM, where center-to-center spacing cannot be only approximated by the actual gap. As such, these models allow for quick and qualitative interpretation of the optical response of interacting nanoparticles, while the more quantitative analysis relies on various numerical methods.

3.5. Nanodisk dimers

Before proceeding to experimental characterization of nanodisk dimers, it is instrumental to introduce the description of typicaly used samples. All of the experimental results presented here were obtained on a glass supported gold nanoparticle dimers, arranged in 50x50 μm 2D array with lattice spacing between 200 nm and 500 nm, depending on applications intended. The fabrication method is described in detail in Chapter 2. Each sample consists of multiple dimer arrays of different inter-particle separations. Extinction spectra are obtained with a simple white-light spectroscopy in a transmission, using conventional commercial Olympus BX50 microscope (Figure 3.6).

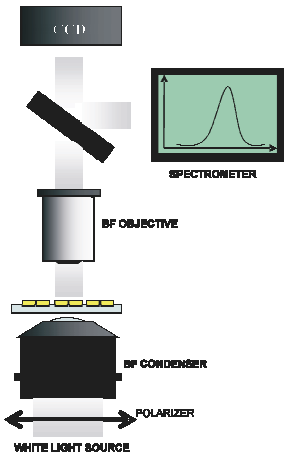

Figure 3.6-Sketch of white-light transmission spectroscopy setup (Olympus BX50): white light source, linear polarizer, bright-field condenser, sample holder, 10x objective, beam-splitter, spectrometer and CCD camera for navigation.

To complete nanofabricated sample characterization, besides extinction maxima determination, very important information is actual gap size distribution within every single array. Since each array consists

of more than 10000 dimers (near-field interacting nanodisks), a standard way to retrieve gap size is to apply statistical analysis to a collection of high-resolution SEM images for each array individually. Manual image acquisition and gap measurement results in a very cost-ineffective and cumbersome task that eventually leads to errors provoked by the limited resolution and the choice of representative subpopulation for the statistical analysis. An automatic image processing software package might be a faster and more reliable solution, but obtained gap size still depends on SEM image contrast and brightness (that might differ from sample to sample). Therefore, I will present a versatile and fast alternative approach that relies solely on far-field spectroscopy and sample design. This algorithm is universally applicable to any dimer system (gap nanorod antennas, bow-ties, or any homo or heterodimer configurations). Its applicability is demonstrated for a variety of near-field coupling geometries (see below).

3.5.1 Spectral Evolution Method for gap assessment in nanodisk dimers

Concerning the fabrication procedures, EBL systems precisely control the position of the electron beam during the exposure with a typical resolution better than 1 nm (disregarding stage and source fluctuations). Actually, for a 32-bit architecture, the minimum EB displacement is equal to the write field size (maximum beam deflection) divided by 2^{32}. Thus, center-to-center distance between particles (Δ_i in

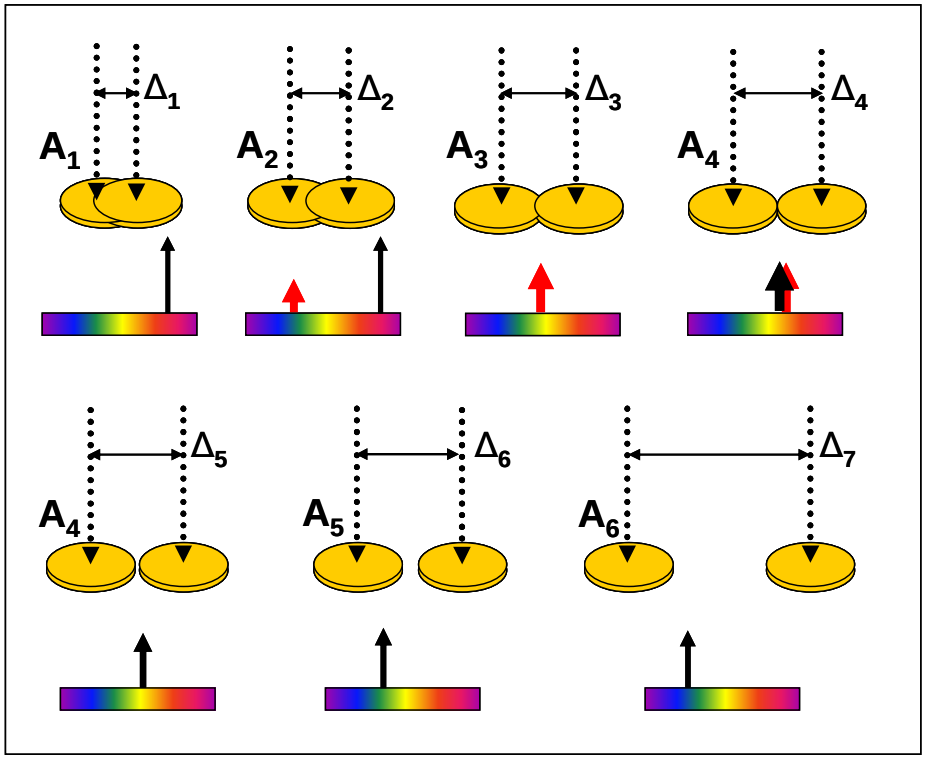

Figure 3.7–Sketch relating EBL dimer design, actual nanoparticle shape and spectral response. Black arrows correspond to dipolar modes, while red are symbols of higher order modes.

Fig. 3.7 A) constituting a dimer pair is known by pre-programmed pattern design. In practice though the diameter of fabricated cylindrical metallic particle depends on many factors including exposure dose, development time, material thickness and typically in research facilities it is not possible to control all of these with high precision (versus industrial processes). According to my experience, better results were obtained when nanodisks are exposed as single pixels (dots), than with circular lines or areas. Daily fabrication process inconsistency is reflected in particle average diameter deviations, typically within the range of ±5-10 nm between different batches. Thus, in order to fabricate requested and/or the smallest possible gaps, one has to control particle diameter with the same degree of precision as center-to-center spacing, or to apply the following algorithm that reveals obtained gaps and shapes, regardless of the process parameter deviations. If one aims for 100 nm particle diameter with known process parameters (pre-calibrated process), the projected inconsistency in the fabrication process should be accounted for (±5 nm or more), and the range of different dimer arrays should be exposed on the same substrate. The designed arrays have to cover all possibilities in order to get the requested gap dimers. For instance, around the expected nanoparticle diameter (100 nm) one needs to expose different gaps, with the gaps being swept in steps of 1-2 nm (center-to-center spacing of Δ_i= …, 96, 98, 100, 102, 104,… nm, for i=1 to N, where N is the total number of arrays). These should result in very small gaps and overlaps if the achieved nanodisk diameter is not unexpectedly different than the estimated 100 nm. The center-to-center step can be increased to 5 nm or 10 nm, in arrays that would expected to have bigger gaps (center-to-center spacing on the order of 150-200 nm), for which the coupling is rather weak (Fig. 3.6 A). Essentially, the sample should consists of overlapping dimers, touching dimers (gap = 0), dimers of increasing gaps, which finally approach single structures due to large nanodisk separation in the dimers. (Note that diameter of all particles exposed on any particular sample should be the same, since exposure dose is kept fixed. As an approximation, proximity effect can be disregarded for single pixel exposure). Fig. 3.7 displays EB dwell position during exposure (dotted arrows), where particle center-to-center spacing is labeled as Δ_i for corresponding array A_i. If particle diameter D is known, then gaps are simply $g_i = \Delta_i - D$, where $g_i < 0$ stands for overlapping structures (instead of a well-defined dielectric (air) gap a conductive bridge is formed). A freshly prepared sample is optically characterized for which every extinction spectra is associated to corresponding dimer array. If one isolate particular array, and look only at its extinction signature with knowledge of Δ_i only, we cannot conclude much about gap/overlap value, especially for $g_i \in [-5,10]$ nm. However, if we take a look at spectra evolution with increasing Δ_i, the information about diameter and gaps can be easily retrieved. As mentioned earlier, fabrication parameters are known provided that the following relations are fulfilled:

1) $\Delta_1 << D_{expected}$,

2) $\Delta_N >> D_{expected}$, where N is total number of arrays exposed.

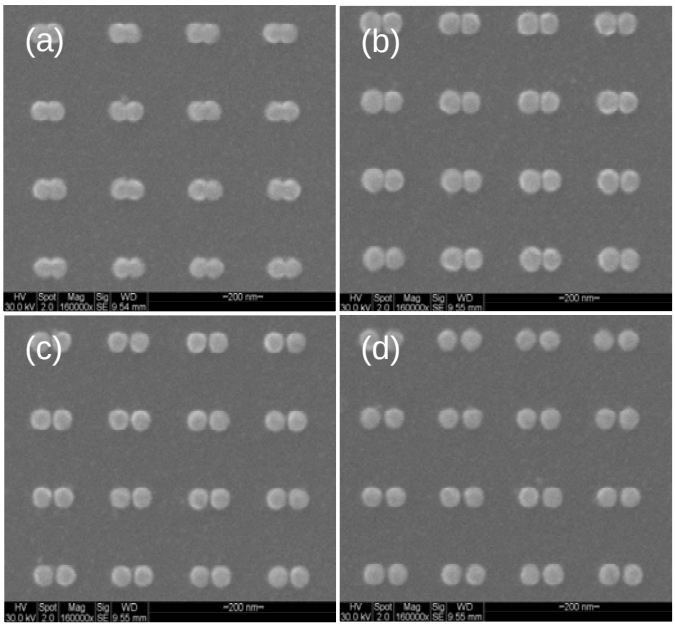

Figure 3.8–SEM images of dimer arrays with different center to center spacing. (a) Moderate overlap (b) Touching dimers (c) Small gap dimers (d) Moderate gap dimers

Relation 1), ensures the existence of array(s) with center-to-center spacing being sufficiently smaller than expected particle diameter, implicating that referring array(s) consist of nanorod-like particles with round extremities (overlapping dimer), Fig. 3.8 (a). Nevertheless, relation 2), ensures the existence of at least one well separated dimer array, Fig. 3.8 (d).

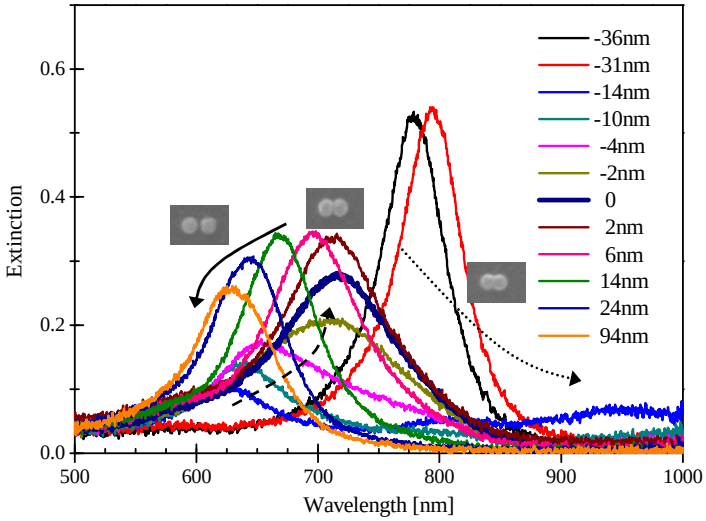

Figure 3.9-Determination of the dimer parameters by the Spectral Evolution Method: The gaps are calibrated according to the Fig. 3.7. Experimental evolution with the gap size of the extinction spectrum of arrays of gold dimers (100×40 nm) for longitudionaly polarized light.

A representative collection of far-field spectra is shown in Fig. 3.9 as evolution with Δ_i growth. Under the validity of relation 1, A_1 array corresponds to nanorod array. Supposing that $\Delta_1 > 0$, nanoparticles consisting of array A_1, closely resemble to nanorods with aspect ratio between 1 and 2. Thus one expects that for considerably small D (ca. 100 nm), A_1 array's particles support only dipolar resonance in VIS/near IR, without presence of $3\lambda/2$ modes due to small overall length. Coupling to the λ mode is also excluded under normal incidence illumination. Nanorod extinction spectra correspond to black line (Fig. 3.9), with resonant peak in the near IR around 775 nm. Additional increase in Δ_i yields nanorod-like particles of increasing aspect ratio (maximum aspect ratio of 2) with the consequential appearance of a bottle-neck region in the middle of joined particles (Fig. 3.8 (a)). The effective length increase shifts the dominant dipolar resonance peak further into IR (red-curve), due to larger dipole moment. Eventually, it exits the spectrometer range (>900 nm here) and cannot be seen any more (blue line). Appearance of bottle neck region diversifies spectra from pure nanorod response. Romero et al. reported that, the development of bottle-neck feature (decrease in conducting region), opens up mechanism for light coupling to high-order modes of short dumbbell structures [Romero et al. 2006], that are clearly visible at 640 nm (Fig. 3.9, blue), and red-shift with further overlap decrease (dark-cyan and pink). Appearance of higher order modes pushes dipolar resonance further into IR due to mode repellence with oscillator strength redistribution that decreases dipolar peak strength [Marhaba et al. 2009]. However, this effect occurs deeper into IR making it unavailable for detection (and excitation), with the employed optical setup used here. The decrease of conducting bridge induces charge pile-up around it, building up very intense near fields. Eventually, an increase in Δ_i brings conductive bridge to "zero" level (when the aspect ratio reaches 2), which is characterized by the reddest resonance that evolved monotonically from the red-shift of high-order modes of dumbbell structures (thick purple line). An additional increase of Δ breaks the conductive bridge, rendering particles electrically isolated [Atay et al. 2004]. In line with previously presented nanoparticle coupling trends, we are in $g_i > 0$ regime, and center-to-center increase, decouples particles, moving successively the dipolar dimer resonance to the blue, until it reaches quasi-isolated nanoparticle resonance for A_N. The quasi-isolated nanoparticles extinction spectrum feature a dipolar resonance located furthest to the blue (640nm, orange curve). Once the point of inversion has been identified, i.e. the change from red shifting to blue shifting trend, one proclaims the corresponding array to be formed by touching particles with 0 nm gap (thick navy blue curve). From the design template (initial separation between dimer centers in exposed EBL pattern design, (Δ_4 in Fig. 3.6 A) we retrieve averaged particle diameter $D = \Delta_4$, as well as gaps/overlaps of all exposed arrays as $g_i = \Delta_i - \Delta_4$. To summarize, spectra evolution with Δ increase exhibit 3 regimes: nanorod behavior (high-overlap), low overlap and dimer regime. High overlap regime is not necessary for gap calibration, but for the sake of completeness is presented here. High overlap is related to the appearance of strong dipolar modes of nanorod structures, which very fast disappears in IR with center-to-center increase. Near-IR sweep of dipolar mode evolution in the high-overlap regime is shown as dotted arrow in Fig. 3.9 and 3.10. Low overlapping regime is characterized by the emergence of high-order modes of dumbbell structures that evolve successively into the reddest peak of touching nanoparticles (dashed arrow). Finally, the dimer regime occurs when the conductive bridge breaks,

characterized by exponential-like blue shift with gap increase (solid arrow). Throughout this thesis, we are mainly focused on dimer regime of different nanoparticle systems (solid arrow).

It is worth discussing the accuracy of this calibration technique in terms the resolution limit of EBL processes and its stability. Dimer spectra evolution is reproduced by the theoretical FEM modeling in Fig. 3.10. The most noticeable difference between experiment and simulations is related to FWHM of LSPRs and larger mode splitting for small gaps. Simulated peaks are sharper due to precisely defined plane wave illumination (in the experiment the condenser NA=0.1), sharply defined edges and identical particles (experiment: polydispersity and limited resolution of fabrication process). However, the evolution trend is reproduced well, except for the very short gaps/overlaps.

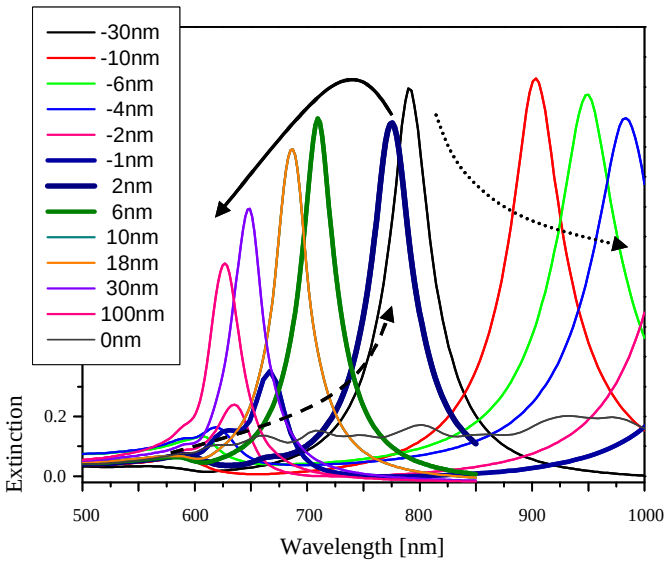

Figure 3.10-Numerical modeling of Spectral Evolution Method. FEM calculations confirm the viability of the proposed gap calibration technique. The three regimes are marked by arrows. A very good qualitative matching with the experiment is obvious.

Behavior of a spherical dimer system in the limit of infinitesimal gaps/overlaps was studied theoretically, with minimum gaps even smaller than gold lattice [Romero et al. 2006]. Gap decrease leads to successive appearance of high order modes, with subsequent red-shift and intensity redistribution with the emergence of every new mode. Same occurs for the overlap decrease. In the single-point touching limit of two spherical nanoparticles, there is no smooth evolution of dipolar dimer mode into the dipolar mode of fused nanoparticles. The nature of two systems (with conductive bridge and dielectric gap) makes these modes distinct. The dipolar dimer mode is associated with coupled (hybridized) state of electrically isolated particles, when each particle is electro-neutral. When a conductive bridge is formed, unphysical charge distribution for dimer case now becomes allowed. Each particle can be oppositely charged when the lowest-energy mode is excited, and this mode is sometimes referred as charge-transfer plasmon (CTP) because it doesn't coincide with dipolar mode of analogous nanorod [Slaughter et al. 2010, Lassiter et al. 2008]. There is thus an abrupt change, i.e. a finite difference between

wavelengths of these modes. Typically, dimer bonding is blue shifted in relations to CTP position. These predictions are based on classical EM, where materials are characterized by their bulk optical properties [Johnson and Christy, 1972]. Recently, various models are developed that incorporate more accurate description of physical phenomena and materials, namely quantum approaches and non-local descriptions of optical properties. Quantum effects gain importance for very small gaps, when electron tunneling across the dielectric barrier occurs (<1-2 nm). The electron tunneling reduces the magnitude of the total mode splitting (red-shift) with further gap decrease as well as the field enhancement in comparison to classical predictions [Zuloaga et al. 2009]. Describing optical properties of materials non-locally (accounting for conductance electron spill-out for instance), also results in differences in comparison to classical predictions for very small gaps [de Abajo, 2008; McMahon et al. 2010]. All of these corrections point out that the classical predictions are overestimated for very small gaps/contacts, resulting in higher coupling-strength and larger field enhancements.

Studying experimentally these regimes where quantum effects kick-in represents quite a challenge. Typical EBL resolution is above 5 nm, thus an alternative nanofabrication or nano-manipulation methods are required. Atay et al. broke conductive bridge in small overlapping dimer arrays with pulsed lasers, reaching gaps <4nm. They observed secondary higher order peak, which is very difficult to observe from EBL nanofabricated arrays. More versatile methods rely on linking spherical colloids in solutions via compatible single-stranded DNAs or di-thiol chemistries, or by random electrostatical agglomeration. The yield is very low with good control on actual gaps, but appropriate particles are located and characterized by single-particle spectroscopy. Strongly-red shifted bonding dimer modes are clearly observed, with a red shift that is far bigger than in EBL arrays, but it can originate partially from the linker molecules in the gaps.

Group of Pellarin (Université de Lyon, Lyon, France) reported the experiments on single colloidal dimers spaced by less than 1 nm [Billaud et al. 2008]. They presented spectra with energy splitting of around 250-300 nm where gaps were assessed by transmission electron microscopy (TEM). Even high resolution TEM couldn't resolve gap size unambiguously. Recently, they reported on optical spectra of somewhat overlapping dimer, that exhibits 3 peaks in visible, similar to the classical predictions [Marhaba et al. 2009]. I was not able to observe high-order peaks of 0 nm dimers due to many reasons:

1) polydispersity and limitations of EBL, and acquiring collective spectral response of >10.000 dimers
2) nano-disk geometry (pancake) is less favorable to display high-order modes than spherical dimers
3) polycrystalline gold

(The maximum coupling strength observed was 140 nm for 75/40 nm nanodisk particles, calibrated as explained above. Even for the largest mode splitting dimer sample, the high-order modes stayed hidden.)

Jain et al. speculated on the shoulder that they observed on blue side of 2 nm gap dimer array might originate from high-order mode [Jain, Huang & El-Sayed, 2007]. The maximum coupling strength

observed there was only between 95-100 nm for 90 nm particle, while I didn't observe high-order dimer mode for maximum coupling strength of 140 nm for smaller nanoparticle disks of 75 nm. Thus, the direct EBL fabrication still doesn't allow for reproducible small gaps. Even though, our calibration method "dares" to assess 0 or 2 nm gaps, these numbers do not represent real values. Accuracy of the calibration will clearly depend of sample quality, since calibration will always result in small gap assessment. Small gap arrays are rather a mixture of overlapping, touching and real dimers, where the average response exhibits red-shift in comparison to the response of array of 2 nm more separated particles in a pre-designed pattern. Thus, the calibration should be always checked by universal distance decay calculation which additionally incorporates the coupling-strength magnitude. Taken all into account, the spectral evolution method is applicable even for a "perfect" EBL process, and results obtained are more reliable than any statistical approach based on SEM imaging. It is fast, cheap and is generally appropriate for any type of dimer structures, as will be demonstrated later on.

3.5.1.1 Influence of fabrication method on dimer far-field spectra

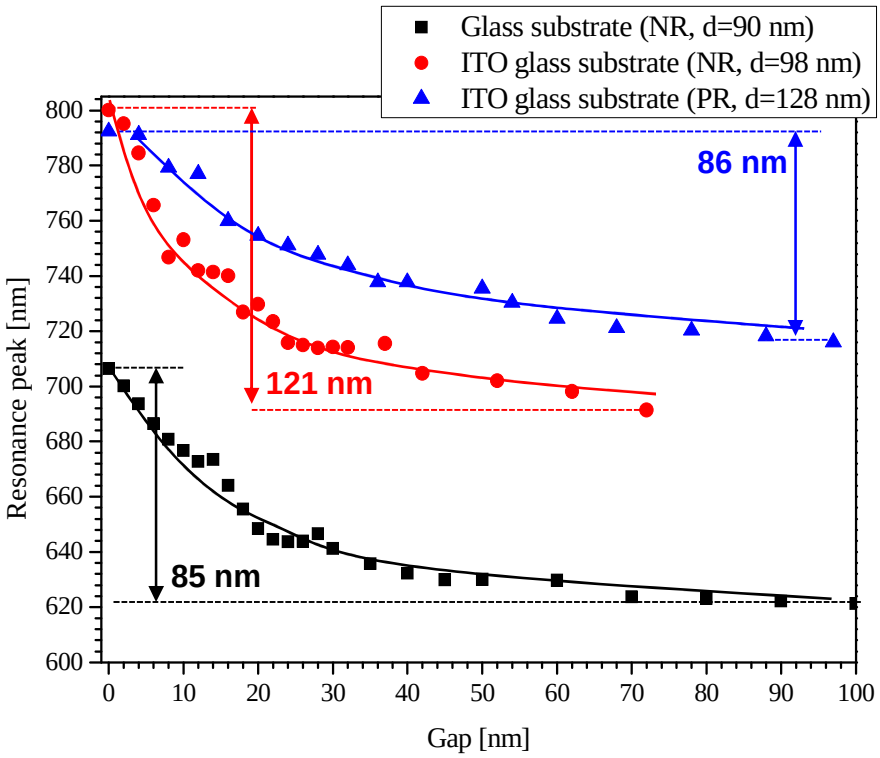

Figure 3.11-Extinction maxima as gap function for dimers fabricated by different methods: negative-resist/RIE on glass (black), negative-resist/RIE on ITO glass (red) and positive-resist/lift-off on ITO glass. Lines are guide for the eye.

Figure 3.11 compares the experimental results of similar samples consisting of fabricated with different processes, positive (PR) vs. negative resist (NR) (see Fig. 2.1, 2.2 and 2.4). The maximum coupling strength achieved is assessed. Samples fabricated by negative resist-RIE process, were 90 nm nanodisks dimers lying on glass (n=1.52) (black squares), exhibit the maximum coupling strength of 0.14 ($\Delta\lambda$=85

nm). If thin ITO layer (10 nm, n=1.9) is deposited before negative resist lithography, the coupling strength (red circles) increases to 0.18 (Δλ=121 nm) for slightly larger nanodisks of 98 nm, due to ITO layer (refractive index sensing) and larger disks (Eq. 3.4) [Jain and El-Sayed, 2008]. On the other hand, dimers fabricated by the positive resist process exhibit the maximum coupling strength decreased further to 0.12 (Δλ=86 nm), even with a considerable larger nanodisks of 128 nm (blue triangles). This comparison clearly evidences increased quality of negative resist process. With the positive resist process, one cannot achieve as small gaps (on average), resulting from a more pronounced nanoparticle polydispersity.

3.5.2. Near-field distribution of hybridized dimer modes

Plasmonic hot spots are responsible for increased light-matter interaction on the nanoscale, mainly due to sub-wavelength decay lengths and enhanced intensity. The simplest way of investigating near-field coupling between interacting nanodisks in the dimer configuration, is primarily through far-field spectroscopy. Previous paragraphs demonstrated the strong influence of the inter-particle distance on the far-field optical properties of dimers. However, the evanescent fields are the ones responsible for the strong light-matter interaction that is employed in biosensing, SERS, trapping, etc. The information about spatial near-field distribution is not available through far-field spectroscopy. However, non-linear and near-field spectroscopic techniques can provide more detailed information about near-field distribution. While the initial attempts of near-field characterization were somewhat dubious [Lereu et al. 2008], recent advances confirmed experimentally the theoretical predictions with sub-wavelength resolution [Schnell et al. 2010]. The question remains about the spatial near-field profile and the parameters that control it, in a way that to achieve “hot spot” engineering. I will discuss dimer near-field extracted from FEM calculations in the case of plane-wave illumination. More advanced control of “hot-spot” apart from simple geometry control (nanoparticle size and shape, gap size), can be achieved through pulse shaping [Stockman, 2011] or through the spatial phase shaping of the beam exciting the system [Volpe et al. 2009]. The oscillating electric field component of the incident light sets the free-charges of the nanoparticle into an oscillatory motion. The conductive electrons are pushed in the direction of the E field lines, leaving the positive ionic background behind, forming in the simplest case, a dipolar modal distribution. If the near-field coupling between two particles is weak, then their near-field distribution remains unchanged, i.e. each nanoparticle will not feel the presence of the other (a radiative coupling in the arrays of such particles might occur, independently, leading to changes in the radiation pattern and spectral shapes mainly due to the interference effects). By bringing the particles closer, within the range of the evanescent fields, free charges start to redistribute due to the change in the local environment of each particle, leading to a new hybridized dimer mode. For a longitudinal bonding mode the charge distribution is characterized with a charge pile-up within the gap region and smearing out of charges located at particle extremities (delocalization) [Rechberger et al. 2003]. The amount of piling-up in the gap depends on gap size, i.e. near-field coupling strength between dimer constituents. Figure 3.12 (inset) shows the near-field localization (hot spot) within the gap, for a bonding dimer mode.

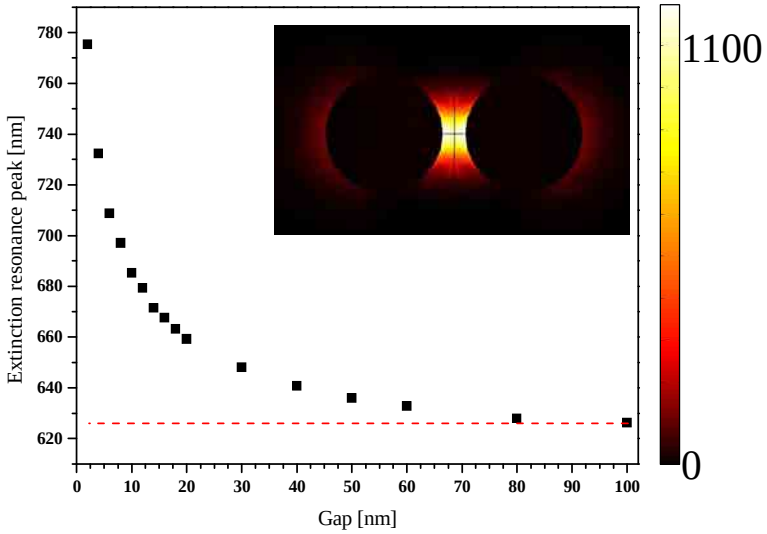

Figure 3.12-Calculated evolution of the dimer arrays resonance as gap function (100/40 nm ideal nanodisk, periodicity of 400x400 nm). Corresponding spectra are shown in Fig. 3.10. Inset: Typical hot-spot formation of EM intensity enhancement under the resonance condition (20 nm gap)

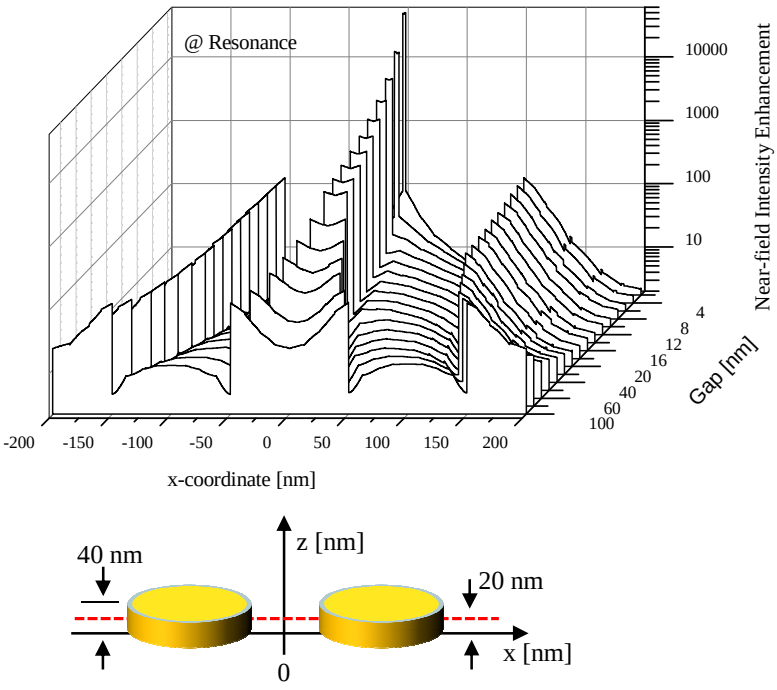

Figure 3.13- Near-field intensity profile on the dimer axis as a function of gap calculated at resonant wavelengths (see Fig. 4.10). The electric-field enhancement is evaluated along the red dashed line shown in the lower sketch.

The strength of nanoparticle near-field interaction has, so far, been characterized in the far-field as $\Delta\lambda/\lambda$ (coupling strength). Although there are experimental techniques for near-field probing within the hot-spot [Cang et al. 2011], in this thesis, I will rely solely on COMSOL simulations that can solve near-field distribution, in the absence of these near-field probing techniques. Figure 3.11 shows calculated far-field extinction maxima for gold disk dimers as a function of the inter-particle separation, as extracted from the spectra shown in Fig. 3.9. Individual nanodisk dimers (D=100 nm, h=40 nm) are arranged into a 2D array with periodicity of 400x400 nm. For the various gaps, plots of the near-field intensity enhancement through the axis connecting particle centers are shown in Fig. 3.13. The enhancement is defined as $|\mathbf{E}|^2/|\mathbf{E_0}|^2$, where $\mathbf{E}$ is total field and $\mathbf{E_0}$ incident field amplitude.

As seen from the enhancement profile, the field maximum is located at the metallic surface inside the gap, while there is a local minimum, right in the middle. For very small gaps (2 and 4 nm), meshing wasn't enough to resolve these subtle differences, so somewhat averaged field is shown. A decrease in the gap amplifies the effect of charge pulling inside gap extremities, provoking charge delocalization on the outer extremities of the dimer. This would in turn induce successive enhancement decrease at the extremities with gap shrinkage, which is not observed here. The charge smearing effect is overruled by the improvement of the optical properties of gold (lower losses) further into the red part of the spectrum (due to red-shift of resonance condition), so a small increase is observed instead. Interestingly, when illuminating these systems with fixed wavelength that corresponds to LSPR of the isolated nanodisks that form dimers (626 nm here), even then, the intensity enhancement in the gap grows with its shrinkage, regardless the fact that resonance of small gap dimers can be completely off the excitation laser line. Figure 3.14 (lower) shows resonance profiles of different gap dimers excited at 626 nm (red line). Mismatches are clearly observable for gaps < 10nm. This feature is the origin of enhanced SERS signals originating from colloidal agglomerates even when excited with a laser line corresponding to that of an isolated colloidal resonance. In addition, for this excitation the enhancement at the extremities of the dimer goes down due to charge delocalization (redistribution) upon the increase of coupling (data not shown). Figure 3.14 (upper) compares the intensity enhancements for these two cases demonstrating clear difference in the enhancement levels. It emphasizes the importance of resonance and geometry engineering (tuning) to achieve optimum performance [Huang et al. 2010].

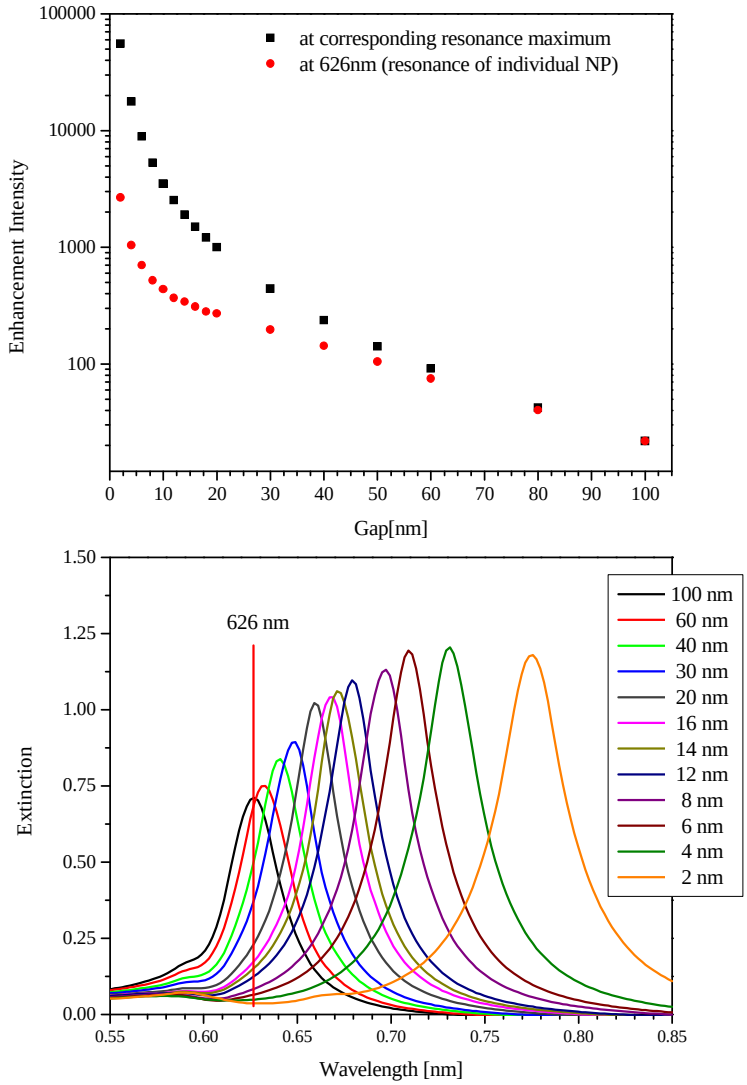

Figure 3.14–Upper: Intensity enhancement in the gap for each dimer illuminated at its resonant condition (black), and when the excitation wavelength is kept fixed to single particle resonance (red) Lower: Far-field spectra of considered dimers. Vertical line represents excitation wavelength (626 nm). Note the mismatch between small gap dimers and excitation.

It is interesting to see what results FEM simulations produce for gaps where quantum effects are not negligible. Essentially, in these regimes many methods suffer divergence problems or solution instability, and referring to FEM, the required mesh density necessary for a reliable solution may be outside of the reach due to limited CPU and memory resources. Figure 3.15 displays calculated optical response of 1 nm gap, 1 nm overlap and single line touching dimer. Although the classical description is not valid here, we can clearly distinguish between dimer dipolar (black) and CTP mode (blue). In the case of touching particles in singular limit, a myriad of higher order modes can be observed, where the near-filed distribution of the lowest energy mode (at 1.34 μm) is shown in the inset. The near-field intensity maximum is located around this touching area, with extremely high field intensity [Romero et al. 2006].

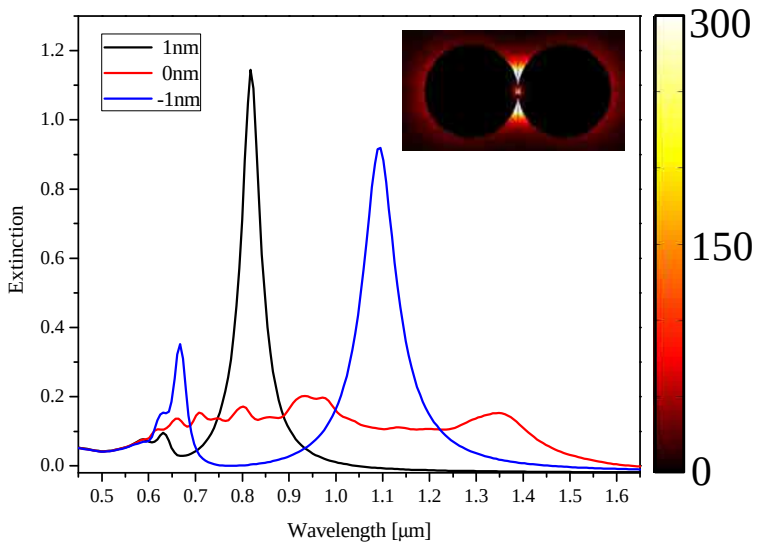

Figure 3.15 FEM calculated extinction spectra of very small gap dimers, including the single touching limit. Inset: The near-field intensity enhancement profile for single touching regime excited at 1340 nm.

3.6. Gap nanoantennas (nanorod dimers) & Honeycomb geometry

In real-time LSPR sensing, the magnitude of the extinction peak influences signal-to-noise ratio, an important component for sensitivity issues [Dahlin et al. 2006]. An increase in the extinction efficiency of the analyzed area (collected by the spectrometer) lowers the noise levels, due to the amplified difference between rates of photo-electron generation over the thermal electron generation in the CCD detector of the spectrometer. The accumulation time for the spectra acquisitions is shorter in such case, allowing longer averaging for the fixed temporal resolution of the extinction peak tracing. As such, an increase in the gold-filling factor of the arrays (density and/or volume of nanoparticles) results in larger overall extinction signal, but can modify the extinction peak spectral position and shape. With a typical rise in the surface packing of nanoparticles (by the reduction of the period of the 2D array lattice) the two effects may lead to an extinction peak modification. The radiative or far-field coupling that depends strongly on periodicity, shifts the central peak wavelength (typical blue shift with the periodicity reduction, until the near-field coupling becomes the dominating effect). A special peak shape modification occurs for a specific set of periodicities/peak position ratio, provoking the effects known as Wood's anomalies that result in Fano-profiles of the resonance curve instead of being Lorentzian in shape (chapter 5). A decrease of array pitch can result in a near-field interaction that embraces more particles than the nearest-neighbors. Such an interaction results in surface charge delocalization (especially in the dimer case), that may lead to the overall hot-spot intensity reduction. Therefore, a compromise between hot-spot "fading" and the increase of the far-field signal should be waged for a particular application. Moreover, typically linearly polarized light is employed for a selective excitation of longitudinal dipolar dimer modes featured by the strongest optical effects. A draw back of having the polarizer within a light path is the light attenuation (ca. 50% of the unpolarized light source) affecting the noise levels (less averaging and shot noise increase). Nanorods, as particularly interesting due to polarization anisotropy and spectral tunabilty of the resonance, are more sensitive to bulk changes as

well as they extinct light stronger than the nanodisks/sphere particles. All said above for the near-field coupling, applies to nanorods, where the corresponding dimer is commonly known as gap nano-antenna. In this section we briefly discuss nanorod dimer arrays and alternative honeycomb (HC) geometry composed of nanorods as building blocks. The extinction peak magnitude increase, together with the polarizer elimination benefit to lower SNR at the cost of the hot-spot intensity drop (due to delocalization of plasmon-supporting charges). However, slight delocalization might be beneficial when large molecules, such as antibodies are employed as analyte receptors (chapter 6). Finally, the spectral evolution method is successfully applied for the characterization of both geometries. The FEM comparison between HC and gap-nanoantenna arrays made of equivalent nanorods is also presented.

3.6.1. Nanogap antenna arrays

Figure 3.16 (a) displays a typical array of gap antennas (tilted SEM image) in a 500x500 nm 2D square pattern (Fig. 3.16 (a)). The spectral evolution method is shown in the same figure (b) with the thick line representing touching dimers. Continuous separation in the EBL pattern design of gap nanoantennas results in a real gap increase of the successive gap antenna arrays, which is reflected with a consecutive exponential blue shift of the extinction maximum. Nanorods alone support at least two modes that are referred as transversal and longitudinal dipolar due to its intrinsic shape anisotropy. The transversal mode corresponds to shorter wavelength charge oscillations, in the direction perpendicular to the rod long axis. These oscillations are rather delocalized yielding low field enhancements and thus are not interesting for our purpose. Longitudinal dipolar mode corresponds to long axis resonant charge oscillations, expressed at larger resonant wavelengths and featured with stronger enhancement and confinement. The longitudinal modes can be classified as $j\lambda/2$ modes, where integer j=1,2,… determines the standing wave nature of the longitudinal oscillations for a nanorod that fulfills the condition $L= j\lambda/2+\phi$ (L is the nanorod length and ϕ is the phase shift) [Taminiau et al. 2011]. The dipolar mode corresponds to λ-half mode, with opposite charges located at nanorod extremities. Other modes are supported by much longer nanorods (and in the symmetry broken conditions for even *j)* having their dipolar resonances in the IR. Therefore, Fig. 3.16 (b) shows evolution of high-order modes of overlapping nanorod dimer (making essentially one long nanorod) into a dipolar mode of gap nanoantennas. The obtained coupling strength for gap-nanoantenna (Fig. 3.16 (c)) is around 90 nm (nanorods of 150 nm length, 100 nm width, 50 nm height), which is the same or lower as compared to the one obtained for 100 nm nanodisk dimers (see Chapter 3.5). According to eq. 3.6 the maximum mode splitting (coupling strength) is expected to be larger for the longer particles with larger dipole moments. However, that is not the case here. The difference to nanodisk dimers comes from the exposure pattern, where area exposure of nanorods (or disks) yields larger fabrication polydispersion in comparison to single pixel exposure of nanodisks, probably due to proximity effect. Additionally, nanorods and HC samples were exposed with a new EBL system in our lab (30 kV, field emission) that was unexpectedly and steadily performing worse than the old thermal emission EBL (at the time of writing). The poor beam stability of the new system resulted in poorer sample qualities (for instance, the coupling strength for nanodisks exposed by new EBL system never exceeded 60 nm, and the obtained nanodisks were very inhomogeneous. If exposed as areas or circles, the coupling strength between nanodisk dimers didn't

improve at all, although the apparent homogeneity increases (as verified by SEM). The spectral evolution method as calculated by FEM is displayed in Fig. 3.16 (d) and corresponds nicely to experimental findings.

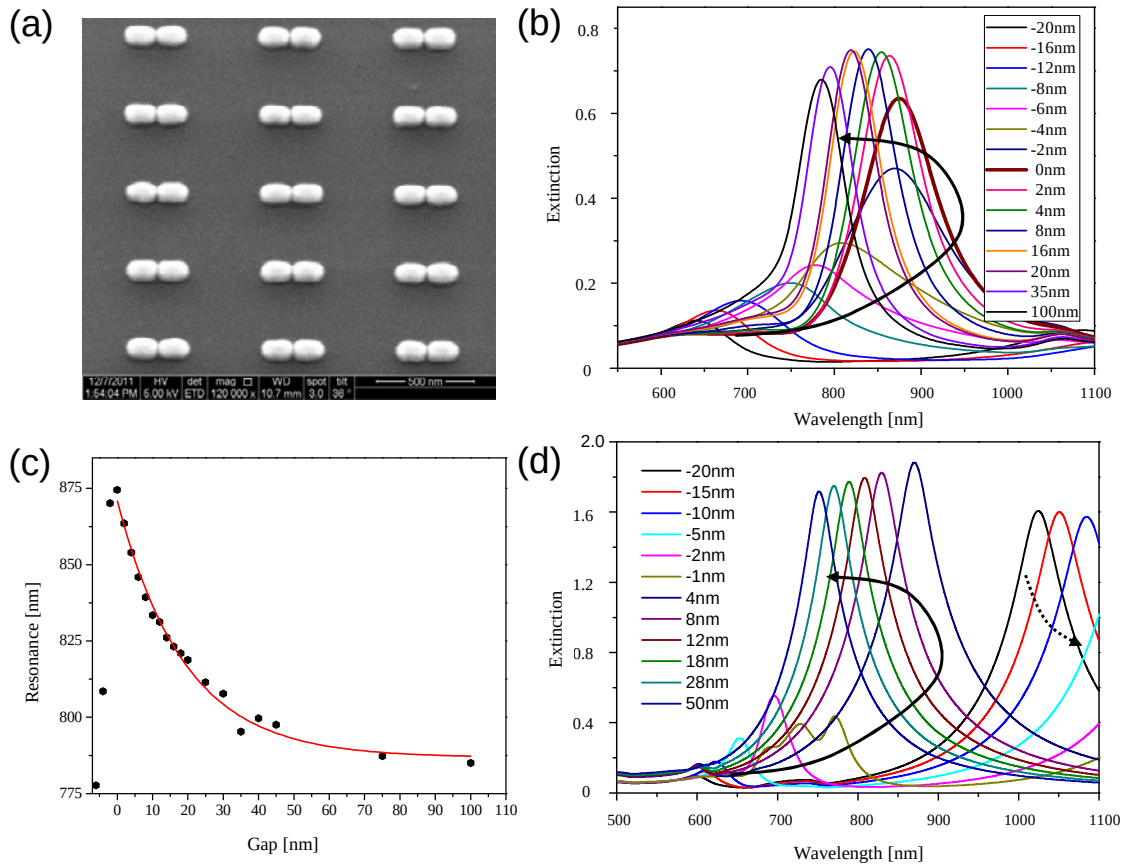

Figure 3.16–Gap nanoantenna arrays (a) SEM image of a typical gap nanoantenna array resonating in near-IR. (b) Spectral Evolution Method for gap and size determination. (c) Gap-nanoantennas' resonances as a function of gap (individual rods are 150x100x50 nm). (d) FEM calculations are performed for similar nanorod shape and size.

3.6.2. Honeycomb nanorod arrangement

Honeycomb geometry consists of an array of nanorods arranged into a special hexagonal lattice that structurally resembles a honeycomb. A primitive lattice consists of three nanorods at 120^{o} angles with adjacent ones (Fig. 3.17 (a)). Every nanorod is neighbored by 4 other nanorods, equally spaced from one another. HC geometry exploits full symmetry, thus preferential illumination is unpolarized or circularly-polarized, while for the gap-antennas polarization is always set parallel to the gap axis (identical to dimer arrays described above). A typical far-field response reveals features identical to its building blocks. The two resonant modes are present, one being at higher energies (600 nm for the presented case) corresponding to transversal and the other the longitudinal (low-energy) at 800 nm. Calculated

associated near-field distribution of higher energy peak exhibit transversal lobes that are slightly pushed toward extremities of the rods upon circularly polarized excitation, with very low intensity enhancement (<3) (data not shown). Longitudinal near-field distribution shows hot-spots with considerably higher enhancements than the transversal one (Fig. 3.19 and 3.20). These low-energy HC modes are potentially useful due to larger hot-spot surface density (LSPR sensing, SERS). HC nanofabrication is described in Chapter 2 with a difference that due to large filling factor, HC geometry suffers significant proximity effect problem during EBL exposure, thus for practical nanorod sizes (with resonances in near-IR) a more advanced negative resist was used (ARN 7520.073, Allresist, Germany). Increased coupling strength is observed with the minimum distance decrease between neighbors as expected. Typical experimental and calculated spectra are shown in Fig. 3.17 (b) and (d), with the spectral evolution method being applied for the gap calibration. Evidently, the difference from the nanorod or disk dimer case, "overlapping honeycomb" regime resembles to regularly perforated gold film, a geometry that has drawn a great deal of attention due to extraordinary optical transmission [Ebbesen et al. 1998]. A significant degree of overlap produces hexagonally arranged small holes, whose diameter grows with overlap decrease, until HC geometry is formed when nanorods become conductively isolated.

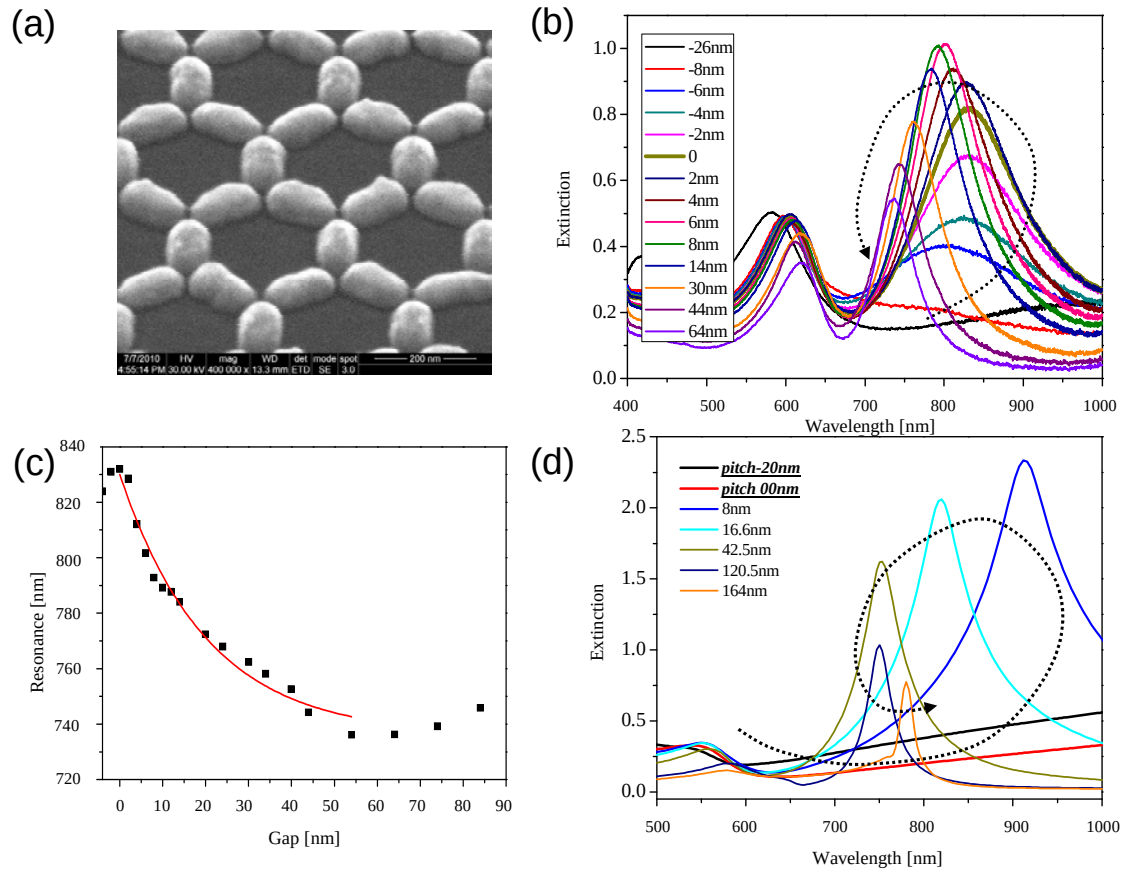

Figure Figure 3.17-Honeycomb geometry (a) SEM image of a typical HC array resonating in near-IR. (b) Spectral Evolution Method for gap and size determination. (c) HC resonances as a function of gap size. (d) FEM calculations are performed for similar set of HC parameters.

Overlapping system displays extinction dip in the visible part of the spectrum, which red shift with an increase in the diameter of the hole. A mixture of isolated and connected nanorod segments contributes to the transition regime, where finally strong and broad longitudinal resonant peak starts blue shifting with further separation. Simultaneously with longitudinal mode blue-shift, transversal mode gets slowly red-shifted in line with PH method. Eventually, for large gaps (where the array lattice approaches resonance wavelength of the array) far-field coupling effects become significant, turning longitudinal mode shifting toward red once again, with significant FWHM reduction, due to an interaction with grating modes [Auguié and Barnes, 2008]. Extinction maxima can be approximated as exponential function of gap distance in the region where near-field interactions are dominating (Fig. 3.17 (c)).

To complete the picture of the HC geometry, it is instructive to compare it with 2D arrays of gap-nanoantennas. Both geometries consist of nanorods 140x70x40 nm with radius of curvature of 35 nm at the rod ends. Gap nano-antennas are arranged in 500x250 nm 2D lattice. Investigated gaps were kept identical for both geometries and the resulting extinction spectra are shown side by side in Fig. 3.18.

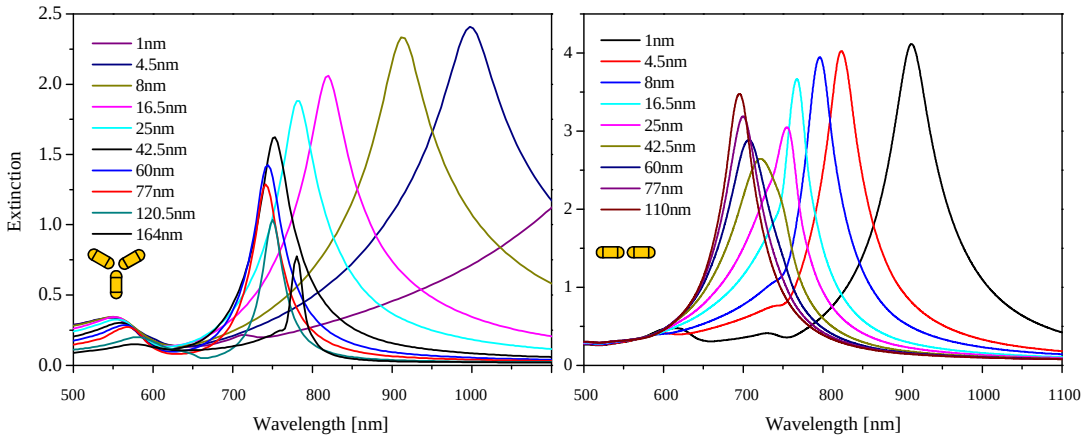

Figure3.18-Equivalent nanorods in HC and 2D arrays of gap nanoantennas. Extinction spectra as function of the dielectric gap between the closest rods. Light polarization is circular for HC and linear for rod geometry.

The most obvious difference lies in the coupling-strength magnitude for particular gap, where HC geometry is featured by a far-stronger coupling strength, as observed in the far-field. Deviation in spectra shape for gap-antennas around 750 nm (the most pronounced for gaps of 25 nm and 45.2 nm) originates from LSPR-grating mode coupling. Due to different resonant wavelengths, maximum of this coupling occurs when LSPR overlaps with the evanescent diffraction order at Rayleigh cutoff (see chapter 5). Note that illumination conditions are different, circular for HC and linear longitudinal for gap-antennas. Furthermore, HC resonances are always displaced further into IR than gap-antennas for the same rod length and gaps (Fig. 3.19. left). This can come in handy if there is a need to tune rod length to match resonance to particular laser line with constant gap. That means that HC nanorods can be shorter, yielding greater surface density of hot spots per sample area. Hot-spot density for gap-antennas considered here is fixed at 8 per μm^2. HC hot spot density is higher and equals 33.32, 31.63, 30.07, 26.63

and 23.5 per μm^2 for gaps 1, 4.5, 8, 16.5 and 25 nm. All of apparent advantages of HC are counter-balanced by the less intense "hot-spots" due to delocalized charge distribution in a comparison to matching gap-antennas. Figure 3.19 (right), compares the resonant near-field intensity enhancements for both cases. The gap nanoantennas produce larger enhancements for the same geometry parameters, for instance one order of magnitude higher for 4.5 nm gaps. In case of HCs, enhancement was calculated in the middle of two nanorods, in the direction that connects two closest points belonging to adjacent nanorods.

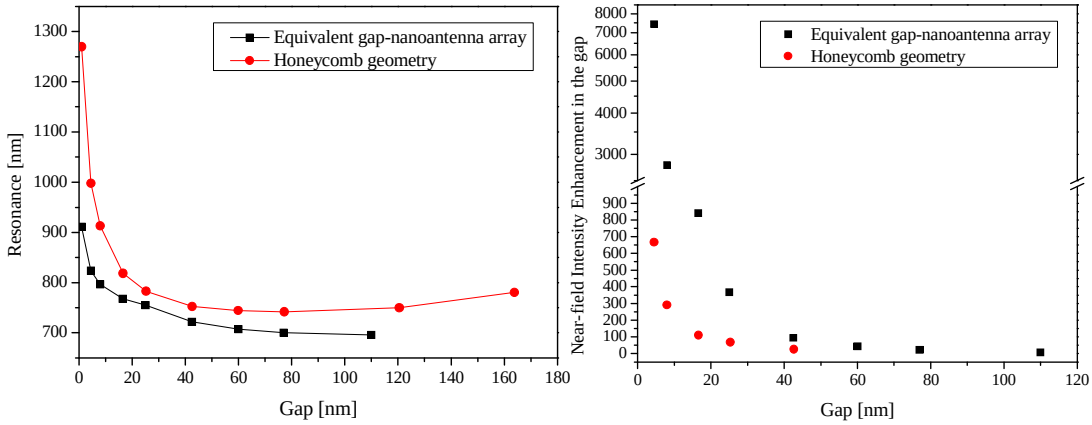

Figure 3.19-Equivalent nanorods in HC and 2D array of gap nanoantennas. Left) Extinction maximum as gap function. Right) Near-field intensity enhancement inside the gap.

Near-field intensity distribution of HC resembles that of individual nanorod for gaps larger than ca. 30 nm, where the local maxima are located exactly at nanorod extremities (Fig. 3.20, 42.5 nm gap). Once near-field coupling becomes dominant, hot-spot splits between adjacent nanorods (this regime is shown in the Fig. 3.20, for 8 and 16.5 nm gaps). Intensity values in the central regions of HC are slightly higher than "cold regions" thus, meaning that they may contribute a little to LSPR shifts upon molecule absorption, or for SERS.

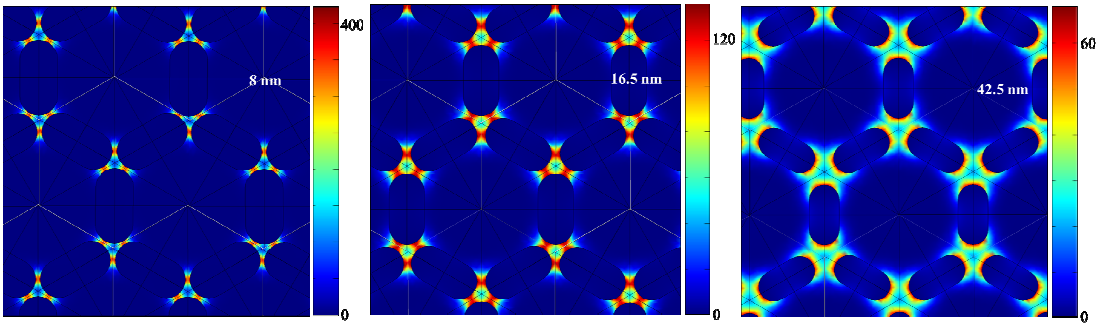

Figure 3.20-Calculated HC near-field intensity enhancement for gaps of 8, 16.5 and 42.5 nm

3.7. Spectral evolution method for bow-tie characterization

The last geometry considered here is the plasmonic bow-tie arrays. The building block of the bow-tie are two tip-to-tip facing nano-triangles, that when close enough to interact, can produce a very strong hot-spot, due to combined lighting-rod and dimer effects [Kim et al. 2008]. A hybridized dipolar bonding mode can be selectively excited by resonant linearly-polarized light parallel to the center-to-center axis. More details about optical properties of bow-ties can be found elsewhere [Marty et al. 2010, Hao et al. 2004].

Herein, the presented bow-ties are exposed as open polygonal lines that are boundaries of equilateral triangles (sides of 115 nm). The exposed arrays (1x0.5 μm periodicity) are differentiated between one another by the increasing tip-to-tip distance in the successive 10 nm steps, starting with the tip-to-tip touching polygonal lines. The spectral evolution of the fabricated nanoparticles is presented in the Fig. 3.21 where the dashed arrow shows the direction of the extinction peak progression with the triangle tip-to-tip distance enlargement. Almost identically to nanodisk dimers, small tip-to-tip distance in the exposing pattern yield overlapping structures that support only higher-order modes in the VIS (CTP is outside of spectrometer's window). These broad and weak modes evolve through the successive red-shift into bow-tie's modes once the resonances turn blue-shifting (due to distance induced decoupling). One can identify the reddest and the broadest dipolar mode (dark yellow line) peaking near 900 nm as a bow-tie array with the smallest obtained gaps in the fabricated sample (touching bow-ties). If it is proclaim as touching, the individual triangle side is projected to be 170 nm. The retrieved gaps are shown in the figure's legend. Due to 10nm gap step size, one cannot assess the geometry parameters with the higher precision than ±10 nm. SEM imaging (Fig. 3.21, right) revealed actual gap size of 35 nm for the array with estimated gap of 40 nm, which fits well with projected inaccuracy. Similar spectral findings were reported for the AFM manipulation of the distance between two colloidal nanotriangles [Jorg et al. 2008].

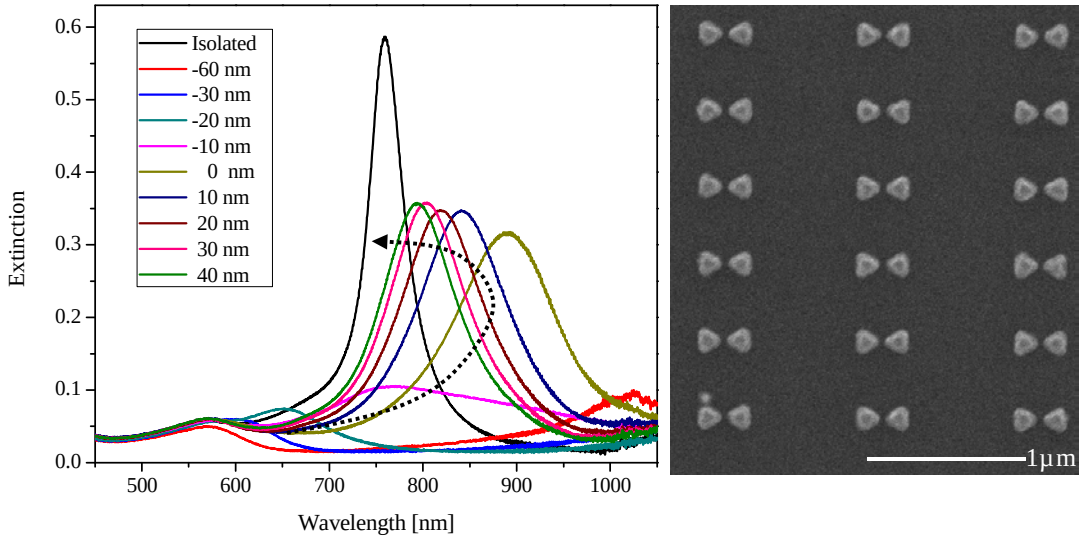

Figure 3.21-Plasmonic bow-tie geometry. Left) Spectral evolution method and calibrated gaps. Right) SEM image of typical bow-tie array.

3.8. Conclusions

Optical properties of metallic nanoparticles are strongly influenced by inter-particle near-field coupling. The coupling strength is clearly related to the range of the evanescent-fields extruding from metallic surface and proximity between interacting particles. Typically, with the interaction increase, far-field detected resonances are red-shifting, while the near-fields get stronger and further confined predominantly in the dielectric gap region. Ability to precisely tune this interaction may allow optimization in sense of molecule detection (subject of following chapters). The averaged spectral response from the ensemble of strongly-coupled nanoparticles is shown beneficial for biosensing, as explained by Dahlin [Dahlin, 2012], and easy characterization of these ensembles is required. In combination with adequate design, a novel spectral evolution method allows for fast and reliable parameter determination (gap and particle dimensions), as have been demonstrated for various geometries.

Chapter 4

Plasmonic mode engineering for enhanced molecular detection

In this section, some general rules to design an efficient LSPR sensor for the detection of small molecules are discussed. To this end, firstly it is important to remind ourselves what dictates the sensitivity of an optical sensor. The change in the optical response of the sensor is in part determined by the magnitude of the perturbation to the optical mode induced by the binding of the target molecules. In the particular case of a sensor based on plasmon nanoparticles, one aims at maximizing the induced shift in the LSP resonance central wavelength, even before attempting to minimize FWHM of the resonance or to increase peak intensity, for instance. Here, I illustrate with FEM numerical simulations how this can be achieved by properly engineering the plasmon mode of the sensor and adapt it to detect a given target molecule. Note that this chapter dominantly deals with the parameters that are physically related to the transducing mechanism (plasmonic effects), and not with the parameters that play extremely important role within the development of the relevant sensing protocols. Sensing proof-of-principle is confirmed on a model molecular entities and assumingly working conditions for the involved chemical reactions, which are very distinct from the real biomolecular sensing schemes. The issues related to development of the protocols for society-relevant analytes are addressed in more details throughout chapter 6.

4.1. Bulk Refractive Index Sensitivity, *m*

There have been attempts to model LSPR sensing performances and identify different parameters that influence the total sensitivity (e.g. Eq. 3.1). A general but yet simple model doesn't exist due to a very complex dependence of the nanoparticle resonance condition with size, shape, material, arrangement, etc. As already mentioned, many techniques result in analytical formulae for the light-nanoparticle interaction, which possess validity in a very limited range of particles' parameters or within the approximations involved in its derivation. For instance, Mie theory works well for spherical objects, Gans extension includes a special shape for nanorods, and the majority of remaining approaches provide us with analytical formulae that are valid in the quasi-static regime and/or for an individual particle. In line with these restrictions, LSPR sensors have been historically characterized by their bulk refractive index sensing (BRIS) capabilities, which one can conclude, thus far, is of very low practical significance. It will be evidenced later, high BRIS value do not necessary imply higher molecular detection sensitivity, and vice versa. However, these models and discussions provide us with a good starting point to understand and choose the optimum LSPR sensing platform for real high-end applications.

4.1.1. Influence of size and shape

Recalling that the LSPR resonance condition (under quasi-static approximation) is given by [Jain et al. 2006]:

$$\mathrm{Re}(\varepsilon) = -(\frac{1-L}{L})\varepsilon_m ,$$

where $L, \varepsilon, \varepsilon_m$ are a shape dependent factor, permittivity of the metal and the nanoparticle's embedding medium, respectively. It becomes clear that BRIS depends intrinsically on the real part of the metallic permittivity. Gold and silver permittivity follow a near-linear dependence with wavelength, hence BRIS is well approximated as a linear function within the practical range of ε_m (around permittivity of water). Thus, BRIS depends on the slope of the real part of the metal's permittivity at first glance. Another easy distinguishable factor should be shape factor L that influences BRIS (rods ($L_{rod} < L_{sphere}$) are more sensitive than spheres $L_{sphere} = 1/3$). Miller et. al. concluded that BRIS increases linearly with plasmon resonance position for some particle shapes [Miller and Lazarides, 2005]. Size increase is also followed by a sensitivity increase, but it is ambiguous if it can be related to volume or aspect ratio or the nanoparticle's shape separately [Jain and El-Sayed, 2010].

4.1.2. Influence of metal losses. Relevance of bulk sensitivity

Additionally, metallic losses can affect the sensitivity by affecting the FWHM of resonance. Metals with lower losses feature higher field enhancement making that higher sensitivities and SERS amplification is achieved for silver nanostructures over gold [Barbillon et al. 2007, Haes et al. 2003]. As a rule of thumb, it can be established that redder (longer wavelength) resonances possess higher BRIS among the same family of particles (shapes, sizes, material).

However, I will point out that LSPR BRIS is so low in comparison to SPR, that putting any effort in increasing it doesn't pay off. Typically, reasonably higher BRIS is a result of mode delocalization, which generally produces a lower sensitivity to bio-molecular detection, plus increased background due to temperature fluctuations and increase of empty sensing volume fraction.

However, it is useful to have our systems pre-calibrated for bulk sensing for various reasons:

1) BRIS's significant deviation from the theoretical prediction can point out some sensor surface contamination, particles annealing or substrate etching tendency of investigated solutions [Otte et al. 2011]. Thus it can be a fast way for screening fabrication defects.
2) Real-time molecular association/dissociation response can be superimposed onto the discreet step-like response, which is a consequence of refractive index change in the bulk solution (Chapter 6). In many situations it cannot be visually separated from molecule adsorption, especially in the case of strong affinity reactions and/or high concentration response. This

requires flowing of a particular buffer before and after the binding step, to get stable, reference base lines and reliable read out, in addition to the washing off of any loosely attached molecules. (Buffer flowing prior to the detection until the base line is stabilized, increases assay times).

3) Subsequent to molecule adsorption, BRIS decreases due to partially occupied sensing volume. If the opposite trend were detected, the sensor output would be erroneous due to various contaminations or unstable nanoparticles.
4) BRIS is necessary in modeling (in the frame of Eq. 3.1)

Representative values of the sensitivities of on-glass immobilized nanoparticles are calculated for the case of gold nanodisks (cylinders) (Fig. 4.1) Three shapes were investigated: ideal nanodisks having identical aspect ratios of 2.5 but differing in size (diameter/out-of-plane height) and one more realistic shape (tip-less cone) of similar dimensions as the larger ideal disk. The large ideal disk of 100 nm in diameter and 40 nm in height is the most sensitive one, with a slope of ca. 190 nm/RIU (black data points). A decrease in size by a factor of two (dimensions 50 nm/20 nm) shows a 135 nm/RIU change (blue data points). The more realistic nanodisk (base of 100 nm, height of 40 nm and side slope of 25 degrees) that mimics nanoparticles described in Chapter 3 displays a slope BRIS of 143 nm/RIU BRIS. Fabricated gold nanodisks usually resonate at around 640 nm in air with sensitivities to bulk changes within the 120-140 nm/RIU range, quite close to the values predicted by theory (red data).

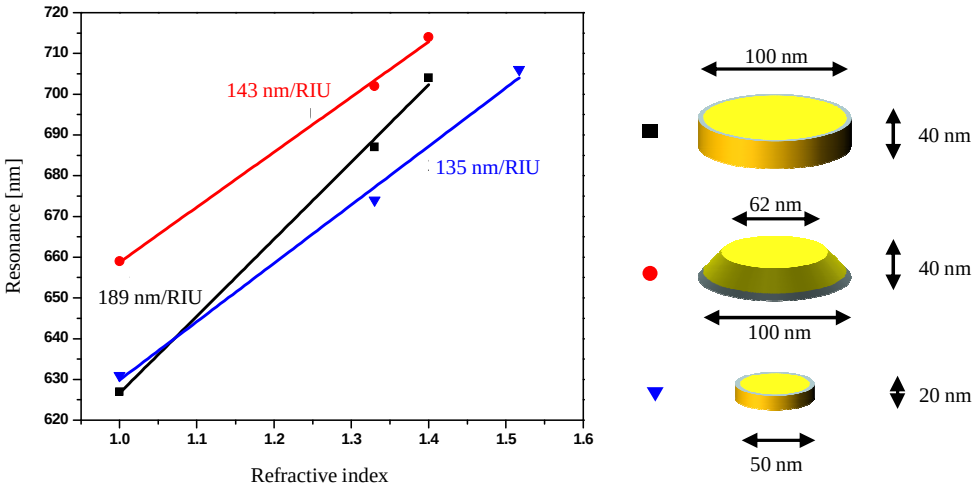

Figure 4.1-Resonance position of various nanodisks in different dielectric media. The slope of the linear fits represents bulk refractive sensitivities in nm/RIU.

4.2. Sensitivity decay length

Another very important parameter of eq. 3.1 is the near-field decay length L_d, that characterizes sensing volume of the SPR system [Jung et al. 1998]. Applied to LSPR, L_d can only represents an averaged parameter, since the LSPR near-field decay length is spatially dependent. Nevertheless, L_d is directly related to the LSPR sensing volume, thus it helps in the optimization of the nanoparticle surface functionalization protocol. Such an optimization should result in the improved mode-analyte overlap, i.e. while the analyte should be brought as close as possible to the surface, the LSPR mode should encompass the analyte but confined sufficiently not to pick-up any background contributions. A typical field extension from nanoparticle surface can be determined by simulations (as shown below) or experimentally. As an illustration, the total thickness of an immunological, molecular layer that is typically used in modifying the surface of a nanoparticle, in order to bind a particular analyte, is usually to the order of 15-20 nm (SAM+antibody). Thus depending on the size of the analyte to be detected, the nanoparticle sensing volume should be optimized to encompass the attached analyte (antigen for the particular biorecognition between an antibody and its target).

A short range and long range distance dependence of the nanoparticle sensitivity upon molecular layer adsorption revealed an inhomogeneous distribution of the sensitivity. These are related to the spatial near-field distribution of resonantly excited nanoparticles, are very dependent on the intrinsic parameters of the resonant particle (size, shape, material) and illumination conditions. It has been reported that the “hotter” (more sensitive) nanoparticle regions display higher sensitivity with shorter sensing range, while “colder” are less sensitive but probing surrounding space (longer decay) [Haes et al. 2003, 2004]. The experimental realization of sensitivity spatial profiling is typically performed by monitoring resonance shift induced by the monotonically increasing the thickness of the adsorbed mass. By controlling the total number of carbon atoms in mercapto-alkane SAMs, the molecular coatings of varying thickness are absorbed onto nanoparticles. More versatile methods are based on a repeating cycle of multilayer MUA-metal ion formation [Haes et al. 2003] or on continuous depositions of polyelectrolyte layers of alternating charge [Sannomiya et al. 2009]. Recently, atomic layer deposition technology has allowed ultra-controlled SiO_2 or TiO_2 layer formation thus improving the reliability and resolution of probing volume profiling [Whitney et al. 2005]. These sets of experiments moreover demonstrated a stronger electromagnetic enhancement and larger field decay of silver over gold nanoparticles [Haes et al. 2003].

4.2.1. Assessment of sensitivity distance decay (FEM calculations)

At this point, we present results of FEM calculations that illustrate the influence of the spatial overlap between plasmonic fields and the target. The nanoparticle system studied here is a gold nanodisk (50/20 nm) on a glass-air interface. The sensing range is tested for two different kind of molecular depositions, here mimicked by a thin dielectric layer (n=1.517) on the side walls and on top of the disk. The

resonance peak is monitored for the thickness increase (Fig. 4.2). The induced resonance shifts clearly exhibit two exponentially decaying trends, depending on the dielectric layer deposition site. An exponential fit yields decay lengths of 6.97 nm (black data points) and 8.07 nm (blue data points) for side and top deposition respectively. For the same layer thickness (d=b), the side binding produces larger shift, with the remaining sensing volume being smaller. The mass ratio of the deposited layers for d=b is 0.8 ($mass_{side}/mass_{top}$) for the disk studied. To correlate the observed decay lengths, the near-field enhancement profile of the resonantly excited disk with the absence of any adsorbed layer was investigated (Fig. 4.2 (c) and (d)). The field and intensity enhancement decay as 9.87 nm and 5.66 nm in the direction parallel to the interface, while out-of-plane decays are 13 nm and 7.14 nm. The sensing range sits in between the field magnitude and intensity decay lengths, though closer to the field enhancement. The spatial distribution of sensitivity (sensing volume) clearly coincides well with the dipolar near-field distribution [Piliarik et al. 2011].

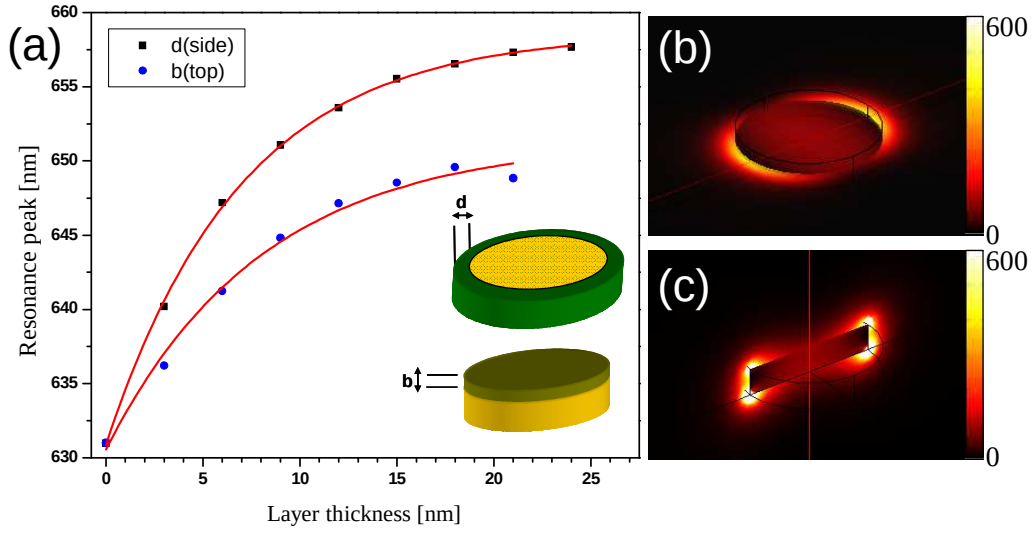

Figure 4.2-LSPR sensing volume (a) The resonance shifts with the locally adsorbed dielectric layers of varying thickness (black data points – side deposition; blue data points top deposition). Exponential fit yields decay of 7.2 and 10.5 nm respectively. Dipolar near-field profiles are shown in the xy plane through the nanodisk center. (b) and yz plane.

Lastly, the remaining issue is related to the inevitable negative influence of the substrate on the induced shift magnitudes. The sensitivity of a substrate immobilized nanoparticle is reduced primarily due to sensing volume blockage by the substrate itself. In comparison to the particles in solutions the sensitivity reduction is not negligible. However, the influence of substrate is not limited only to the physical blockage of the nanoparticle surroundings. The LSPR mode of nanoparticle at the dielectric interface is more concentrated into the medium of higher refractive index. The scattered light and the evanescent fields are directed predominantly slightly above the critical angle in the substrate [Novotny and Hecht, 2006]. This means that an increase in the dielectric interface contrast results in a penetration

of the sensing volume (LSPR mode) into the substrate, resulting in lowering further the BRIS as well as the molecular sensitivity. The evidence of the substrate influence by Brian at al. showed that the BRIS increases with substrate refractive index reduction [Brian et al. 2009]. Prior studies have suggested elevating nanoparticles on supporting dielectric pillars, thus releasing more of the sensing volume initially trapped within the substrate [Dmitriev et al, 2008]. A very similar strategy was applied to LOC device to increase the sensitivity of nanoparticles upon specific DNA hybridization [Otte et al. 2011], and is discussed in more details below in the frame of non-specific absorption (chapter 6).

4.3. Influence of the background matrix

Equation 3.1 shows a linear dependence of the induced resonance shift to the refractive index contrast between the adsorbed analyte and its surroundings. Thus, measuring in air or in water, surely has an influence on the measured shift. Measurements in air were practiced at the beginning of LSPR sensing era with fixed nanoparticles due to larger associated shifts [Haes et al. 2004, Malinsky et al. 2001], but binding kinetics were unavailable and uncertainty due to drying procedure was present. The effect of the medium change from air to water for the adsorption of the thin dielectric layer (mimicking SAM) is displayed in Figure 4.3. The resulted resonance shifts are 6 nm in air and 2 nm in water as background. Subsequent dielectric layer that mimics a protein adsorption, yields shifts of 49 and 22 nm, respectively. At early stage, resolving small resonance shifts was limited to a couple of nanometers, but following the work in Höök's group (Chalmers university of technology, Gothenburg, Sweden) the resolution of resonance monitoring was pushed to picometer levels thus allowing the real-time sensing in aqueous medium [Chen et al. 2009, Jonsson et al. 2010, Sannomiya et al. 2009].

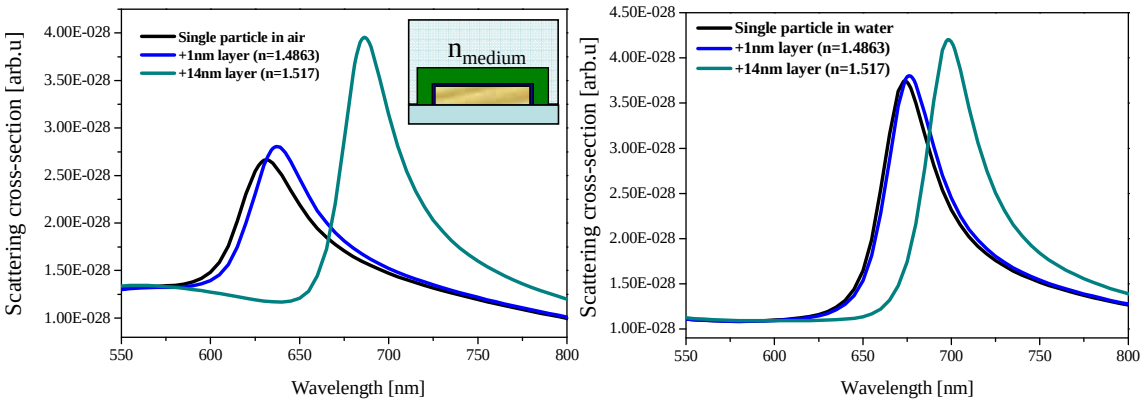

Figure 4.3-The influence of the background media to the magnitude of the shifts induced by the different perturbations (small and large molecular layers). Left) Resonances in air. Right) Resonances in water matrix (FEM calculations).

4.4. Enhanced sensing performance of near-field coupled structures (dimers)

Plasmonic dimers have been subject of extensive studies due to its potential applications for enhanced light-matter interaction, more precisely for SERS [Shegai, Chen et al. 2011, Zhang et al, 2009], two-photon polymerization [Ueno et al. 2010], plasmon-assisted optical trapping [Righini et al, 2009], nanoantennas for single emitters [Curto et al. 2011] and more. Their unique properties were recognized as potentially beneficial for LSPR biosensing. However, early research was limited within the theoretical domain, particularly due to complexity involved in nanofabrication and associated surface chemistry. A particularly extensive theoretical study was conducted in the group of El-Sayed (Georgia institute of technology, Atlanta, USA), but apart from successful dimer array fabrication [Jain, Huang & El-Sayed 2007], all of the remaining LSPR work stayed within the frame of theoretical BRIS studies and optical characterization [Jain and El-Sayed, 2008, Lee and El-Sayed, 2006]. Enoch et. al. pushed this subject further by the theoretical investigation of dimer response upon continuous molecular layer deposition modeled as thin dielectric film [Enoch et al. 2004]. Just recently, we were able to experimentally prove all of the relevant theory referring to dimer LSPR sensing and to reveal some very interesting phenomena that are the direct consequence of field confinement within the gap [Aćimović et al. 2009]. It is worthwhile acknowledging the work of Sannomiya et al. in which experiments similar to ours were conducted. However, the effects we observed were undetectable by them, mainly due to the less advanced fabrication method and a slightly different choice of the investigated geometry (densely packed arrays produce somewhat more delocalized modes) [Sannomiya et al. 2009]. One of their results is linear relationship between BRIS and the response to BSA proteins, which is strongly opposed to our findings. The remainder of this chapter is devoted to the description of the results obtained on the dimer geometry related to LSPR biosensing.

To begin with, I will present both theoretical and experimental BRIS data, to be followed by the theoretical study of the induced resonance shift by a single-molecule perturbation. The molecule position is varied showing hot-spots as the most sensitive positions. Our data on molecule detection of different molecules (small molecular weight SAMs and large globular proteins) as function of the nanoparticle coupling strength will lead to the conclusion about the importance of mode-analyte overlap (MAO) in the LSPR biosensing.

4.4.1. Nanodisk dimers as bulk refractive index sensors

The BRIS of dimers as function of gap size are are summarized in Fig. 4.4. For a typically studied nano-cylinder (ideal disk) particles FEM modeling yields the doubled bulk sensitivity as the gap shrinks (black data). This reproduces well prediction of El-Sayed's group obtained with DDA numerical method. The experimental data (stars (two samples)) show a similar trend, with an overall decrease in the observed values in comparison to the ideal nanocylinder case. Additionally, unlike what predicts the simulations, for sub-10 nm gaps the sensitivity exhibits a drop. This effect is rather related to the size dispersity of the fabricated sample, which is further backed up by the fact that overlapping structures of particular overlap show lower bulk sensitivities compared to the dimers of the same gap sizes (see Fig. 4.9). It is

worth noting that Fig. 4.9 expresses the BRIS value of the higher-order modes of overlapping structures, not the CTP mode (see chapter 3). These modes are spectrally adjacent to the dimer dipolar modes, as seen in the graphs of chapter 3 describing spectral evolution methods for gap calibration. Thus, any mixture of small gaps/overlapping structures that can be characterized by an averaged gap value, would display smaller bulk sensitivity than the ideally homogeneous array of the same gap value, due to lower bulk sensitivity contribution by the overlapping structures. (This doesn't hold for the case of thin molecular layer detection, where the monotonic growth of the sensitivity is demonstrated even for the sub-10 nm dimer arrays (Fig. 4.8). However, a better correspondence between theory and the experiment is achieved for a more realistic modeling of the nanoparticles. The nanoparticles are modeled as a tip-less cone (100 nm base, 40 nm height, 25 degrees side wall slope) exhibit BRIS shown as red circles, a bit lower than those in the experiments. Another effect that may be responsible for the deviations of the experiments from the simulations is the unknown temporal character of the nanoparticle shape modification upon exposure to various solvents (solvent annealing, see below); since the acquiring of the experimental data is triggered instantaneously once the air environment is replaced by water, but in the sequential manner, typically lasting between 30 to 45 min. Additional sources of discrepancies between theory and experiments are bulk optical constants, shape uncertainties, sharp edges, meshing density, etc.

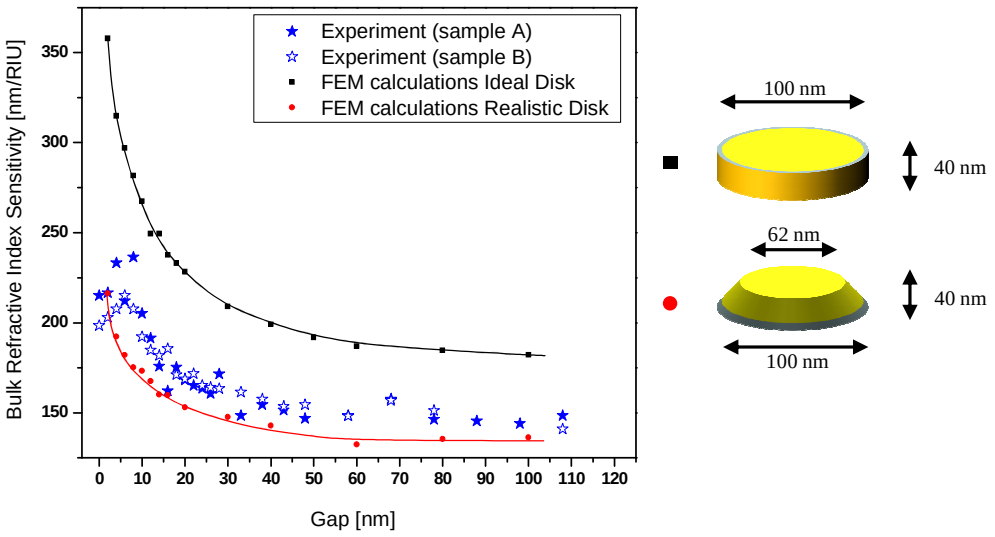

Figure 4.4-Bulk refractive index sensitivity as a function of gap sizes: Experiment vs. Theory. Blue data points (stars) correspond to experiments. Black and red data show FEM calculated values for two disk dimer shapes (showed on the right)

4.4.2. Single-molecule detection. Influence of the sensor geometry and molecule position

In order to map the sensing volume of dimer, we monitor resonance shift upon single molecule (e.g. protein) binding as a function of the binding location. Such protein can be reasonably mimicked in the FEM model by an 8 nm dielectric sphere of refraction index 1.5. Let us first consider an isolated cylindrical gold nanoparticle lying upon a glass substrate. Figure 4.5 B shows the unperturbed electric near field distribution in the half-height plane of the particle in resonance for an incident plane wave polarized along the X-axis. Upon this illumination condition, the plasmon mode features two lobes located at opposite edges of the particle and aligned along the incident electric field direction (dipolar mode). For a single molecule binding to the metal, there is a strong mismatch between the volume of the target molecule and the plasmon mode volume leading to a very small resonance shift (Fig. 4.5). Note that this shift would be even smaller if the molecule would be bound in the "dark regions" located along the Y-axis or Z-axis (Fig. 4.5 A).

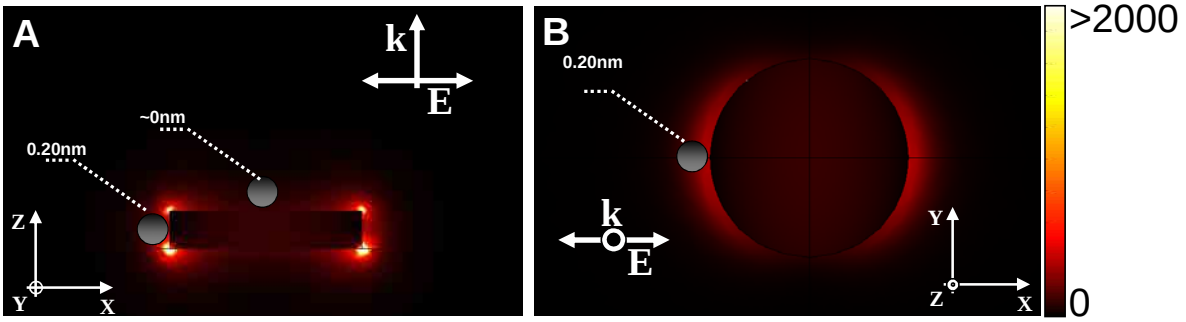

Figure 4.5-Near-field intensity distribution computed for an isolated cylindrical gold particle (50 nm diameter, 10 nm height) illuminated by a linearly polarized plane wave at 626 nm (in resonance) and resonance shift induced by the presence of a single 8 nm dielectric sphere (n=1.5) A) Side cross-section view. B) Top cross-section through the middle of nanoparticle.

In order to increase the perturbation one needs to squeeze the mode volume to dimensions that are commensurable with the size of the target molecule, as can be done using plasmonic dimers. Locating the target molecule in the gap of a gold dimer formed by two identical gold cylinders leads to a resonances shift about 10 times larger than with a single particle (Fig. 4.6). The near-field distributions shown in Figures 4.5 and 4.6 are the unperturbed modal distributions. The presence of the perturbation besides the shift in the resonance induces the perturbation of the near-field distribution, as well, which is not presented here.

In a configuration involving a large number of molecules binding all over the nanoparticle, the different molecules do not all have the same contribution to the resonance shift depending on where they are located. Figure 4.6 illustrates the influence of the location of a single molecule on the magnitude of the shift in the dimer case. It is shown that a molecule sitting in the gap leads to a shift at least one order of magnitude larger than for any other location of the structure. Such ratio becomes even larger for gap antennas formed by two adjacent elongated gold rods or bow-tie antennas instead of cylinders (data

not shown). This underlines the importance of specifically binding the target molecules within the gap regions where the dimer effect could be fully exploited, especially when the analyte molecules are not abundant enough to cover the whole structure. The question about delivery of such a molecule to the gap region is not within the scope of the thesis, and is currently one of the hot topics in single (to a few) analyte detection.

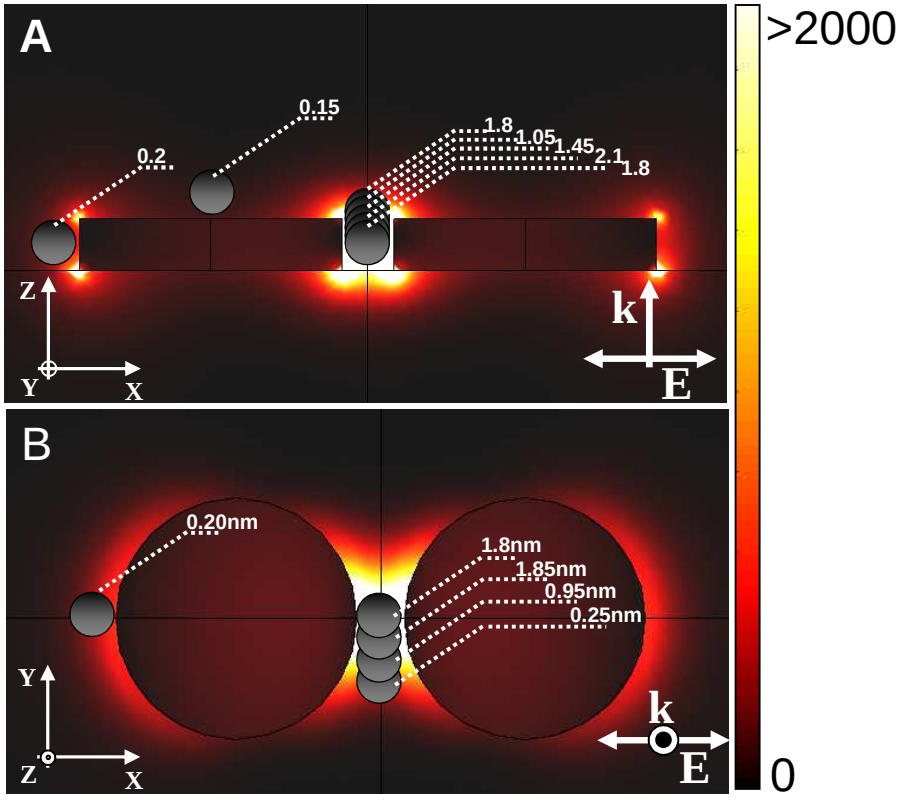

Figure 4.6-Near-field intensity distribution computed for a gold dimer illuminated by a linearly polarized plane wave at 659nm and resonance shift induced by the presence of a single 8nm dielectric sphere (n = 1.5). A) Side cross-section view B) Top cross-section through the middle of nanoparticle.

Recently, it has been shown that for sensors based on nanoholes in metallic films, a faster kinetics and therefore shorter read-out time is achieved when the analyte selectively binds on the walls of the holes where the plasmonic mode is mostly confined. This was managed by coating the bottom of holes and the top surface of the gold film by a thin layer of titanium dioxide (TiO_2), enabling selective functionalization of the gold wall of the hole [Feuz et al. 2010]. The improvement lies in the decrease of averaged depletion zone near the sensor interface [Sheehan and Whitman, 2005], since molecules cannot be consumed by non-active regions of metallic film. Besides, the detected signal originates from the smaller number of analytes. In the case of dimer structures, a similar approach where the top surface is covered can be considered. In practice though, analyte delivery for very small concentrations of target molecules represent a major challenge, since molecule transport is then governed by diffusion, making the detection time required for a few molecules to get to the sensing volume, unreasonably

excessive (to the order of days or weeks) [Ferreira et al. 2008]. Possible improvements can be foreseen by further miniaturization from microfluidics to nanofluidics or using the very promising flow-through sensing configuration [Sheehan et al. 2005, Eftekhari et al. 2009, Jonsson et al. 2010].

A substantial enhanced resonance shift of dimers over isolated particle is still expected when considering a large ensemble of molecules binding uniformly all over the nanoparticles. In that case the bound molecules can be modeled by a thin dielectric layer covering the substrate. Simulations based on the Fourier Modal Method showed an enhancement in the resonance shift of about five as compared to isolated particles [Enoch et al. 2004].

4.5. Enhanced molecular detection of nanodisk dimers

Once completed optical characterization and the gap sizes calibration, binding experiments were conducted to test and prove the enhanced sensitivity of small molecule detection with gold dimers. It will be demonstrated that the response of a dimer LSPR sensor strongly depends on two main parameters: gap and analyte size. Prior to the introduction of the analyte of interest to the gold nanoparticles, the resonance position has to be stabilized with respect to the so-called solvent annealing.

4.5.1. Solvent annealing

In 2001, it was reported that metallic particles produced by nanosphere lithography (NSL) were prone to structural changes induced by surface tension alterations after changing the liquid environment surrounding the nanoparticle [Malinsky et al. 2001]. Although rarely reported, these transformations might play an important role in the operation of LSP sensing platforms. The alteration in the total interfacial surface tension when transferring NSL structures from air or nitrogen to solvents provoked a substantial resonance shift that reached up to 100 nm as a consequence of nanoparticle edge smoothing, in-plane size shrinkage and out-of-plane height increase. Even though total solvent annealing decreases with time, particles have to be stabilized prior to any molecular binding in order to correctly ascertain the true relative plasmon shift associated with such binding events. Interplay of surface tension on glass/metal and metal/environment interfaces determine the extent of shape modification. Since these subtle modifications may be difficult to observe by AFM or SEM in case of nanodisk dimers, the evaluation of the particle reshaping by the solvent annealing is conducted by monitoring the resonant shift magnitudes induced by the annealing as the function of the gap.

For EBL fabricated dimers, after immersion of the particle arrays into an ethanolic solution, the resonances subsequently shift to the blue (lower wavelengths) by an amount nearly exponentially dependent on the initial gap size. Blue shift of gold, single (uncoupled) particle arrays can typically change up to 10 nm. This implies that particle diameter is on average shrinking, while the out-of-plane height is possibly just slightly increasing. Yet another indication of diameter shrinkage is the effect

dependence of the initial gap size, where a blue shift for closest dimers can change typically up to 20-30 nm. Figure 4.7 shows the result of solvent annealing after 7 days immersed in ethanol, where the exponential trend is clearly reproduced. When compared to organic solvents, water annealing is significantly less pronounced. Thus in order to preserve gaps, it is in practice more suitable to work with water-based solvents. Also, substantially less solvent annealing is observed when using adhesion layers (Ti, for instance). In that case, nanoparticles keep their shape in contact to substrate, and annealing curve is inverted relative to previous, i.e. the maximum annealing occurs for isolated particles. Hence for small gaps, resonance is governed mainly by shortest distance between particles, and due to oblique side walls, thus the induced structural changes provoke larger resonance shift for uncoupled particles in comparison to closely spaced dimer (data not shown). However, the solvent annealing for particles on Ti layer were not thoroughly and systematically investigated here, thus the last statement, based on only few experimental observations, should be taken with a caution.

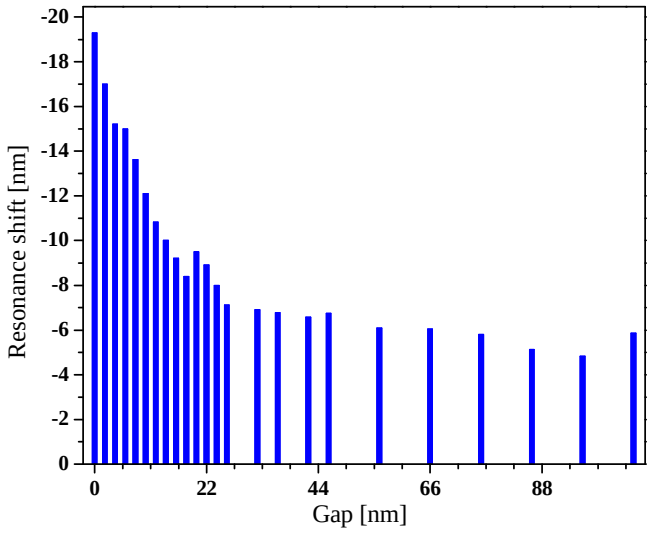

Figure 4.7-Solvent annealing of gold dimers after residing 7 days in ethanol

4.5.2. Case of small analytes where mode-analyte overlap not influenced by steric hindrance

Here, we consider binding/detection of small molecules (smaller than the typical gap sweeping steps of 2 nm) such as thiolated-alkanes. The thiol head-group (-SH) forms complex-coordinate bond with gold, and is commercially available conjugated with alkane chains, poly-ethylene glycol (PEG) or other moieties. The opposite end of the alkane chain can consist of a variety of chemical functionalities, for binding a receptor of interest (intrinsic functionality present in DNA, proteins or antibodies for example) or rendering the surface hydrophilic/hydrophobic (chapter 6).

A different range of alkane chain lengths are available, from very short to very long ones. As stated earlier, these molecules tend to self-assemble on gold surfaces, making an homogeneous and uniform functional carpet (monolayer). Employing the short chain self-assembling monolayers (SAM) is beneficial due to the low occupancy of sensing volume. However, stability and uniformity of monolayer is increased for longer chains due to side chain interactions between adjacent molecules. The initial SAM of choice, within this work was mercapto-undecanoic-acid ($SH-(CH_2)_{10}-COOH$), a cheap compound of total length of 1.5 nm once bound to gold. It is mainly soluble in organic solvents and we used pure ethanol in our experiments. Typically, a 10 mM MUA solution in ethanol was prepared and dimer samples were immersed completely during 24h, which is recommended time for monolayer formation. Despite the small size of MUA (<1.5 nm), the monolayer formation is easily monitored by the induced relative resonance shifts [Barbillon et al. 2007]. The typical response of the dimer system after the 24h MUA binding process in static conditions, complete with a rinsing and drying step prior to measurement, is shown in Figure 4.8.

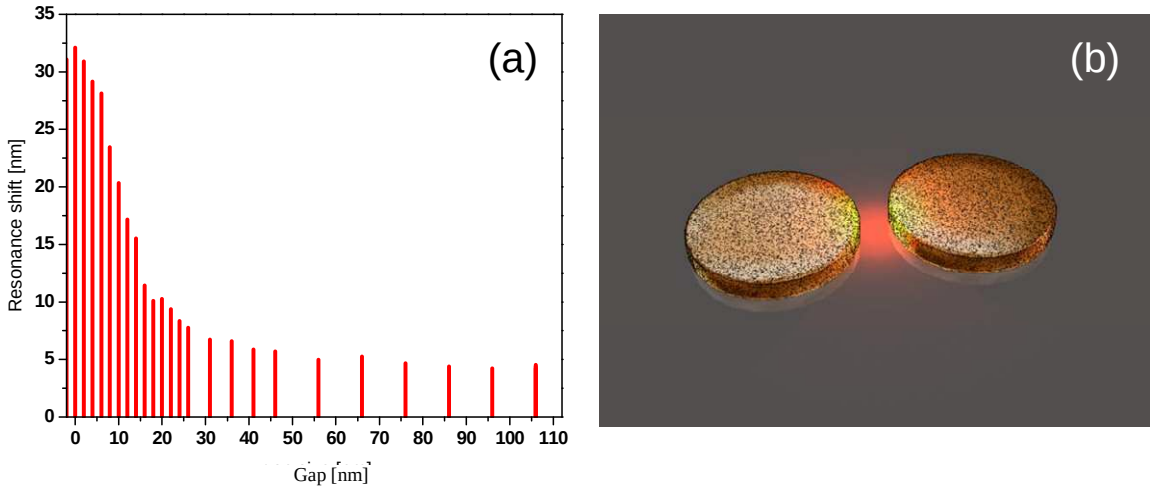

Figure 4.8-MUA self-assembly onto gold dimers. (a) Equilibrium resonance shift induced by MUA for dimers as a function of gap size. (b) Depiction of self-assembled monolayer formation

One can clearly observe that the squeezing of the modal volume (gap shrinkage) increases exponentially the induced resonant shift magnitude, with more than six-fold enhancement for the touching dimers. The total shift after the equilibrium state is reached (and subsequent sample drying) depends on the MUA concentration employed in the first place. Barbillon et al. reported plasmonic response and calibration curves of MUA monolayer formation for EBL fabricated nanodisk arrays [Barbillon et al. 2007]. In our case, the system is not concentration calibrated, since this is not a part of relevant sensing protocol, nor MUA is relevant molecule for the detection. The standard concentration for the complete monolayer formation (so called saturation concentration), according to the literature is between 5 and 10 mM [Barbillon et al. 2007].

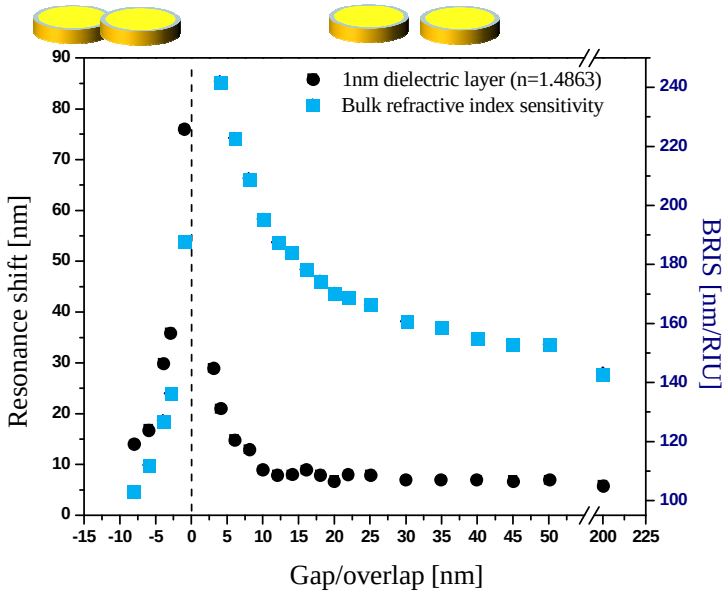

Figure 4.9- FEM calculated BRIS (blue) and the resonance shift magnitudes as gap function upon coating with 1nm thick dielectric layer.

Beside the exponential increase of the relative resonance shifts with the coupling-strength, for the sub-10 nm gaps, we don't see the sensitivity drop, as was the case for the BRIS (Fig. 4.4). The observed monotonical increase in the sensitivity to MUA is the direct consequence of a different influence of nanoparticle size dispersion to the different MAOs. Namely, higher or similar sensitivities of low overlapping structures (small overlaps) in comparison to small gap dimers are expected according to Fig. 4.9 (FEM calculations) for thin molecular layers. Although it is very probable that the meshing density used here wasn't sufficient for a more reliable quantitative results, especially for the 1 nm thick molecular layer (black circles, Fig. 4.9), the qualitative prediction agrees well with the experiments, in which the induced shifts for the overlapping structures are even higher than for corresponding gap dimers. This clearly differs from the BRIS ratio of overlapping structures and dimers, where the overlapping structures feature lower BRIS values (blue squares, Fig. 4.9).

Here it is worth noting that solvent annealing reduces the expected sensitivity due to gap enlargements (see above). Therefore it is very important to stabilize nanoparticles prior to any measurements, via long exposure to low-annealing solvents (water instead of ethanol). Additional stability can be achieved by an ultra-high temperature annealing processes [Langhammer et al. 2010, Larsson et al. 2009].

4.5.3. Larger analytes (mode-analyte overlap influenced by the steric hindrance)

When the MUA monolayer is formed on the gold sensor surface, the outer extremity shows a carboxyl functionality (COOH). Given that our goal is a subsequent covalent binding of proteins, the -COOH termination has to be modified in the process called activation for an intermediate more reactive amino ($-NH_2$) moieties expressed on the surface of proteins. This process of activation is accomplished by the

standard carbodiimide route through the use of a combination of EDC and NHS chemistry, that exchange –COOH termination into NHS-ester, whic readily couples to proteins (see chapter 6). Shortly after the activation step is finished, the dimer sensors are immersed in a buffered solution of BSA molecules (0.15 mM) for 1h in static conditions. It is worth noting that BSA likes to stick electrostatically to gold as well to other charged surfaces. This actually suggests that there might be two different components of the BSA attachment to MUA-coated gold surface i.e., covalent and physisorption. However, considering both the prior surface protection by MUA SAM and the favorable kinetics associated with protein binding via EDC/NHS route, it is unlikely that physisorption plays a significant role here. Nevertheless, in real label-free immunoassay systems, non-specific binding to the sensor represents a very serious issue. How to circumvent "non-specific adsorption" is discussed in more details in chapter 6.

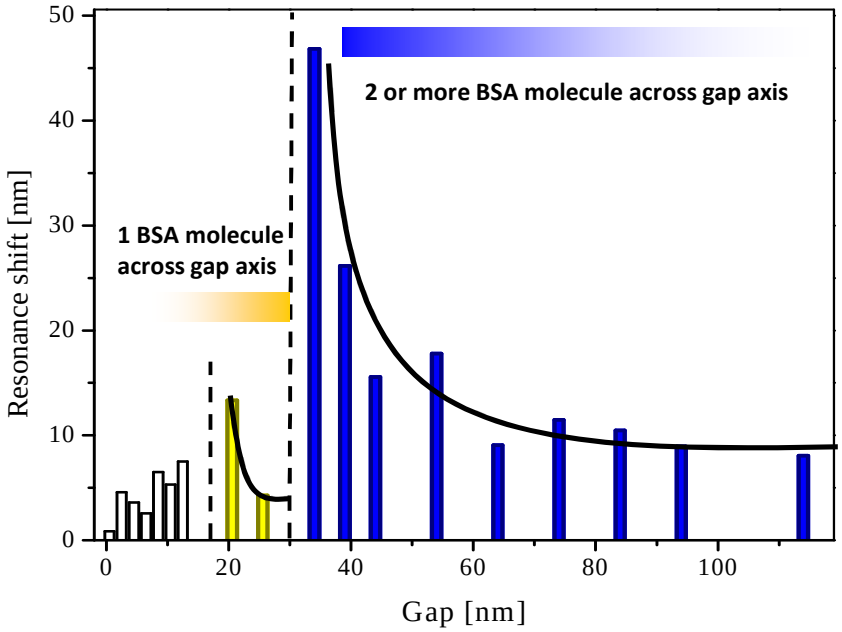

Figure 4.10-Equilibrium resonance shift induced by BSA binding to the dimers as a function of the gap. Lines are used as a guide to the eyes.

Figure 4.10 show the equilibrium resonance shift of the binding of BSA to MUA-coated arrays after the sample rinsing (removal of loosely attached proteins). Contrary to the curve in Figure 4.8, the BSA binding curves are far richer in features. Pertaining to previous observations, starting from isolated or well separated nanoparticles, the red shift magnitude follows an exponential rise with decreasing gap. The maximum resonance shift is obtained when the gap reaches the size of ca. 30 nm. Thereafter, as the gap further decreases, a sudden drop in resonance shift is observed, followed by an additional increasing trend. We should remember that the concentration of BSA across all the arrays constituting each gap condition, is uniform, i.e. we assume the same number of BSA molecules to attach (within the error). Therefore, this sudden drop in resonance is not concentration related and must derive from

some other effect. Again, when the gap size reaches ca. 15 nm, another discrete drop occurs. We attribute these discrete drops to the relation between the size of the dimer gap and that of the protein. Considering the shape of a BSA molecule is rod-like (4 ×4 ×14 nm^3) [Malmsten, 1995], when the gap is big enough (≥30 nm), two such molecules can fit across the shortest distance between the dimer structure. By reaching this limiting gap size of 30 nm, large resonance shifts are expected due to the optimum overlap of mode volume and BSA molecules Fig. 4.11 (a). When the gap decreases further below the first critical value, only one molecule can now fit along the dimer axis due to steric crowding, bound either to one or the other particle forming the dimer. As the gap further diminishes, overlap of hot spot and molecule increases again Fig. 4.11 (b), up to a point when the molecule can no longer fit

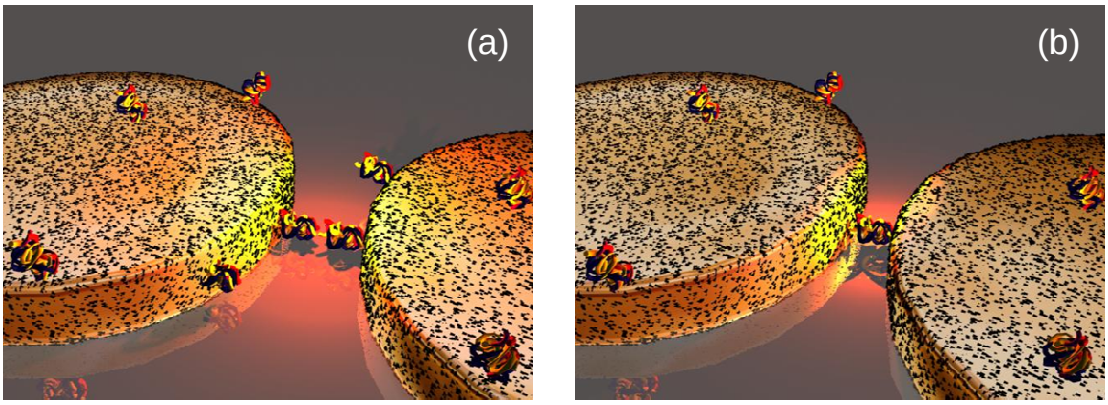

Figure 4.11-Schematic of BSA binding in the gap of a gold nanoparticle dimer. (a) gap facilitates two molecules across the dimer axis (corresponding to the gap of 30 nm) (b) only one molecule can fit across the dimer axis (gap of 16 nm).

inside (gap of ca. 15 nm).

This interpretation may look simplified considering that BSA is not a spherical molecule and its binding orientation inside the gap could vary. However, it is known that binding of BSA to glass substrates at the protein's isoelectric point favors a long axis linking and therefore suggests that BSA will protrude perpendicularly out from the surface [Malmsten, 1995, Fukuzaki et al. 1996]. Although this system is not glass, the protein should behave in an analogous fashion under similar binding conditions and thus on average extend from the surface. The second drop, although less pronounced, occurs at 15±2 nm, corroborating the hypothesis of specific BSA binding orientation. After the second drop, we observed smaller BSA-induced shifts than for the isolated MN case, as a consequence of reduced mode extension away from the gap and the inability of the BSA molecules to penetrate into the sensing area due to size exclusion.

Figure 4.12 displays normalized resonance shift upon BSA adsorption for three different experiments. Reproducibility in abrupt shift changes for the corresponding gaps of 30 nm and 16 nm is demonstrated. Sensitivity enhancement is determined as the ratio of dimer resonance shift magnitude over the quasi-isolated particle case. For the three samples presented here, maximum induced shifts are not the same. In our recent publication, we have correlated corresponding MUA resonant shift to literature values that indicated the insufficient MUA concentration for the surface saturation condition. The measured MUA shifts correspond to 45, 25 and 15% of the maximum that would correspond to a fully formed monolayer. Incomplete MUA formation restricts the number of available binding sites for BSA, thus influencing the overall observed shifts upon the introduction of the standard BSA concentration that was kept the same in all three experiments [Aćimović et al. 2009]. However, there is a weakness in this explanation. We know that BSA shows sufficient affinity for exposed gold, thus presence or absence of activated MUA site might not affect BSA adhesion. Since the activation protocol was not fully optimized for this system [Wang et al. 2005] and keeping in mind that unmodified MUA doesn't possess protein repelling properties, most likely the difference in measured, observed shifts (between experiments in Fig. 4.12) originates partially due to on-going annealing (that lowered measured shifts) or incontrollable nature of in-air measurement strategy. However, the sensing reproducibility was not demonstrated here. As in fact, for the concept proof-of-principle, the overall increased sensitivity with gap decrease is clearly established, with the following discussion about mode-analyte overlap and the assessment of the number of molecules detected.

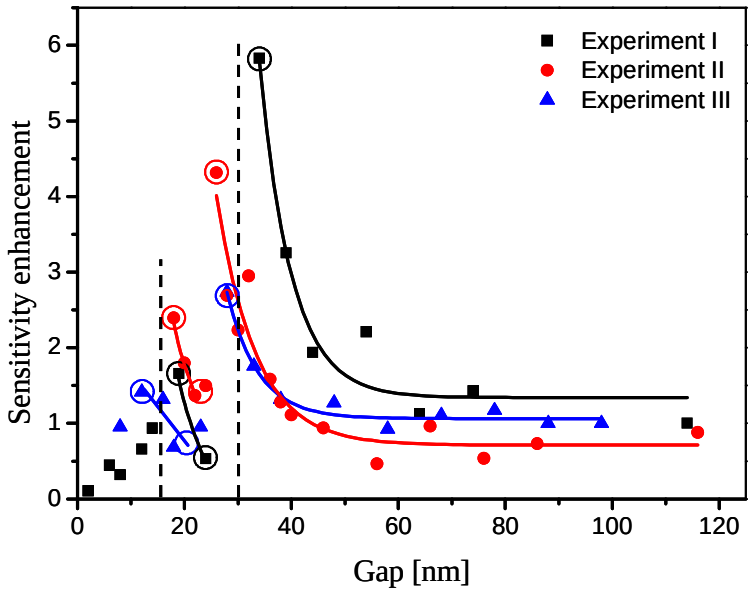

Figure 4.12-Evolution with the gap size of the sensitivity enhancement due to BSA binding: The enhancement is defined as the resonance shift normalized to the shift for isolated particles. Lines are partial exponential fit and used as a guide to the eyes.

4.5.4. FEM model

Under the assumption that BSA concentration in our experiments was sufficient for full coverage of the dimers (protein monolayer or multilayers), the following model can be adopted. Adsorbed proteins can be modeled as a 14 nm thick dielectric layer (n=1.517) around nanoparticle pre-coated with a 1 nm dielectric layer representing MUA (n=1.4863). We can further assume BSA molecules to be rigid rod-like particles that are densely packed into modeled layer. Additionally, the molecule can bind via long axis only (case I) where binding is preferentially accomplished via long-axis but under steric hindrance constraints, the bound molecules can be randomly orientated (case II). These two binding regimes are modeled and sketched in Fig. 4.13.

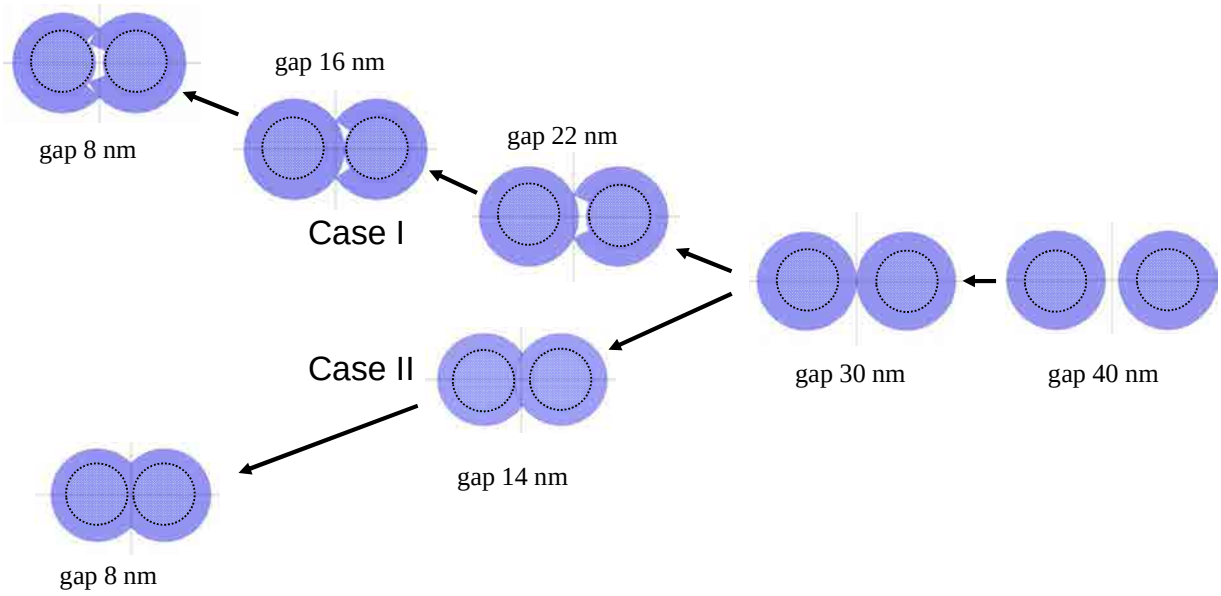

Figure 4.13-Protein (BSA) binding to a dimer. Upper branch (case I): only long axis binding allowed. Lower branch (case II): long axis preferential binding

Inner circles are nanodisk boundaries, while outer region delimit the dielectric protein layer. Because molecules bind to long axis preferentially, both cases are identical for gaps larger than and equal to 30 nm. For gaps smaller than 30 nm, only allowed long axis binding suffers from steric hindrance, leaving some empty space in the gap, where we somehow account for the discreet nature of the molecules (Case I). The lower branch presents the situation where any type of binding orientation is allowed, but still, the long axis binding is preferential when possible (the discreet nature of BSA molecule is disregarded - Case II). If one assesses the number of molecules in the dielectric layer as layer volume divided by individual molecule volume, the total number of adsorbed molecules as function of the gap is expressed in Fig. 4.14.

For Case I, the molecule number slope abruptly changes for the gaps between 30 nm and 16 nm. The 30 nm gap dimers allow a maximum of 906 BSA molecules, while 25 nm gap facilitates 869 molecules. Thus, the difference of 37 BSA molecules is the mass difference that provokes a decrease of around 40 nm

(see Fig. 4.10). Difference of 24 BSA molecules between 16 nm and 14 nm gap induces around 6 nm shift. It is worth nothing that the induced shift difference per molecule is around 1 nm (30 nm gap) and 0.25 nm (6 nm gap), and is within the resolution limit of the typical optical setup.

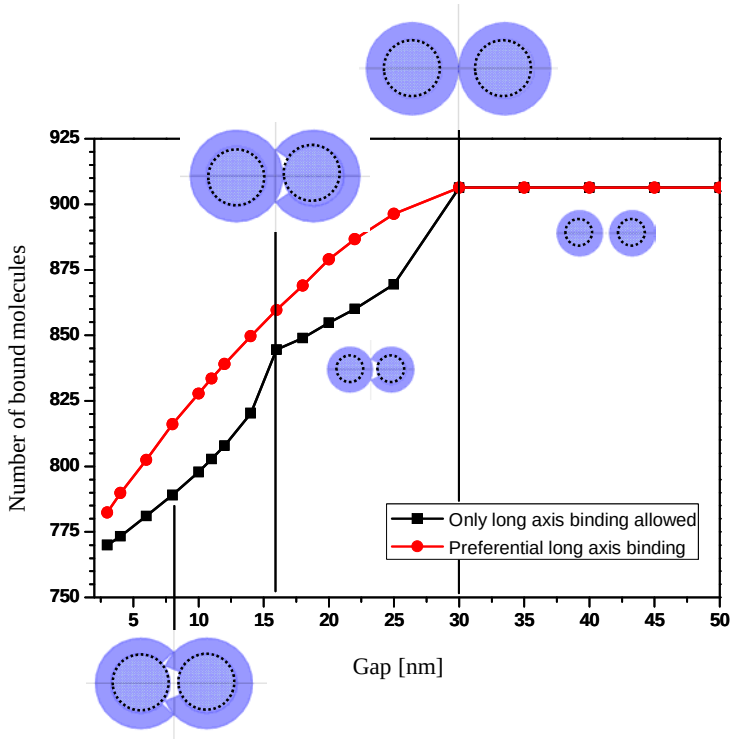

Figure Figure 4.14–Assessing the number of BSA molecules bound to the dimer (100/40 nm) as the function of the gap under the saturation concentration limit and close packing of the proteins.

A set of FEM calculations based on the Case I and Case II models were performed (Fig. 4.13). SCF was employed due to more optimal memory consumption, with iterative solving procedures, as the consequence of relatively large number of meshing elements, that were necessary to represent thin molecular layers and especially small geometry features for the Case I study. The calculation results were obtained after more than 6 months of solving time. The presented result doesn't quantitatively agree with the experiment. The mesh tuning was performed rather intuitively rather than systematically (see Ch.3), while the model parameter tuning (refractive indices, more realistic nanoparticle shapes, etc) would require too much time. The qualitative behavior though partially matches the experiments. The total cross-section extraction in SCF was compared with COMSOL-Green Dyadic Method [Miljković et al. 2012], and the two methods showed a reasonable matching. Still, some general conclusions can be made.

Figure 4.15 shows the calculation results for the 14 nm long protein molecule close-pack binding, applying to both discussed cases. Less interesting case of preferential long axis binding yields monotonically increasing shifts with gap shrinkage, despite the decrease in the adsorbed mass on the sensor. This is expected due to increase in hot-spot's intensity with further mode confinement. When the "only long-axis binding" is accounted for, a discreet change for the characteristic gaps (30 nm and 16 nm) are observed, although the effect is much weaker in comparison to the experiment. The origin of such underestimation is certainly meshing refinement, which was already at the upper limit of our server.

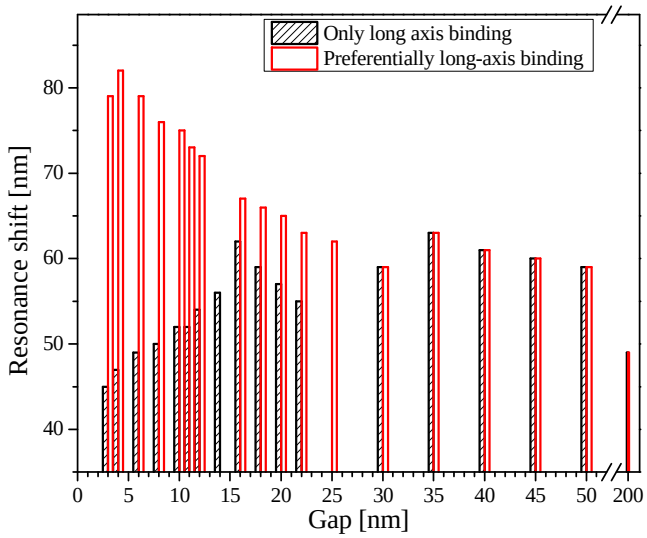

Figure 4.15-FEM calculated resonance shifts upon 14 nm long protein binding for the case of highly orientated binding (only to the protein long axis) and preferentially long-axis binding.

In the case of smaller molecules, for instance 9 nm or 4 nm in length that only binds via the long-axis, a mass change in the successive gaps will be sufficient to produce local maxima. These always occur at gaps equal to molecule length, or twice larger as seen in the Fig. 4.16, as in our experiments. This establishes the idea of "static" plasmon ruler system, which would reveal analyte binding length in addition to its concentration. With further advent of EBL and electron beam sensitive resists, it may be expected that high quality samples will be reality soon, with high reproducibility and homogeneity. However, to resolve the size of different analytes it will require an optimization of the size of the nanoparticles forming the dimers, as expressed by the regular "plasmon-ruler" equation. Even if particular analytes randomly bind, the induced signal would show broader maxima, and still one would be able to resolve averaged size. One important note is related to the size determination from the difference between two local peaks. The resolution clearly depends on the smallest step between the subsequent dimer arrays, while the range of the sensor can be estimated through the standard plasmon ruler equation. This range can be extended by the nanodisk size increase.

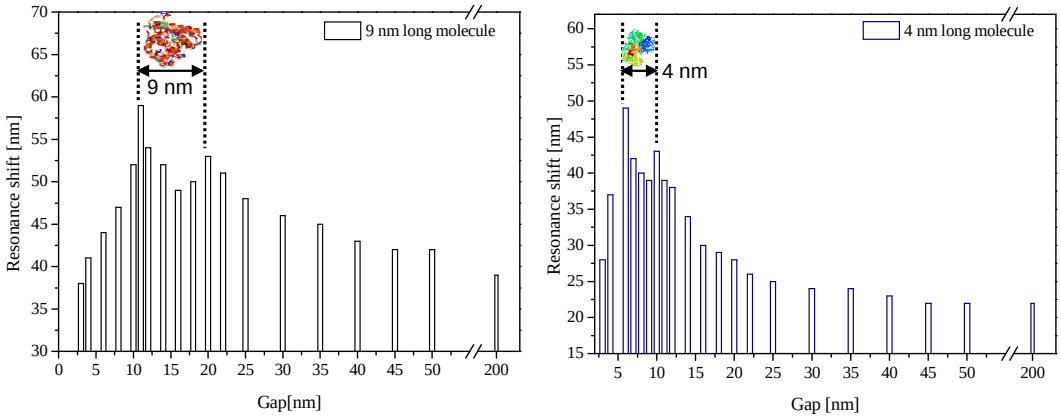

Figure 4.16-Static plasmon ruler concept Left) FEM calculated response induced by a 9 nm longe molecules Right) 4 nm long molecules

As a way to summarize the main results of our BSA "detection" protocol with gold dimers, Fig. 4.17 displays the comparative normalized resonance shift with gap decrease (normalized to resonance shift of quasi-isolated particles) for a number of sensing conditions.

4.6. Concluding remarks

The bulk refractive index sensing characterized by m (see eq. 3.1) is closely related to both the mode distribution and the electromagnetic field enhancement. The near-field coupling in dimers induces a mode redistribution that leads to a hot spot formation within the gap. The electromagnetic enhancement results in the higher m (BRIS), as illustrated by the black curve in Figure 4.17, typically twice as large as compared to isolated particles [Jain and El-Sayed, 2008, 2010]. The bulk refractive index sensing corresponds to the sensing regime with the maximized MAO, i.e. MAO=1 in the eq. 3.1 and eq. 3.3. In the case of very small molecules (characteristic sizes smaller than the minimum attainable gaps), the MAO is clearly gap dependent. With the mode redistribution due to coupling-strength increase (gap shrinkage) the MAO grows. Additionally, such molecules can uniformly bind all over the nanoparticle surfaces and the red data points (in Fig. 4.17) express the normalized resonance shift upon monolayer formation. A maximum increase of 7 is achieved for the smallest gaps of few nm. However, the majority of bio-molecules (proteins, antibodies, DNAs) are considerably bigger, typically 5-15 nm. These sizes of dimer gaps are readily achievable with state-of-the-art lithography processes, and the binding of such molecules cannot be described with eq. 3.1. In particular, as shown in Figure 4.17, steric hindrance and molecular binding orientation influence the magnitude of resonance shift. For sensing protocols in which the total molecular layer thickness (SAM+recognition molecule+target molecule) is smaller than one half of the smallest considered gap, the resonance shift curve exhibits continuous exponential growth with decreasing gaps (blue data). On the other hand, for molecules like BSA, the maximum shift occurs when the overlap is maximized, i.e. when the molecular layer thickness (MUA+BSA molecule) is equal to half of the gap. For smaller gaps, the overlap abruptly falls, and then

reaches local maximum for gap equal to one molecular layer thickness. Further decrease of the gap size increases the mismatch between the hot spot and the protein, inducing very small shifts. MAO is obviously discontinuous as such, and depends on gap and analyte ratio. Recalling the Eq.1, the decay length L_d is dependent on d (adsorbed layer thickness) for the fixed gap.

Figure 4.17 points out parameters that are not crucial for the majority of LSPR schemes based on 'quasi-

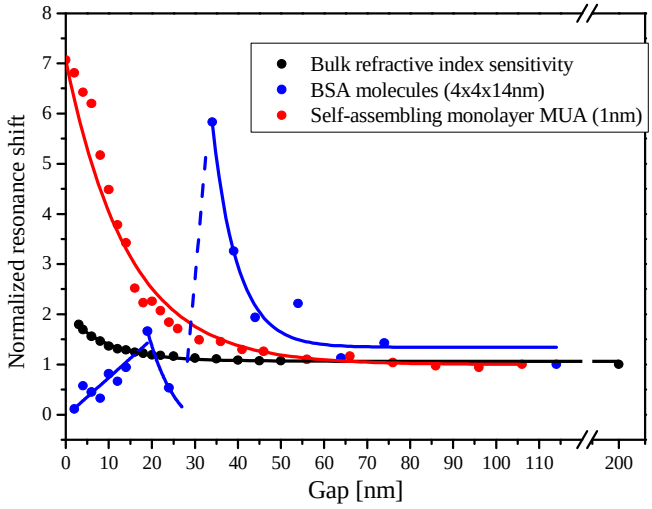

Figure 4.17–Normalized resonance shift as a function of gap size in the case of different MAOs: bulk refractive sensitivity (black), self-assembling monolayer of 1nm thickness (red) and BSA protein (blue) (4x4x14 nm).

isolated' particles [Malinsky et al. 2001, Kreno et al. 2010], but become crucial in the optimization of more sensitive close coupling base LSPR platforms. For every detection protocol involving a particular molecule of interest, it is thus necessary to optimize the distance between particle pairs to obtain the highest sensitivity, as well as the sensing range of dimer building particles. It is shown in the same figure (blue data set) that the shift enhancement can reach 5 for optimized gap. We foresee that other sensor geometries readily enable even higher enhancements (e.g. bow-ties). The benefits of dimer configurations can be exploited in the two directions, where one aims at the already mentioned sensitivity increase upon the homogeneous (non-localized) binding, while the other may be associated with the ultra-sensitive systems for the detection of single molecule. It has been shown indirectly, that induced shift strongly depends on the steric hindrance, i.e. the number of molecules that can approach the hot-spot region. Just recently it has been demonstrated that the thickness of the recognition layer is crucial problem for nanosensors utilizing hot spots. Additionally, the shift per locally bound protein in the selectively functionalized gap region of disk dimer yielded 4x larger shift per bound molecule [Feuz et al. 2012], that goes in line with the results presented here.

Assessing the absolute sensitivity of presented dimer system (in the terms of minimum detectable surface coverage, or in the limit of detection concentration) requires implementing a few additional technical and bio-chemical procedures; one of them being its integration into a microfluidic platform

(chapter 6). The controlled delivery of different samples to the sensing area along with a high-speed and high-resolution read-out should provide more competitive LSP sensing platforms and most likely turn LSPR sensors into an important player on the chemical and biomedical sensor market [Gerion and Day, 2010]. The development of the plasmon-microfluidic LOC prototype is the subject of chapter 6.

Chapter 5

Fano resonances in periodic arrays of metallic nanoparticles for LSPR sensing

While the near-field interaction between two nanoparticles lead to larger sensitivity, nanoparticle dimers exhibit much broader resonances compared to isolated particles. As shown previously, dimers sensitivity strongly depends on MAO, which emphasized the necessity of the coupling strength optimization for the detection of an analyte of interest through the nanoparticle and gap tuning. However, such an optimization applied to relevant biosensing assays represents quite a challenge. Firstly, typical biorecognition layers may result too thick (SAM+antibody), occupying significant portion of sensing volume, as recently shown by Feuz et al. [2012]. Though in chapter 4 it has been demonstrated that 30nm gap still exhibits considerable sensitivity, the considered biorecognition based on antibodies can completely block the gap, leaving no space for analyte recognition. Enlarging further gap imposes according to (Eq. 3.4) use of larger particles and/or other materials (silver or aluminum). However, larger particles suffer stronger damping (radiative and nonradiative) reflected in the near-field enhancement drop and line-shape broadening, with resonances deeper into IR, while other materials are less inert than gold. Additionally, Feuz et al. showed that selective binding in the gap yields indeed bigger shift per bound molecule, but smaller total shift than the homogeneous binding over the isolated nanodisk for the relevant protein concentrations [Feuz et al. 2012]. As consequence, LSPR sensing may benefit field localization, but with whole antibodies as receptors, the degree of localization has to be carefully controlled. Still, the realization of the optimum dimer system for the real assay configurations remains an attractive topic.

Alternatively, far-field coupling between nanoparticles can decrease considerably resonance FWHM in arrays supporting Fano-type resonances. The renewed interest in such narrow resonances initially steamed from the possible applications for biosensing and SERS [Zou and Schatz, 2005, Zou et al. 2004, Offermans et al. 2011]. Sharp peaks can be easily tracked due to higher signal-to-noise ratio (SNR). Additionally, it has been predicted and demonstrated that such resonances are particularly sensitive to the bulk changes expressed in figure-of-merit (FOM) units [Offermans et al. 2011]. However, it is still not clear if these resonances are suitable to biosensing application, especially due to restrictions of homogeneous dielectric which requires the immersion oil as superstrate medium.

Fano-type resonances are result of the interference between broad and narrow resonant modes. For the metallic nanoparticle plasmonics, there have been two distinct strategies for the generation of asymmetric Fano-profiles [Luk'yanchuk et al. 2010]. One is based on cleverly designed oligomeric nanoparticle systems that support broad bright plasmonic modes spectrally overlapping with narrow dark modes (Fano-shells [Hao et al. 2008], dolomite structures [Wu et al. 2012], etc.) The other approach utilizes the periodicity induced LSPR Fano-resonances, sometimes referred as surface lattice

resonances [Zou et al. 2004]. Here we exclusively deal with the later type, since they can be in principle, combined within the dimer nanoparticle arrays [Kravets et al. 2008]. Although the key point is the improvement of the FOM due to resonance narrowing, we are here particularly interested into the nature of such hybridized modes, especially due to indication of their delocalized character that might benefit in the detection with thick biorecognition layers. Here we propose the route to produce ultra-sharp resonant features without embedding nanoparticle array into impractical homogeneous environment of n=1.45-1.52 as generally required [Offermans et al. 2011, Auguié and Barnes, 2008, Felidj et al. 2005] or under oblique incidence [Kravets et al. 2008, 2010]. By using thin slab waveguide as substrate, a suitable spatial and spectral overlap between plasmonic and photonic resonances results in narrow spectral features.

This chapter starts with a short discussion about coupled Lorentz oscillators, and the regimes leading to Fano-type resonances. The extinction spectrum of metallic gratings with sub-micron periodicity is studied in the case of the homogeneous environment, uniform substrate (glass) and wave-guiding substrates. The discussion is expanded to nanoparticle arrays and parameters that govern the resonance shape. The chapter finishes with an example of real-time tracking of sharp resonances upon glucose-water flow cycles. Finally, the combination of Fano resonance with plasmonic dimers is demonstrated.

5.1. Coupling between two identical coupled Lorentz oscillators (mechanical oscillator model)

The dimer response can be described, in first epproximation by a simple model based on coupled Lorentz oscillators [Rechberger et al. 2003]. The schematic representation is displayed in Fig.5.1, where the nanoparticle response to an external electric (EM) field is described by the harmonic oscillator model. The parameters of such resonator (uncoupled nanoparticle) are its resonance frequency ω_0 (related to internal restoring forces between displaced electron cloud and fixed ionic background) and γ that accounts for its homogeneous resonance broadening (FWHM/2). The general equations for two coupled linear oscillators are given as:

$$\frac{d^2 x_{1,2}}{dt^2} + 2\gamma_{1,2}\frac{dx_{1,2}}{dt} + \omega_{01,02}^2 x \mp \omega_c^2 x_{2,1} = \frac{q_{1,2}}{m}E(t) \qquad \text{(Eq. 5.1)}$$

where x_i, ω_c and q_i are the displacements representing localized plasmon oscillations, coupling strength and the strengths of each oscillation (so-called oscillator strength). The total polarization of the system is given as $P = N\sum_i q_i x_j$. The system is solved in the steady-state, excited by a monochromatic excitation $E(t) = E_0 e^{-j\omega t}$. The absorption coefficient is extracted as $\alpha(\omega) = \frac{\omega}{c}\mathrm{Im}(\frac{P(\omega)}{\varepsilon_0 E_0})$ [Klein et al. 2005]. The absorption of an isolated linear oscillator is plotted as blue

curve in the Fig.5.1, with resonance at 620 nm and FWHM of 80 nm. In the case of longitudinal coupling (Fig. 5.1, L-coupled) the opposite charges interact over the gap, lowering the total restoring forces. The term $\omega_{cl}^2 x_j \quad (j \neq i)$ comes with negative sign in the Eq.5.1. The black line corresponds to such a situation ($\hbar\omega_{cl} = 0.9$ eV) and results in red-shifted resonant response. The near-field coupling between dimer constituents as stated earlier depends on the distance due to rapid near-field decay. The transversal excitation increases the total restoring forces, but due to the distance between the interacting charges, the effect is weaker with the center-to-center distance change (see Chapter 4). The coupling term in Eq.5.1 comes here with positive sign, and the system response is represented by the red curve in the Fig.5.1 for $\hbar\omega_{ct} = 0.5$ eV. While the coupled oscillator model gives similar results to chapter 4. (see Fig. 4.1), the coupling strength is empirically introduced into equations. In addition, it also predicts the response in a more general situation of two coupled dissimilar oscillators. A particularly interesting case occurs when the two coupled oscillators have very different damping rates that can result in the asymmetric response of the system, known as Fano resonance.

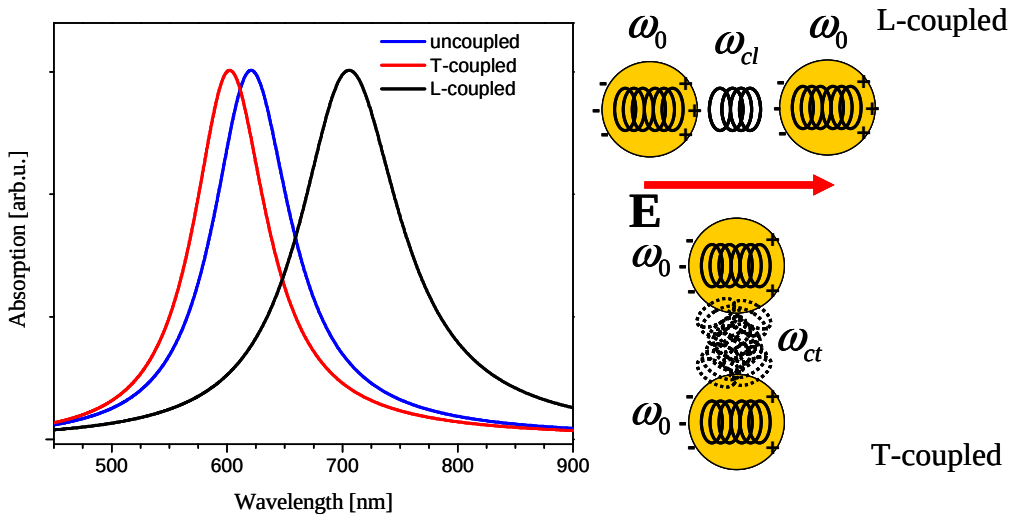

Figure 5.1-Normalized absorption of the homo-dimer system (modeled as coupled mechanical oscillator Eq.5.1.) Blue line represents absorption of a single oscillator. Transversely coupled two identical oscillators (ω_c term comes with + sign) and longitudinally coupled (ω_c term comes with - sign) are shown in red and black, respectively. The similarity with the Fig. 3.2 is accomplished by the proper parameter choice. Right: Simple spring model adopted from [Rechberger et al. 2003] sketches the influence of the excitation polarization and the dimer orientation on the resonance of the system.

5.2. Coupling between sharp and broad resonances (Fano profiles)

Hybridized modes of a coupled plasmonic system feature modified near-field and far-field optical properties. In LSPR sensing, the increased sensitivity of such systems for bio-molecular detection has been demonstrated (Ch. 4). However, as resonances of "quasi-isolated" nanoparticle arrays, dimer arrays suffer even further from relatively large FWHM (60-200 nm). The biosensing would benefit of a LSPR resonance linewidth reduction. Recently, the route to decrease the resonance width (by suppressing the radiative decay) was proposed, that relied on far-field or radiative coupling in periodic nanoparticle arrangements. The spectral properties of these systems can be at the most basic level described by Eq. 5.1 [Klein et al. 2005]. Depending on the oscillators parameters the spectral response can be asymmetric, displaying very sharp features. A particularly sharp peak is exhibited by a system of two coupled oscillators, one with a resonance and the other featuring narrower resonance. For instance, the absorption of system described by Eq.5.1. is shown in Fig.5.2 where the broad resonance oscillator ($\hbar\omega_{01} = 1.997$ eV ($\lambda = 620$ nm)), ($\gamma_1 = 1/(2\tau_1), \tau_1 = 2.5$ fs), interacts with narrow resonance ($\gamma_2 = 1/(2\tau_2), \tau_2 = 100$ fs), with $q_1 / q_2 = 10$, $\hbar\omega_c = 0.5$ eV while ω_{02} is varied. One of the main features of Fano-line shape (which is not a simple superimpose of two Lorentzians) is the suppressed absorption at the frequencies very close to ω_{02} and the anti-crossing behavior. The absorption suppression is attributed to the destructive-interference phenomena as the two oscillations are out of phase. As a consequence, the absorption minimum is located between the two modes (Fig.5.2). When the narrow mode cannot be directly excited by external excitation ($q_2 = 0$) and infinitively narrow ($\gamma_2 \to \infty$), the magnitude of the narrow absorption maxima is constant, independent of the spectral difference between the two interfering resonances [Klein et al. 2005]. However, in more realistic case shown in Fig.5.2 ($q_1 / q_2 = 10$) the sharp peak assigned with the narrow mode is weaker on the high-energy side of the broad resonance.

The previous model is only used to illustrate the response of coupled resonant systems, and is not applied for any quantitative modeling in the following sections. Although, there is an apparent matching between fig. 5.2 and fig. 5.10, the photonic-plasmonic Fano-resonances are treated in different manner. To begin with, the most basic plasmonic systems showing Fano-resonances based on a sub-wavelength gold grating is investigated, where the conclusions are further expanded to more relevant case of nanoparticle array.

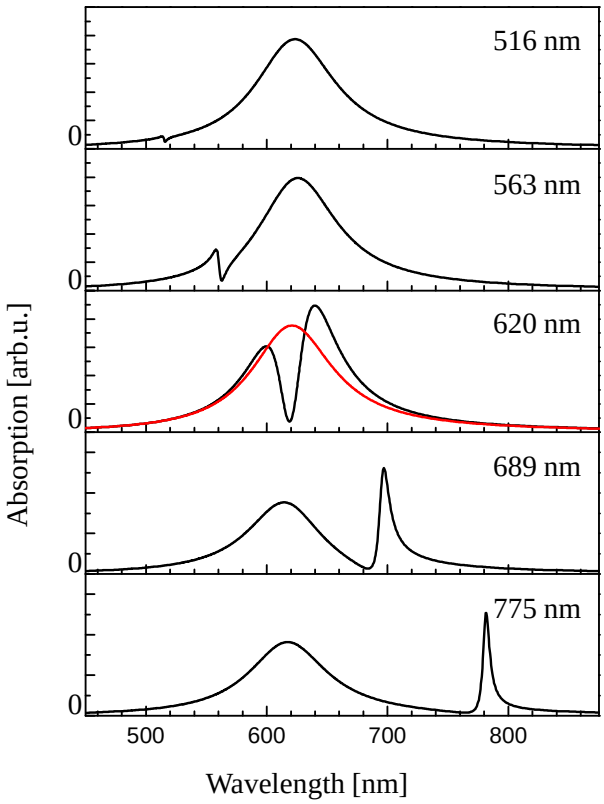

Figure 5.2-Absorption spectra of hetero-dimer system consisting of the two different oscillators (modeled with coupled mechanical oscillator Eq.5.1). The variable parameter is the central resonance wavelength of the narrow resonance (516, 563, 620, 689, 775 nm) that sweeps through the resonance of strongly dampened oscillator (620 nm). Note the asymmetrical absorption profile. Red curve represents the response of isolated broad oscillator.

5.3. Metallic 1D gratings

Metallic gratings are the most convenient configuration for the study of periodicity induced plasmonic Fano-resonances. Their versatility is based on the fact that by changing polarization of the incident light (TM or TE) the Fano response can be switched on and off. Namely, for the TE polarization, the broad plasmonic resonance is not excited leaving only the response that corresponds to narrow surface modes. This allows for the possibility to identified "primitive" oscillations that participate in the Fano-profile, in this case for TE when plasmonic oscillation is absent. The first experimental observation of photonic Fano-profiles is attributed to Wood in 1902, who observed narrow bright and dark bands when investigating metallic (reflection) gratings. Originally known as Wood's anomalies, they were later

classified into two groups, one being Rayleigh's type and other resonant Wood's anomalies [Hessel and Oliner, 1965].

The Rayleigh's type of anomaly is related to the appearance (disappearance) of new diffraction orders that suddenly modifies the spectral response. If we consider normal incidence white-light illumination, periodic arrangements diffracts the light into 0^{th} , $\pm1^{st}$, $\pm2^{nd}$ and so on, diffraction orders. In the typical optical configuration (see Fig. 4.5), the non-diffracted (0^{th}) order is collected and passed to the spectrometer. The diffracted rays of m^{th} orders emerge at angles given by:

$$\theta_m = \tan^{-1}\left(\frac{m\frac{2\pi}{a}}{\sqrt{(n\frac{2\pi}{\lambda_0})^2 - (m\frac{2\pi}{a})^2}}\right) \qquad \text{(Eq. 5.2)},$$

where n, λ_0 and a are the refractive index of the medium, the vacuum wavelength of light and the grating period respectively. However, for the wavelengths that satisfy $\lambda_0 > \frac{na}{m}$, diffraction orders are not propagating but evanescent (inhomogeneous), thus the energy redistributes back into existing orders, resulting in the sudden variations in the optical properties (for instance, the extinction drop for TE in Fig. 5.4, since the system is transmission grating). Particular diffraction orders that propagate at the grazing angle for $\lambda_0 = \frac{na}{m}$ are able to interact with the grating and/or other surface modes.

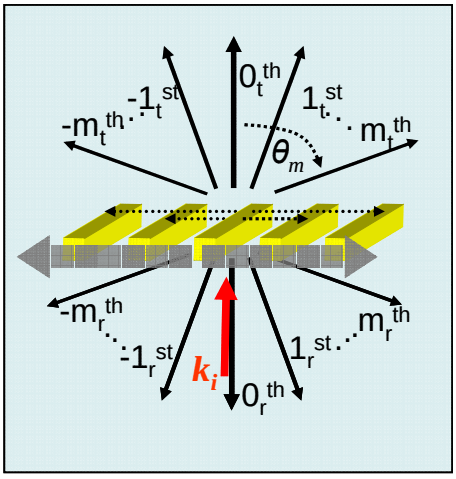

Figure 5.3-Sketch of a metallic 1D grating showing incident light wave vector k_i (red) at normal incidence, transmitted and reflected diffracted orders (solid black), grating reciprocal vectors (dashed), and surface modes (gray).

5.3.1. Homogeneous environment

The extinction of gold grating embedded into homogeneous environment (n=1.52) as function of the grating period for the two polarizations (TE and TM) is plotted in Fig. 5.4. For TE polarization, localized plasmons are not excited, and the response clearly shows the typical gold response, which changes once the Rayleigh's cut-off condition is fulfilled for the particular wavelength. This results in the abrupt extinction decrease as explained above for the $\pm 1^{st}$ and $\pm 2^{nd}$ order Wood's anomaly of Rayleigh's type. Note that the spectra are not normalized to the gold filling factor, thus the extinction decreases with the increase of grating period. TM polarized light excites transversal LSPR mode of the infinite long bars (width 100 nm, height 40 nm) at 590 nm. With the decreasing periodicity, $\pm 1^{st}$ order Rayleigh's anomaly enters at the high energy side, and induces Fano-response while it sweeps through the plasmon resonance. However, the resulting Fano-profile is a weakly modified Lorentzian line shape, and the extinction suppression is not observed, most likely due to insufficiently strong coupling. The asymmetry of the resonance profile is more pronounced for the higher refractive index embedding media (data not shown) with the Rayleigh's cut-offs shifted to the longer wavelengths for the fixed grating period.

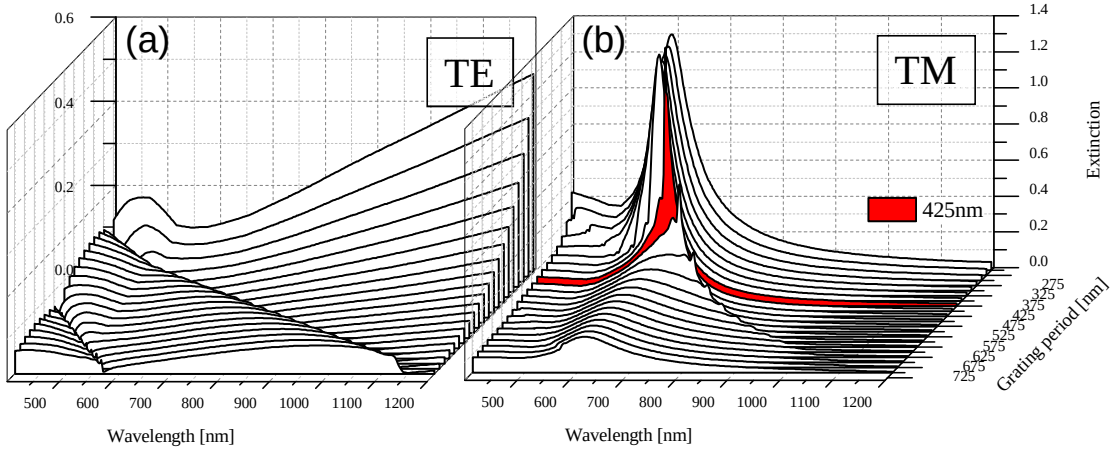

Figure 5.4-FEM calculations of extinction spectra for transmission gold 1D grating embedded into homogeneous environment of n=1.52. Gold bar's cross-section is 100x40 nm. Extinction spectra are shown for the two polarizations: (a) TE (E-field along the bar) and (b) TM (H-field along the bar). TE case reveals the presence and spectral position of Wood's anomalies. TM case of a=425 nm is highlighted as guide for the eyes.

5.3.2. Inhomogeneous environment

When the gold grating is experiencing inhomogeneous environment the response is more complicated. In the most simple inhomogeneous situation, i.e. grating on the substrate, there are two Rayleigh's cut-offs, one for the substrate (reflected) and other for superstrate (transmitted orders) [Steele et al. 2003]. The spectral distance for the same order anomalies depends on the refractive index contrast between substrate (glass) and superstrate (water, in my case). TE extinction reveals the presence of both

anomalies (1st and 2nd orders), where the glass anomaly is advancing one, on the red side of the spectra with the larger grating constants (Fig. 5.5).

The excitation of the localized plasmon for the TM illumination results in a stronger Fano-profile in comparison to the homogeneous glass case. One can clearly observe the interaction of LSPR with both anomalies for a=400 till a=550 nm; the interaction with the glass one being more pronounced. This originates from the higher spatial overlap between the grazing diffraction orders on the glass side with the LSPR compared with the one in the superstrate, regardless the fact that the larger portion of nanoparticle's surface is in contact with superstrate medium.

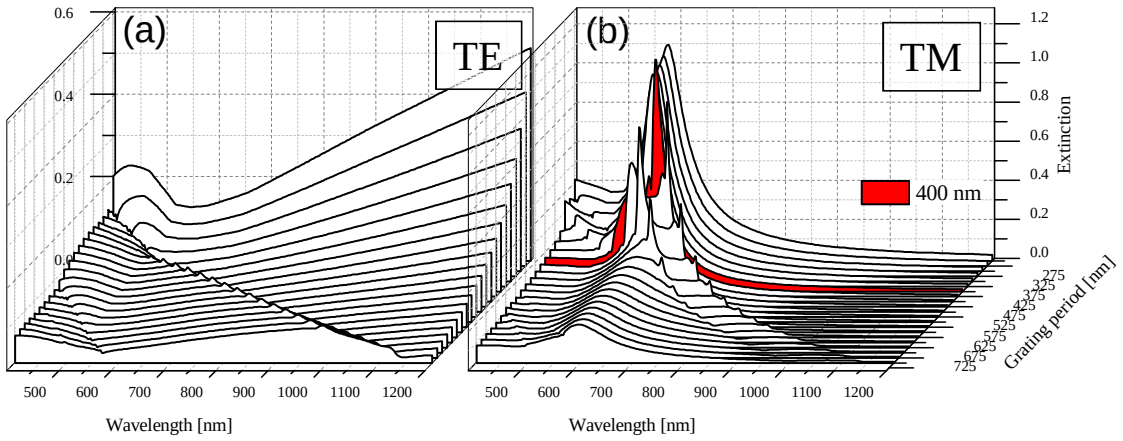

Figure 5.5-FEM calculations of extinction spectra for transmission gold 1D grating on the glass substrate (n=1.52) with water (n=1.33) as superstrate. Gold bar's cross-section is 100x40 nm. Extinction spectra are shown for the two polarizations: (a) TE (E-field along the bar) and (b) TM (H-field along the bar). TM case for a=400 nm is highlighted as guide for an eye.

Fano-profiles of periodic metallic nano-objects can be further tailored through the coupling of resonant diffraction orders (resonant Wood's anomalies) [Sarrazin et al. 2003] with broader LSPR. Such resonant orders (of inhomogeneous type – above Rayleigh's wavelength) may correspond to SPPs or wave-guided modes, depending on the substrate properties. These modes interact stronger with the broad LSPR, yielding stronger asymmetry, and the extent of coupling can be controlled through the parameters of the supporting substrate, for instance thickness, and materials of dielectric waveguide. Typically, conductive ITO films are used as core medium [Christ et al. 2003, 2004] for such waveguides, but due to its intrinsic losses sputtered TiO_2 has been employed instead, which confines modes stronger due to its high refractive index (n≈2.5). The extinction spectra of a gold grating residing on 40 nm thick TiO_2 layer, where the asymmetric slab waveguide is comprised of TiO_2 as core (n=2.5), glass (n=1.52) and water (n=1.33) as cladding layers, are shown in the Fig. 5.6.

Both polarizations display sharp peaks, though TE peaks are much weaker, due to absence of transversal resonance (LSPR) [Hessel and Oliner, 1965]. In the TE case alone, resonant Wood's anomaly (excitation of guided TE_0 modes) interferes with transmission 0th order, inducing asymmetric Fano-profile (Fig. 5.6.

TE), especially for the thicker core layer case (Fig. 5.7). More details can be found in the work of Sarrazin et al. [Sarrazin et al. 2003]. The lower graphs within Fig. 5.6-7 plot the dispersion-like curves for uncoupled resonances (wave-guided modes, Wood's anomalies of Rayleigh's type and localized plasmons). The calculated EM fields profiles (data not shown) indicate that Rayleigh's cut-offs are manifested only in the cladding layers, because the guiding layer is too thin. For the chosen waveguide parameters, TM mode has cut-off at 500 nm, while TE_0 propagation is not forbidden in the spectral range of interest. For the TE illumination, the spectral anisotropy due to the interaction between quasi-guided TE_0 (black) and homogeneous diffraction orders is stronger for grating period between 300 nm and 425 nm, while for larger periods the spectral proximity of Rayleigh's wavelength cut-offs the resonant profile (The mode cannot be excited with radiative (homogenous) diffraction order) [Sarrazin et al. 2003]. While the quasi-guided modes (TM_0) cannot be excited in TM case due to its cut-off (Fig.5.6), the interaction between Wood's nonresonant anomalies and LSPR is much stronger (Fig. 5.6) than in the absence of TiO_2 film (Fig. 5.5).

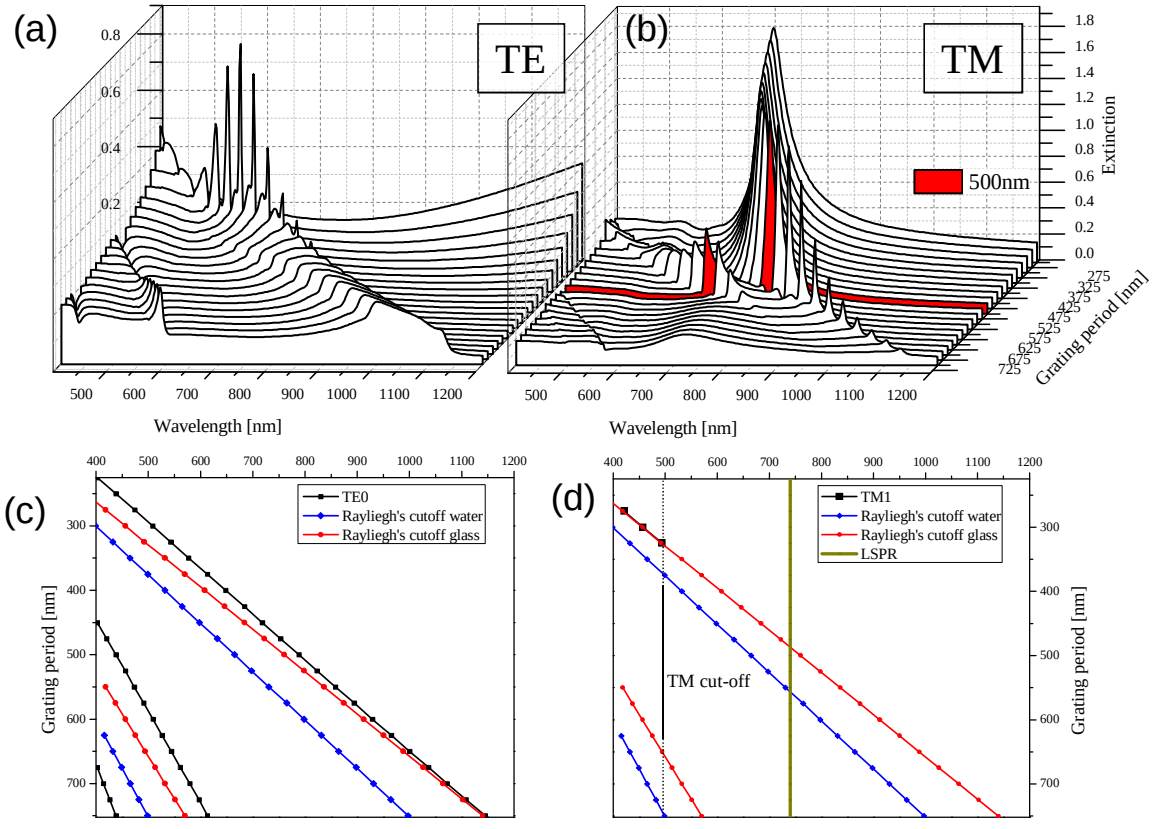

Figure 5.6-FEM calculations of extinction spectra for transmission gold 1D grating on the multilayered substrate (40 nm of TiO_2 (n=2.5) on semi-infinite glass (n=1.52)) with water (n=1.33) as superstrate. Individual gold bar's cross-section is 100x40 nm. Extinction spectra are shown for the two polarizations: (a) TE (E-field along the bar) and (b) TM (H-field along the bar). TE shows interaction of TE_0 mode with Wood's anomalies. TM case of a=500 nm is highlighted as guide for an eye. (c,d) Dispersion-like curves showing characteristic features: bound modes of slab-waveguide (black), glass and water light lines (red and blue), and the dispersion of single gold bar. Cut-off for TM_0 mode is also indicated in (d).

In order to allow the case of the interaction between LSPR and supported TM modes, a thicker core layer (100 nm) that supports TM_0 modes in the VIS/near-IR is employed. There, one can expect strong coherent interaction between photonic (quasi-guided) mode and LSPR of metallic grating [Christ et al. 2003]. For TE illumination, the supported TE modes strongly interact with the diffraction orders due to separation between Rayleigh's cut-off in glass and TE_0 dispersion (see Fig. 5.7 lower). TM modes interact with LSPR near the crossing points of their dispersion lines (Fig.5.7), while the proximity of glass anomaly cuts the lower wavelength side of Fano profile of the TM0 and LSPR interaction.

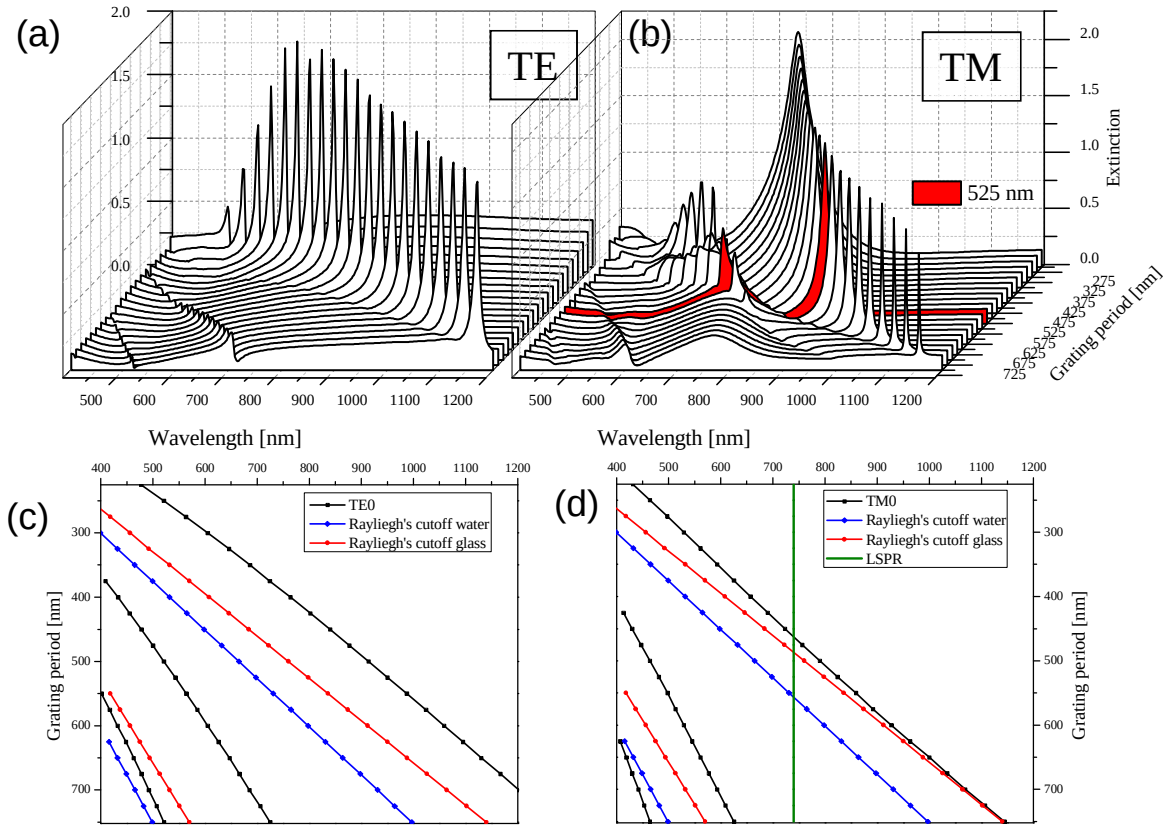

Figure 5.7-FEM calculations of extinction spectra for transmission gold 1D grating on the multilayered substrate (100 nm of TiO_2 (n=2.5) on semi-infinite glass (n=1.52)) with water (n=1.33) as superstrate. Individual gold bar's cross-section is 100x40 nm. Extinction spectra are shown for the two polarizations: (a) TE (E-field along the bar) and (b) TM (H-field along the bar). TE shows interaction of TE0 modes with Wood's anomalies. TM case of a=525 nm is highlighted as guide for an eye. (c,d) Dispersion-like curves showing characteristic features: bound modes of slab-waveguide (black), glass and water light lines (red and blue), and the dispersion of single gold bar.

In practice, the complexity of the spectra of such coupled systems can be even higher due to unavoidable deviations from ideal normal incidence. It has been reported, that beam divergence smaller than 0.02 degrees allows for the good agreement between calculations (normal incidence) and the experiment [Christ et al 2003, 2004]. The optical setup use a bright field condenser of NA=0.1 that illuminates with light having non-zero parallel k-vector components, that after grating effect result in a spreading of diffraction orders ($\left|k_p - m\frac{2\pi}{a}\right| \neq \left|k_p + m\frac{2\pi}{a}\right|$, for $k_p \neq 0$, where k_p is wave vector component parallel to the grating plane). This results in the excitation of two broad guided modes, or fulfilling of the Rayleigh's cutoff for a larger spectral range.

When comparing the experiment with the calculations (Fig. 5.8 (a)), a good agreement is found with the calculated averaged response of the incident angles between 0^o and 6^o (NA=0.1), as well as for the angle of incidence in the middle of the range (2^o or 3^o). The optimum incident angle is derived by comparing the distance between two minima in the extinction spectra, as shown by two vertical dashed lines. This will be used for the FEM calculations of nanoparticle arrays, since the averaging of the response is not time effective in case of full 3D calculations.

In conclusion, 1D metallic gratings embedded into homogeneous medium interfere only slightly with diffraction orders responsible for Wood's anomalies. The main reason for such weak interaction is the delocalized nature of the excited transversal LSPR of infinitely long nanowires building the grating, i.e. far-field radiation pattern of such system doesn't favor the long-range interaction between adjacent bars. Situation is fairly different for nanoparticle gratings, as suggested in [Auguié, 2009], due to localized nature of the modes supported by sub-wavelength nanoparticles and point-dipole like emission pattern of nanoparticles. The asymmetric case of semi-infinite substrate further modifies the optical properties of the system, due to the two different lattice modes assigned to superstrate and substrate, respectively. The decrease of the refractive index contrast between superstrate and substrate can additionally increase the extinction suppression as demonstrated in Fig. 5.8 (b). The presence of a thin, optically dense dielectric material furthermore contributes to the asymmetry of the line shape, regardless the fact that it does not support Rayleigh's anomalies or guided modes. It redistributes spectrally and spatially the LSPR mode in a way to increase spatial overlap between localized plasmon and lattice surface modes. However, in the case of waveguiding modes propagating near the interface, the Fano-coupling of LSPR with quasi-guided modes is the dominant process that governs the optical response of the system. This type of interactions is known as resonant Wood's anomaly interaction with broad LSPR [Klein et al. 2005, Sarrazin et al. 2003, Christ et al. 2004].

Our experiments reproduce well the simulations although spectral features are broadened due to illumination and collection conditions. It is interesting to note that lower graph in Fig. 5.8 (b) displays the transition from the spectra with two extinction dips into spectral featured with one broad dip with the primitive vector increase (525 nm and 550 nm), when the superstrate is air. The reason for the shape transformation is due to cut-off TE_0 condition for glass-40 nm TiO_2-air slab waveguide around λ=850 nm in the experiment. The calculated cut-off value is around λ=900 nm, but the discrepancies originate from the refractive index of TiO2, which is taken to be 2.5 in all calculation, while the elipsometry

characterization yielded considerably more complicated dependence. Additionally, the inaccurate thickness of the sputtered material as well as optical constants of other materials involved are sources of deviations.

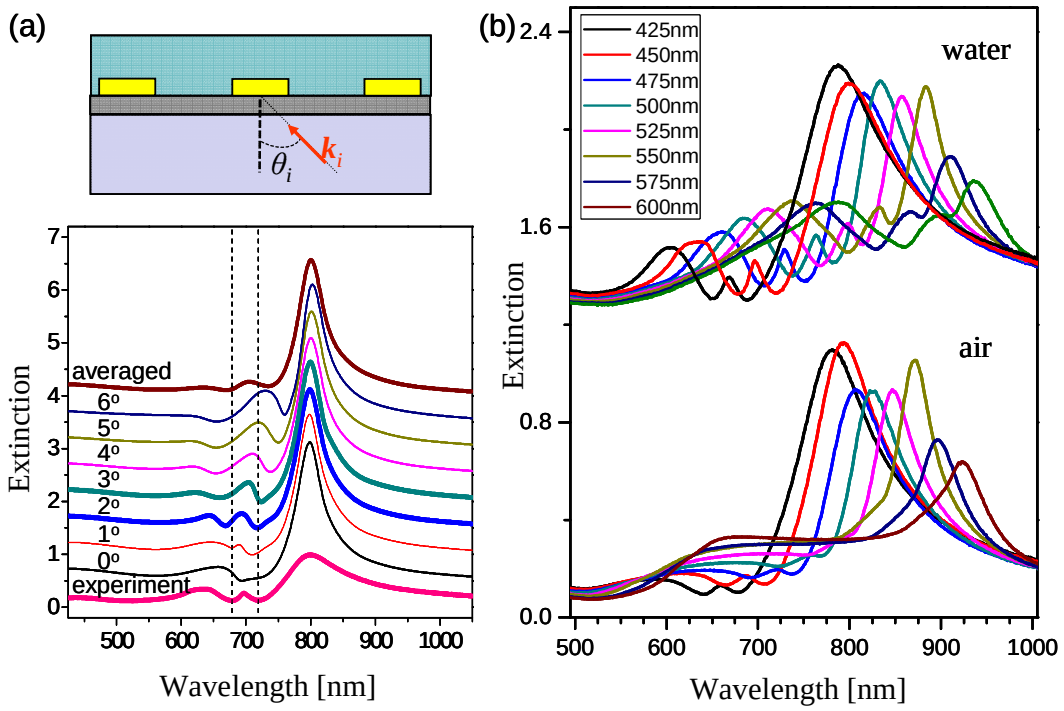

Figure 5.8-(a) Influence of the incidence angle on the extinction spectrum of 1D gold sub-wavelength gratings. Sketch of the optical configuration and the extinction spectra (500 nm grating period) deposited on TiO_2 (40 nm)-glass substrate with water as superstrate. The incident angle θ_i is varied from 0 till 6 degrees, in order to mimic angular spread of the illumination optics. The calculated extinction spectra were compared with the experiment measurement. The best correspondence is obtained for the angle in the middle of the range (3°), while the averaged response is also reasonably good. The best match condition is the equal distance between two extinction dips for the experiment and the calculation. (b) The extinction of the same system as (a) as function of grating periodicity as measured for the two superstrate media (water and air).

5.4. Radiative coupling in nanoparticle arrays (2D gratings)

Metallic gratings are versatile in the sense of facile switching between on and off states of LSPR excitation by simple polarization rotation from TE (off) to TM (on). The LSPR of typical sub-wavelength sized nanoparticles is always excited, regardless of the light polarization. However, as being 2D gratings, by simple tuning the periodicity in x- and y- direction, various surface modes can be selectively excited or suppressed within the spectral range of interest [Linden et al. 2001]. The interaction of localized plasmons with grazing diffraction orders has been so far mostly studied using a dipolar model [Auguié and Barnes, 2008, Augié et al. 2010, Mousavi et al. 2011]. Intuitively, radiation pattern of an electric dipole excited by linearly polarized electric field is spatially inhomogeneous, i.e. the far-field radiation lobes are directed perpendicularly to the electric field direction. As such, the radiation coupling (far-

field or long-range interaction) between nanoparticles within an array, are more pronounced in the direction of radiation lobes. (the near-field interaction is mainly governed through the x-direction coupling due to near-field "lobes" that are parallel to the excitation electric field.) The long-range interaction is schematically represented in the Fig.5.9 (a) where locally excited nanoparticle at the center excites predominantly the nearest-neighbors in the y-direction. To suppress one set of grating-vectors (x-axis), the condition $p_y << n_{sub}\lambda_{LSPR}$ is satisfied in all of geometries considered, that additionally leads to denser nanoparticle packing. Periodicity in x-direction is varied, allowing the coupling process via momentum exchange of incident light with reciprocal grating vectors $\pm m2\pi / p_x$, where m being integer. Two different configurations will be considered: the simplest case of nanoparticle array deposited on glass substrate will be analyzed first. Then, the more complex case of a dielectric waveguiding substrate supporting nanoparticle array is subsequently analyzed.

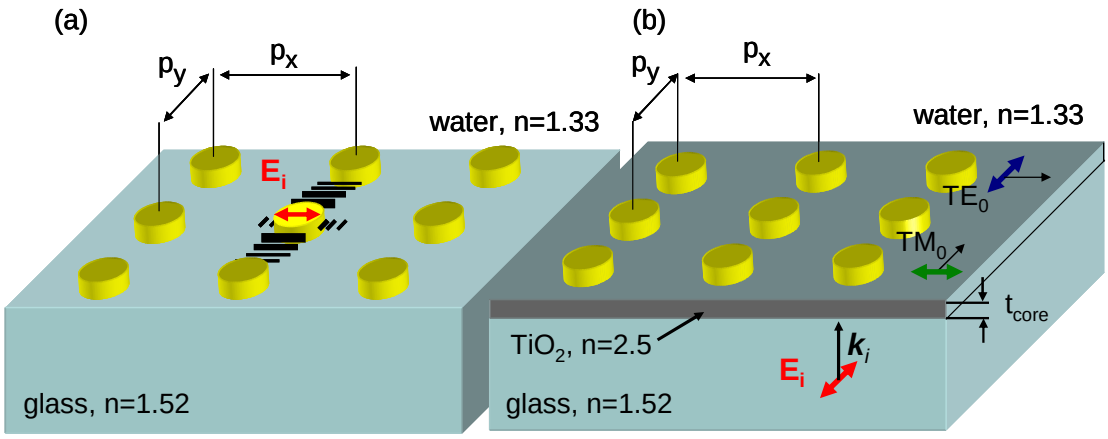

Figure 5.9-Geometry of typical nanoparticle systems investigated in the frame of Fano-resonant coupling (a) Regular rectangular 2D nanoparticle array deposited on the glass substrate with water as superstrate. The far-field interaction is sketched for the excitation of the central particle with the E-field polarized as red double-arrow. (b) Thin optically dense dielectric (TiO_2) is deposited below the nanoparticle array and glass, making slab-waveguide with glass and water as cladding regions. The supported modes are sketched (TE_0 and TM_0)

The optical properties of nanoparticles arranged into periodical arrays embedded into homogeneous medium are typically analyzed through the dipole model. In the frame of dipole model, the dipole moment $\mathbf{p}_i$ of i-th particle in the array is expressed as $\mathbf{p}_i = \boldsymbol{\alpha}_s(\omega)\mathbf{E}_{i,local}$, where $\boldsymbol{\alpha}_s(\omega)$ is the polarizability of single particle. The local excitation field sensed by the i-th particle is $\mathbf{E}_{i,local} = \mathbf{E}_{incident} + \sum_{j\neq i}\mathbf{E}_{dipole,j}$. In the limit of infinite arrays, the local field at each particle is same for every particle, thus $\mathbf{E}_{loc} = \mathbf{E}_{incident} + S(\mathbf{r},\mathbf{k})\boldsymbol{\alpha}_s(\omega)\mathbf{E}_{loc}$, where $S(\mathbf{r},\mathbf{k})$ is called the retarded dipole sum and the analytical expression can be found elsewhere [Auguié and Barnes, 2008, Augié et al. 2010, Mousavi et al. 2011]. The effective polarizability of an array is given as:

$$\boldsymbol{\alpha}_{\mathbf{eff}} = \frac{\boldsymbol{\alpha}_{\mathbf{s}}(\omega)}{1 - S(\mathbf{r},\mathbf{k})\boldsymbol{\alpha}_{\mathbf{s}}(\omega)} \qquad \text{(Eq. 5.3)}$$

Eq. 5.3 demonstrates that even though the dispersion relation of isolated nanoparticle is considered as "flat", in the case of nanoparticle arrays that may not hold anymore. Recently it has been predicted (from the Eq. 5.3) that it is possible to reduce radiative damping (to achieve narrow resonances) by proper tailoring of such interparticle interaction [Zou et al. 2004]. The properly arranged metallic nanoparticles, can participate in the coherent multiple scattering processes, than can lead to stronger interaction with the incident light. These multiple scattering processes can result in increased interaction with nanoparticles through the grazing diffraction orders, or other surface resonances. As shown for 1D metallic gratings, these interactions can induce modification in the spectral properties of the system as whole, such as resonance narrowing and extinction suppressions in particular spectral bands. The observed extremely narrow resonances may contribute to plasmonic sensing, which are characterized by larger FOM than in ordinary (random) nanoparticle arrays [Offermans et al. 2011]. Regarding sensing applications, the observed asymmetry is stronger when water is applied as superstrate instead of air, as observed with metallic gratings. Fig. 5.10 compares resonances (x-polarizations) for the different gratings without any waveguiding layer. The negligible modification is observed for nanodisk (125x50 nm) arrays at the air/glass interface, while increasing the individual particle diameter (polarizability) to 150 and 175 nm increases the inter-particle far-field coupling. The decrease in ref.index contrast between substrate and superstrate favors the coupling, while in combination with larger nanoparticle diameter extinction displays well defined and narrow resonant features. Note that extinction spectra are not normalized to nanoparticle density. The maximum narrowing is obtained for spectral overlap for $\lambda_{res} \approx \lambda_{Rg}$ (see Fig. 5.10, (c)), where λ_{res} is dominant resonance and λ_{Rg} is Wood's anomaly in the glass. Indeed, Auguié et al. predicted that larger particles (larger polarizability) are more robust to refractive index contrast between substrate and superstrate, i.e. the sharp features can be obtained at higher contrasts than in the case of smaller particles [Auguié et al. 2010]. Thus, the spectral overlap between grazing-diffraction order (λ_{Rg}) and nanoparticles is not the only condition for sharp spectral features, but the polarizability of the individual particles and refractive index contrast at the interface. In other words, LPSR lobes direction strongly depends on the substrate-superstrate interface contrast as mentioned earlier, thus the optimum spatial overlap with grazing diffraction beams is in the case of homogeneous environment.

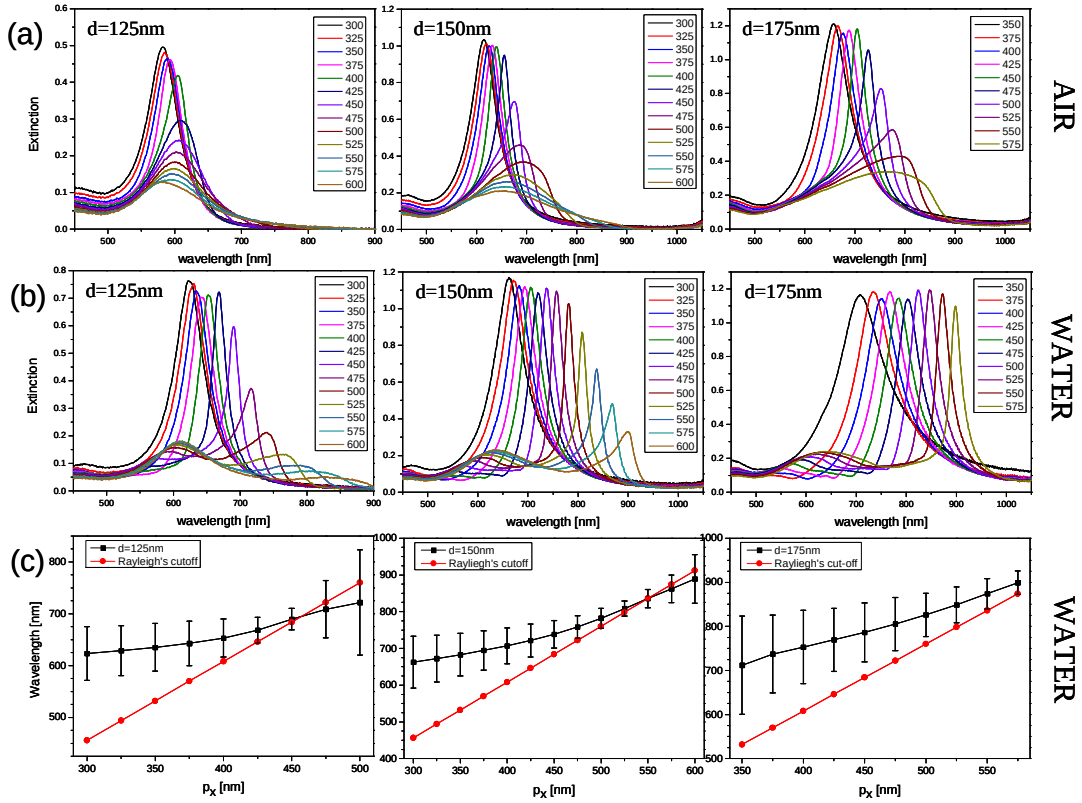

Figure 5.10-Experimental extinction spectra of nanodisk arrays deposited on glass substrate as function of the periodicity for two superstrate media and three disk sizes: air (a) and water (b), diameters 125 nm (left), 150 nm (middle) and 175 nm (right). Periodicity in x-direction is varied (see Fig. 5.9 (a)), while in y-direction is kept fixed at 300 nm. (c) Plot of dominant extinction peaks with corresponding FWHMs. Note that peak narrowing continues with spectral proximity increase between LSPR and Rayleigh's cut-off in glass λ_{Rg}. Once $\lambda_{res} > \lambda_{Rg}$ the effect is diminished.

In analogy with 1D gratings, the presence of dielectric waveguiding layer changes the dominant interaction type from Rayleigh's anomaly to quasi-guided mode interacting with LSPR. Although one cannot suppress LSPR response, still by changing the polarization direction we can switch on-off the TE_0-LSPR interactions (for $p_y << n_{sub}\lambda_{LSPR}$ TM_0 cannot be excited with x-polarized light). The influence of the core thickness on the extinction profile is investigated for two cases. Nanodisk arrays are deposited either on the 44 nm or 88 nm thick TiO_2 layer, sputtered on the glass substrates. The array primitive vector p_x is varied, while the p_y is kept fixed to 300 nm in order to increase gold filling factor (see Fig. 5.9 (b)). The presence of optically thick dielectric layer (n≈2.5) shifts the resonance to longer wavelengths due to the nanoparticle bulk sensing effect by an amount dependent on layer's thickness. The TiO_2 layer shifts the resonances of 120-130 nm disks (50 nm height) from 700-750 nm deeper into IR (ca. 900-950 nm), which is already at the limit of our spectrometers range. In order to be able to observe Fano effects, initially 130 nm large disks (50 nm high) are thermally annealed at 140°C for 10 min to blue-shift resonance, before assembling them within the microfluidic device where they were additionally annealed during the chip preparation (see Ch. 6). The annealed arrays are resonant at 750-800 nm (in

water). The observed blue shift typically originate from the nanoparticle surface roughness smoothing with slight increase in out-of-plane height. The spectra of various nanodisk arrays inside microfluidic channels filled with water for 44 nm thick TiO_2 are presented in Fig. 5.11.

Since x-polarized light cannot couple to TM_0 mode via interaction with $\pm 2\pi / p_x$ reciprocal vectors, the interaction is mediated through the Wood's anomalies exclusively; anyway, the spectral dependence on the p_x is rather weak, due to the reasons explained in the Fig. 5.9 (a). For y-polarized illumination (TE case), the TE_0 mode is excited, and interacts strongly with the LSPR. This interaction is qualitatively similar to the non-waveguide case (especially to the case of homogeneous environment [Auguié and Barnes, 2008], due to very similar field patterns. Namely, in the spectral range of interest, TE_0 dispersion relation lies very close to the light line in the glass (Rayleigh's cutoff, Fig. 5.6 lower, left), thus the mode preferentially leaks into the glass, being spatially very similar to the grazing diffraction order in the glass. (When these spectrally coincide, the cut-off condition is reached.) Furthermore, the low thickness of the guiding layer only slightly affects the LSPR-TE_0 spatial overlap as such. Sharp-peaks are mainly produced on the lower-energy side of the plasmonic resonance, as expected from the coupled oscillator model and other models [Auguié and Barnes, 2008].

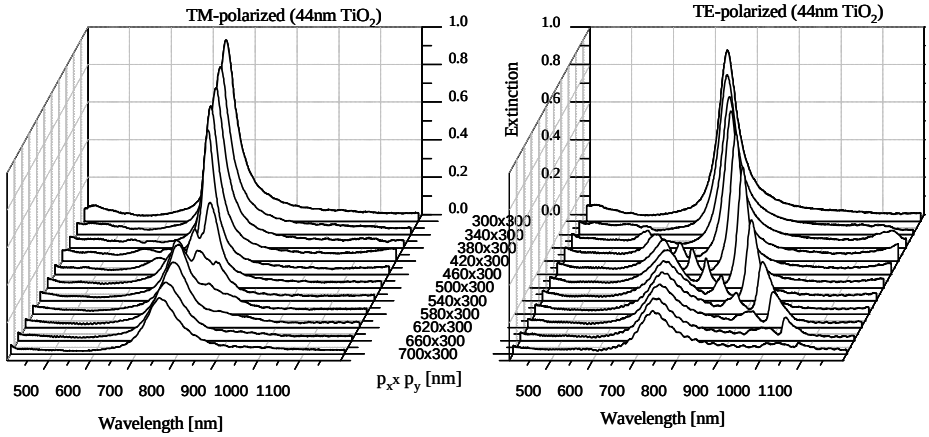

Figure 5.11-Experimental extinction spectra of the system sketched in Fig. 5.9 (b). The TiO_2 thickness is 44 nm. p_y is varying from 300 to 700 nm, while p_x is fixed to 300 nm. The spectra were taken for the system assembled in the active microfluidic device, and with flowing water as superstrate medium. The observed ripples in the extinction line profile are typical for the systems with a slowly drifting stage due to Fabry-Perot effect. Note that TM_0 mode cannot be excited due to cut-off condition and small p_y.

The guided-light is more confined for the slab-waveguide consisting of glass-88 nm TiO_2-water compared to twice thinner core layer, and it supports both TM_0 and TE_0 modes; however TM_0 mode cannot be efficiently excited, as evidenced from the identical spectra for TM of Fig. 5.11 and Fig. 5.12. Under normal incidence, E_x polarized light cannot couple to the TM_0 mode through x-reciprocal lattice vectors. As consequence, the response is almost identical to the TM case of Fig.5.11. Furthermore, the efficient coherent interaction between nanoparticles alone is prevented due to fast field decay in the direction of the variable periodicity producing only the weak modification.

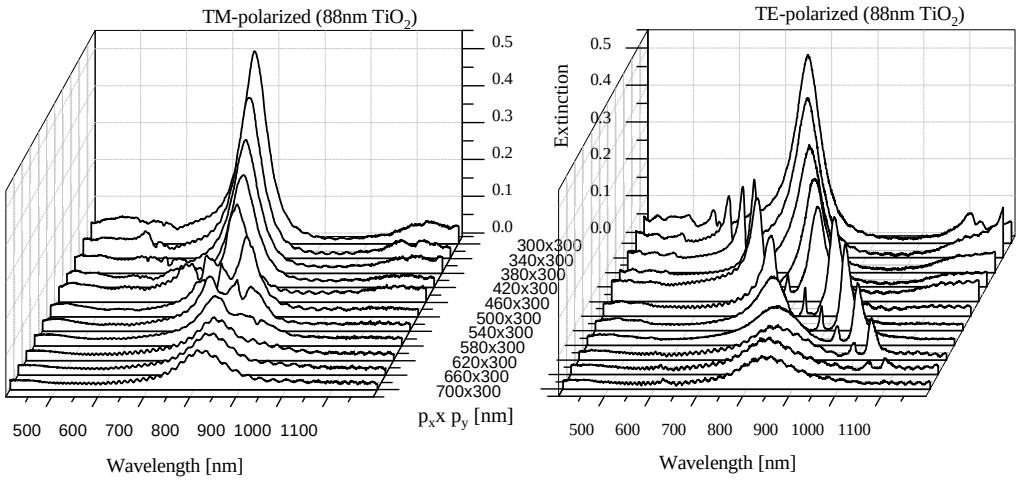

Figure 5.12-Experimental extinction spectra of the system sketched in Fig. 5.9 (b). The TiO_2 thickness is 88 nm. The spectra were taken for the system assembled in the active microfluidic device, and with flowing water as superstrate medium. The observed ripples in the extinction line profile are typical for the systems with a slowly drifting stage due to Fabry-Perot effect. Note that TM_0 mode cannot be excited due to small p_y.

The extinction levels are additionally reduced (in comparison to 44nm TiO_2), since the nanodisks are intentionally made smaller than in the previous case, due to larger bulk refractive index sensing effect from the thicker guiding layer. As the TE_0 mode spectrally overlaps with plasmonic resonance, the produced Fano-profile exhibits two absolute extinction minima, where the extinction is fully suppressed. Moreover, the spectral profile is more symmetrical (the peak close to TE_0 spectral position (bounded case) is not dependent on the spectral location in comparison to LSPR), which is a typical signature of strong plasmon-guided mode interaction [Linden, Christ et al. 2001; Yannopapas and Stefanou, 2004; Linden, Kuhl and Giessen, 2001], as opposed to previous systems. As the TE_0 dispersion relation is located in-between the water and glass light-lines, the mode is more confined and the interaction with the metallic charges is stronger. The characteristic extinction profiles are shown in Fig. 5.13 for the periodicity of 460x300 nm, y-polarization (TE) for both waveguide thicknesses. Clearly, the intensity of the sharp resonance contributes to larger FOM, but the symmetric extinction-profile may possess some beneficial properties for shift readout. Similar to [Dahlin et al. 2006], it is possible to monitor relative difference of centroids of two sharp peaks. It is interesting to note that the crossing of TE_0 mode through the LPSR produces different profiles for the 2 waveguide core thicknesses. For 88 nm thick, resonances on the higher energy side of LSPR are more pronounced than in the case of 44 nm core waveguide.

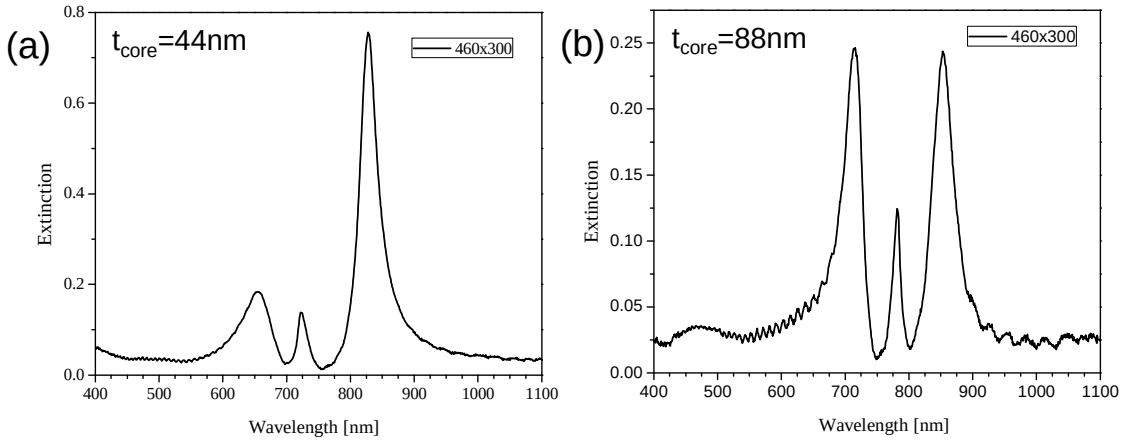

Figure 5.13-Influence of the dielectric core thickness on experimental extinction spectrum. Two characteristic extinction profiles for the same systems with 44 nm (a) and 88 nm (b) thick TiO_2 layer. Superstrate medium is water.

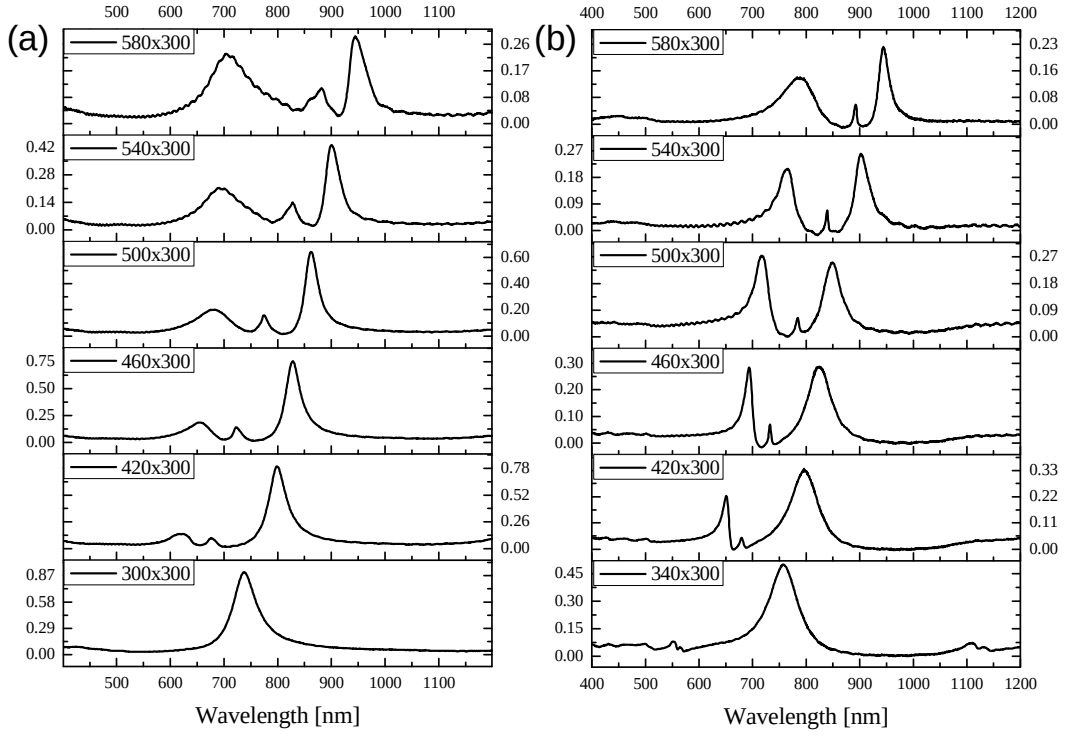

Figure 5.14-Evolution of the experimental extinction spectra as function of the grating parameters for waveguiding layer thickness of 44 nm (a) and 88 nm (b). Notice that transition profile differs in peak's FWHM. Additionally, (a) resemble strongly to larger nanoparticle arrays directly assembled onto glass substrate (Fig. 5.10(b))

To gain insight into the mode supported by such systems, we calculate near-field mode distributions using full 3D FEM calculations. The application of periodic boundary conditions allows modeling and meshing of only single unit of 2D lattice, consisting of one gold nanoparticle. In the model, the y-period is varying, while the x-period is kept to p_x=275 nm. Both waveguiding layer thicknesses are implemented in the model, with 40 nm and 100 nm of TiO_2 with non-dispersive refractive index of n=2.5. The wave-vector of the incident light has two components due to small incident angle of 3^o (k_z and k_Y), according to the results of Fig. 5.8 (a). First, the calculated far-field spectra are presented in the Fig. 5.15. The wavelength is swept in 10 nm steps, while sharp spectral features were refined with a step of 2 nm. The agreement between the experiment and the calculation is good, displaying a single narrow peak for 40 nm TiO_2 and two spectral features for 100 nm TiO_2. The middle peak was not observed as was in calculations of metallic gratings.

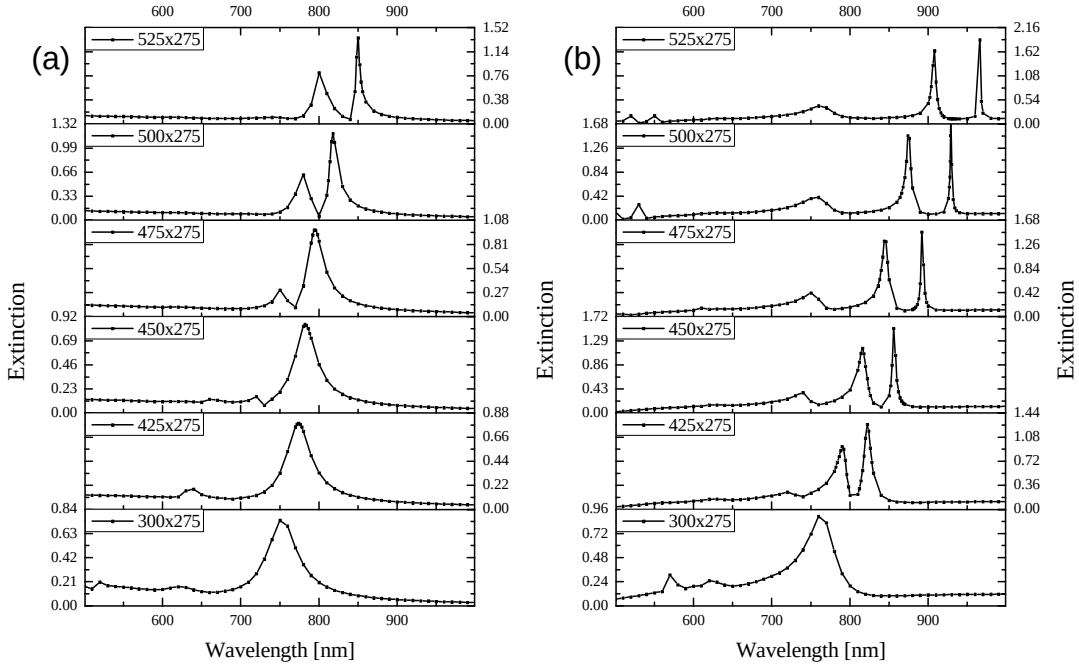

Figure 5.15-Calculated far-field spectra of LSPR-waveguide nanoparticle system as function of array periodicity in case of 40 nm (left) and 100 nm (right) thick TiO_2 layer. Superstrate medium is water.

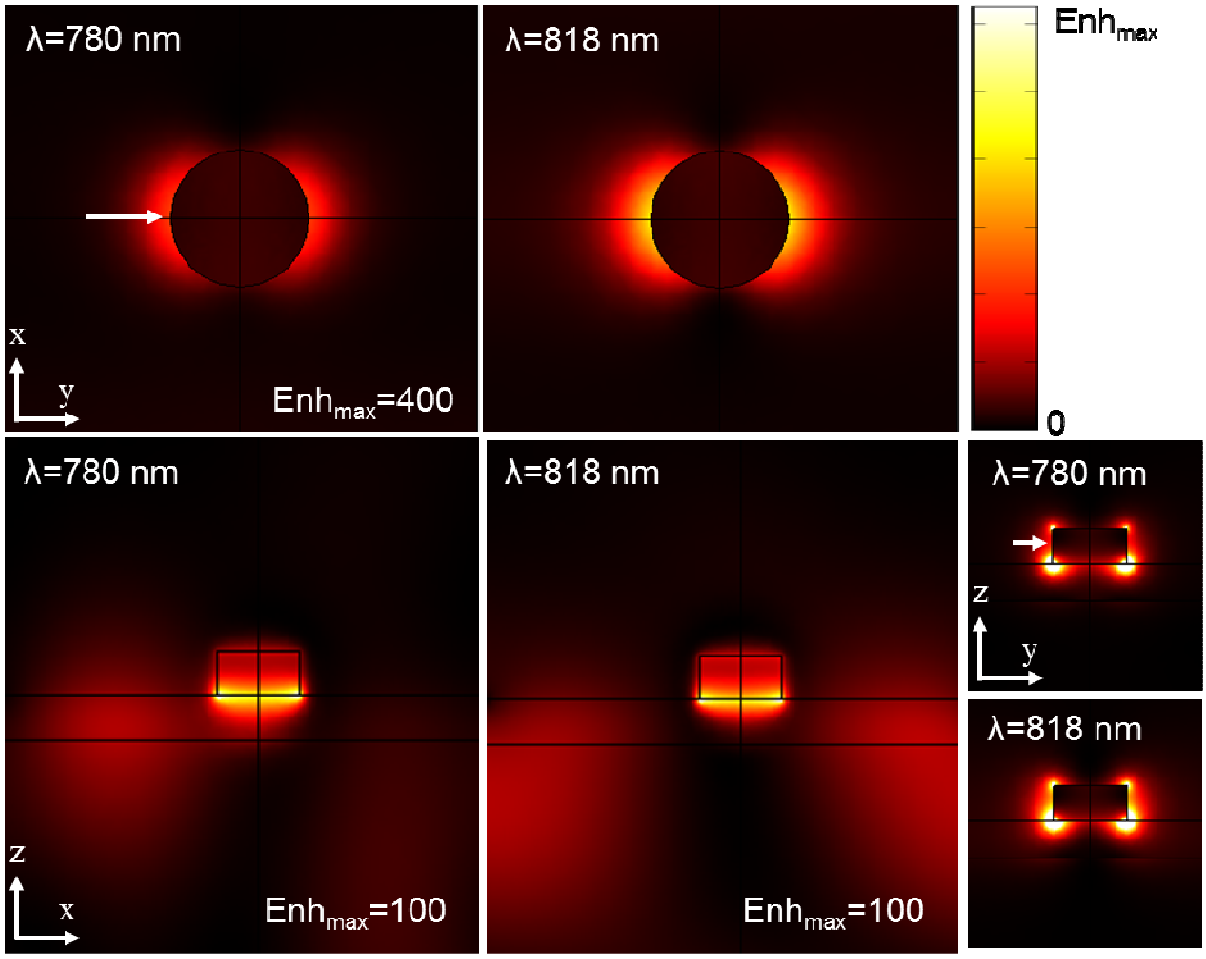

Figure 5.16-Calculated near-field intensity enhancement for gold nanodisks (80x40 nm) array (p_x=500 nm, p_y=275 nm) residing on 40 nm thick TiO_2 (n=2.5) asymmetric slab waveguide. Cladding media are glass (n=1.52) and water (n=1.33). Excitation is y-polarized plane-wave incident from the glass (incidence angle is 3^o). Note: Enh$_{max}$ is 400 if not marked differently. Chosen wavelengths of λ=780 and λ=818 nm correspond to local extinction maxima detected in the far-field.

Figure 5.16 displays the near-field intensity distribution for 40 nm thick waveguiding layer and periodicity in y-direction of 500 nm. The chosen wavelengths correspond to the maxima in the far-field extinction spectra as obtained from previous figures.

The lower energy peak that corresponds to diffractive sharp peak at λ=818 nm, is characterized with higher near-field intensity enhancement, than the broader peak at λ=780 nm, which can be attributed to LSPR. The y-z cross-section reveals the TE_0 mode at 818 nm. The mode is weakly confined (it expands into glass, due to the proximity of the glass light line), and the node of the formed standing wave coincides to the position of the nanoparticle. The two bound modes of unperturbed slab-waveguide can be excited due to $k_y \neq 0$, at λ=773 nm and λ=801 nm, which is pretty close to the 780 and 818 nm peaks in the coupled system. However, the calculated field distribution shows no clear signature of the higher energy TE_0 mode.

The near-field intensity enhancement spectra plotted in Fig. 5.17 were assessed in the particular point near nanoparticle (-45,0,z=20 nm), where the nanoparticle center is located at (0,0,20 nm) for the diameter of 80 nm and height of 40 nm. The near-field intensity enhancement maps for 500 nm y-period and 100 nm thick waveguide are shown in Fig. 5.18. Clearly, the enhancement is larger and the mode is more delocalized for the peaks with longer wavelengths. The bound modes for 500 nm periodicity are located at 901 nm and 927 nm. The interaction with the LSPR supporting lattice perturbs their location as well as character, from bound to leaky.

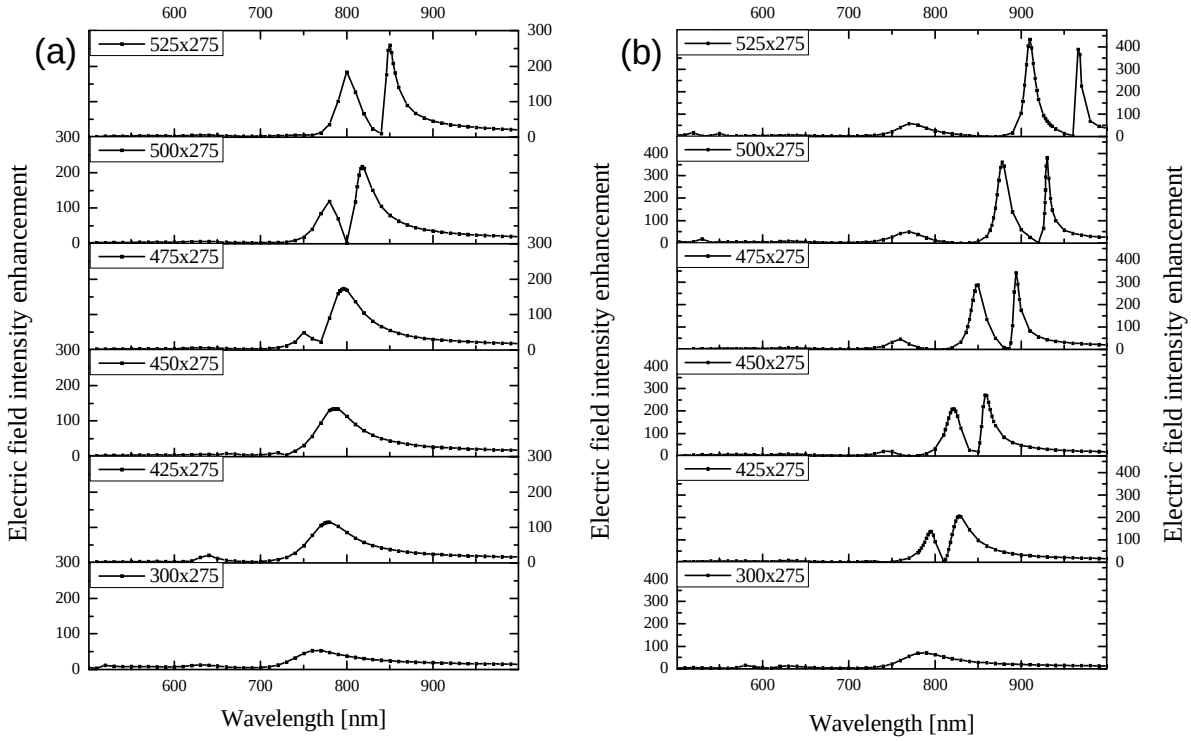

Figure 5.17-Calculated near-field intensity enhancement spectra of LSPR-waveguide nanoparticle system as function of array periodicity in case of 40 nm (left) and 100 nm (right) thick TiO_2 layer. Superstrate medium is water. The near-field intensity enhancement is evaluated at a single point with coordinates (-45, 0, 20 nm) for nanodiks of 80 nm diameter and 40 nm out-of-plane height with center located at (0,0,20 nm). Evaluation spot is marked with thick white arrow in Fig. 5.16 and 5.18

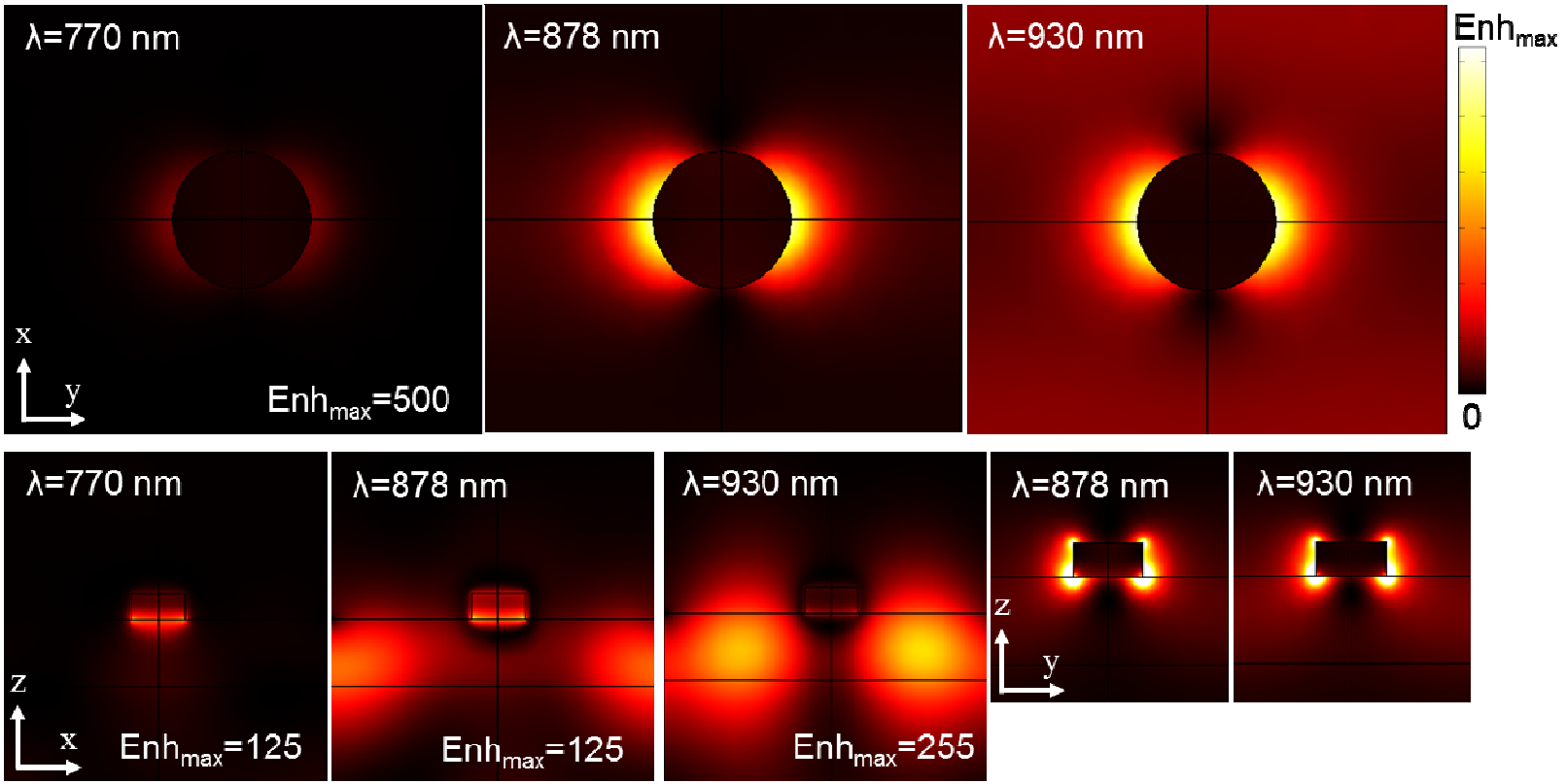

Figure 5.18-Calculated near-field intensity enhancement for gold nanodisks (80x40 nm) array (p_x=500 nm, p_y=275 nm) residing on 100nm thick TiO_2 (n=2.5) asymmetric slab waveguide. Cladding media are glass (n=1.52) and water (n=1.33). The excitation is x-polarized plane-wave incident from the glass (incidence angle is 3^o). Note: Enh_{max} is 500x if not marked differently. Chosen wavelengths of λ=770, 878 and 930 nm correspond to local extinction maxima detected in the far-field.

5.5. Sensing perspective

Sharp spectral features that change position and/or intensity can provide better SNR than broad ones [Dahlin et al. 2006], as long as a higher resolving-power grating is used within the spectrometer. The radiative decay suppression of LSPR oscillation (resonance narrowing) was one of the main motivations that have driven the research of the systems explained above, especially for the biosensing applications. Here we evaluate the applicability of this approach for sensing purposes.

5.5.1. Glass as substrate

To investigate potential for LSPR sensing of the periodic arrays supporting sharp spectral features, out of chip BRIS experiments were performed on the nanoparticle arrays very similar to ones presented in Fig. 5.10. The reference medium was water (n_0=1.335), while the bulk perturbation was glucose solution of refractive index n_1=1.3775. The dominant peak spectral positions was assessed using iterative Lorentzian fitting in Origin 8.5, where the first fit provided range of data points (λ_{res}±FWHM) for the successive fit yielding λ_{res} and FWHM. Once the condition $\lambda_{res} > \lambda_{Rg}$ is fulfilled, the fitting gets unreliable, but the qualitative trend of FOM decrease is reproduced (Fig. 5.19). The BRIS sensitivity is assessed from the difference between central resonant wavelengths in both media, dividing it by relative refractive index change. The FOM is calculated as ratio of BRIS and FWHM, and all are tabulated in Table 5.1. The data clearly indicate that the peak narrowing plays more important role in the FOM improvement, than the BRIS increase with the larger λ_{res} [Miller and Lazarides, 2005]. FOM values typically increase from 2-3 for dense arrays, till maximum of close to 10 for the narrowest resonances obtained with the fixed particle size, which is followed by FOM decrease as shown in Fig. 5.19. Additionally, large relative refractive index bulk perturbation can strongly affect FWHM of the narrowest resonances (especially if close to Wood's anomaly).

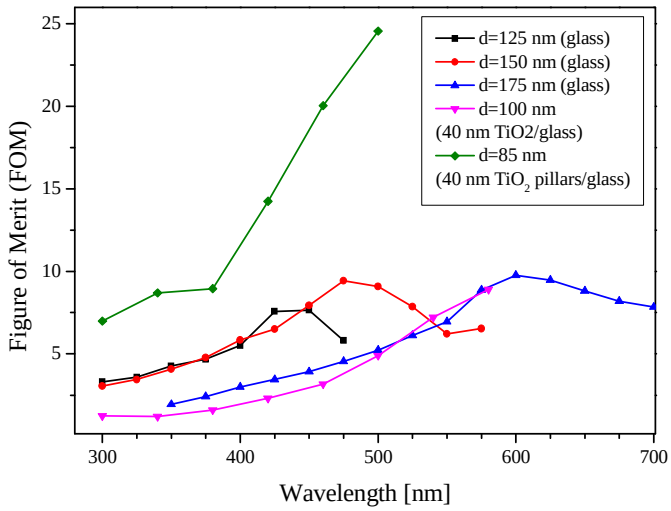

Figure 5.19- Experimentally observed FOM for periodic nanoparticle arrays as function of periodicity p_x. Black, red and blue data points correspond to nanoparticle arrays (disk diameters of 125, 150 and 175 nm respectively) deposited directly on glass substrate.

5.5.2. TiO_2 as substrate

Nanoparticle arrays deposited onto thin TiO_2 layer (44 nm) were assembled within the microfluidic cell of an active type. The spectral shape corresponding to particular lattice primitive vectors (p_x in the table) for the y-polarized illumination are already presented in the Fig. 5.11. The centroid algorithms were simultaneously applied to monitor the sharpest feature available during the sequence of water and glucose (n=1.385) flow. The first set of measurements provided information about BRIS together with the FWHM of the tracked peak, which gives FOM values that increase with the sharp peaks resonant wavelength (violet data points), as similar to nanoparticles on glass. These BRIS in these cases are generally lower than the values observed previously for glass substrate, as expected due to TiO_2 substrate (focusing of the sensing volume deeper into substrate). This was additionally verified by FEM calculations (data not presented).

Having TiO_2 as substrate allows facile substrate etching in acidic solution that is typically used for microfluidic channel and sensor cleaning . The adhesion of gold to TiO_2 is very similar to Ti alone, and as such nanoparticles can withstand substrate erosion. The acidic solution (H_2O:H_2O_2:HCl in proportion of 5:1:1) induces rapid resonance blue shift and Fano-profile redistribution in the first 5-20s of the exposure (fast etching rate), after which the cleaning solution is rinsed out from the microfluidic chambers. This step is followed by water-glucose cycles, and the BRIS of the new system is determined. New values are 5-7 time larger than ones prior to 5:1:1 solution flow. The FWHM decreased for the observed periodicities due to LSPR-photonic mode mismatch. The extinction levels of “quasi-isolated’” nanodisk arrays also dropped (almost twice), pointing to a possible stronger erosion of gold material when the TiO_2 is used instead of Ti, which can further diminish the coupling effect by the nanoparticle

size decrease [Zou et al. 2004, Auguié et al. 2010] or through the defect appearances (vacancies in the lattice) [Auguié, 2009]. The FEM calculations yield 87 nm/RIU for 80x40 nm perfect cylinders arranged into 2D square grating of 300x275 nm, which is close to the value observed in the Table 5.1 (68 nm/RIU) before exposure to the etching solution. The larger sensitivities are expected for nanoparticle on pillar formation, as discussed in chapter 6. The FWHM of the "etched" arrays can be predesigned in order to achieve the strongest FOM after the 5:1:1 treatment is accomplished.

Gold nanodisks	p_x [nm]	BRIS	FWHM	FOM
Diameter:	300	182.2	55.1	3.31
125 nm	325	188.2	52.6	3.58
Substrate:	350	214.7	50.3	4.27
glass	375	222.9	47.7	4.67
	400	219.8	39.9	5.51
	425	230.1	30.9	7.58
	450	272	35.6	7.65
	475	444	76.46	5.81
Diameter:	300	235.9	76.9	3.06
150 nm	325	241	69.8	3.45
Substrate:	350	254.7	62.4	4.08
glass	375	273.4	51.2	4.78
	400	306.3	52.4	5.84
	425	294.5	45.3	6.5
	450	291.1	36.7	7.94
	475	275.7	29.2	9.43
	500	273.5	30.1	9.09
	525	265.7	33.8	7.86
	550	310.4	49.9	6.22
	575	505	77.3	6.53
Diameter:	350	250	129	1.94
175 nm	375	263.9	109	2.42
Substrate:	400	292.6	98	2.99
glass	425	310.5	90.3	3.44
	450	322.9	82.4	3.92
	475	332.7	73.1	4.55
	500	338.8	64.9	5.22
	525	342	56	6.11
	550	335.3	48.2	6.96
	575	341	38.4	8.88
	600	327.5	33.6	9.76
	625	316.8	33.5	9.46
	650	336.4	38.1	8.82
	675	356.0	43.4	8.2
	700	415.1	53	7.84

Gold nanodisks	p_x [nm]	BRIS	FWHM	FOM
Diameter:	300	54.77	67.68	1.2
≈100 nm	340	52.38	63.06	1.20
Substrate:	380	48.47	77.6	1.60
TiO_2 44nm/glass	420	38.7	89.74	2.31
	460	30.74	97.76	3.18
	500	22.48	110.12	4.99
	540	16.56	119.36	7.21
	580	14.41	128.34	8.9
Diameter:	300	446.51	64	6.98
≈85 nm	340	545.11	62.69	8.69
Substrate:	380	482.81	53.94	8.95
TiO_2 pillars/glass	420	576.22	40.42	14.25
	460	586.07	29.25	20.04
	500	636.89	25.93	24.56

Table 5.1-Experimentally determined values of bulk refractive index sensitivity (BRIS), FWHM of the sharpest resonance and Figure of Merit (FOM) as function of array period, nanoparticle size and substrate type.

5.5.3. Mechanical oscillator model

As the first approximation one can suspect that the interacting "broad" LSPR and narrow "guided mode" react independently to the superstrate refractive index perturbation. The observed asymmetric profile strongly depends on the central frequencies of both interacting modes (according to mechanical oscillator model), i.e. the resonance wavelength difference. Thus, if the two modes differently react to the same perturbation, the Fano-profile may undergo a different shape change depending on the reference spectrum (before perturbation) and sensitivities of both interacting modes. Naturally, one can assume that both LSPR and guided-modes will react to superstrate refractive index change, while the sensitivity of guided-mode toward thin molecular layer locally formed on the gold surface is well approximated with zero. If this would be the case, solution of Eq.5.1 is presented in Fig.5.20 and corresponds to two possible scenarios, one for the bulk and other for molecular absorption. This is

illustrated in Fig. 5.20 for a system similar to the section 5.2, except that the resonances of LSPR and guided mode are λ=690 nm (1.8 eV) and λ=750 nm (1.65 eV). The black curve represents the reference spectra, before any perturbation. The blue curve is constructed under the assumption that the BRIS of LSPR and photonic mode alone are identical, and resulting red-shifts are 20 nm. The obtained curve is

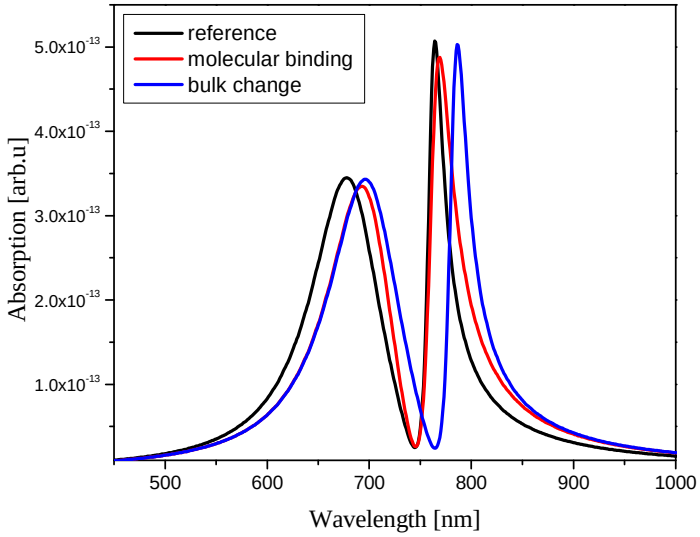

Figure 5.20-Modeling molecular and bulk sensing with coupled mechanical oscillator system. Black line represents absorption spectra of unperturbed system. The molecular binding induces spectral shift of the primitive resonance of broad mode (LSPR), which changes the coupling condition resulting in small shift of narrow peak of Fano-profile (red curve). Both primitive oscillators are equally sensitive to bulk refractive index changes, resulting in Fano-profile red shift, as shown by blue curve.

expectedly uniformly red-shifted, and tracking of the sharp resonance clearly may increase signal-to-noise ratio over regular LSPR. On the other hand, molecular binding takes place on the nanoparticles, thus hardly perturbing the guided mode at all. In this approximation, the red curve is the result of a 20 nm shift of the LSPR alone. This in turn, disturbs the mode coupling, repelling the sharp resonance just slightly from its starting position. However, this picture may not hold, as suggested by the preliminary results of molecular binding (not shown here). These results point out that the magnitude of the total shift is just slightly smaller for the sharp resonant peak of asymmetric Fano-profile than for the regular Lorentzian, for the gold surface coating with SH-PEG-COOH (3K). Additionally, the BRIS still remained superior to bare LSPR peak, even after PEG layer formation. This might suggests that the effect of molecular adsorption on gold effects the hybridized mode, and not separately to individual primitive modes (oscillations). Further on, the field delocalization (evidenced by larger BRIS, but lower shifts upon molecular binding) might come beneficial, especially for the large biorecognition molecules (such as antibodies) and for more effective sandwich assays, if possible to control the delocalization extent carefully. Anyhow, further experiments may reveal more about properties of these hybrid-modes referring to biosensing applications.

5.6. Diffractive coupling among dimers

Finally, we demonstrate that far-field coupling can coexist with near-field coupling by the simple combination of the methodology described in the ch. 4 and within this one. The proper engineering of the nanosystem parameters (particle size, shape, gap size, grating primitive vectors, underlying materials) would certainly yield some benefits whenever high-field enhancement is crucial (florescence enhancement and channeling, SERS, etc.) and certainly may contribute to lower noise and higher sensitivity for the LSPR, which is the aim of further investigation. However, as starting point, the system that combines near-field and far-field interactions was fabricated and optically characterized. Gap nano-antenna arrays were fabricated on glass substrates, and arranged into 2D gratings, where the primitive cell is composed of a single gap nano-antenna (Fig. 5.21 (a)). The superstrate medium is water. The nominal size of the individual nanorod is 160 nm length, 85 nm width and 50 nm height. The gaps considered here are of 20, 40, 60, and 100 nm, while the array periodicity is 500x500, 550x500, 500x550 nm. The longitudinal dipolar bonding modes are selected by the appropriate linearly polarized white light. Typically transversal modes were used in the literature to produce these sharp features due to further delocalization [Vecchi et al. 2009] or easier tuning with lattice modes [Kravets et al. 2010, Vecchi et al. 2009], since the binding-dipolar modes are typically strongly red-shifted in comparison to the bonding transversal ones.

The near-field distance dependent coupling is clearly demonstrated by the resonance red-shift as the gap decreases from 100 nm till 20 nm. However, the smooth transition, as observed in ch. 4. is absent here due to interaction with the Rayleigh's anomalies, predominantly the ones in the glass (at λ=760 nm for 500 nm period, and at λ=836 nm for 550 nm period). The weaker, but still visible water Wood's anomalies are located at λ=665 nm and λ=732 nm for 500 nm and 550 nm period. It is apparent that change of x-axis periodicity also yields moderate effects, which was less effective for nanodisk arrays. Most likely, due to large overall size of gap antenna (of 300 nm plus gap size), the adjacent rods of neighboring nanoantennas can still couple due to relatively short distance (<200 nm).

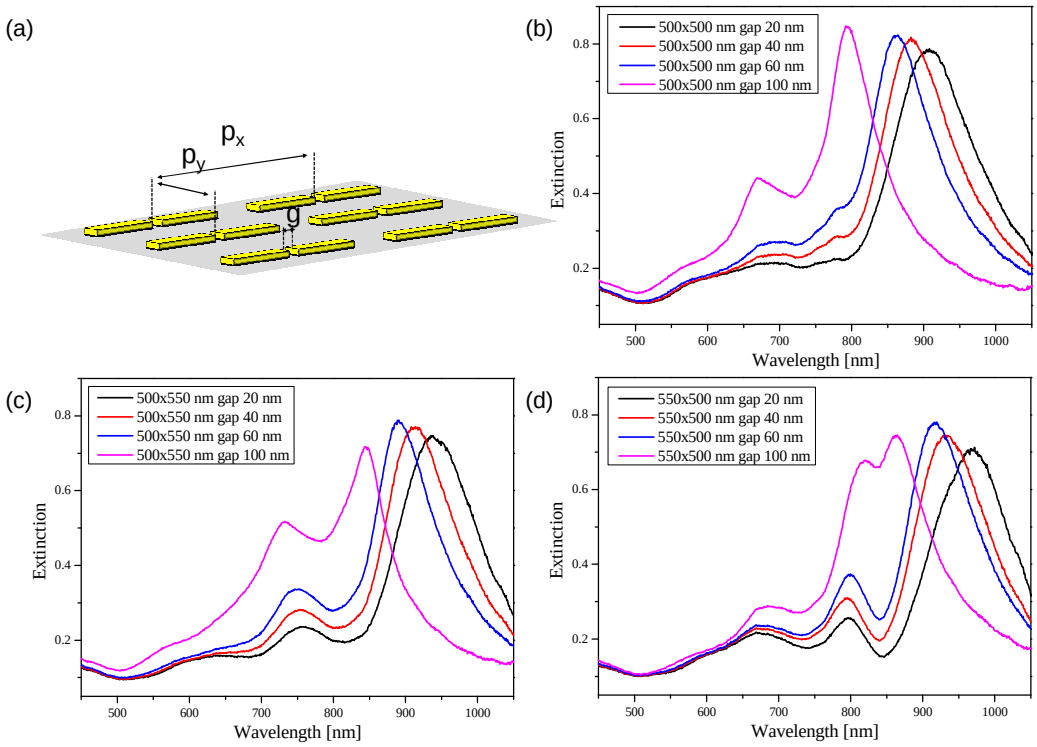

Figure 5.21-Nanoparticle arrays experiencing both the near-field and the far-field interaction. (a) Sketch of considered geometry consisting of periodically arranged gap nanoantennas, with parameters controlling the extent of near-field coupling within the individual pair (gap-g) and array periods p_x and p_y influencing far-field interaction between nanoantennas. (b), (c) and (d) display resonant profiles for the chosen set off parameters g, p_x and p_y.

5.7. Conclusion and future aspects

By adding a thin guiding layer one can significantly enriched the spectra of closed-coupled nanoparticle arrays, and open up new ways in various applications. As concerned for the sensing, sharpening of the relevant resonance peaks may contribute for the ultimate improvement of signal to noise ratio. Using optimized waveguiding layer, the symmetric environment (with immersion oil as superstrate) is no longer necessary for the observation of single ultra-narrow spectral peak in normal incidence for relatively small nanoparticles (sub 100 nm dimensions). Actually, these systems are robust to refractive index asymmetry, that sharp peaks are even observed for air as superstrate medium.

Another direction for biosensing based on ultra-narrow resonance peaks can rely on the isotropic substrate etching (proposed in chapter 6), that can increase the far-field coupling efficiency, by releasing the nanoparticle modes from the substrate into the superstrate, once the nanoparticles are supported by thinner substrate pillars.

The work on these subjects is still ongoing during the moment of thesis writing.

Chapter 6

Toward a LSPR lab-on-a-chip (LOC)

With the ever increasing numbers of worldwide detected cancer cases, although the advances in the medical science have led to the increase in the healing rate, the numbers of cancer victims keep growing [World Health Organization]. The high degree of cancer awareness have triggered more efforts and more investments into cancer-related research that should contribute to the healing rates, and additionally to a better understanding of its origins, development pathways, etc. Still, the fully unsolved riddle about cancer triggering mechanisms limits early diagnosis and successful choice of medical treatments. The scale levels of cancer research span from body organs to individual cells, and beyond to genes. As the origins of cancer are meant to be sought inside the gene domain, the cancer development research is somewhat localized to the levels of cell-cell interaction as part of the immune response [Nishikava et al. 2008, Pockley 2003], while the global picture of cancer spread among the population might be related to the sociological and environmental parameters of contemporary society (life style, environment pollution (chemical, electromagnetic), climate change, life dynamics, etc), whereas it has been also investigated as a phenomenon related to the evolutionary process of human race [Merlo et al. 2006]. In the scope of medical cancer treatment, early detection and diagnosis would lead to the increased chances of the patient's survival and successful recovery. While numerous treatment methods are proposed, very few are contributing to the main-stream accepted medical methods so far, due to very strict regulation within treatment approval [Stern et al. 2008], or due to lack of interest related to patent exploitation and potentially low profit [Bonnet et al. 2007]. The efficiency of the accepted treatment methods in disease eradication would clearly benefit from a reliable early detection, which partially relies on the availability of ultra-sensitive bio-sensors and assays. However, the missing "holy-grail" in the early cancer detection is the universal cancer marker, and it is still not clear if it exists at all [Seigneuric et al. 2011]. The successful identification of the universal cancer marker in combination with a sufficiently sensitive and easy operating biosensor would certainly pave the way to decreased cancer mortality worldwide.

Within the European FP7 framework, the SPEDOC project endeavors to combine the latest advances of nano-optics, optical manipulation and microfluidics with the ultimate understanding of Heat-Shock Protein 70 (HSP70) to develop a novel integrated and sensitive platform for early cancer detection. This thesis contributes significantly to the SPEDOC project goals, more precisely to the LSPR LOC early detection of free-circulating HSP70 in blood, as a potential cancer marker. Bearing in mind that SPEDOC is still an on-going project, many interesting aspects will not be touched by this thesis, due to yet uncompleted investigation and/or confidentiality reasons. More details can be found elsewhere [www.spedoc.eu].

In this chapter, we are combining the fundamental techniques and the findings from the previous chapters with the purpose of developing a fully-functional LSPR biosensor, as close as possible to the

commercial product that will allow for automatic control of fluid delivery, parallel sample investigation with relevant sensitivity and selectivity toward aimed analytes. Surface chemistry protocols have been indentified as the most problematic part, due to complex nature of numerous reactions that are involved in the sensor preparation steps. Owing to the fact that HSP70 and complementary bio-recognition elements are scarce and expensive, the major part of surface chemistry protocols have been developed for the model system of the common IgG antibodies, with "relatively" easy protocol modification for the aimed HSP detection. It is expected that the system modification toward different analytes, would usually require a change of the corresponding bio-recognition. However, it is not sure at the time of the thesis writing, if such an easy protocol modification is feasible, which is covered in the discussion at the end of the chapter. Nevertheless, the full development of LSPR systems is still highly rated and to our knowledge not being reported so far.

The following chapter firstly deals with the LSPR platform fabrication, fusing the techniques covered in chapter 2. Active microfluidic networks in PDMS are aligned on top of LSPR patterned substrate thus comprising an LSPR-microfluidic platform. Operation principles of such a device are briefly introduced with some results related to bulk refractive index sensing. The second part is devoted to on-going research related to surface-chemistry preparation of the sensor, and the issues faced.

6.1. LSPR-microfluidic LOC assembly

A patterned substrate integration with complementary microfluidic PDMS is shown in Figure 6.1 (although only steps (e) and (f) show the assembly process) and for the sake of completeness, PDMS active microfluidic fabrication steps are also sketched. The displayed assembly represents an actively

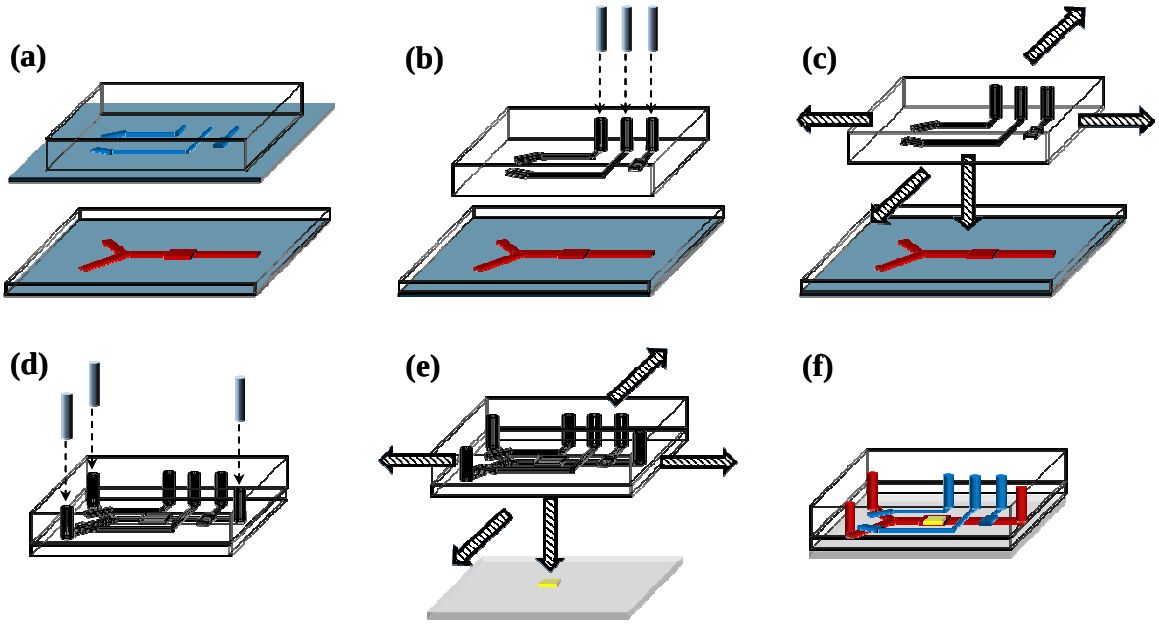

Figure 6.1-LOC assembly (a) Cross-linking of PDMS flow and control layers (b) Control layer inlet hole punching (c) Control-flow layer aligning (d) Flow layer inlet/outlets holes punching (e) PDMS chip aligning over patterned substrate (f) Final look of LOC device

controlled Y-channel, with a sensing chamber located in the middle of the central channel.

Figure 6.1 (a) shows a partially cross-linked PDMS residing on the control layer network (thick layer) and the corresponding flow layer (ultra-thin). The thick PDMS chip frame is cut, inletting holes are punched (b) and the PDMS pattern is manually aligned onto the thin flow layer PDMS, that is still residing on its mold (c). These actions should be accomplished as fast as possible in order to prevent chip delamination (leaking). The bare aligning process is done manually with the help of low magnification microscope. It requires some practice before achieving 10-20 µm aligning accuracy, and additionally the design should be optimized to facilitate aligning process by having orthogonal features in close proximity (within the microscope field of view) that determine aligning axes. Though the wet aligning can be much easier, the alignment procedure here is done without any aligning liquids (see Chapter 3.3). Once the cross-linking and layer bonding is completed, chip frame is cut in the thin PDMS and inlets/outlets of flow layer are punched (d). This step is the finishing of the active-microfluidic chip fabrication. A glass substrate with patterned metallic areas is aligned over the microfluidic chip (e). This process is facilitated by a thin liquid layer that allows substrate sliding during alignment, while once aligned the surface and capillary forces keep the alignment fixed during the liquid evaporation just before glass-PDMS bond starts forming. Figure 6.1 (f) displays a simple Y-channel LOC device, where the yellow pad represents the sensor and the red and blue microfluidic networks correspond to the flow and control layers. The aligning precision is demonstrated in Fig. 6.2 where numerous arrays of plasmonic structures and identification marks are precisely located within 100 µm wide channels separated by 200 µm between one other.

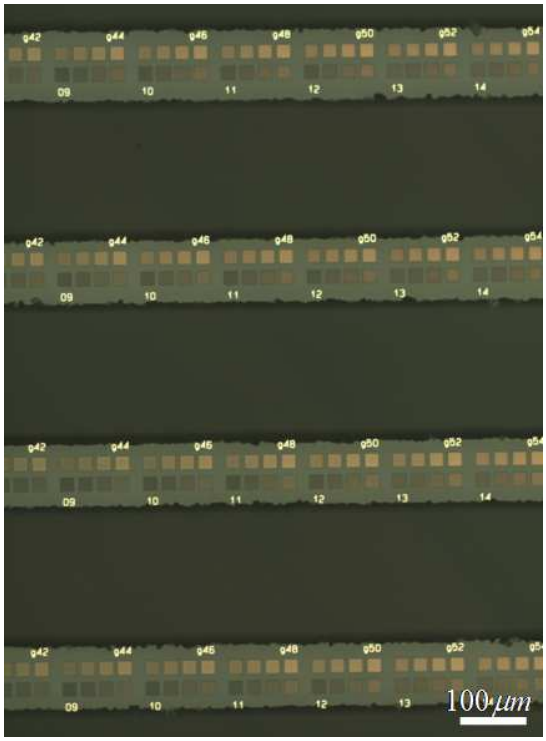

Figure 6.2-Microfluidic-plasmonic substrate manual alignment precision. Individual channel width is around 100 µm.

6.2. Active microfluidic LSPR device operation (SPEDOC prototype 1)

SPEDOC prototype 1 (SPpr1) device was initially designed in order to achieve all the functionalities necessary for the efficient assay platform in collaboration with Sebastian Maerkl (EPFL, Lausanne, Switzerland). It is not optimized for the surface chemistry protocol developments, due to possible cross-contaminations provoked by non-specific interactions of molecules towards PDMS and glass, and other active microfluidic devices developed by thesis author and partners were used instead. Nevertheless, microfluidic chip operations will be demonstrated on this device that is pretty close to its final design. Fabricated microfluidic device is shown in the Fig. 6.3, where control lines were filled with a red dye while flow lines are filled with a blue dye. Chip size corresponds to a standard 24x24 mm glass slides (Fig.6.3 (a)). Figure 6.3 (b) shows SPpr1 in higher detail.

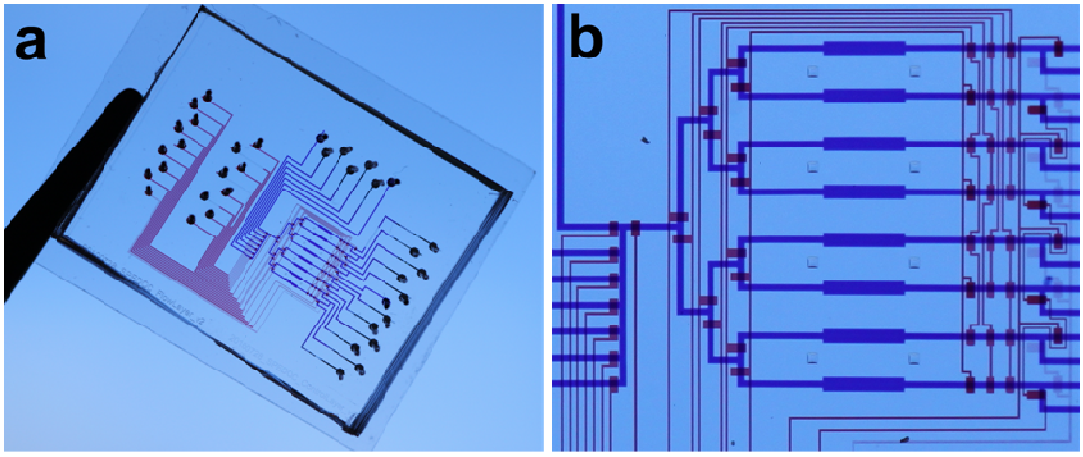

Figure 6.3-SPEDOC prototype 1 active microfluidic chip (a) Chip bonded to 24x24 mm glass substrate (b) Magnified active area of the chip. Courtesy of Dr. Jose Garcia-Cordero and Prof. Sebastian Maerkl (EPFL, Lausanne, Switzerland)

It consists of 8 individually addressable sensing chambers I-VIII (1200x200 µm), 6 General Inlets (GI), 1 General Outlet (GO), 8 Individual Inlets (II) and 4 outlets shared by every 2 chambers. There are 19 inletting/outletting holes in the flow layer, while control layer consists of 17 inlets of dead-end channels. Multiplexor is build up by 6 control lines (front and back part), while GIs and GO are actuated by individual control lines. There is MMV that separates general inlets from the sensing chambers, and also 3 control lines that are used in two different modes of operation as described below. A full microfluidic layout is represented in the Fig. 6.4 with magnified multiplexing and outlet/inlet selecting parts. The doubling of the chamber number would require only 2 more control lines, and 12 additional inlets and outlets as there is a plenty of space available.

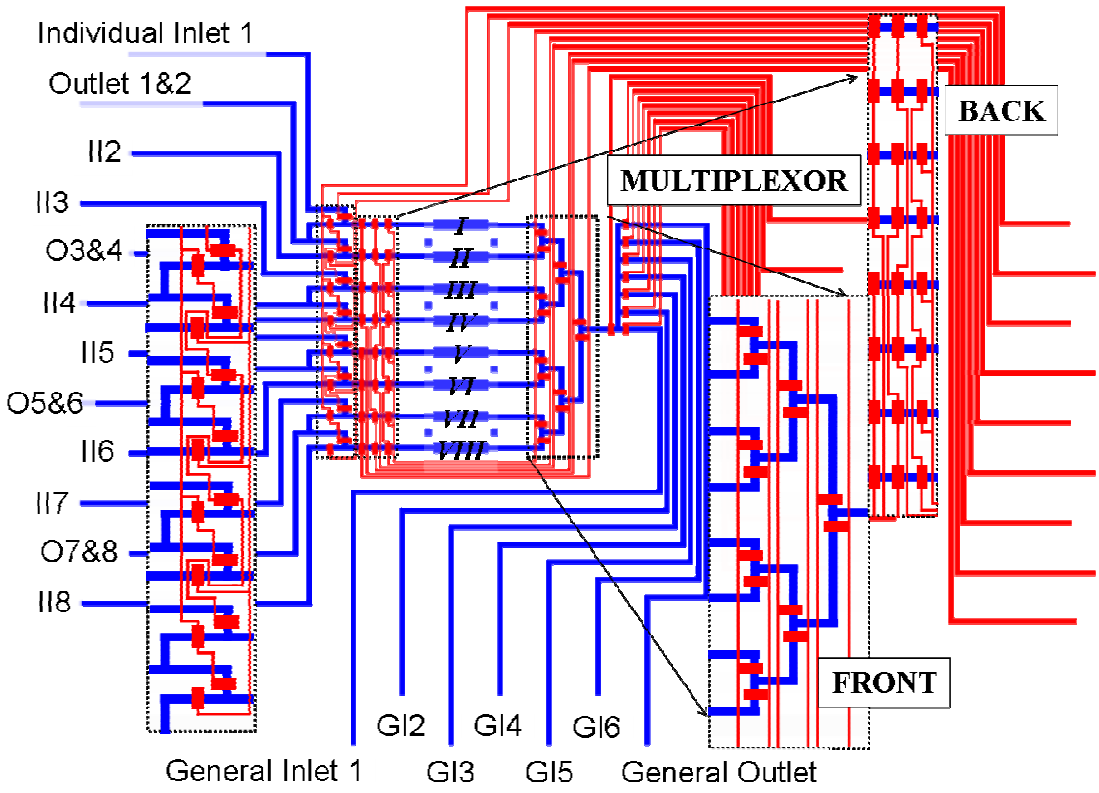

Figure 6.4-SPEDOC prototype 1 layout. Magnified multiplexor is overlayed on the right, while 3 control selecting network is overlayed on the right.

One can distinguish few modes of operations that are available within the functionality of the SPpr1 device. The first mode is related to the inlet priming that represents a very elegant method of bubble handling. If liquid sample is loaded carefully into the tubing and connected to the inlets, bubbles are generally concentrated at the advancing liquid interface. The advancing liquid volume mixed with bubbles is directed and flown out into priming outlet until only bubble-free liquid remains. The time required depends on the operating pressures (liquid velocity), channels design and liquid viscosity, but in our experience it never exceeds more than a couple of minutes. Figure 6.5 (a) shows liquid path from GI1 to the GO in black, and associated MMV that are actuated during priming time. Second operational mode is “all chambers flow through” from one of the GIs toward outlets (Fig. 6.5 (b)) with the minimum number of the actuated MMVs. It is important to design all liquid pathways with the identical hydrodynamic resistance (i.e. length) so that liquid velocity is constant in the case of the pressure driven flow. This mode of operation is suitable for functionalization of all the chambers at once, like initial cleaning and buffer rinsing, passivation and sensor functionalization in the case when the optimal parameters of the protocols have been already identified. Figure 6.5 (c) shows liquid flow from the GIs to the individual chamber. This mode can be useful if the glass and PDMS passivation works sufficiently well or during protocols development, but is not intended to be used during standard device operation.

And finally, it is possible to use individual inlets of the individual chambers to load investigating sample and to avoid cross-contamination (Fig.6.5 (d)). This operational mode is intended for the sequential real sample manipulation, chamber after chamber, for instance in clinical tests. These are the most typical functionalities of the microfluidic chips employed here, and they can be combined within the different device protocols by an external computer.

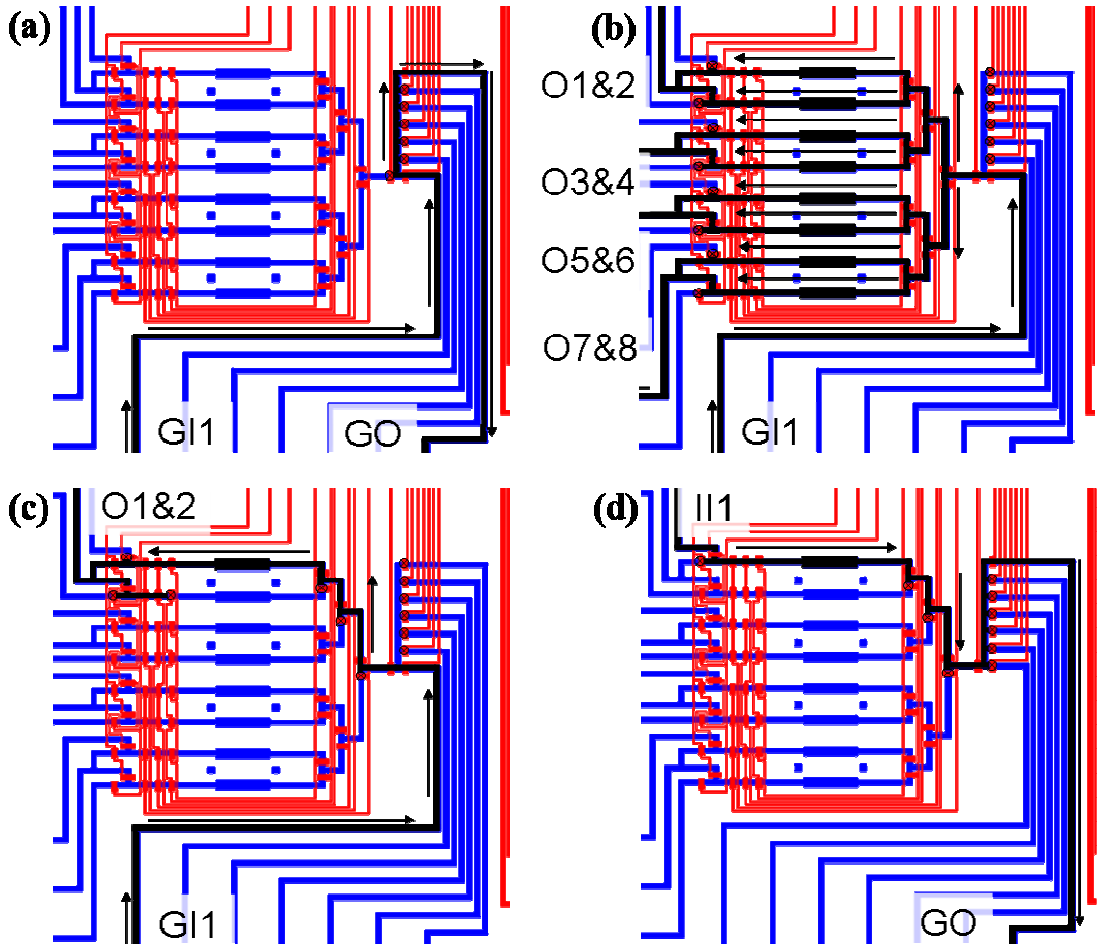

Figure 6.5-The standard operation modes of SPpr1 chip (a) Inlet priming (b) All chamber flow-through (c) Individual chamber flow through (General Inlet) (d) Individual chamber flow through (Individual Inlets)

6.3. BRIS performance of LSPR device

Having LSPR sensors distributed within the different chambers of the SPpr1 device greatly simplifies BRIS experiments due to very precise flow control (fast temporal resolution) and additionally, multiple structures can be easily and reversibly BRIS investigated within a very short period of time. To perform BRIS, a set of glucose solutions with different refractive indices are prepared and calibrated by an Abbe 5 refractometer (Bellingham & Stanley, UK). Calibrated solutions were loaded into general inlets and the LSPR centroid is real-time monitored with the temporal resolution of 3 seconds. The result of the BRIS response for a quasi-isolated nanoparticle array is presented in the Figure 6.6 Baseline centroid position is at 721.17 nm and approx. 1 min long pulses of glucose solutions were introduced into sensing chamber. The flow velocity is high enough in order not to see the effects of Taylor's dispersion for the 3 seconds sampling rate and 1 min pulse duration. Inset displays magnified part of the centroid plateau during 1.36 refractive index solution flow. It is noticeable that the low measurement noise (around 7-10 pm) is superimposed on the slowly varying centroid drift. The origins of this noise stems from the commercial microscope's stage drift, which was used at the beginning. Nowadays, optical systems consist of home-made microscope setup with stable and precise stages, which eliminates slow drift in the measured centroid position.

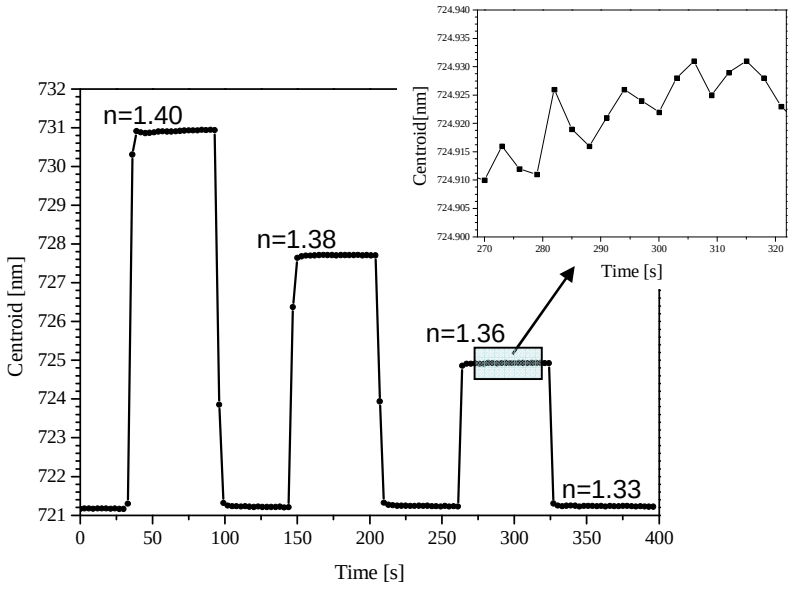

Figure 6.6-Real time bulk refractive index sensing measurements on a quasi-isolated gold nanoparticle array. Different glucose solutions were directed into the sensing chamber for a short period of time. Inset shows noise profile that is dominated by a slow drift. The drift in the base line originates from the stage instability of commercial microscope.

In line with the results of Ch. 5, we repeat glucose experiment with dimer arrays (10 nm gap) as shown in Fig. 6.7. The yielded results show a very similar type of the response curves as shown in the Fig. 6.6.

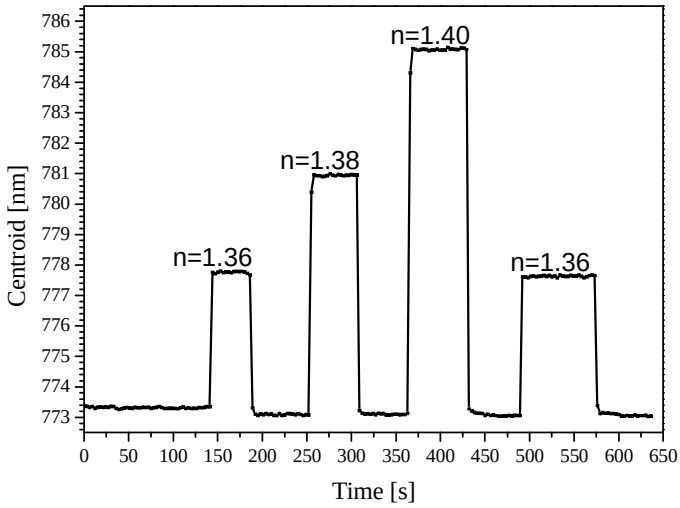

Figure 6.7-Real time bulk refractive index measurements on a 10nm gap disk dimer array.

From the observed real-time measurements, one easily obtains BRIS of the investigated structures. Linear fit through the experimental data yields the slopes of 137 (quasi-isolated) and 169 nm/RIU (10 nm separated dimers), respectively (Fig. 6.8). The higher sensitivity of dimers is confirmed once again, but with a slightly smaller enhancement of BRIS with the dimer formation as compared to the static off-the-chip BRIS measurements seen in chapter 4. The possible reason can be sample quality (different EBL machines were used) and (or) an increased annealing degree during the chip assembly that may change the estimated initial gaps. When PDMS is aligned over plasmonic substrates (see Chapter 6.1), short term solvent annealing occurs (in the boiling solvent until it evaporates) in combination with the long term thermal annealing (>6h) at low temperature (80^{o}C). I noticed that structures that were resonant at λ_1 in air (before chip assembly) are resonating at λ_2 in water (after the chip assembly) where typically $\lambda_2 \leq \lambda_1$. Having the flexibility to quickly investigate BRIS of a nanoparticle sensor can be highly beneficial due to various reasons. Quite often, even though the chip assembly has been performed in a clean-room environment, there can be some contamination, typically aligning liquid residues inside the channels. This can be detected through very low values of the BRIS. With thorough washing, residues can be eliminated, and BRIS values can be restored to the expected value (theoretically obtained or from the previous experiments). If the BRIS doesn't improve with washing, the device can be discarded. Also, the reproducibility tests between different devices can be performed at the initial levels with only the BRIS checking. If the BRIS is not consistent between different batches, it is very unlikely that molecular binding response will be reproducible. Additionally, it is easier to model bulk responses of nanoparticles with numerical and analytical methods and to compare it with the experiments, while the modeling of molecular binding is still time ineffective. A real-time monitoring of bulk sensitivity can bear valuable

information about solvent influence on substrate (substrate etching) or particle reshaping. At least, it can serve as an elegant method of detecting refractive index of adsorbed molecular film. Namely, if BRIS is obtained before and after the molecular assembly onto sensor surface, the crossing point of two BRIS curves points out to the refractive index of the film [Haes et al. 2003].

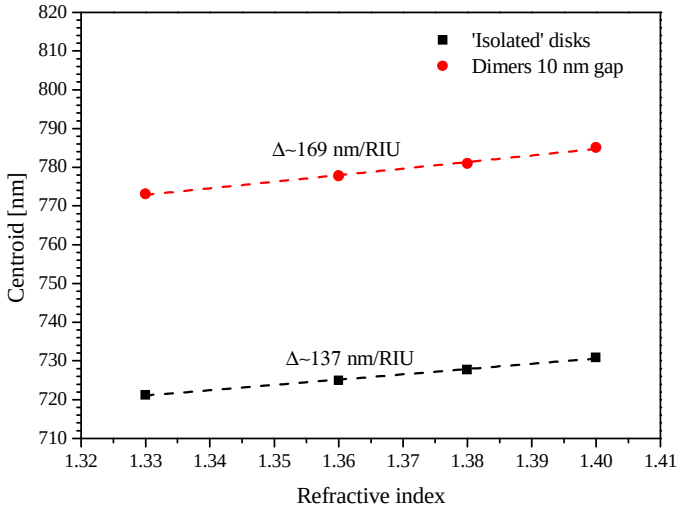

Figure 6.10–BRIS of quasi-isolated nanoparticle arrays (black) and 10 nm gap dimer array (red). Data points are obtained from Fig. 7.6 and Fig. 7.7. Slope of the fitted linear curve determines BRIS of corresponding arrays.

6.4. Surface-chemistry protocols for the sensor preparation

Surface functionalization protocol (SFP) includes all of the controlled chemical reactions sequentially performed with the aim to prepare a sensor (and device) for sample interrogation (analyte detection). The importance of the optimization of the sequence steps certainly highlights SFPs as the most crucial and the most complicated stage in the biosensor's development. Encompassed reactions provide sensor with its performing characteristics and are the most important factors in determining sensitivity, selectivity, specificity, reproducibility, etc. The precise reaction conditions (sequence order, reactants, catalyzers, temperature, pH, ionic strength, compatibility with the previous steps and devise materials) have to be identified in order to reach the optimum sensors performance. While there are numerous strategies specially adopted for similar biosensing devices (SPR, QCM) that also require a set of extensive surface modification steps, the majority stay in the domain of fundamental science; very few found themselves in the wider use. As previously mentioned, the full compatibility between SFP for SPR and LSPR are not typically met, due to different passivation step and sensing range.

In the following paragraphs, a few SFP strategies are presented that are intended to be optimized in the near future. These are typical routes in LSPR biosensing device preparations, and are relying on

antibodies immobilization as biorecognition. Generally, the basic steps in the LSPR SFP flow-path can be identified as follows:

1) Primary gold surface functionalization (typically, the self-assembling monolayer (SAM) formation)
2) Substrate and microfluidic channel passivation
3) Bio-recognition element anchoring
4) Analyte recognition and the detection scheme (sensing)

Accordingly, the remaining of this chapter is devoted to introduction of all of these steps, their implementation and the current progress and status. Unfortunately, every strategy about to be mentioned is still not fully optimized at the time of the thesis submission, thus displaying unsatisfactory function (primarly due to low efficiency of antibody immobilization). However, some conclusions are drawn, the preliminary data are presented and discussed, and the projected directions in the future (ongoing) development are taken out with the aim of achieving fully operational end-user LOC LSPR device for the detection of the free-circulating HSP70 in blood (expandable to other relevant species as well).

6.4.1. Primary surface modification of gold by SAMs

Apart the fact that gold nanoparticles exhibit LSPRs in VIS/near IR, the reason for the widest acceptance of gold in the bio-related applications lies in its bio-compatibility and inertness. The advantageous bio-compatibility allows for a various in-vivo applications, as briefly emphasized in introductory chapters. The inertness guaranties the bio-chemical and physical stability of the gold entities (biosensors, drug-delivery carriers, imaging tags, thermal nano-sources, etc.). The intrinsic inertness, besides being advantageous (for instance, low-degree of oxidation) also features gold as a very rigid material referring to the ease of bio-chemical surface modification. Recalling that typical nanoparticle sensitivity ranges of 20-30 nm from the surface, the analytes (5-15 nm in size) have to be brought near to the sensor surface for a sufficiently long time for a stable readout. Many proteins tend to interfere with gold (and substrate) via longer-range electrostatic and other short-range interactions (hydrophobic forces, van-der Waals, etc). Fig.6.9 demonstrates the extent of physisorption of Rb IgG protein (bulk conc. of 50 μg/ml) onto an intact gold surface, followed by specific interaction with injected anti-species of the same concentration (Gt anti-Rb IgG). In general, these interactions can be employed for the protein detection or as primary surface modification step, but the sensor's operation lacks stability and control as such, particularly away from buffered solutions and in more harsh environments, like blood or serum. Moreover, for the label-free detection, the sample matrix needs to be extremely purified; i.e. only the analyte molecules as such can be present in the interrogated sample, making the proposed sensing scheme suffer severe lack of selectivity. Thus, a primary surface modification needs to provide very stable and flexible chemical functionality, not intrinsically expressed by the gold itself and should provide a stable and efficient means to forming biorecognition layer, while keeping it functional and stable.

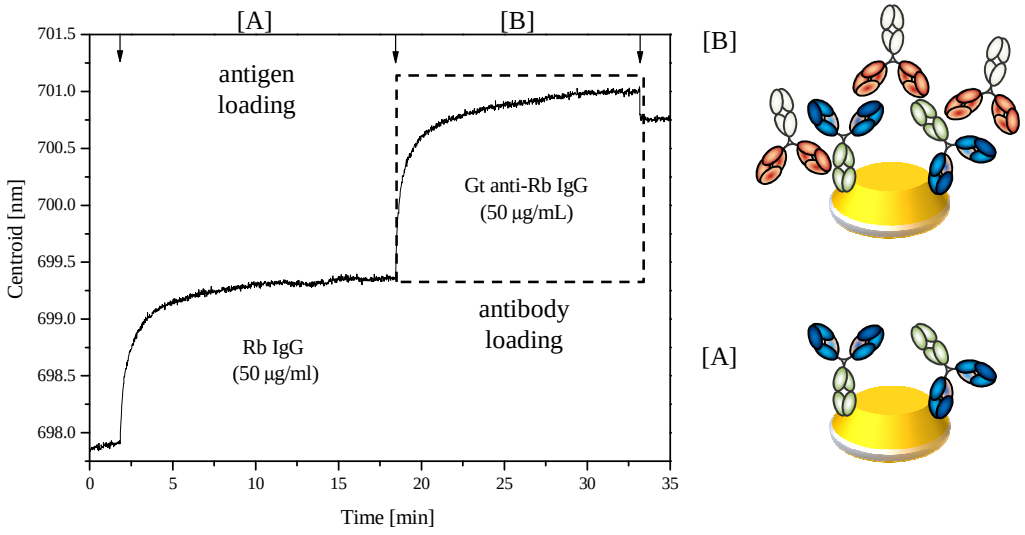

Figure 6.9-Real-time monitoring of electrostatic physisorption of Rb IgG protein onto bare gold. Specific anti-species (Gt anti-Rb IgG antibody is injected at t=19 min, that results in fast binding kinetics. Larger shift for the same concentration indicates more than 1:1 binding, since the antibodies are located farther away from the surface (in the lower sensitivity zone). Arrows indicate the time instance of new liquid injection.

Since the sulfur (S) forms semi-covalent (complex-coordinate) bond with the gold that is (one of) the strongest chemical bonds of gold with any other atom, the thiol-group bearing molecules (-SH) are generally employed for primary surface modification of gold. Additionally, such molecules have to express a supplementary (added) functionality that will render sensor's surface with desired chemical properties. The modified surface should expose a high degree of overall functional homogeneity. In some cases modified surface is intentionally rendered as chemically bi-functional (e.g. mixed SAMs [Malinsky et al. 2001, Marie et al. 2007]), but the overall homogeneity should be preserved. Clearly, beside homogeneity, the performance of the modified surface depends on the attained surface density of the functional sites (groups), implying the importance of controlling (optimizing) assembling/binding process.

Traditionally, the most common classes of molecules that are used for the primary gold surface modification are known as thiol-SAMs. These are alkanes terminated with a thiol group at least at one of the chain ends. The monolayer assembly of a thiol SAM starts with relatively fast sulfur-gold bond formation, while the subsequent mono-layer organization is a slower process. Alkane chains interact side-ways through the hydrophobic hydrocarbon chains and other inter-molecular forces, thus arranging themselves into a compact, densely packed and homogeneous layer. Monolayer orientation and packing density varies with molecule type, substrate material and the conditions in within reaction takes place. Typically recommended SAMs incubation time is around 24h in organic solutions (methanol, ethanol), but under a flowing condition layer formation can be faster. Fig. 6.10 (a) presents the general formulae of alkane-thiols with some typical functionalities (methyl, hydroxyl, carboxylate and amino) as examples

(d). Mercapto-undecanoic acid (MUA, R=COOH) was exploited in the experiments presented in chapter 4.

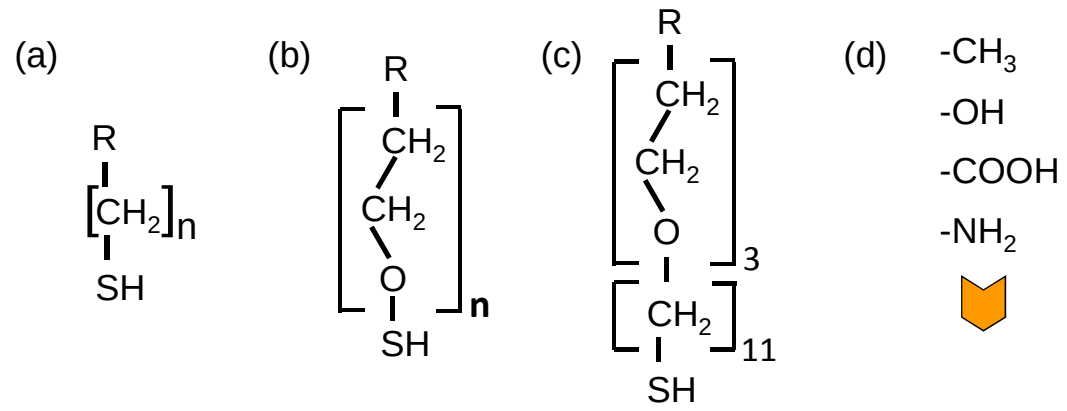

Figure 6.10-Most common compounds used for primary gold surface modification. (a) alkane-thiol (b) thiol-PEG (c) thiol-alkane-PEG (d) typical bearing functionalities: methyl, hydroxyl, carboxyl, amino, biotin.

The number of carbon atoms in the alkane chain is one of the parameters that can be tailored for particular applications. By assembly of different chain-length alkane-thiols onto nanoparticles, the sensing range can be assessed by measuring plasmon shift upon absorption [Haes et al. 2003]. For the nanoparticle coatings, the optimal layer is typically observed for the alkane chains of 10-12 carbon atoms, where there is a balance between inter-chain interactions and low-folding of the chains.

Recently, alternatives to alkane-thiol SAMs are getting more attention, explicitly, poly-ethylene-glycol polymers (PEG) that are responsible for the drastic reduction of protein non-specific absorption onto PEG functionalized surfaces [Frederix et al. 2004, Silin et al. 1997]. These polymers can consist of only a few EG units or can be grown very large (>10 kDa), with polymer chains being multiple folded. The hydrophilic properties of PEGs owing to reduced protein adsorption, and the efficiency clearly depends on the number of PEG units. Additionally, the amount of nonspecific binding is influenced by the terminus group exposed (at the end of PEG chain). For instance, depending on the hydrophobic and associated charge at the working pH, methoxy ($-OCH_3$) and hydroxyl (-OH) terminated molecules possess better repelling characteristics than carboxyl groups (-COOH). The packing density of such molecules is low, due to reduced inter-molecule interactions, which also affects homogeneity as well. Additionally, the uncontrolled nature of the PEG chain folding can suppress availability of the terminus groups, thus reducing binding affinity to the gold, or rendering the coated surface less effective for the successive reactions in SFPs. Nonspecific interactions of proteins with PEG coated gold surfaces were assessed by the exposure of the surfaces to antigen protein, followed by the reaction with antibody labeled with gold colloidal particles. As such, perfectly protein repelling surfaces would show very low surface coverage of colloids, once imaged by SEM. The results of testing various PEG molecules showed that 3-4 kDa thiol-PEGs form incomplete layers, resulting in visible colloidal agglomerations within the voids where PEG hasn't efficiently bound. The PEG bearing molecules, that yielded the minimum gold colloidal

density, are the ones that combine favorable properties of alkane-thiols (i.e. the self-assembling due to side-chain interactions) and protein repelling properties of PEGs. These compounds are commercially available, and the one tested are SH-$(CH_2)_{11}$-$(EG)_3$-R types of molecules (Fig. 6.9 (c)). Even the three ethylene-glycol (ethane-1,2-diol) units still possess sufficient protein repelling properties (although less than larger PEGs). Such short PEG chain is not prone to folding, and as such is not suffering the steric hindrance problems of the terminus group expression. Additionally, it is size comparable to bearing eleven carbon alkane chains that governs the monolayer formation. The layer thickness increase due to addition of three EG units is minimum, thus the sensing volume portion occupied is still low. This molecule also showed the biggest shift upon gold coating suggesting the much better packing density and layer homogeneity in comparison to larger PEG molecules.

The functional terminal group (-R) can be chosen depending on the subsequent steps in the SFP. Distinct strategies for the attachment of the various bio-recognition elements require different surface modifications, where the most common are depicted in Fig. 6.9 (d).

Also worth mentioning is the solubility issues of all of these molecules in water and organics, that might result in compatibility problems with the PDMS device, or chemical solvent annealing problems that reflect in nanoparticle LSPR drift.

6.4.2. Microfluidic channel passivation (glass and PDMS)

Passivation problem relates directly to nonspecific adsorption of proteins that has wider impact than considering only biosensors. Designing coatings resistant to protein adsorption addresses the issues facing in medicine, especially for various implants, since strong adsorption can lead to its function failure.

Stable and optimal performance of any biosensor (especially label-free) strongly depends on passivation procedures. Although it is clear that as many various surfaces can be found within the sample flow-thought path, generally, we can differentiate among three levels of passivation:

1) blocking active sensor surface

2) passivation of inactive surfaces adjacent to active ones

3) passivation of remaining surfaces (channel walls, tubes, etc.)

The first passivation level is related to the choice of nanoparticle primary surface modification, where typically two approaches are applied, or by using thiol-alkane-PEG acid layers or by alkane-thioles in combinations with blocking reagents. Blocking reagents are used once the antibodies are immobilized to fill the gaps within the form surface. These are rather small entities with amine groups (ethanol-amine), or more advanced oligo-ethylene glycol-amines (3 structural units) [Frederix et al. 2004]. These agents together with immobilized antibodies guarantee the sensor specificity and selectivity.

The remaining passivation levels are equally important, and these are addressed in the following subsections.

6.4.2.1. Problem of fast delivery of molecules (at large concentrations)

As stated earlier, a majority of proteins tend to physisorb to the glass substrate and more-so to PDMS [Li et al. 2009, Sapsford and Ligler, 2004], primarily due to long-range electrostatic interactions and short-range hydrophobic interactions. The absorption mechanisms, rates and the amounts of adsorbed proteins are dependent on protein type, surface charge, hydrophobicity of both, surface topography, pH, bulk concentration of protein, incubation time, etc. [Norde, 1996]. An antibody, usually employed as a bio-recognition element on the LSPR biosensor surface, as any other protein suffers non-specific adsorption to various surfaces. It has been reported that IgGs typically adsorb to higher extent to various surfaces (hydrophobic and hydrophillic) in comparison to BSA [Silin et al. 1997]. If one employs the most popular NHS/EDC reaction to anchor antibodies to -COOH functionalized sensor surfaces, the half-life of the active state of the surface is reported to be 4-5h at pH 7.4, after which the half of the molecules have undergone hydrolysis and returned to their intrinsic, inactive COOH state [www.piercenet.com]. At some other conditions, the half-life of the surface (activated COOH) activity can be in the orders of minutes, thus it is important to deliver the flux of proteins immediately after the solution is exchanged (antibodies, antigens) in order to maximize the reaction outcome. If the microfluidic channel is not passivated, antibodies at the advancing front of the carrying solvent may be physisorbed to the substrates along the flow direction. This process can significantly deplete the reaching antibody local concentration in the vicinity of the sensor, thus affecting the binding rates which are competing with the fast active surface decay. This scenario is sketched in Fig. 6.10. The channels are being passivated with the adsorbed proteins, and the steady state concentration will arise at some particular time instance after the solution was injected. However this delay time may be crucial. Increasing the flow velocity rises the amount of the delivered molecules in the validity of the mass transfer limit [Sjoelander and Urbaniczky, 1991], but sometimes the maximum operating pressures (flow velocities) are limited by the chip delamination threshold. Additionally, to improve the confinement of the molecules to the nanosensor surface, the channel cross-section (height) may be decreased, which simultaneously lowers the maximum flow velocity as a consequence of the increased hydrodynamic resistance. Quite often, the biorecognition compound may be costly, thus countering the necessity of the use of very concentrated solutions within the sensor preparations. Lastly, if the antigen/antibody species are physisorbed onto the channel walls, it can additionally deplete the concentration of the complementary antibody/antigen molecules, due to affinity reaction with physisorbed protein. However, the justification of such scenario depends strongly on the extent of protein conformational change upon adsorption, that is governed by many factors: type of protein (pI, secondary structure), its concentration and incubation time before secondary protein injection (related to protein spreading [Norde, 1996]), hydrophobicity/hydrophilicity of surfaces, operating pH and ionic strength, etc.[Sapsfprd and Ligler, 2004, Jeyachandran et al. 2009]

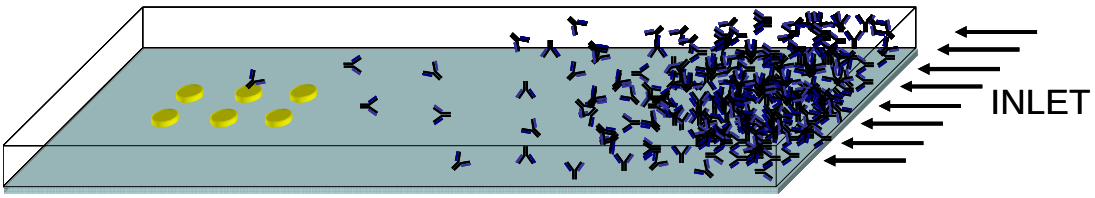

Figure 6.11 -Physisorption profile of the antibodies onto the inner walls of the microfluidic channels at the particular time instance after the antibody solution injection. Very few molecules are reaching the gold nanoparticles due to provoked concentration depletion after nonspecific binding.

6.4.2.2 Problem of the cross-talk from the substrate nonspecifically bound proteins

The nonspecific binding directly onto the LSPR biosensor is generally circumvented by the use of PEG functionalized SAMs, or by using blocking reagents after receptor immobilization. However, even after reducing it by proper gold functionalization, there is an additional nonspecific binding component originating from the glass bound species. Since the near-fields extend 20-30 nm away from the metallic nanoparticle surface, the LSPR sensing volume as such encompasses a portion of the substrate/medium interface (Figure 6.11). Any protein physisorbtion (antigen, protein A and B in the sketch) onto the glass area within the sensing range (marked by the big cylinder edges (Fig. 6.11)) will contribute to the total resonance shift. The effect is to be taken seriously due to several reasons. Firstly, the most sensitive nanoparticle area is located at the glass/medium/nanoparticle interface due to the inhomogeneous dielectric environment felt by the nanoparticle. Secondly, the limitation in the fabrication process, yields nanoparticles with the side-wall slope, which additionally strengthens the local evanescent fields in the glass vicinity due to lightning-rod effect [Haes et al. 2003]. Finally, analyte detection in the blood serum as matrix involves many interfering proteins that are present in much higher concentrations than the targeted one, provoking false-positives or deteriorating the limit of detection if the passivation is not efficiently solved. Of course, one assumes that the sensor surface has been properly modified to prevent direct nonspecific adsorption.

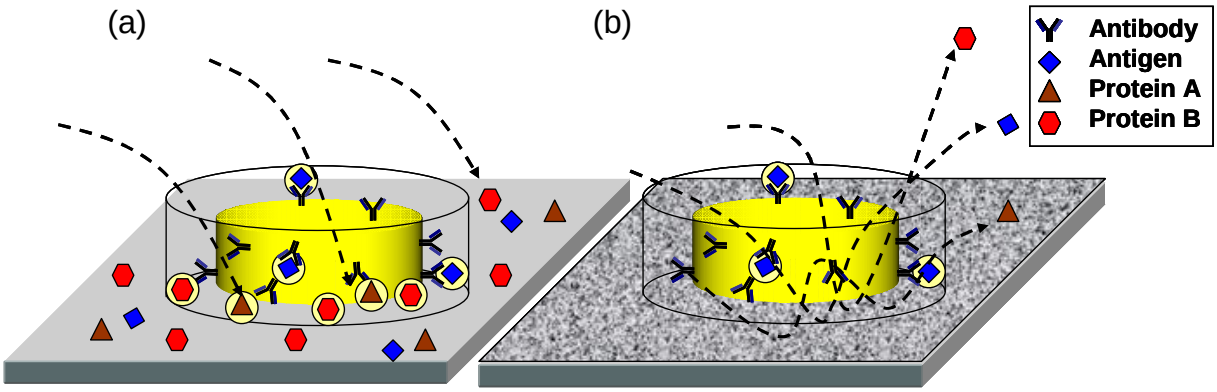

Figure 6.12-The nonspecific binding contribution due to physisorption of the matrix proteins to the glass substrate. (a) In the non-passivated substrate case, any proteins present in the matrix can attach to the glass within the sensing volume (b) In the case of the passivated substrate, nonspecific binding of the proteins to the glass should be greatly reduced.

6.4.3. A brief review of the passivation strategies compatible with LOC LSPR device

Passivation of microfluidic walls is a very important aspect, especially for LSPR based biosensing devices due to reasons previously discussed. An effective passivation layer should screen every potential interaction between internal walls of microfluidic network and molecules that may be circulating within, thus repelling them back into the flow. A special care must be dedicated to prevent the nonspecific protein sticking (antibodies, analytes, and other molecules that might be found in the matrix) due to stable and reliable sensing outputs and proper sensor functionalization. Hence, the ideal strategy would not differentiate between glass and PDMS, which is not plausible due to different hydrophobicity. PDMS is strongly hydrophobic, and as such induces strong conformational changes of proteins upon the adsorption. It has been recently reported that levels of nonspecific adsorption of some proteins onto PDMS may be orders of magnitude higher than on glass at all relevant pH values [Li et al. 2009]. However, due to the fact that the nanoparticles are immobilized onto glass substrates, it makes passivation of both materials equally important.

6.4.3.1. Non-covalent formation of passivation layers

Traditionally, high excess of (B)SA for surface saturation is used as passivation agent due to highly abundance in sera (low cost of production and extraction). However, the nonspecifically bound BSA can cross-contaminate metallic surfaces during the surface modification protocols, thus preventing its use in the stages earlier than the antigen detection (see below). As an alternative, recently, another type of recombinant compound has been proposed for the same task, also relying to electrostatic interactions with negatively charged substrates, but more compatible with the SFP sequences. The compound consists of PEG moieties grafted to poly-L-Lysine (PLL) backbone that carries all positive charges (NH_2^+) at pH<10 [Kenausis et al. 2000]. Thus PLL sticks to negatively charged surface, while the grafted PEGs express their well know protein repelling properties, facing towards the sample matrix. The efficiency of PLL-g-PEG was demonstrated for many LSPR sensing applications [Feuz et al. 2010, 2012]. As a very efficient PDMS nonspecific binding repellent n-Dodecyl-β-D-maltose is proposed, due to strong interaction with hydrophobic surfaces [Huang et al. 2005].

6.4.3.2. Covalent formation of passivation layer

More permanent passivation strategies are related to covalent immobilization to strongly-activated glass or PDMS (high-surface expression of silanol groups). The most typical mechanism are linked to immobilization of different types of silane ($-SiH_3$) molecules, in a single step reaction [Sui et al. 2006], or in a cascade reactions. Typically, silane SAMs are formed that are later modified with covalent attachment of PEGs, proteins or similar. The difficulty of such approach is closely related to low compatibility to LOC device assembly steps or complexity of the reaction control. Namely, efficient substrate activation inside the microfluidics is very difficult to obtain, although some reports suggest that is feasible, with acidic or basic hydrogen peroxide solutions, for instance. Plasma activation that yields the highest surface density of silanol groups is not compatible with the device assembly in most of the cases, since if passivation is performed onto patterned substrates prior the chip assembly, it prevents bond formation between PDMS polymer and such substrates. It is possible though to use

epoxy-functionalized substrates (with the plasma activation of the glass), however the resistance of epoxy-ring to chip assembly conditions (exposure to temperature and substrate aligning liquid) is still under investigation.

6.4.3.3. Substrate etching

The influence of substrate nonspecific binding of proteins can be further diminished by inducing the mismatch between sensing volume and substrate regions. The LSPR associated evanescent fields of nanoparticle residing on the high refractive index substrate is concentrated predominantly inside the substrate (with the lobes around the critical angle). On the other hand, in a homogeneous environment (nanoparticles in solution) the evanescent fields are symmetrically arranged and complete sensing volume is available. Between these two limiting cases, nanoparticles arrays on dielectric pillars are proven to be the optimum configuration that combines fixed arrangement of nanoparticles on the substrate with the more sensitive case of nanoparticles in a homogeneous medium. Pillar supporting nanoparticles have been theoretically investigated [Otte et al. 2009] and fabricated by the standard lift-off process (SiO_2 evaporation prior gold evaporation) [Dmitriev et al. 2008], substrate dry-etching (RIE) [Verellen et al. 2011] or inside-the-chip wet-etching of glass by a highly diluted hydrogen fluoride (HF) solution [Otte et al. 2011]. The latter case is very convenient due to compatibility with the LSPR microfluidic device, however, the special care has to be taken when working with HF. Additionally, etching rate can be monitored in real-time with the peak (or centroid) position tracking. The stability of nanoparticles depends on the supporting pillars' size and shape, and if the substrate is etched too much, the nanoparticles-pillar system can collapse. Thus, the stability of the nanoparticle-pillar system limits the total etching time (thickness), and additionally enforces the use of thin adhesive Ti layer [Otte et al. 2011].

In case of nanodisks, the most sensitive area is located at the glass/water interface, and gets occupied by the nonspecifically bound proteins on the glass (typically during the biorecognition element attaching) or by the glass passivating agents (such as PLL-g-PEG, for instance). Taking into the consideration that the remaining area adjacent to the nanoparticle's surface has been already occupied by SAM and biorecognition (capturing antibodies), the remaining sensitivity for the antigen is already diminished considerably. To release sensing volume trapped within the substrate, substrate etching becomes very handy, as shown in the Fig.6.13. Beside the sensitivity gain, the interference from the substrate adsorbed species can be reduced, if the LSPR lobes are sufficiently distanced from the substrate. Fig. 6.13 shows the LSPR mode release for 10, 20, 30 and 40 nm depth of isotropically etched glass for the gold nanodisk (100x40, 25 degrees slope) in water. BRIS as function of etched depth is shown in Fig. 6.14. for two disk diameters (D=100 and D=200 nm). From the observed BRIS evolution with etched depth that the sensitivity plateau are reached after the etching depth equal to 60% of disk radius. In such a case, the supporting pillar is already located in the low sensitivity region (see chapter 5). Thus any absorbed molecular species will weakly perturb the mode. This method is fully compatible with the LOC, since it can be performed prior to or after the device assembly. Additionally, it can be combined with any substrate passivation strategy (PLL-g-PEG, silanization) although the layer formation onto curved surface may be more difficult.

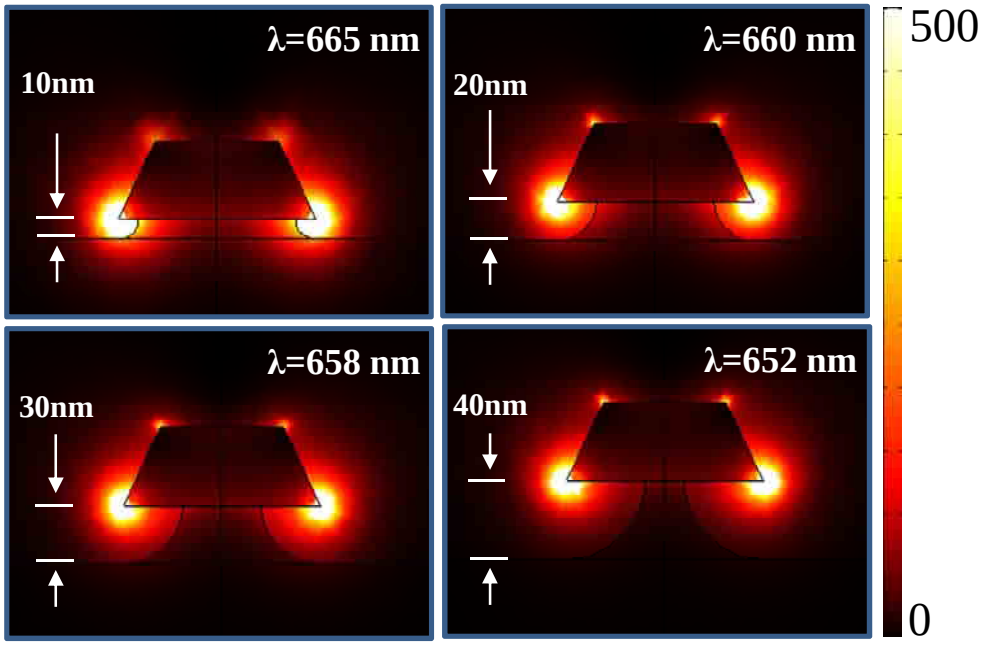

Figure 6.13-LSPR mode volume for the 100x40 nm disk (25° slope) in water, for the different etching depths. The near-field distribution is calculated for the resonant wavelength excitation, and clearly displays increase of mode-substrate mismatch.

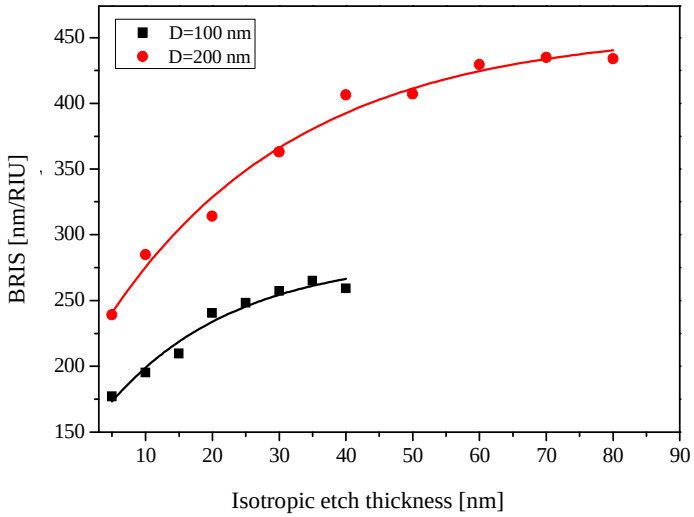

Figure 6.14-Calculated BRIS of gold nanodisk arrays as function of isotropic substrate etching depth for 2 disk diameters. The calculated are performed up to thicknesses equal to 80% of nanodisk radius.

The effectiveness of the passivation can also benefit from the substitution of glass substrate with other materials. As particularly suitable TiO_2 stands out, since recent studies showed the decreased nonspecific adsorption on PLL-g-PEG layers formed on the TiO_2 in comparison to the SiO_2 [Feuz et al.

2010, 2012]. Apart from decreased interference of LSPR sensing volume and nonspecifically adsorbed species on the substrate, nanoparticles supported by pillars are, as mentioned previously, more sensitive [Dmitriev et al. 2008].

6.4.4. Bio-recognition element immobilization (antibodies)

The finishing step in the biosensor's preparation aims at bio-recognition elements immobilization that features the surface property of the selectivity and specificity toward the desired analyte. In this thesis, the bio-recognition elements used are mainly antibodies, as the most typical in LSPR applications. The antibody typical structure, natural function and synthesis method are briefly introduced. The following are paragraphs devoted to antibody immobilization strategies that were tested so far, with the discussion about the immobilization procedure complexity, obtained immune-reactivity of such layers, and the issues encountered.

6.4.4.1. Antibody - basic overview

Antibody's function and structure is one of the most important subjects in the field of immunology, since the adaptive immune response to extracellular microbes and toxins starts with the antibodies secretion (humoral immunity). B cells (type of lymphocytes) upon the antigen recognition (by the cell membrane's antibodies), and subsequent cell activation, proliferate in the process of clonal expansion into the population of the antibody secreting cells. Secreted antibodies circulate through the body, seeking for the explicit extracellular intruder, of the same type as the one that provoked B cell activation. Once the antibody finds and binds to its antigen, the eradication of the antigen (the effector phase of the immune response) proceeds with the antigen elimination in coordination with the proteins of the complement system or phagocytes, depending on the antigen type.

The antibodies belong to the immunoglobulin class of proteins. The important structural subunits consisting antibody molecule are polypeptide chains: two identical heavy (HC) and two identical light chains (LC), arranged into Y-shaped structure. Each LC is attached to the corresponding HC via disulphide bonds. The two HC are also connected to each other with disulphide bonds. As shown in the Fig. 6.14, the typical antibody (IgG) consists of three regions, two of which are responsible for the interaction with the antigen – Fragment antigen binding (Fab) region. The remaining portion is called Fragment crystallizable (Fc) and it is responsible to the signaling within the remaining stages of the immune response. Namely, the Fc region expresses the receptors that signal and activate other parties (phagocytes, proteins, T cells) that mainly eliminate antigen. There are 4 other types of human antibodies besides IgG: IgA, IgD, IgE and IgM, with distinct Fc regions. Fab region is made of variable and constant subunits. The paratope section of variable region recognizes and binds to the specific part of antigen (called epitope). The interactions that mediate antibody-antigen binding are of non-covalent character (Van-der Waals, hydrogen bonding, etc) mainly recognizing conformational shape instead of chemistry properties [Abbas and Lichtman, 2006]. The very strong affinity of the antibody for the specific antigen is one of it advantages for the bio-recognition role in the sensing. Two paratope regions can bind up to two epitopes belonging either to the same, or to two individual antigens. The flexible

hinge region between Fc and Fabs, allows to the Fabs a certain degree of freedom for the efficient antigen binding.

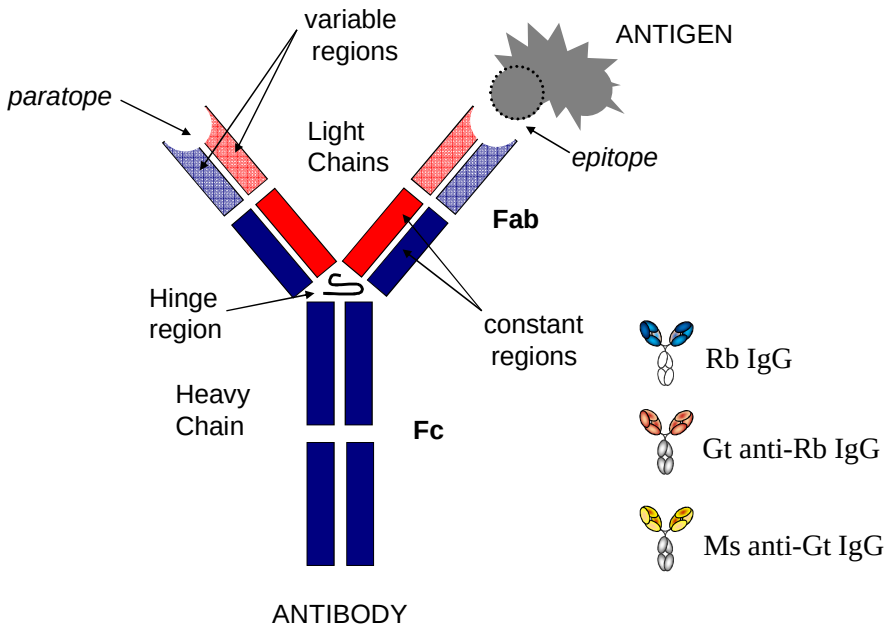

Figure 6.15-Basic structure of the IgG antibody and simbol of 3 types of antibodies employed throughout this chapter: Rabbit IgG (blue), Goat anti-Rabit IgG (orange) and Mouse anti-Goat IgG (yellow)

A particular antibody is produced to expose the strongest affinity toward the unique epitope. This owes to the selectivity property of the antibody as a bio-recognition element. The immune system of mammals can produce antibodies specific to any invading antigen species, due to the almost infinite possibility of epitope's structures (mutations in the genes coding the antibody, during the B cell maturation). This represents the third advantage of the antibodies for the biosensors beside high affinity and selectivity. Namely, the each naive B cell codes its paratope prior to the knowledge of any potential antigens. Thus, only if the cell passes maturation steps (no response toward the self-antigens), and if encounters the complementary antigen, such a cell undergo activation and clonal expansion, resulting in the augmentation of the corresponding antibody secreting B cells. Thus, it takes some time before organism builds up defenses against the intruding species, which is a typical feature of adaptive immunity.

To produce antibody specific to the required antigen, there is no synthetically available method yet. The desired antibodies need to be harvested from the serum of the mammalian organism (mouse, goat, rabbit, etc), once the immune response is reached the stage characterized with the peak population of the antibodies circulating the animal's bloodstream after the antigenic specie injection. The raised antibodies against any particular antigenic specie can recognize the different parts of the antigen with the different affinity. The collection of such antibody population is referred to as polyclonal antibodies, since they originate from different B cell lines. Monoclonal antibodies are produced from the single B

cell line, and are typically optimized to produce antibody that shows the highest affinity. Such a cell is crossed with myeloma (cancerous cell), resulting in rapidly growing population of identical cells secreting exacting antibody.

Chemical moieties expressed on the antibody surface are used to anchor antibody through the covalent linkage to the pre-modified metallic surface of plasmonic sensors. The surface of a typical antibody molecule is abundant of primary amines, as being characteristic to the proteins. These are randomly scattered over the whole antibody. More localized, there are carbohydrates on the sides and few COOH groups at the root of Fc region in case of polyclonal antibodies. These are absent in the case of monoclonal, which is probably the trait belonging to the myeloma cell's genetic heritage. It is also possible to cleave the antibody in different manners by disrupting disulphide bond between HCs with the help of some enzymes (papain and pepsin), or to isolate only Fabs, and even to separate more specific regions. However, besides being cumbersome, the antibody rupture though controlled may affect its immunoreactivity, i.e. affinity or its ability to bind the antigen completely. In this thesis, the antibody immobilization is achieved via amine coupling, or by its modification with various linkers. Although, randomly distributed amines result in a random orientation of the immobilized antibodies, this strategy is used due to it simplicity over alternative methods. As opposed, protein G or protein A can bind directly to the root of the Fc region, which generally results in the optimized orientation of the antibody layer. However, surface modification with proteins G/A induces additional complexity in the surface functionalization protocols. It has been also reported that beside improved homogeneity of antibodies arranged onto protein Gs, these surfaces typically expose less overall binding affinity in comparison to randomly orientated through primary amine coupling [Vijayendran and Leckband, 2000].

6.4.4.2. Antibody immobilization via carbodiimide chemistry

The surface immobilization of antibodies onto carboxyl (–COOH) functionalized gold nanoparticles is accomplished through the EDC/NHS chemistry. Acidic terminal groups of SAMs reacts very weakly with primary amines of proteins, thus additional catalysts that provide better leaving group for the amine coupling to the SAMs is required. Historically, 1-ethyl-3-(3-dimethylaminopropyl) carbodiimide (EDC) hydrochloride is used as carboxyl activated catalyst, forming unstable intermediate (Fig. 6. 16 (2)), before reacting with amines (3a) in a secondary step. This reaction yields around 5% efficiency, most likely due to the competition of the amide bond formation with the intermediate hydrolysis that yields the initial carboxyl groups (3b) in the common pH range [Haes and Van Duyne, 2002].

Since the proteins are dissolved in aqueous PBS buffer (phosphate buffered saline), it is advantageous to prevent the exposure of unstable intermediate (2) to the water based solvents by transforming it into the more stable compound susceptible to the reaction with amines. Therefore, N-hydroxysuccinimide (NHS) reacts with the EDC intermediate forming the semi-stable amine-reactive NHS-ester (3), which has half-life of roughly 4-5h at pH 7 [Thermo scientific, USA]. These reactions are typically performed in a single step, where both compounds (EDC and NHS) are dissolved in MES buffer (2-(N-morpholino) ethanesulfonic acid) in the pH range 4.5 – 6.0. The real time LSPR tracing during the EDC/NHS reaction is characterized by the bulk refractive index step (due to the refractive index difference between PBS and MES) superimposed onto weak but relatively rapid (ca. 15-30 min) binding response due to NHS-ester

formation, as shown in the Fig. 6.18 ([B]). The hydrolysis of the NHS-activated groups occurs surprisingly fast (orders of minutes) in the flowing conditions used here (same time as association phase), thus to increase coupling efficiency the excessive antibody concentration has to be flown immediately. Lowering the pH of the antibody solution from 7.4 to 6.4 and further to 5.5 seems to decrease NHS-ester hydrolysis (data not shown), but still yielding low degree of antibody immobilization as compared to the reported values [Chen et al. 2009].

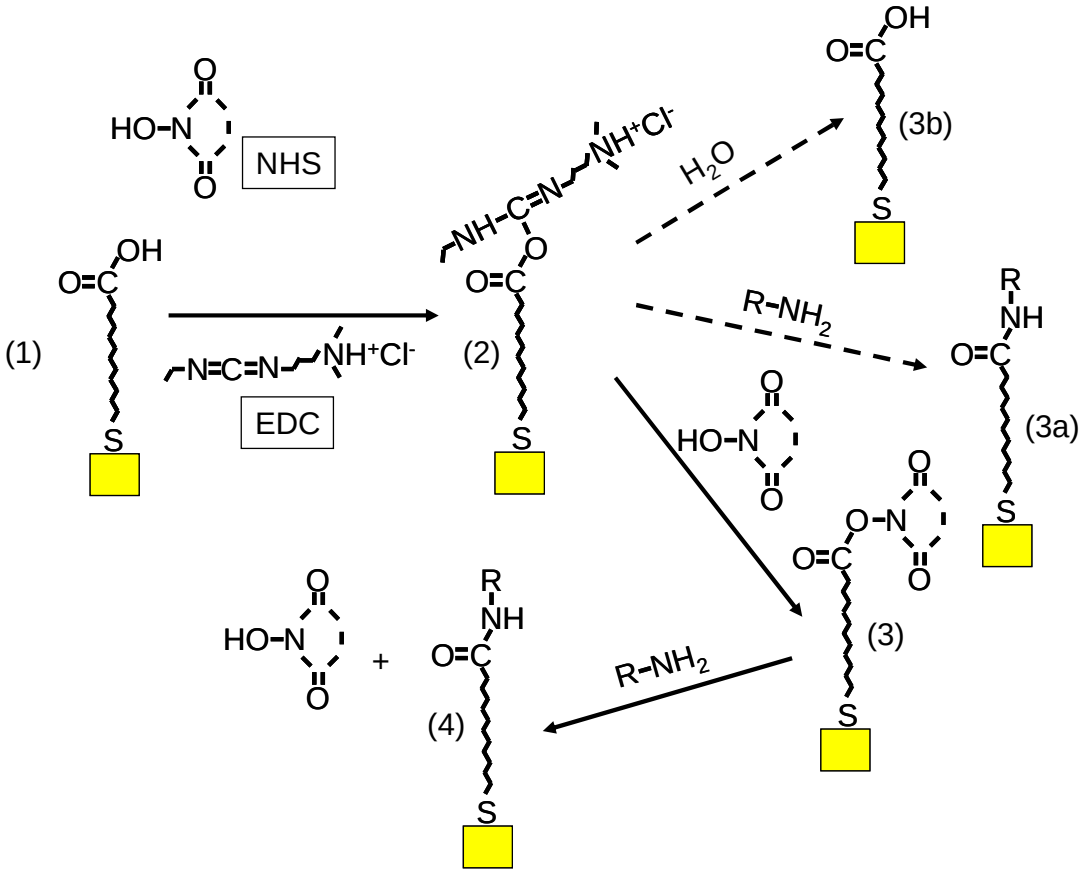

Figure 6.16-Possible EDC/NHS reaction pathways for binding to a carboxy group

As a consequence of still unsolved problem of primary protein attachment via EDC/NHS chemistry, the antibody coverage yield is unacceptably low. Additionally, the reproducibility of the EDC/NHS binding reaction is high, but the following step is typically very unpredictable, with around 50% probability of reaction failure. The observed shifts for relatively large concentrations (500-1000 µg/ml) are from undetectable to less than 1 nm. The expected shifts for very similar system of gold nanodisks are of 3-4 nm for 1-2 orders of magnitude lower concentrations of antibody [Chen et al. 2009]. The different ratios of EDC : NHS were tested using real-time LSPR as well as other methods. However, ratio tuning so far didn't improve the reaction yield. It is assumed that the fast decay of NHS-ester actually points to the failed NHS-ester formation, and that fast decay is actually due to EDC-compound desorption (2). The half-life of EDC-ester reported in the literature is similar to the decay time we observe. However, separation of the two reaction steps didn't help solving the problem, neither. EDC coupling to carboxyl-

functionalized sensor's surface produces observable shift, while successive NHS is difficult to trace, since the molecular mass exchange is very low to clearly detect formation of NHS-ester.

The first results obtained using large SH-PEG-COOH (4 kDa) and EDC/NHS showed that performance of EDC/NHS didn't influenced the observed LSPR shifts upon the successive cycles of protein injections. These results suggest that here employed PEG layer is badly formed (since there was still resonant shift upon the exposure of Rb IgG to inactive –COOH PEG layer which is supposed to show considerable repelling feature (Fig. 6.17 (b))).

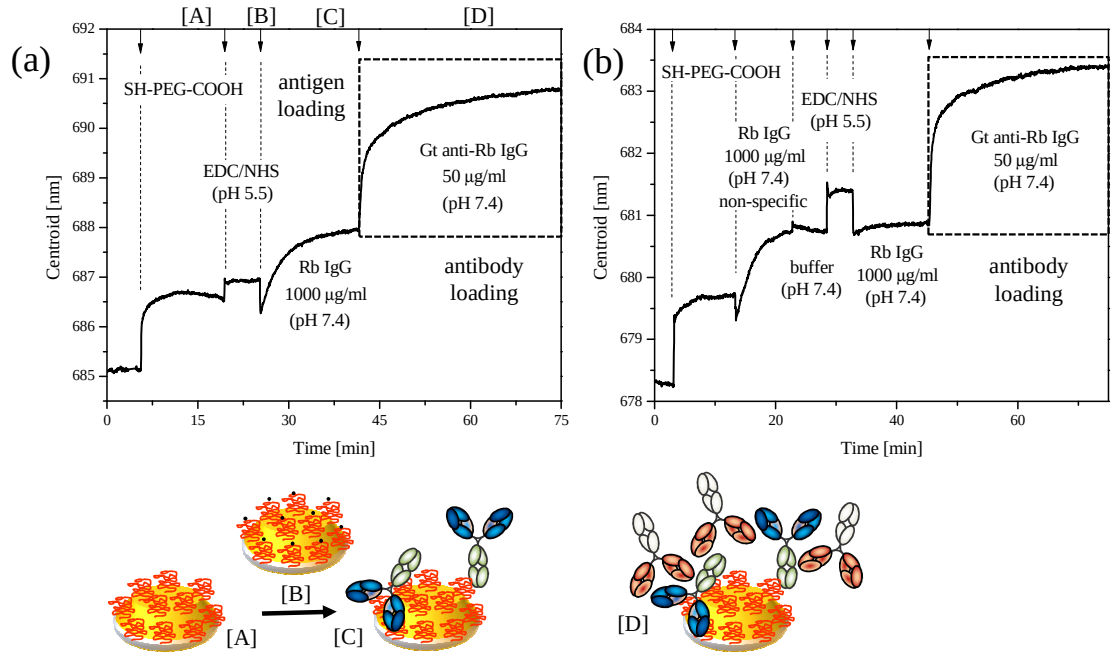

Figure 6.17-LSPR real-time tracking for surface chemistry protocol based on EDC/NHS for sensor preparation with final antibody detection. (a) The bad formation of PEG layer followed by badly conditioned activation (EDC/NHS) reaction. The sensor response to antigen and antibody is very similar to the response on untreated surface (b) The exchange order of antigen and activation steps reveals that chosen PEG layer is badly formed (not repelling proteins). Note that in both cases high-affinity reaction between physisorbed antigen (huge conc.) and freely moving antibody (low conc.) provokes relatively large resonance shift, regardless that fact that shift due to physisorption into higher sensitivity region of much higher bulk conc. of antigen provoked smaller shift. Arrows indicate the time instance of new liquid injection.

As such, all of the detected shifts originated from direct nonspecific (electro-static) binding of proteins into defects (gaps) within the formed PEG layers, yielding very similar to results presented in Fig. 6.9 in the absence of any coating.

Model antibody-antigen system consists of rabbit IgG (polyclonal, purified) as biorecognition, while goat anti-rabbit IgG (unpurified, monoclonal) is used as antigen, and vice versa. As a rule, binding of freely moving antibody to immobilized antigen induces maximum response. Binding of freely moving antigen to amino-coupled antibody is indicated by a typically smaller response than in the previous case, which

is expected due to random binding orientation of antibody to activated SAM (and/or due to unpurified Gt anti-Rb IgG stock). Such random orientation of antibody results in a blockage of some paratope sites of surface immobilized species. Additionally, by introducing successively cycles of antigen and antibodies, the occupied portion of sensing volume can be assessed (indicating the obtained protein surface coverage). Considering the size of antibodies used and typical LSPR detection volume, the second protein layer should occupy less sensitive volume. If the third and other cycles provide even lower shifts that would clearly indicate the homogeneity of formed layers in terms of surface coverage and packing density.

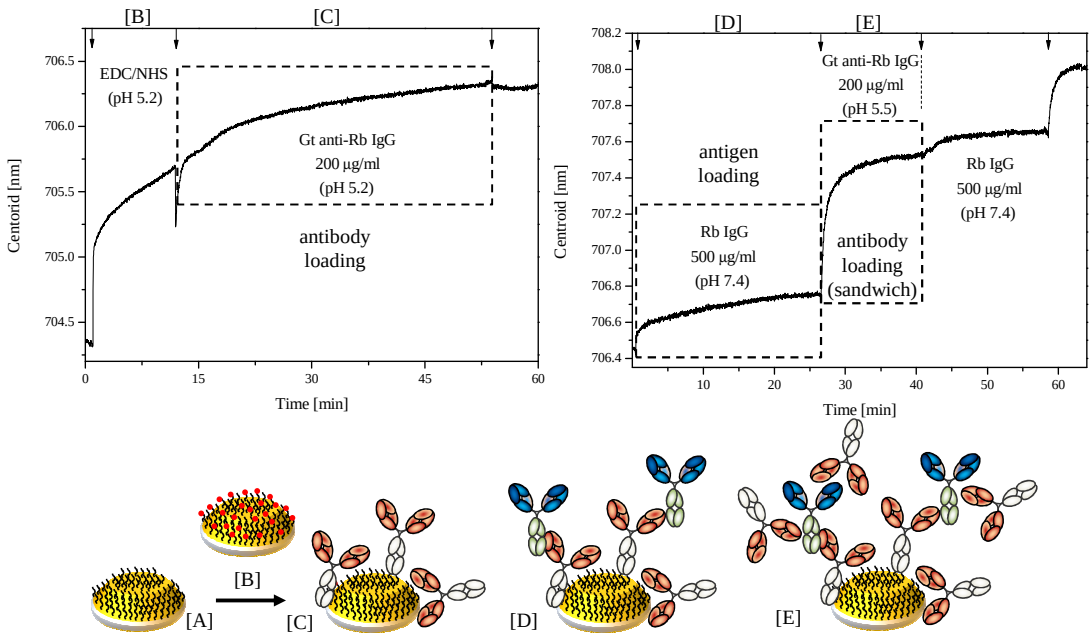

Figure 6.18-EDC/NHS surface protocol sequences and corresponding LSPR real-time response. (a) The injection of antibodies in pH 5.5 immediately after EDC/NHS activation, doesn't favor amine to NHS-ester reaction (faster in pH 7.4), but NHS-ester doesn't desorb in pH 5.5. (b) Injection of antibody, followed by additional cycles of antigen injection (sandwich assay) and antibody, demonstrating the sensing volume saturation and difference between binding of antigen vs. binding of antibody. Arrows indicate the time instance of new liquid injection.

The LSPR centroid evolution for the case of antibody immobilization at lower pH=5.5 (compatible with NHS-esters) but less favorable to amino-NHS-ester coupling, are displayed at Fig. 6.18. The amount of immobilized antibodies are once again lower, similarly to pH=7.4 cases when there is visible shift upon exposure to antibody solution. As stated before, the origin of such a low coupling is still under investigation.

6.4.4.3. Modified antibodies immobilization

The EDC/NHS activation of carboxylated surfaces can be avoided through different antibody-conjugation strategies. One tested here was based on traut's reaction that exchanges amine to thiol functionality of the pre-coated gold surface. If cross-linked with particular linkers, antibodies can be attached to such thiolated surfaces.

The linker used for antibody modification is Succinimidyl-4-(*N*-maleimidomethyl) cyclohexane-1-carboxylate (SMCC), which couples to scattered amine moieties of IgGs at standard pH=7.4 and forms stable bond. Such modified antibodies expose maleimide groups that react with thiols on the gold surface, thus form very stable thioeter bond.

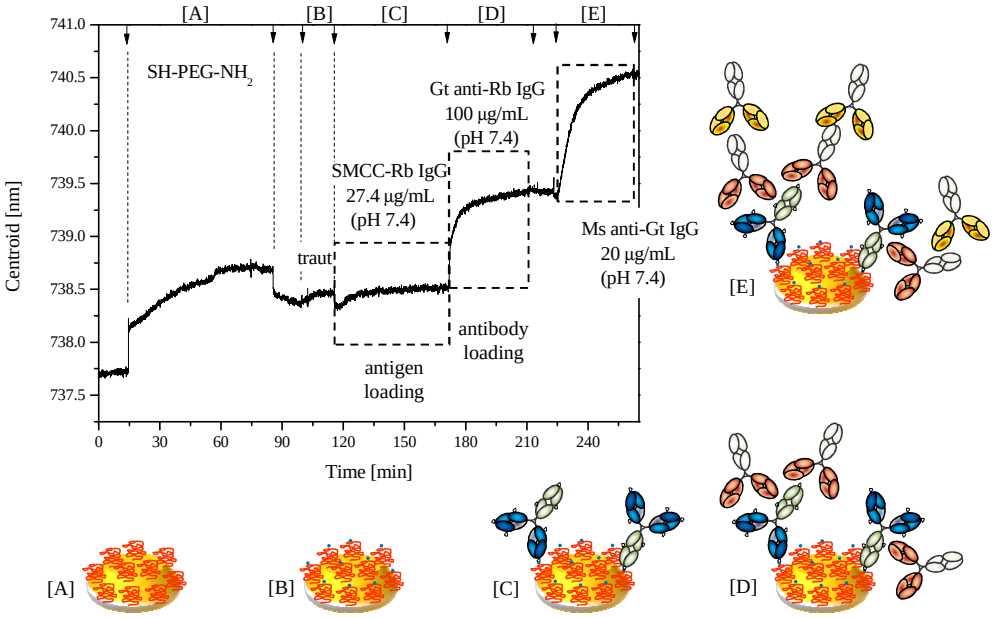

Figure 6.19-LSPR real-time tracking for surface chemistry protocol based on traut reaction and modified antibodies. Traut reaction exchanges amine to thiol functionality of PEG layer. Immediately after, SMCC-conjugated antibodies are injected, followed by two cycles of antigen-antibody reactions. Note that for this particular case modified antigen didn't disturb the epitopes sites for the subsequent antibody reaction. Sketch shows immobilization of SMCC-modified antibody onto thiol-expressing surface. The linker positions are typically scattered all over the antibody, however the amount of attached SMCCs can be controlled, but not the location. Arrows indicate the time instance of new liquid injection.

Fig. 6.19 plots real-time LSPR tracking during the protocol that employs traut's modification and conjugated SMCC antibodies. SH-PEG-NH_2 layer is formed prior to the traut reaction that exchanges –NH_2 into –SH functionality (the quality of PEG layer can also be questioned, since the protocol was abandoned before more detailed investigation). An alternative to amino-PEG and traut's reaction can be the usage of di-thiol PEGs, but for large molecular weight molecules there is a possibility of double anchoring to gold surface. Immediately, after the traut reaction is accomplished, SMCC-conjugated Rb IgG is injected, resulting in relatively low antibody attachment, similar to results obtained with EDC/NHS

(Fig. 6.18), however here an order of magnitude lower concentration of antibody was employed. The sensing volume under this concentration of antibody was far from saturated, as demonstrated by the successive antigen-antibody high-affinity reactions between immobilized SMCC-Rb IgG and Gt anti-Rb IgG. Additional injection of antibody specific to Gt anti-Rb IgG resulted in once again fast binding kinetics of mouse anti-Gt IgG to immobilized Gt anti-Rb IgGs.

6.4.4.4. Biotin-Streptavidin reaction

The previous examples possibly infer that the efficient attachment of antibodies onto sensing surface requires or high antibody concentration or high-affinity reactions. The high-concentration of biorecognition antibodies may introduce flow problems due to increased viscosity as well as low cost-efficiency. If there is a problem with stability of surface chemistry for anchoring of antibodies (as in our case with EDC/NHS), it was expected that the injection of high-concentration of antibodies under higher-flow velocities will improve the reaction yield, but this was not the case. To try to overcome such problems, the high-affinity biotin-streptavidin system was used as a very popular strategy in surface modification of biosensing surfaces. Namely, protein avidin possesses the highest known affinity toward biotin binding among any high-affinity constituents. The biotin can bind up to 4 binding sites of avidin, and additionally due to its small size, finds the application as linker of various proteins (process of biotinylation), since it typically doesn't affect protein's function. The high isoelectric point of avidin (ca. 10) makes it positively charged in typical buffers, like PBS (pH=7.4) and as such very prone to nonspecific binding to negatively charged glass surfaces. Recombinant streptavidin has lowered isoelectric point of 5.8-7.6, but slightly lowered affinity than avidin and lower solubility. The newest generation Neutravidin or Extravidin combines advantages of both avidin (high affinity, low cost production) and streptavidin (lower nonspecific binding).

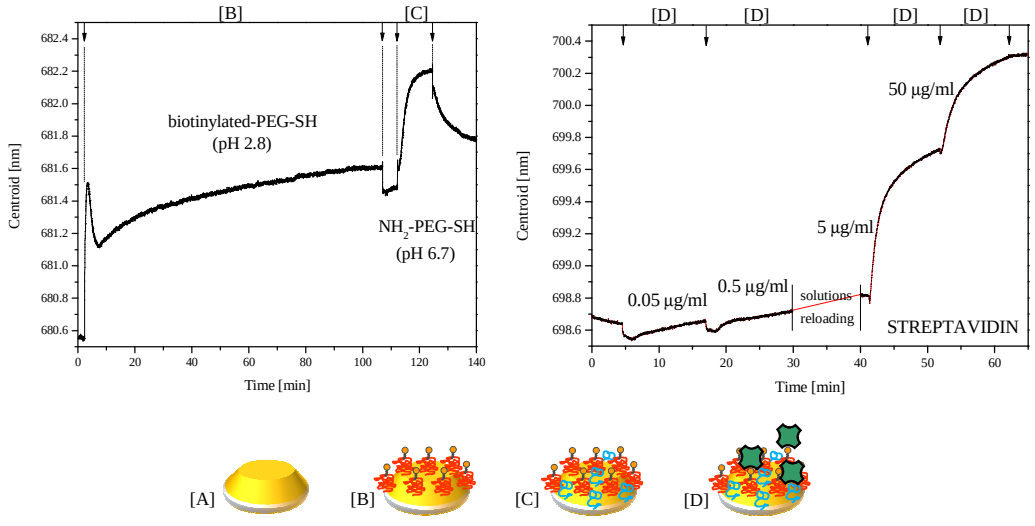

Figure 6.20-LSPR real-time tracking for surface chemistry protocol based on biotin-streptavidin high-affinity system. (a) Sensor surface is pre- coated with biotinylated thiol-PEG, followed by smaller thiol-PEG with amino functionality. (b) Binding kinetics of different streptavidin concentrations injected onto biotinylated nanoparticles. Red curve connects two measurements (the brake is due to solution replacing and inlets priming). Arrows indicate the time instance of new liquid injection.

The typical antibody binding sequence using biotin-streptavidin (Fig. 6.20 and Fig. 6.21) in SPR or LSPR systems starts with the immobilization of biotinylated -PEG-SH (Fig. 7.20 [B]), which is commercially available. The layer is typically mixed with smaller non-biotinylated SH-PEG-OCH_3 that spreads away streptavidin binding sites depending on the ratio of the two molecules Fig. 6.20 [C]). Figure 6.20 ([B]) displays LSPR centroid shift due to binding of 5 mM solution of biotinylated-thiol-PEG (Prochimia, Poland) at pH 2.8. This pH has given the best binding, among the tested pHs of 10 and 6.4. Following the biotinylated-PEG binding, smaller SH-PEG-NH_2 was injected to fill up any available space. The small observed shift points to the some binding of the amino-PEG, although longer exposure of biotinylated-PEG would result in better layer formation. Figure 6.20 [D] displays centroid real-time scan during the few injection cycles of increased concentration of streptavidin, starting at 0.83 nM, followed by 8.3 nM, 83 nM and 830 nM (calculated for streptavidin molecular weight of 60 kDa). The intermediate step between [C] and [D] (Fig. 6.20) was the flow cycle of PLL-g-PEG for the substrate passivation (data not shown)). Spreading biotin sites by mixing biotinylated -PEG with inactive one can produce more uniform coatings which benefit for the subsequent steps [Feuz et al. 2010].

The biotinylated Gt anti-Rb IgG (polyclonal) can be locally modified with biotin at Fc region via coupling to polysaccharide moieties that may guarantee proper antibody orientation upon surface immobilization. However, the conjugate supplying company didn't share information about biotinylation procedure, thus we suspect that the biotinylation is done through amino coupling (due to relatively low product price). Injected 1:20 dilution of original antibody stock obtained from Sigma-Aldrich (Spain), displayed reasonably fast kinetics, reaching quickly the equilibrium state. Since pure deionized water was used to rinse loosely bound molecules, successive curve of antigen recognition looks unusual, due to higher refractive index of water than the protein solutions. The total shift for the injection of 50µg/ml of antigen (Rb IgG) is marked as vertical difference between two red spots in Fig. 6.21.

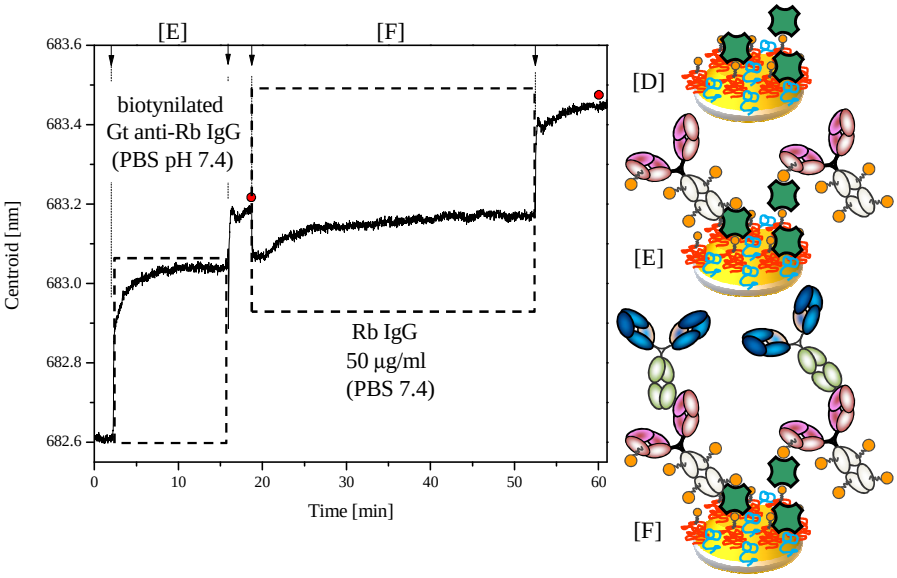

Figure 6.21-LSPR real-time tracking for biotinylated antibody immobilization to streptavidin rich surface, followed by injection of particular antigen. Arrows indicate the time instance of new liquid injection.

6.5. Conclusion and future work

Obviously, for each of the SFPs discussed, there is no expected outcome reported in this document – a calibrated sensing response of centroid shift as function of analyte concentration. To foresee how close we are is also difficult. None of the protocols worked sufficiently well, which is verified by very small observable shifts upon antibody immobilization. The primary gold surface functionalization is still not optimized, and the extensive work is in the process during the thesis submission. The other bottleneck is surely the inefficient antibody immobilization step, where relatively low surface coverage is obtained, in comparison to the expected values [Chen et al. 2009]. The surface volume is typically only partially occupied for the cases shown in previous figures, which is verified by measuring BRIS before and after the antigen binding step. Usually, drop in the BRIS value is very low (few %).

6.5.1. The comparison of three SFPs

To summarize, EDC/NHS strategy, although being well documented in literature, didn't provide the expected result so far. The biggest issue was actual instability of formed active NHS-ester (or EDC-ester) reflected as the fast hydrolysis back to –COOH functionality (in the working pH=7.4), orders of magnitude faster than reported in product sheets [Thermo scientific, USA; Sigma-Aldrich, Spain]. As such, the efficient coupling of amines to NHS-ester is in strong competition with NHS-ester decay. As the usual outcome, the formation of biorecognition layer was quite poor (produced shift is orders of magnitude lower than reported with similar systems) and not always reproducible. Even if we solve the problem of EDC/NHS coupling of antibodies to the sensor surface, the random orientation of immobilized antibodies may reduce the sensitivity (However, it will depend on biologically relevant minimal concentration of particular analyte that is to be detected). Additionally, this strategy is poorly compatible with electrostatic passivation protocols (BSA, PLL-*g*-PEG), therefore implying covalent passivation protocols with silanes. This in turn significantly increases the complexity of the protocol stages and its condition control. Yet, as a good side, direct attachment of antibodies via EDC/NHS keeps antibody closer to the surface, leaving more sensing volume available for successive antigen detection, and doesn't interfere with the immunoreactivity.

The protocol related to the traut reaction and SMCC-antibody conjugation shares majority of drawbacks characteristic to EDC/NHS. The only clear advantage is very stable SH-SAMs (after traut reaction) as well as stable antibody-SMCC conjugates. Similarly to EDC/NHS, it is not compatible with electrostatic passivation. Conjugation of antibodies involves additional labeling-like step (or additional cost), and control of cross-linked antibody concentration is very tedious. Since SMCC to antibody crosslinking is also performed via coupling to scattered amino moieties throughout the antibody surface it is possible that linker molecules (although being really small) can interfere with paratope sites. The degree of the immune-reactivity of SMCC-antibody complex is difficult to assess, however it didn't interfere with epitope sites of conjugated SMCC-Rb IgG, since the successive binding of Gt anti-Rb IgG displayed expected fast binding kinetics (Fig. 6.19).

For the both protocols, the amount of immobilized biorecognition is insufficient, which is verified by few cascade antibody reactions (Fig. 6.18 (b) and Fig. 6.19).

The biotin-streptavidin protocol relies on the highest-affinity reactions known for the sensor functionalization. Biotinylated products are commercially available, while the streptavidin-biotin is featured with very fast kinetics. Moreover it is fully compatible with PLL-g-PEG or BSA substrate passivation, and biotinylated polyclonal antibodies (through polysacharide coupling) don't suffer orientation problems. However, the biotinylation process is kept secret, therefore the orientation problems may still be present. Additionally, streptavidin layer occupies significant portion of sensing volume, thus lowering the resonance shift upon antigen binding.

6.5.2. Detection of antibodies vs. detection of antigens

Although analyte species can be various types of biomolecules, I will restrict the discussion onto proteins (antigens) and antibodies. By browsing the LSPR biosensing literature, the first noticeable fact is that ratio of antibody detection systems vs. antigen detecting systems is highly asymmetric in favor of antibody detection.

The antibody detection assays are important part of blood test analyzes in medicine, since the antibody concentration (especially if considered over larger time period) can reveal the on-going or previous exposure to particular antigens (foreign substances) and the actual stage in the phase of antigen eradication by adaptive mechanisms of immune system. On the other side, if the analyte is host (endogenous) species, normally healthy host organism will not launch the immune response, as in the case of some bio-markers. However, although the HSPs are endogenous proteins, they are normally confined only within the healthy cell. In the various stages of cancer development, the HSP may be present in the body fluids, which is considered not normal and induces the immune response, resulting in antibody production. The relevant concentrations of antibodies and HSPs are still under debate [Seigneuric et al. 2011], making uncertain if they possess universal cancer marker property and the detection pathways (antigen or antibody).

Thus when detecting antibody, biorecognition is antigen coating, while in the opposite case, biorecognition is antibody. Formerly, in case of multiple epitopes on antigen or polyclonal antibody detection, antigen orientation is irrelevant, and together with freely moving antibody, sensor response is larger, that in the previous case, where antibody coating formation is crucial (orientation and taken conformation upon surface immobilization).

As consequence, instead of direct detection assay, a competition style assay may increase the sensitivity, at the expense of reagent costs/consumption and increased assay's complexity.

6.5.3. Monoclonal vs. polyclonal antibodies

Monoclonal antibodies are typically selected from polyclonal mixture as one with the highest expressed affinity. As such, the will guarantee higher sensitivity over the polyclonal coatings. Regarding our IgG models the difficulty comes from the fact that both antigen and antibodies are polyclonal, making really complicated the binding analysis. Beside the cost, monoclonal antibodies lack of polysaccharide moieties at Fc region, preventing the site-specific biotinylation antibody strategy.

6.5.4. Smaller biorecognition

A smaller biorecognition would clearly boost the sensitivity due to lower occupation of the sensing volume. As potential candidates, the different sections of cleaved monoclonal antibodies may be employed [Yoshimoto et al. 2010] or a relatively new class of recombinant short polypeptide chains, called aptamers [Balamurugan et al. 2006, 2008]. The antibody cleaving and immobilization with the immune-reactivity loss typically represents the important obstacles to be surpassed, while the aptamers display less affinity than antibodies. Aptamer surface immobilization can further on affect its immunoreactivity.

Some of these strategies are being considered in line with the protocols described previously.

6.5.5. LSPR sensing range increase

For the real label-free assays, the evanescent field around nanoparticles might be too confined, at least for the biotin-streptavidin SFPs. As such, SPR still represents possibly better solution for immune-assays based on antibody-antigen reactions. Typically, isolated or far-field coupled nanoparticle systems that display higher BRIS are considered to have larger sensing range. As such, the periodicity induced Fano resonant modes (chapter 5) may be one of the routs toward more sensitive LSPR systems.

6.6. Conclusions and future aspects

The first question that arises after a quick look at this chapter is where are the sensograms, i.e. is there a report of calibrated sensor's response. Unfortunately, apart of Fig. 6.20 which can be understood as somehow calibrated response upon streptavidin detection, at this stage, I was not able to obtain any. The reasons clearly lay in the complexity of the adoption of the ideal surface functionalization protocols to this new type of LSPR LOC device.

There are many obstacles that have to be passed before having working bio-sensor based on nanoparticle arrays interfaced with PDMS microfluidics. At first, all three of passivation levels have to be addressed, which is not easy task at all. Three coexisting, essentially very different surfaces have to be modified to express particular chemical functionality or total inertness toward various biomolecules, and as especially limiting factor the modification protocol has to be compatible with LOC manufacturing

protocols. While gold and glass are somewhat robust, PDMS is challenging since it dissolves various compounds (toluene, alchocols, etc.) making it swell and can be degraded with moderate exposures to acidic and basic solutions. Additionally, although PDMS and glass have low isoelectric points, these are very different in terms of hydrophilicity/hydrophobicity. The studies of protein nonspecific adsorption typically don't give general answers to the nature and extent of such interactions. The general conclusion is that the contribution of various forces to the strength of protein-surface interaction is unpredictable, thus not allowing for any general and straight-forward way of quickly dealing with passivation of microfluidic inner walls. As such, possibly the different but compatible strategies have to be develop to address PDMS and glass passivation.

Secondly, the choice and optimization of antibody immobilization strategy is also challenging. Starting with increasing the surface density of antibodies alone would eventually bring the question of the availabilities of recognition sites due to uncontrolled/controlled orientation. Additionally, use of linkers may reduce immunoreactivity. Reduced antibodies can come with interesting immobilization through thiol residues, however the immunoreactivity together with lasting stability of immobilized fragment has to be verified.

And, finally, if the displayed sensitivity of the sensor (and SFP) doesn't overlap with analyte's relevant concentration, the whole approach has to be remodified. A serious issue may be performance of the system with whole-blood matrix where some additional functionality should be implemented in the device operation like pre-concentrating and purifying chamber [Stern et al. 2010].

The work addressing all of these issues is ongoing in the time of thesis submission.

Conclusions

The work reported in this thesis extends current understanding and applications of Localised Surface Plasmon Resonance for biosensing in lab-on-a-chip format. Attractiveness of such approach and motivation for pushing it toward the real-life applications owes to the unique properties of metallic nanoparticles, not expressed by the leading technique in the field, Surface Plasmon Resonance. Recent reports have induced the LSPR development further on by demonstrating similar levels of sensitivity for both methods [Svedendahl et al. 2009], where in addition, LSPR may introduce distinctive advantages that are discussed within Chapter 1. The benefit of nanoparticle concept is directly related to deep-sub-wavelength light confinement that is responsible for strong light-matter interaction, especially with biomolecules (due to similar spatial occurrence). In comparison to arrays of non-interacting nanoparticles, closely-interacting nanoparticle pair (known as dimers) confines light even-stronger to even-smaller areas contained within the space between them. Albeit it was proposed theoretically a decade ago, the experimental realization of closely-coupled nanoparticle pairs was prohibited by serious nanofabrication limitations. A novel and optimized nano-fabrication method introduced in Chapter 2 allows for a highly homogeneous production of nanoparticle systems, surpassing the current state-of-the-art. Since dimer optical properties exponentially depend on actual gap size, determination of obtain nanoparticle parameters such as gap and sizes is important. Widely used technique uses cumbersome statistical analysis of the collection of high resolution scanning electron microscopy images. A novel Spectral Evolution Method based on optical interrogation of averaged nanoparticle response retreats the required geometry parameters very quickly thus enabling extremely fast quality screening control of fabricated structures, as described in Chapter 3. The first ever experimental demonstration of dimer configuration employed for biosensing (Chapter 4.) confirms the theoretical predictions of exceptional sensitivity [Enoch et al. 2004, Jain et al. 2007], however sheds new light onto the importance of MAO engineering. As a consequence of direct relation between sensitivity (as dependent on gap size) and a size of an analyzed molecule, the dimer systems can act as static plasmon-ruler sensors for analyte bulk concentration and its conformational averaged size [Aćimović et al, 2009]. However, improved but yet limited fabrication precision yields somewhat broad resonances that reduce maximum signal-to-noise ratio (SNR), as shown by [Dahlin et al. 2006, Feuz et al. 2012]. As one of the routes for resonance narrowing, the far-field interaction between nanoparticles consisting array is investigated in Chapter 5. A set of parameters that influence such resonance narrowing are investigated, and various practical implementations that can induce 20-25 nm narrow resonance are discussed in the frame of LSPR biosensing. These narrow peaks certainly will contribute to larger SNRs and the feasibility of combining previously introduced far-field interaction approaches with near-field interacting dimers is demonstrated.

On the other hand, transferring and applying all this knowledge for the real-life application goes much beyond of the realization of any LSPR device proposed so far. Many of reported devices doesn't go further than detection of model-systems such as biotin-streptavidin, or are not properly interfaced for large-scale fabrication. The development stages of inhere proposed close-box LSPR device are in the finishing stage, except the core of the system, i.e. the surface functionalization protocols. All of the steps

of the development are covered throughout this document, starting with microfluidic chip design and fabrication, sensing substrate patterning and LOC device assembly that is covered mainly in the introducing sections of Chapter 6. The optical setup is based on a simple home-made bright-field microscope operating in transmission with a spectrometer and a camera for the sample navigation [Dahlin et al. 2006, 2009]. The most important component of the setup turns out to be the stage and its mechanical stability. (We found that commercial microscopes not equipped with micrometer stages are not the best choice, due to fast wear-off of the stage control that may results in slow drifts. This drift (in sample plane, or focus) may result in output baseline drifts, with time constant similar to molecule kinetics.) Nanoparticle substrates are interfaced with an active multiplexed microfluidic networks (Chapter 3.) allowing for highly-miniaturized and parallel operation in analyte detection [Thorsen et al. 2002]. The microfluidic control hardware consists of various tubes, pressure gauges, mechanical valves, and compressed air sources. Depending on the external pressure valve control (manual or solenoid), the chip operation can be manually or PC controlled. The system shown in Fig. C.1 has built-in manual control of microfluidic integrated valves (A), stable micrometer stage (B) and flow pressure control (C). The inset shows mounted and operational LOC LSPR devise.

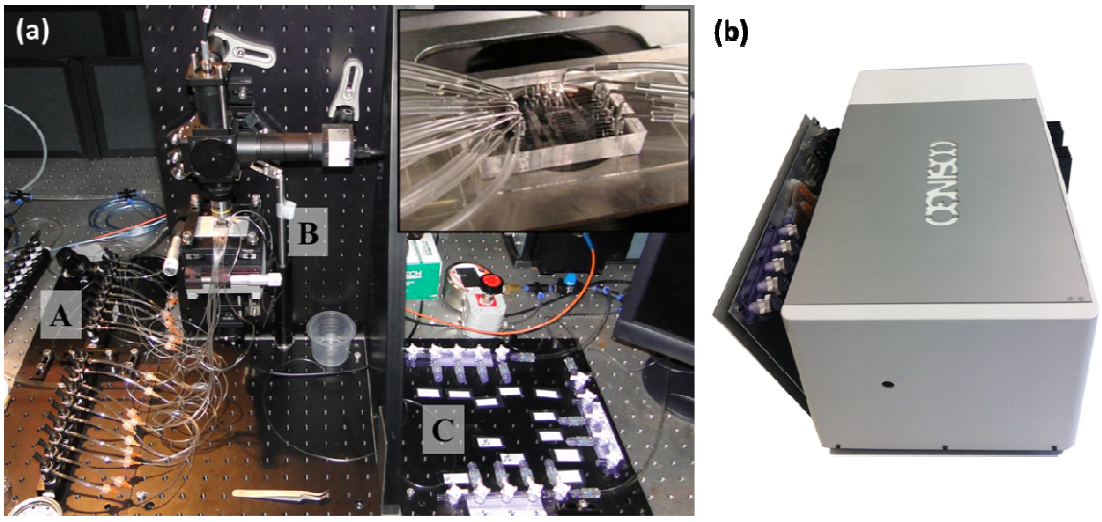

Figure C.1-(a) Home-made real-time LSPR opto-microfluidic platform: manual microfluidic network control (A), micrometer stage with mounted LOC devise (B) and (C) flow control. Inset shows mounted LOC only. (b) In-the-box opto-microfluidic LSPR platform (prototype). Courtesy of Rafael Porcar, COSINGO-Imagine Optics Spain SL.

A fully-operational and automatic (PC controlled) portable system (Fig. C.1 (b)) has been developed by our SPEDOC partner COSINGO (www.cosingo.com). As important extra functionality, all chip operational functions (as described previously) are programmable. Additionally, parallel real-time monitoring of multiple independent sensors (together with the reference sampling) further increases the device-throughput and reliability.

Finally, I expect that in-the-box system may find its place on the market, in various packages: the opto-microfluidic control platform alone (without chip), with the sensing chip included (for protocol

development), or the full package (platform, chip and protocols). The first package may be interesting to science research centers; the second upgrade may be attractive to pharmaceutical companies, while the full package can be standard equipment of analytical laboratories or health centers. However, there is still a great amount of work ahead to obtain the full package, and is mainly limited to current stage in the surface functionalization protocols development that should provide sensor with sensitivity, stability, reproducibility and repeatability and software optimization. The potential flexibility to adopt system to a different relevant proteins and biomolecules, necessitates consideration of various functionalization strategies in sensor preparation, apart from passivation which should be standard as well as primary surface modification (to some extent). The choice and modifications of receptor layers, as well as determination of relevant analyte concentrations, requires additional synergy with various disciplines such as molecular biology, immunology and finally, applied medicine.

APPENDIX

Derivation of dispersion relation for SPP

We will directly look for bound solutions of Maxwell's equation on the interface between two materials. Derived equations will describe conditions that have to be full field in order to allow existence of such inhomogeneous waves.

Let's assume that plane of incidence lays is xz plane, and interface between two materials is in xy plane. Materials are characterized with relative permitivities ξ_- (z<0) and ξ_+ (z>0). First we will deal with TM polarization with time dependence convention $e^{-j\omega t}$. Thus general TM wave is described by it's magnetic field vector

$$H = (0, H_0, 0)e^{-j(\omega t - k_x x - k_z z)} \qquad \text{(A.1)}$$

where for waves bounded to the interface k_z has to be purely imaginary to provide no field components in infinity. Thus if we agree that k_z^-, k_z^+ >0 , magnetic field is described as

$$H^{\pm} = (0, -H_0, 0)e^{-j(\omega t - k_x x)}e^{\mp k_z^{\pm} z}. \qquad \text{(A.2)}$$

Maxwell's equations $\nabla \times E = -\frac{\partial B}{\partial t}$ and $\nabla \times H = \frac{\partial D}{\partial t}$ become

$$\left(\frac{\partial E_z}{\partial y}, \frac{\partial E_z}{\partial x} - \frac{\partial E_x}{\partial z}, -\frac{\partial E_x}{\partial y}\right) = j\mu_0\omega(0, -H_0, 0)e^{-j(\omega t - k_x x)}e^{\mp k_z^{\pm} z} \qquad \text{(A.3)}$$

$$\left(-\frac{\partial H_y}{\partial z}, 0, -\frac{\partial H_y}{\partial x}\right) = j\omega\xi_0\xi_{\pm}(E_x, 0, E_z) \qquad \text{(A.4)}$$

From (4) we obtain components of electric field as

$$-\frac{\partial H_y}{\partial z} = \pm k_z^{\pm} H_0 e^{-j(\omega t - k_x x)}e^{\mp k_z^{\pm} z} = \xi_0\xi_{\pm}E_x \qquad \text{(A.5)}$$

$$\frac{\partial H_y}{\partial x} = jk_x H_0 e^{-j(\omega t - k_x x)}e^{\mp k_z^{\pm} z} = \xi_0\xi_{\pm}E_z \qquad \text{(A.6)}$$

Continuity of tangential components of H_y, E_x is already satisfied, while continuity of normal components of electric displacement vector gives:

$$\xi_- E_z(0^-) = \xi_+ E_z(0^+) \qquad \text{(A.7)}$$

By combining (A.6) and (A.7) we get equality

$$\frac{k_z^+}{\xi_+} + \frac{k_z^-}{\xi_-} = 0 \qquad \text{(A.8)}$$

From (A.5) and (A.6) we obtain

$$E_x = \pm \frac{k_z^{\pm} H_0 e^{-j(\omega t - k_x x)} e^{\mp k_z^{\pm} z}}{j\omega \xi_0 \xi_{\pm}} \qquad \text{(A.9)}$$

$$E_z = \frac{j k_x H_0 e^{-j(\omega t - k_x x)} e^{\mp k_z^{\pm} z}}{j\omega \xi_0 \xi_{\pm}} \qquad \text{(A.10)}$$

Substituting (A.9) and (A.10) into (3) we get

$$k_z^{\pm} = \sqrt{k_x^2 - k_0^2 \xi_{\pm}} \qquad \text{(A.11)}$$

Finally, substituting (A.11) into (8) yields

$$k_x = \frac{\omega}{c} \sqrt{\frac{\xi_+ \xi_-}{\xi_+ + \xi_-}} \qquad \text{(A.12)}$$

For TE polarization, electric field vector is

$$E^{\pm} = (0, E_0, 0) e^{-j(\omega t - k_x x)} e^{\mp k_z^{\pm} z} \qquad \text{(A.13)}$$

Maxwell´s equation with curl operator give similar to the previous case relation between magnetic and electric field as:

$$-\frac{\partial E_y}{\partial z} = \pm j k_z^{\pm} E_0 e^{-j(\omega t - k_x x)} e^{\mp k_z^{\pm} z} = -j\mu_0 \omega H_x \qquad \text{(A.14)}$$

$$\frac{\partial E_y}{\partial x} = -j k_x E_0 e^{-j(\omega t - k_x x)} e^{\mp k_z^{\pm} z} = j\mu_0 \omega H_z \qquad \text{(A.15)}$$

Continuity of tangential components of magnetic field ($H_x(0^-) = H_x(0^+)$) yields

$$E_0(k_z^+ + k_z^-) = 0 \quad \text{(A.16)}$$

Since we assumed k_z^- , k_z^+ >0, equation (A.13) stands only for E_0 =0.

Thus, SPP can exists only as TM inhomogeneous wave.

Bibliography

Abbas, A. K. & Lichtman, A. H. (2006). *Basic Immunology: Functions and disorders of immune system*. Philadelphia: Saunders Elsevier.

Aćimović, S. S. (2011). Introduction to nanoparticle characterization in COMSOL. from http://srdjancomsol.weebly.com

Aćimović, S. S., Kreuzer, M. P., González, M. U., & Quidant, R. (2009). Plasmon Near-Field Coupling in Metal Dimers as a Step toward Single-Molecule Sensing. *ACS Nano, 3*(5), 1231-1237.

Aćimović, S. S., Kreuzer, M. P., & Quidant, R. (in production). Engineering through mode shaping and lithographical nanofabrication of ultrasensitive nano-plasmonic sensors for molecular detection. In A. Dmitriev (Ed.), *Nanoplasmonic Sensors*. New York: Springer.

Aizpurua, J., Hanarp, P., Sutherland, D. S., Käll, M., Bryant, G. W., & García de Abajo, F. J. (2003). Optical Properties of Gold Nanorings. *Physical Review Letters, 90*(5), 057401.

Albrecht, M. G., & Creighton, J. A. (1977). Anomalously intense Raman spectra of pyridine at a silver electrode. *Journal of the American Chemical Society, 99*(15), 5215-5217.

Ament, I., Prasad, J., Henkel, A., Schmachtel, S., & Sönnichsen, C. (2012). Single Unlabeled Protein Detection on Individual Plasmonic Nanoparticles. *Nano Letters, 12*(2), 1092-1095.

Anderson, G. P., & Taitt, C. R. (2008). Evanescent wave fiber optic biosensors. In F. S. Ligrer & C. R. Taitt (Eds.), *Optical biosensors: Today and tomorrow*. Amsterdam, The Nederlands: Elsevier.

Andrew, M. C., David, A. C.-Y., & Bruce, K. G. (2005). Characterization of interconnects used in PDMS microfluidic systems. *Journal of Micromechanics and Microengineering, 15*(5), 928.

Anker, J. N., Hall, W. P., Lyandres, O., Shah, N. C., Zhao, J., & Van Duyne, R. P. (2008). Biosensing with plasmonic nanosensors. [10.1038/nmat2162]. *Nat Mater, 7*(6), 442-453.

Atay, T., Song, J.-H., & Nurmikko, A. V. (2004). Strongly Interacting Plasmon Nanoparticle Pairs: From Dipole−Dipole Interaction to Conductively Coupled Regime. *Nano Letters, 4*(9), 1627-1631.

Atwater, H. A., & Polman, A. (2010). Plasmonics for improved photovoltaic devices. [10.1038/nmat2629]. *Nat Mater, 9*(3), 205-213.

Auguié, B. (2009). *Optical properties of gold nanostructures.* University of Exeter, Exeter, United Kingdom.

Auguié, B., & Barnes, W. L. (2008). Collective Resonances in Gold Nanoparticle Arrays. *Physical Review Letters, 101*(14), 143902.

Auguié, B., Bendaña, X. M., Barnes, W. L., & García de Abajo, F. J. (2010). Diffractive arrays of gold nanoparticles near an interface: Critical role of the substrate. *Physical Review B, 82*(15), 155447.

Axelrod, D. (2001). Total Internal Reflection Fluorescence Microscopy in Cell Biology. *Traffic, 2*(11), 764-774.

Balamurugan, S., Obubuafo, A., Soper, S., & Spivak, D. (2008). Surface immobilization methods for aptamer diagnostic applications. *Analytical and Bioanalytical Chemistry, 390*(4), 1009-1021.

Balamurugan, S., Obubuafo, A., Soper, S. A., McCarley, R. L., & Spivak, D. A. (2006). Designing Highly Specific Biosensing Surfaces Using Aptamer Monolayers on Gold. *Langmuir, 22*(14), 6446-6453.

Barbillon, G., Bijeon, J. L., Lérondel, G., Plain, J., & Royer, P. (2008). Detection of chemical molecules with integrated plasmonic glass nanotips. *Surface Science, 602*(16), L119-L122.

Barbillon, G., Bijeon, J. L., Plain, J., de la Chapelle, M. L., Adam, P. M., & Royer, P. (2007). Electron beam lithography designed chemical nanosensors based on localized surface plasmon resonance. *Surface Science, 601*(21), 5057-5061.

Becker, J., Schubert, O., & Sönnichsen, C. (2007). Gold Nanoparticle Growth Monitored in situ Using a Novel Fast Optical Single-Particle Spectroscopy Method. *Nano Letters, 7*(6), 1664-1669.

Becker, J., Trügler, A., Jakab, A., Hohenester, U., & Sönnichsen, C. (2010). The Optimal Aspect Ratio of Gold Nanorods for Plasmonic Bio-sensing. *Plasmonics, 5*(2), 161-167.

Bek, A., Jansen, R., Ringler, M., Mayilo, S., Klar, T. A., & Feldmann, J. (2008). Fluorescence Enhancement in Hot Spots of AFM-Designed Gold Nanoparticle Sandwiches. *Nano Letters, 8*(2), 485-490.

Billaud, P., Marhaba, S., Cottancin, E., Arnaud, L., Bachelier, G., Bonnet, C., Del Fatti, N., Lerme, J., Vallee, F., Vialle, J. L., Broyer, M., & Pellarin, M. (2008). Correlation between the Extinction Spectrum of a Single Metal Nanoparticle and Its Electron Microscopy Image. *The Journal of Physical Chemistry C, 112*(4), 978-982.

Bingham, J. M., Willets, K. A., Shah, N. C., Andrews, D. Q., & Van Duyne, R. P. (2009). Localized Surface Plasmon Resonance Imaging: Simultaneous Single Nanoparticle Spectroscopy and Diffusional Dynamics. *The Journal of Physical Chemistry C, 113*(39), 16839-16842.

Biswas, A., Wang, T., & Biris, A. S. (2010). Single metal nanoparticle spectroscopy: optical characterization of individual nanosystems for biomedical applications. *Nanoscale, 2*(9), 1560-1572.

Bocchio, N. L., Unger, A., Álvarez, M., & Kreiter, M. (2008). Thin Layer Sensing with Multipolar Plasmonic Resonances. *The Journal of Physical Chemistry C, 112*(37), 14355-14359.

Bohren, C. F., & Huffman, D. R. (Eds.). (1998). *Absorption and Scattering of Light by Small Particles*. New York, USA: Jon Wiley and sons.

Bonnet, S., Archer, S. L., Allalunis-Turner, J., Haromy, A., Beaulieu, C., Thompson, R., Lee, C. T., Lopaschuk, G. D., Puttagunta, L., Bonnet, S., Harry, G., Hashimoto, K., Porter, C. J., Andrade, M. A., Thebaud, B., & Michelakis, E. D. (2007). A Mitochondria-K+ Channel Axis Is Suppressed in Cancer and Its Normalization Promotes Apoptosis and Inhibits Cancer Growth. *Cancer Cell, 11*(1), 37-51.

Brian, B., Sepúlveda, B., Alaverdyan, Y., Lechuga, L. M., & Käll, M. (2009). Sensitivity enhancement of nanoplasmonic sensors in low refractive index substrates. *Opt. Express, 17*(3), 2015-2023.

Cang, H., Labno, A., Lu, C., Yin, X., Liu, M., Gladden, C., Liu, Y., & Zhang, X. (2011). Probing the electromagnetic field of a 15-nanometre hotspot by single molecule imaging. [10.1038/nature09698]. *Nature, 469*(7330), 385-388.

Chen, S., Svedendahl, M., Duyne, R. P. V., & Käll, M. (2011). Plasmon-Enhanced Colorimetric ELISA with Single Molecule Sensitivity. *Nano Letters, 11*(4), 1826-1830.

Chen, S., Svedendahl, M., Käll, M., Gunnarsson, L., & Dmitriev, A. (2009). Ultrahigh sensitivity made simple: nanoplasmonic label-free biosensing with an extremely low limit-of-detection for bacterial and cancer diagnostics. *Nanotechnology, 20*(43), 434015.

Cheng, D., & Jiang, H. (2009). A debubbler for microfluidics utilizing air-liquid interfaces. *Applied Physics Letters, 95*(21), 214103-214103.

Chinowsky, T. M., Jung, L. S., & Yee, S. S. (1999). Optimal linear data analysis for surface plasmon resonance biosensors. *Sensors and Actuators B: Chemical, 54*(1-2), 89-97.

Chou, S. Y., Krauss, P. R., & Renstrom, P. J. (1996). Nanoimprint lithography. *Journal of Vacuum Science & Technology B: Microelectronics and Nanometer Structures 14*(6), 4129 - 4133

Chou, S. Y., Krauss, P. R., Zhang, W., Guo, L., & Zhuang, L. (1997). Sub-10 nm imprint lithography and applications *J. Vac. Sci. Technol. B 15*(6), 2897-2904.

Christ, A., Tikhodeev, S. G., Gippius, N. A., Kuhl, J., & Giessen, H. (2003). Waveguide-Plasmon Polaritons: Strong Coupling of Photonic and Electronic Resonances in a Metallic Photonic Crystal Slab. *Physical Review Letters, 91*(18), 183901.

Christ, A., Zentgraf, T., Kuhl, J., Tikhodeev, S. G., Gippius, N. A., & Giessen, H. (2004). Optical properties of planar metallic photonic crystal structures: Experiment and theory. *Physical Review B, 70*(12), 125113.

Cui, Z. (Ed.). (2005). *Micro-Nanofabrication: Technologies and application*: Springer.

Curto, A. G., Volpe, G., Taminiau, T. H., Kreuzer, M. P., Quidant, R., & van Hulst, N. F. (2010). Unidirectional Emission of a Quantum Dot Coupled to a Nanoantenna. *Science, 329*(5994), 930-933.

Dahlin, A. B. (2012). Size Matters: Problems and Advantages Associated with Highly Miniaturized Sensors. *Sensors, 12*(3), 3018-3036.

Dahlin, A. B., Chen, S., Jonsson, M. P., Gunnarsson, L., Käll, M., & Höök, F. (2009). High-Resolution Microspectroscopy of Plasmonic Nanostructures for Miniaturized Biosensing. *Analytical Chemistry, 81*(16), 6572-6580.

Dahlin, A. B., Tegenfeldt, J. O., & Höök, F. (2006). Improving the Instrumental Resolution of Sensors Based on Localized Surface Plasmon Resonance. *Analytical Chemistry, 78*(13), 4416-4423.

De Angelis, F., Patrini, M., Das, G., Maksymov, I., Galli, M., Businaro, L., Andreani, L. C., & Di Fabrizio, E. (2008). A Hybrid Plasmonic−Photonic Nanodevice for Label-Free Detection of a Few Molecules. *Nano Letters, 8*(8), 2321-2327.

Dmitriev, A., Hägglund, C., Chen, S., Fredriksson, H., Pakizeh, T., Käll, M., & Sutherland, D. S. (2008). Enhanced Nanoplasmonic Optical Sensors with Reduced Substrate Effect. *Nano Letters, 8*(11), 3893-3898.

Dondapati, S. K., Sau, T. K., Hrelescu, C., Klar, T. A., Stefani, F. D., & Feldmann, J. (2010). Label-free Biosensing Based on Single Gold Nanostars as Plasmonic Transducers. *ACS Nano, 4*(11), 6318-6322.

Donner, J. S., Baffou, G., McCloskey, D., & Quidant, R. (2011). Plasmon-Assisted Optofluidics. *ACS Nano, 5*(7), 5457-5462.

Dregely, D., Taubert, R., Dorfmuller, J., Vogelgesang, R., Kern, K., & Giessen, H. (2011). 3D optical Yagi-Uda nanoantenna array. [10.1038/ncomms1268]. *Nat Commun, 2*, 267.

Ebbesen, T. W., Lezec, H. J., Ghaemi, H. F., Thio, T., & Wolff, P. A. (1998). Extraordinary optical transmission through sub-wavelength hole arrays. [10.1038/35570]. *Nature, 391*(6668), 667-669.

Edward, K., Dae Ho, L., Chang-Beom, K., Sung Ju, Y., & Sang-Hoon, L. (2010). A hemispherical microfluidic channel for the trapping and passive dissipation of microbubbles. *Journal of Micromechanics and Microengineering, 20*(4), 045009.

Eftekhari, F., Escobedo, C., Ferreira, J., Duan, X., Girotto, E. M., Brolo, A. G., Gordon, R., & Sinton, D. (2009). Nanoholes As Nanochannels: Flow-through Plasmonic Sensing. *Analytical Chemistry, 81*(11), 4308-4311.

Einav, S., Gerber, D., Bryson, P. D., Sklan, E. H., Elazar, M., Maerkl, S. J., Glenn, J. S., & Quake, S. R. (2008). Discovery of a hepatitis C target and its pharmacological inhibitors by microfluidic affinity analysis. [10.1038/nbt.1490]. *Nat Biotech, 26*(9), 1019-1027.

Enoch, S., Quidant, R., & Badenes, G. (2004). Optical sensing based on plasmon coupling in nanoparticle arrays. *Opt. Express, 12*(15), 3422-3427.

Felidj, N., Laurent, G., Aubard, J., Levi, G., Hohenau, A., Krenn, J. R., & Aussenegg, F. R. (2005). Grating-induced plasmon mode in gold nanoparticle arrays. *The Journal of Chemical Physics, 123*(22), 221103-221105.

Ferreira, J., Santos, M. J. L., Rahman, M. M., Brolo, A. G., Gordon, R., Sinton, D., & Girotto, E. M. (2008). Attomolar Protein Detection Using in-Hole Surface Plasmon Resonance. *Journal of the American Chemical Society, 131*(2), 436-437.

Feuz, L., Jonsson, M. P., & Höök, F. (2012a). Material-Selective Surface Chemistry for Nanoplasmonic Sensors: Optimizing Sensitivity and Controlling Binding to Local Hot Spots. *Nano Letters, 12*(2), 873-879.

Feuz, L., Jönsson, P., Jonsson, M. P., & Höök, F. (2010). Improving the Limit of Detection of Nanoscale Sensors by Directed Binding to High-Sensitivity Areas. *ACS Nano, 4*(4), 2167-2177.

Fidalgo, L. M., & Maerkl, S. J. (2011). A software-programmable microfluidic device for automated biology. *Lab on a Chip, 11*(9), 1612-1619.
Fischer, H., & Martin, O. J. F. (2008). Engineering the optical response ofplasmonic nanoantennas. *Opt. Express, 16*(12), 9144-9154.
Fleischmann, M., Hendra, P. J., & McQuillan, A. J. (1974). Raman spectra of pyridine adsorbed at a silver electrode. *Chemical Physics Letters, 26*(2), 163-166.
Frederix, F., Bonroy, K., Reekmans, G., Laureyn, W., Campitelli, A., Abramov, M. A., Dehaen, W., & Maes, G. (2004). Reduced nonspecific adsorption on covalently immobilized protein surfaces using poly(ethylene oxide) containing blocking agents. *Journal of Biochemical and Biophysical Methods, 58*(1), 67-74.
Fukuzaki, S., Urano, H., & Nagata, K. (1996). Adsorption of bovine serum albumin onto metal oxide surfaces. *Journal of Fermentation and Bioengineering, 81*(2), 163-167.
Futai, N., Gu, W., & Takayama, S. (2004). Rapid Prototyping of Microstructures with Bell-Shaped Cross-Sections and Its Application to Deformation-Based Microfluidic Valves. *Advanced Materials, 16*(15), 1320-1323.
Ganic, D., Gan, X., & Gu, M. (2004). Trapping force and optical lifting under focused evanescent wave illumination. *Opt. Express, 12*(22), 5533-5538.
García de Abajo, F. J. (2008). Nonlocal Effects in the Plasmons of Strongly Interacting Nanoparticles, Dimers, and Waveguides. *The Journal of Physical Chemistry C, 112*(46), 17983-17987.
Garet, G. N., Marek, P., & Jirí, H. (2002). Data analysis for optical sensors based on spectroscopy of surface plasmons. *Measurement Science and Technology, 13*(12), 2038.
Gerion, D., & Day, G.-J. (2010). Label-Free and Labeled Technology for Protein Characterization and Quantitation. *BioPharm International, 23*(9), 38-45.
Ghenuche, P., Cherukulappurath, S., Taminiau, T. H., van Hulst, N. F., & Quidant, R. (2008). Spectroscopic Mode Mapping of Resonant Plasmon Nanoantennas. *Physical Review Letters, 101*(11), 116805.
Gobin, A. M., Lee, M. H., Halas, N. J., James, W. D., Drezek, R. A., & West, J. L. (2007). Near-Infrared Resonant Nanoshells for Combined Optical Imaging and Photothermal Cancer Therapy. *Nano Letters, 7*(7), 1929-1934.
Grigorenko, A. N. (2006). Antisymmetric plasmon resonance in coupled gold nanoparticles as a sensitive tool for detection of local index of refraction. [10.1063/1.2187432]. *Appl. Phys. Lett., 88*(12), 124103.
Gunnarsson, L., Rindzevicius, T., Prikulis, J., Kasemo, B., Käll, M., Zou, S., & Schatz, G. C. (2004). Confined Plasmons in Nanofabricated Single Silver Particle Pairs: Experimental Observations of Strong Interparticle Interactions. *The Journal of Physical Chemistry B, 109*(3), 1079-1087.
Haes, A. J., Chang, L., Klein, W. L., & Van Duyne, R. P. (2005). Detection of a Biomarker for Alzheimer's Disease from Synthetic and Clinical Samples Using a Nanoscale Optical Biosensor. *Journal of the American Chemical Society, 127*(7), 2264-2271.
Haes, A. J., Hall, W. P., Chang, L., Klein, W. L., & Van Duyne, R. P. (2004). A Localized Surface Plasmon Resonance Biosensor: First Steps toward an Assay for Alzheimer's Disease. *Nano Letters, 4*(6), 1029-1034.
Haes, A. J., & Van Duyne, R. P. (2002). A Nanoscale Optical Biosensor: Sensitivity and Selectivity of an Approach Based on the Localized Surface Plasmon Resonance Spectroscopy of Triangular Silver Nanoparticles. *Journal of the American Chemical Society, 124*(35), 10596-10604.
Haes, A. J., Zou, S., Schatz, G. C., & Van Duyne, R. P. (2003). A Nanoscale Optical Biosensor: The Long Range Distance Dependence of the Localized Surface Plasmon Resonance of Noble Metal Nanoparticles. *The Journal of Physical Chemistry B, 108*(1), 109-116.

Haes, A. J., Zou, S., Schatz, G. C., & Van Duyne, R. P. (2004). Nanoscale Optical Biosensor: Short Range Distance Dependence of the Localized Surface Plasmon Resonance of Noble Metal Nanoparticles. *The Journal of Physical Chemistry B, 108*(22), 6961-6968.

Halas, N. J., Lal, S., Chang, W.-S., Link, S., & Nordlander, P. (2011). Plasmons in Strongly Coupled Metallic Nanostructures. *Chemical Reviews, 111*(6), 3913-3961.

Hao, E. (2004). Electromagnetic fields around silver nanoparticles and dimers. [10.1063/1.1629280]. *J. Chem. Phys., 120*(1), 357.

Hao, F., Sonnefraud, Y., Dorpe, P. V., Maier, S. A., Halas, N. J., & Nordlander, P. (2008). Symmetry Breaking in Plasmonic Nanocavities: Subradiant LSPR Sensing and a Tunable Fano Resonance. *Nano Letters, 8*(11), 3983-3988.

Haynes, C. L., McFarland, A. D., Zhao, L., Van Duyne, R. P., Schatz, G. C., Gunnarsson, L., Prikulis, J., Kasemo, B., & Käll, M. (2003). Nanoparticle Optics: The Importance of Radiative Dipole Coupling in Two-Dimensional Nanoparticle Arrays†. *The Journal of Physical Chemistry B, 107*(30), 7337-7342.

Haynes, C. L., & Van Duyne, R. P. (2001). Nanosphere Lithography: A Versatile Nanofabrication Tool for Studies of Size-Dependent Nanoparticle Optics. *The Journal of Physical Chemistry B, 105*(24), 5599-5611.

Hessel, A., & Oliner, A. A. (1965). A New Theory of Wood's Anomalies on Optical Gratings. *Appl. Opt., 4*(10), 1275-1297.

Hicks, E. M., Zou, S., Schatz, G. C., Spears, K. G., Van Duyne, R. P., Gunnarsson, L., Rindzevicius, T., Kasemo, B., & Käll, M. (2005). Controlling Plasmon Line Shapes through Diffractive Coupling in Linear Arrays of Cylindrical Nanoparticles Fabricated by Electron Beam Lithography. *Nano Letters, 5*(6), 1065-1070.

Homola, J. (2006) *Surface Plasmon Resonance Based Senosors*. Berlin: Springer-Verlag Berlin and Heidelberg GmbH & Co. K.

Homola, J. (2008). Surface Plasmon Resonance Sensors for Detection of Chemical and Biological Species. *Chemical Reviews, 108*(2), 462-493.

Hu, M., Yan J., He Y., Lu H., Weng L., Song S., Fan C., & Wang L. (2010). Ultrasensitive, Multiplexed Detection of Cancer Biomarkers Directly in Serum by Using a Quantum Dot-Based Microfluidic Protein Chip, *ACS Nano, 4*(1), 488-494

Huang, B., Wu, H., Kim, S., & Zare, R. N. (2005). Coating of poly(dimethylsiloxane) with n-dodecyl-[small beta]-d-maltoside to minimize nonspecific protein adsorption. *Lab on a Chip, 5*(10), 1005-1007.

Huang, C., Bouhelier, A., Berthelot, J., des-Francs, G. Colas, Finot, E., Weeber, J. –C., Dereux, A., Kostcheev, S., Baudrion, A. –L., Plain, J., Bachelot, R., Royer, P., Wiederrecht, G. P. (2010). *Appl. Phys. Lett., 96*(14), 143116.

Huang, J.-S., Kern, J., Geisler, P., Weinmann, P., Kamp, M., Forchel, A., Biagioni, P., & Hecht, B. (2010). Mode Imaging and Selection in Strongly Coupled Nanoantennas. *Nano Letters, 10*(6), 2105-2110.

Huang, X., Jain, P., El-Sayed, I., & El-Sayed, M. (2008) Plasmonic Photothermal Therapy (PPT) Using Gold Nanoparticles. *Lasers in Medical Science, 23*(3), 217-228

Huang, W., Qian, W., Jain, P. K., & El-Sayed, M. A. (2007). The Effect of Plasmon Field on the Coherent Lattice Phonon Oscillation in Electron-Beam Fabricated Gold Nanoparticle Pairs. *Nano Letters, 7*(10), 3227-3234.

Israel, B., Yu, X., & Walt, D. R. (2008). Optrode-based fiber optic biosensors In F. S. Ligrer & C. R. Taitt (Eds.), *Optical biosensors: Today and tomorrow*. Amsterdam, The Nederlands: Elsevier.

Jain, P. K. (2008). *Plasmons in assembled metal nanostructures: Radiative and non-radiative properties, near-field coupling, and its universal scaling behavior.* Georgia Institute of Technology.

Jain, P. K., & El-Sayed, M. A. (2007). Surface Plasmon Resonance Sensitivity of Metal Nanostructures: Physical Basis and Universal Scaling in Metal Nanoshells. *The Journal of Physical Chemistry C, 111*(47), 17451-17454.
Jain, P. K., & El-Sayed, M. A. (2008). Noble Metal Nanoparticle Pairs: Effect of Medium for Enhanced Nanosensing. *Nano Letters, 8*(12), 4347-4352.
Jain, P. K., & El-Sayed, M. A. (2010). Plasmonic coupling in noble metal nanostructures. *Chemical Physics Letters, 487*(4-6), 153-164.
Jain, P. K., Eustis, S., & El-Sayed, M. A. (2006). Plasmon Coupling in Nanorod Assemblies: Optical Absorption, Discrete Dipole Approximation Simulation, and Exciton-Coupling Model. *The Journal of Physical Chemistry B, 110*(37), 18243-18253.
Jain, P. K., Huang, W., & El-Sayed, M. A. (2007). On the Universal Scaling Behavior of the Distance Decay of Plasmon Coupling in Metal Nanoparticle Pairs: A Plasmon Ruler Equation. *Nano Letters, 7*(7), 2080-2088.
Jeanmaire, D. L., & Van Duyne, R. P. (1977). Surface raman spectroelectrochemistry: Part I. Heterocyclic, aromatic, and aliphatic amines adsorbed on the anodized silver electrode. *Journal of Electroanalytical Chemistry and Interfacial Electrochemistry, 84*(1), 1-20.
Jeyachandran, Y. L., Mielczarski, E., Rai, B., & Mielczarski, J. A. (2009). Quantitative and Qualitative Evaluation of Adsorption/Desorption of Bovine Serum Albumin on Hydrophilic and Hydrophobic Surfaces. *Langmuir, 25*(19), 11614-11620.
Jin, J.-M. (2002). *The Finite element method in electromagnetics*. New York: John Wiley & Sons. Inc.
Jin, J.-M., & Riley, D. J. (2009). *Finite element analysis of antennas and arrays*. New Jersey: Jon Willey & Sons. Inc.
Johnson, P. B., & Christy, R. W. (1972). Optical Constants of the Noble Metals. *Physical Review B, 6*(12), 4370-4379.
Johnson, S. G. (2007, 2010). Notes on Perfectly Matched Layers (PMLs). from http://www-math.mit.edu/~stevenj/18.369/pml.pdf
Johnston, K. S., Booksh, K. S., Chinowsky, T. M., & Yee, S. S. (1999). Performance comparison between high and low resolution spectrophotometers used in a white light surface plasmon resonance sensor. *Sensors and Actuators B: Chemical, 54*(1-2), 80-88.
Jonsson, M. P., Dahlin, A. B., Feuz, L., Petronis, S., & Höök, F. (2010). Locally Functionalized Short-Range Ordered Nanoplasmonic Pores for Bioanalytical Sensing. *Analytical Chemistry, 82*(5), 2087-2094.
Jorg, M., Kahl, M., Zuschlag, A., Sell, A., Halm, A., Boneberg, J., Leiderer, P., Leitenstorfer, A., & Bratschitsch, R. (2008). Nanomechanical control of an optical antenna. [10.1038/nphoton.2008.27]. *Nat Photon, 2*(4), 230-233.
Ju, J. J., Park, S., Kim, M.-s., Kim, J. T., Park, S. K., Park, Y. J., & Lee, M.-H. (2007). 40 Gbit/s light signal transmission in long-range surface plasmon waveguides. *Applied Physics Letters, 91*(17), 171117-171113.
Jung, L. S., Campbell, C. T., Chinowsky, T. M., Mar, M. N., & Yee, S. S. (1998). Quantitative Interpretation of the Response of Surface Plasmon Resonance Sensors to Adsorbed Films. *Langmuir, 14*(19), 5636-5648.
Kabashin, A. V., Evans, P., Pastkovsky, S., Hendren, W., Wurtz, G. A., Atkinson, R., Pollard, R., Podolskiy, V. A., & Zayats, A. V. (2009). Plasmonic nanorod metamaterials for biosensing. [10.1038/nmat2546]. *Nat Mater, 8*(11), 867-871.
Kappeler, R. (2006). *Engineering the Field Enhancement at the Apex of a Structured Noble Metal Tip.* ETH, Zurich.
Kenausis, G. L., Vörös, J., Elbert, D. L., Huang, N., Hofer, R., Ruiz-Taylor, L., Textor, M., Hubbell, J. A., & Spencer, N. D. (2000). Poly(l-lysine)-g-Poly(ethylene glycol) Layers on Metal Oxide Surfaces:

Attachment Mechanism and Effects of Polymer Architecture on Resistance to Protein Adsorption†. *The Journal of Physical Chemistry B, 104*(14), 3298-3309.
Kim, S., Jin, J., Kim, Y.-J., Park, I.-Y., Kim, Y., & Kim, S.-W. (2008). High-harmonic generation by resonant plasmon field enhancement. [10.1038/nature07012]. *Nature, 453*(7196), 757-760.
Klein, M. W., Tritschler, T., Wegener, M., & Linden, S. (2005). Lineshape of harmonic generation by metallic nanoparticles and metallic photonic crystal slabs. *Physical Review B, 72*(11), 115113.
Knight, M. W., & Halas, N. J. (2008). Nanoshells to nanoeggs to nanocups: optical properties of reduced symmetry core–shell nanoparticles beyond the quasistatic limit. *New Journal of Physics, 10*(10), 105006.
Knight, M. W., Wu, Y., Lassiter, J. B., Nordlander, P., & Halas, N. J. (2009). Substrates Matter: Influence of an Adjacent Dielectric on an Individual Plasmonic Nanoparticle. *Nano Letters, 9*(5), 2188-2192.
Kravets, V. G., Schedin, F., & Grigorenko, A. N. (2008). Extremely Narrow Plasmon Resonances Based on Diffraction Coupling of Localized Plasmons in Arrays of Metallic Nanoparticles. *Physical Review Letters, 101*(8), 087403.
Kravets, V. G., Schedin, F., Kabashin, A. V., & Grigorenko, A. N. (2010). Sensitivity of collective plasmon modes of gold nanoresonators to local environment. *Opt. Lett., 35*(7), 956-958.
Kreno, L. E., Hupp, J. T., & Van Duyne, R. P. (2010). Metal−Organic Framework Thin Film for Enhanced Localized Surface Plasmon Resonance Gas Sensing. *Analytical Chemistry, 82*(19), 8042-8046.
Kreuzer, M., Quidant, R., Salvador, J. P., Marco, M. P., & Badenes, G. (2008). Colloidal-based localized surface plasmon resonance (LSPR) biosensor for the quantitative determination of stanozolol. *Analytical and Bioanalytical Chemistry, 391*(5), 1813-1820.
Lamprecht, B., Schider, G., Lechner, R. T., Ditlbacher, H., Krenn, J. R., Leitner, A., & Aussenegg, F. R. (2000). Metal Nanoparticle Gratings: Influence of Dipolar Particle Interaction on the Plasmon Resonance. *Physical Review Letters, 84*(20), 4721-4724.
Langhammer, C., Larsson, E. M., Kasemo, B., & Zorić, I. (2010). Indirect Nanoplasmonic Sensing: Ultrasensitive Experimental Platform for Nanomaterials Science and Optical Nanocalorimetry. *Nano Letters, 10*(9), 3529-3538.
Larsson, E. M., Langhammer, C., Zorić, I., & Kasemo, B. (2009). Nanoplasmonic Probes of Catalytic Reactions. *Science, 326*(5956), 1091-1094.
Lassiter, J. B., Aizpurua, J., Hernandez, L. I., Brandl, D. W., Romero, I., Lal, S., Hafner, J. H., Nordlander, P., & Halas, N. J. (2008). Close Encounters between Two Nanoshells. *Nano Letters, 8*(4), 1212-1218.
Lee, H.-M., & Wu, J.-C. (2010). *Radiative Properties of Butt-Ring Gold Nanoantenna Array.* Paper presented at the 7th International Conference on Optics-photonics Design and Fabrication, Yokohama.
Lee, J. N., Park, C., & Whitesides, G. M. (2003). Solvent Compatibility of Poly(dimethylsiloxane)-Based Microfluidic Devices. *Analytical Chemistry, 75*(23), 6544-6554.
Lee, K.-L., & Wei, P.-K. (2010). Enhancing Surface Plasmon Detection Using Ultrasmall Nanoslits and a Multispectral Integration Method. *Small, 6*(17), 1900-1907.
Lee, K.-S., & El-Sayed, M. A. (2006). Gold and Silver Nanoparticles in Sensing and Imaging: Sensitivity of Plasmon Response to Size, Shape, and Metal Composition. *The Journal of Physical Chemistry B, 110*(39), 19220-19225.
Lee, S.-W., Lee, K.-S., Ahn, J., Lee, J.-J., Kim, M.-G., & Shin, Y.-B. (2011). Highly Sensitive Biosensing Using Arrays of Plasmonic Au Nanodisks Realized by Nanoimprint Lithography. *ACS Nano, 5*(2), 897-904.
Lereu, A. L., Sanchez-Mosteiro, G., Ghenuche, P., Quidant, R., & Van Hulst, N. F. (2008). Individual gold dimers investigated by far- and near-field imaging. *Journal of Microscopy, 229*(2), 254-258.
Li, K., Stockman, M. I., & Bergman, D. J. (2003). Self-Similar Chain of Metal Nanospheres as an Efficient Nanolens. *Physical Review Letters, 91*(22), 227402.

Li, N., Tang, H., Gai, H., Dong, X., Wang, Q., & Yeung, E. (2009). Determination of protein surface excess on a liquid/solid interface by single-molecule counting. *Analytical and Bioanalytical Chemistry, 394*(7), 1879-1885.

Ligler, F. S., Taitt, C. R., & Sapsford, K. (2008). Planar waveguides for fluorescence biosensors. In F. S. Ligler & C. R. Taitt (Eds.), *Optical biosensors: Today and tomorrow*. Amsterdam, The Nederlands: Elsevier.

Linden, S., Christ, A., Kuhl, J., & Giessen, H. (2001). Selective suppression of extinction within the plasmon resonance of gold nanoparticles. *Applied Physics B: Lasers and Optics, 73*(4), 311-316.

Linden, S., Kuhl, J., & Giessen, H. (2001). Controlling the Interaction between Light and Gold Nanoparticles: Selective Suppression of Extinction. *Physical Review Letters, 86*(20), 4688-4691.

Liu, Z., Boltasseva, A., Pedersen, R. H., Bakker, R., Kildishev, A. V., Drachev, V. P., & Shalaev, V. M. (2008). Plasmonic nanoantenna arrays for the visible. *Metamaterials, 2*(1), 45-51.

Liz-Marzán, L. M. (2005). Tailoring Surface Plasmons through the Morphology and Assembly of Metal Nanoparticles. *Langmuir, 22*(1), 32-41.

Lou, N., Jha, R., Domínguez-Juárez, J. L., Finazzi, V., Villatoro, J., Badenes, G., & Pruneri, V. (2010). Embedded optical micro/nano-fibers for stable devices. *Opt. Lett., 35*(4), 571-573.

Luk'yanchuk, B., Zheludev, N. I., Maier, S. A., Halas, N. J., Nordlander, P., Giessen, H., & Chong, C. T. (2010). The Fano resonance in plasmonic nanostructures and metamaterials. [10.1038/nmat2810]. *Nat Mater, 9*(9), 707-715.

Malaquin, L., Kraus, T., Schmid, H., Delamarche, E., & Wolf, H. (2007). Controlled Particle Placement through Convective and Capillary Assembly. *Langmuir, 23*(23), 11513-11521.

Malinsky, M. D., Kelly, K. L., Schatz, G. C., & Van Duyne, R. P. (2001). Chain Length Dependence and Sensing Capabilities of the Localized Surface Plasmon Resonance of Silver Nanoparticles Chemically Modified with Alkanethiol Self-Assembled Monolayers. *Journal of the American Chemical Society, 123*(7), 1471-1482.

Malmsten, M. (1995). Ellipsometry studies of the effects of surface hydrophobicity on protein adsorption. *Colloids and Surfaces B: Biointerfaces, 3*(5), 297-308.

Marazuela, M., & Moreno-Bondi, M. (2002). Fiber-optic biosensors - an overview. *Analytical and Bioanalytical Chemistry, 372*(5), 664-682.

Margueritat, J. r. m., Gehan, H. l. n., Grand, J., Lévi, G., Aubard, J., Félidj, N., Bouhelier, A., Colas-Des-Francs, G., Markey, L., Marco De Lucas, C., Dereux, A., & Finot, E. (2011). Influence of the Number of Nanoparticles on the Enhancement Properties of Surface-Enhanced Raman Scattering Active Area: Sensitivity versus Repeatability. *ACS Nano, 5*(3), 1630-1638.

Marhaba, S., Bachelier, G., Bonnet, C., Broyer, M., Cottancin, E., Grillet, N., Lermé, J., Vialle, J.-L., & Pellarin, M. (2009). Surface Plasmon Resonance of Single Gold Nanodimers near the Conductive Contact Limit. *The Journal of Physical Chemistry C, 113*(11), 4349-4356.

Marie, R., Dahlin, A., Tegenfeldt, J., & Höök, F. (2007) Generic Surface Modification Strategy foe Sensing Applications Based on Au/SiO_2 nanostructures. *Biointerphases, 2*(1), 49-55

Marty, R., Baffou, G., Arbouet, A., Girard, C., & Quidant, R. (2010). Charge distribution induced inside complex plasmonic nanoparticles. *Opt. Express, 18*(3), 3035-3044.

McDonald, J. C., & Whitesides, G. M. (2002). Poly(dimethylsiloxane) as a Material for Fabricating Microfluidic Devices. *Accounts of Chemical Research, 35*(7), 491-499.

McFarland, A. D., & Van Duyne, R. P. (2003). Single Silver Nanoparticles as Real-Time Optical Sensors with Zeptomole Sensitivity. *Nano Letters, 3*(8), 1057-1062.

McMahon, J. M., Gray, S. K., & Schatz, G. C. (2010). Optical Properties of Nanowire Dimers with a Spatially Nonlocal Dielectric Function. *Nano Letters, 10*(9), 3473-3481.

Melin, J., & Quake, S. R. (2007). Microfluidic Large-Scale Integration: The Evolution of Design Rules for Biological Automation. *Annual Review of Biophysics and Biomolecular Structure, 36*(1), 213-231.

Merlo, L. M. F., Pepper, J. W., Reid, B. J., & Maley, C. C. (2006). Cancer as an evolutionary and ecological process. [10.1038/nrc2013]. *Nat Rev Cancer, 6*(12), 924-935.

Miljković, V. D. (2011). *Simulations of directionality effects and optical forces in plasmonic nanostructures.* Chalmers University of Technology, Gothenburg.

Miljković, V. D., Shegai, T., Johansson, P., & Käll, M. (2012). Simulating Light Scattering from Supported Plasmonic Nanowires. *Opt. Express, 20,* 10816-10826

Miller, M. M., & Lazarides, A. A. (2005). Sensitivity of Metal Nanoparticle Surface Plasmon Resonance to the Dielectric Environment. *The Journal of Physical Chemistry B, 109*(46), 21556-21565.

Mousavi, S. H., Khanikaev, A. B., Neuner, B., Fozdar, D. Y., Corrigan, T. D., Kolb, P. W., Drew, H. D., Phaneuf, R. J., Alù, A., & Shvets, G. (2011). Suppression of long-range collective effects in meta-surfaces formed by plasmonic antenna pairs. *Opt. Express, 19*(22), 22142-22155.

Mukhopadhyay, R. (2005). Surface plasmon resonance instruments diversify. *Analytical Chemistry, 77*(15), 313 A-317 A.

Nehl, C. L., Liao, H., & Hafner, J. H. (2006). Optical Properties of Star-Shaped Gold Nanoparticles. *Nano Letters, 6*(4), 683-688.

Nishikawa, M., Takemoto, S., & Takakura, Y. (2008). Heat shock protein derivatives for delivery of antigens to antigen presenting cells. *International Journal of Pharmaceutics, 354*(1–2), 23-27.

Norde, W. (1996). Driving forces for protein adsorption at solid surfaces. *Macromolecular Symposia, 103*(1), 5-18.

Novotny, L., & Hecht, B. (Eds.). (2006). *Principles of Nano-Optics*: Cambridge University Press.

Nusz, G. J., Curry, A. C., Marinakos, S. M., Wax, A., & Chilkoti, A. (2009). Rational Selection of Gold Nanorod Geometry for Label-Free Plasmonic Biosensors. *ACS Nano, 3*(4), 795-806.

Offermans, P., Schaafsma, M. C., Rodriguez, S. R. K., Zhang, Y., Crego-Calama, M., Brongersma, S. H., & Gómez Rivas, J. (2011). Universal Scaling of the Figure of Merit of Plasmonic Sensors. *ACS Nano, 5*(6), 5151-5157.

Otte, M. A., Estévez, M. C., Carrascosa, L. G., González-Guerrero, A. B., Lechuga, L. M., & Sepúlveda, B. (2011). Improved Biosensing Capability with Novel Suspended Nanodisks. *The Journal of Physical Chemistry C, 115*(13), 5344-5351.

Otte, M. A., Sepúlveda, B., Ni, W., Juste, J. P. r., Liz-Marzán, L. M., & Lechuga, L. M. (2009). Identification of the Optimal Spectral Region for Plasmonic and Nanoplasmonic Sensing. *ACS Nano, 4*(1), 349-357.

Pérez-Juste, J., Pastoriza-Santos, I., Liz-Marzán, L. M., & Mulvaney, P. (2005). Gold nanorods: Synthesis, characterization and applications. *Coordination Chemistry Reviews, 249*(17-18), 1870-1901.

Piliarik, M., Kvasnička, P., Galler, N., Krenn, J. R., & Homola, J. (2011) Local Refractive Index Sensitivity of Plasmonic Nanoparticles. *Opt. Express, 19*, 9213-9220.

Pockley, A. G. (2003). Heat shock proteins as regulators of the immune response. *The Lancet, 362*(9382), 469-476.

Polycarpou, A. C., & Balanis, C. A. (1998). An Optimized Anisotropic PML for the Analysis of Microwave Circuits. *IEEE Microwave and Guided wave Letters, 8*(1), 3.

Prodan, E., Radloff, C., Halas, N. J., & Nordlander, P. (2003). A Hybridization Model for the Plasmon Response of Complex Nanostructures. *Science, 302*(5644), 419-422.

Psaltis, D., Quake, S. R., & Yang, C. (2006). Developing optofluidic technology through the fusion of microfluidics and optics. *Nature, 442*(7101), 381-386.

Raether, H. (Ed.). (1988). *Surface Plasmons on Smooth and Rough Surfaces and on Gratings*: Springer-Verlag Berlin and Heidelberg GmbH & Co. K.

Rechberger, W., Hohenau, A., Leitner, A., Krenn, J. R., Lamprecht, B., & Aussenegg, F. R. (2003). Optical properties of two interacting gold nanoparticles. *Optics Communications, 220*(1–3), 137-141.

Renger, J., Kadic, M., Dupont, G., A?imovi, S. S., Guenneau, S., Quidant, R., & Enoch, S. (2010). Hidden progress: broadband plasmonic invisibility. *Opt. Express, 18*(15), 15757-15768.

Rérole, A.-L., Gobbo, J., De Thonel, A., Schmitt, E., Pais de Barros, J. P., Hammann, A., Lanneau, D., Fourmaux, E., Deminov, O., Micheau, O., Lagrost, L., Colas, P., Kroemer, G., & Garrido, C. (2011). Peptides and Aptamers Targeting HSP70: A Novel Approach for Anticancer Chemotherapy. *Cancer Research, 71*(2), 484-495.

Righini, M. (2010). *Plasmon-based optical trapping.* UPC, Barcelona.

Righini, M., Ghenuche, P., Cherukulappurath, S., Myroshnychenko, V., García de Abajo, F. J., & Quidant, R. (2009). Nano-optical Trapping of Rayleigh Particles and Escherichia coli Bacteria with Resonant Optical Antennas. *Nano Letters, 9*(10), 3387-3391.

Righini, M., Zelenina, A. S., Girard, C., & Quidant, R. (2007). Parallel and selective trapping in a patterned plasmonic landscape. [10.1038/nphys624]. *Nat Phys, 3*(7), 477-480.

Ringler, M., Klar, T. A., Schwemer, A., Susha, A. S., Stehr, J., Raschke, G., Funk, S., Borowski, M., Nichtl, A., Kürzinger, K., Phillips, R. T., & Feldmann, J. (2007). Moving Nanoparticles with Raman Scattering. *Nano Letters, 7*(9), 2753-2757.

Ringler, M., Schwemer, A., Wunderlich, M., Nichtl, A., Kürzinger, K., Klar, T. A., & Feldmann, J. (2008). Shaping Emission Spectra of Fluorescent Molecules with Single Plasmonic Nanoresonators. *Physical Review Letters, 100*(20), 203002.

Romero, I., Aizpurua, J., Bryant, G. W., & García De Abajo, F. J. (2006). Plasmons in nearly touching metallic nanoparticles: singular response in the limit of touching dimers. *Opt. Express, 14*(21), 9988-9999.

Sannomiya, T., Hafner, C., & Voros, J. (2008). In situ Sensing of Single Binding Events by Localized Surface Plasmon Resonance. *Nano Letters, 8*(10), 3450-3455.

Sannomiya, T., Sahoo, P. K., Mahcicek, D. I., Solak, H. H., Hafner, C., Grieshaber, D., & Vörös, J. (2009). Biosensing by Densely Packed and Optically Coupled Plasmonic Particle Arrays. *Small, 5*(16), 1889-1896.

Sapsford, K. E., & Ligler, F. S. (2004). Real-time analysis of protein adsorption to a variety of thin films. *Biosensors and Bioelectronics, 19*(9), 1045-1055.

Sarrazin, M., Vigneron, J.-P., & Vigoureux, J.-M. (2003). Role of Wood anomalies in optical properties of thin metallic films with a bidimensional array of subwavelength holes. *Physical Review B, 67*(8), 085415.

Schider, G. (2001). Optical properties of Ag and Au nanowire gratings. [10.1063/1.1404425]. *J. Appl. Phys., 90*(8), 3825.

Schnell, M., Garcia-Etxarri, A., Alkorta, J., Aizpurua, J., & Hillenbrand, R. (2010). Phase-Resolved Mapping of the Near-Field Vector and Polarization State in Nanoscale Antenna Gaps. *Nano Letters, 10*(9), 3524-3528.

Schnell, M., Garcia-Etxarri, A., Huber, A. J., Crozier, K. B., Borisov, A., Aizpurua, J., & Hillenbrand, R. (2010). Amplitude- and Phase-Resolved Near-Field Mapping of Infrared Antenna Modes by Transmission-Mode Scattering-Type Near-Field Microscopy†. *The Journal of Physical Chemistry C, 114*(16), 7341-7345.

SchnellM, Garcia Etxarri, A., Huber, A. J., CrozierK, AizpuruaJ, & HillenbrandR. (2009). Controlling the near-field oscillations of loaded plasmonic nanoantennas. [10.1038/nphoton.2009.46]. *Nat Photon, 3*(5), 287-291.

Seigneuric, R., Mjahed, H., Gobbo, J., Joly, A.-L., Berthenet, K., Shirley, S., & Garrido, C. (2011). Heat shock proteins as danger signals for cancer detection. [Review]. *Frontiers in Oncology, 1*.

Sheehan, P. E., & Whitman, L. J. (2005). Detection Limits for Nanoscale Biosensors. *Nano Letters, 5*(4), 803-807.

Shegai, T., Brian, B. R., Miljković, V. D., & Käll, M. (2011). Angular Distribution of Surface-Enhanced Raman Scattering from Individual Au Nanoparticle Aggregates. *ACS Nano, 5*(3), 2036-2041.
Shumaker-Parry, J. S., Zareie, M. H., Aebersold, R., & Campbell, C. T. (2004). Microspotting Streptavidin and Double-Stranded DNA Arrays on Gold for High-Throughput Studies of Protein−DNA Interactions by Surface Plasmon Resonance Microscopy. *Analytical Chemistry, 76*(4), 918-929.
Silin, V., Weetall, H., & Vanderah, D. J. (1997). SPR Studies of the Nonspecific Adsorption Kinetics of Human IgG and BSA on Gold Surfaces Modified by Self-Assembled Monolayers (SAMs). *Journal of Colloid and Interface Science, 185*(1), 94-103.
Sjoelander, S., & Urbaniczky, C. (1991). Integrated fluid handling system for biomolecular interaction analysis. *Analytical Chemistry, 63*(20), 2338-2345.
Skelley, A. M., & Voldman, J. (2008). An active bubble trap and debubbler for microfluidic systems. *Lab on a Chip, 8*(10), 1733-1737.
Slaughter, L. S., Wu, Y., Willingham, B. A., Nordlander, P., & Link, S. (2010). Effects of Symmetry Breaking and Conductive Contact on the Plasmon Coupling in Gold Nanorod Dimers. *ACS Nano, 4*(8), 4657-4666.
Smythe, E. J., Cubukcu, E., & Capasso, F. (2007). Optical properties of surface plasmon resonances of coupled metallic nanorods. *Opt. Express, 15*(12), 7439-7447.
Sonnichsen, C., Reinhard, B. M., Liphardt, J., & Alivisatos, A. P. (2005). A molecular ruler based on plasmon coupling of single gold and silver nanoparticles. [10.1038/nbt1100]. *Nat Biotech, 23*(6), 741-745.
Squires, T. M., & Quake, S. R. (2005). Microfluidics: Fluid physics at the nanoliter scale. *Reviews of Modern Physics, 77*(3), 977-1026.
Steele, J. M., Moran, C. E., Lee, A., Aguirre, C. M., & Halas, N. J. (2003). Metallodielectric gratings with subwavelength slots: Optical properties. *Physical Review B, 68*(20), 205103.
Stern, E., Vacic, A., Rajan, N. K., Criscione, J. M., Park, J., Ilic, B. R., Mooney, D. J., Reed, M. A., & Fahmy, T. M. (2010). Label-free biomarker detection from whole blood. [10.1038/nnano.2009.353]. *Nat Nano, 5*(2), 138-142.
Stern, J. M., Stanfield, J., Kabbani, W., Hsieh, J.-T., & Cadeddu, J. A. (2008). Selective Prostate Cancer Thermal Ablation With Laser Activated Gold Nanoshells. *The Journal of Urology, 179*(2), 748-753.
Stockman, M. I. (2004). Nanofocusing of Optical Energy in Tapered Plasmonic Waveguides. *Physical Review Letters, 93*(13), 137404.
Stockman, M. I. (2011). Nanoplasmonics: past, present, and glimpse into future. *Opt. Express, 19*(22), 22029-22106.
Su, K. H., Wei, Q. H., Zhang, X., Mock, J. J., Smith, D. R., & Schultz, S. (2003). Interparticle Coupling Effects on Plasmon Resonances of Nanogold Particles. *Nano Letters, 3*(8), 1087-1090.
Subrahmanyam, S., Piletsky, S. A., & Turner, A. P. F. (2002). Application of Natural Receptors in Sensors and Assays. *Analytical Chemistry, 74*(16), 3942-3951.
Sui, G., Wang, J., Lee, C.-C., Lu, W., Lee, S. P., Leyton, J. V., Wu, A. M., & Tseng, H.-R. (2006). Solution-Phase Surface Modification in Intact Poly(dimethylsiloxane) Microfluidic Channels. *Analytical Chemistry, 78*(15), 5543-5551.
Svedendahl, M., Chen, S., Dmitriev, A., & Käll, M. (2009). Refractometric Sensing Using Propagating versus Localized Surface Plasmons: A Direct Comparison. *Nano Letters, 9*(12), 4428-4433.
Taminiau, T. H., Stefani, F. D., & van Hulst, N. F. (2011). Optical Nanorod Antennas Modeled as Cavities for Dipolar Emitters: Evolution of Sub- and Super-Radiant Modes. *Nano Letters, 11*(3), 1020-1024.
Tan, W.-H., & Takeuchi, S. (2007). A trap-and-release integrated microfluidic system for dynamic microarray applications. *Proceedings of the National Academy of Sciences, 104*(4), 1146-1151.

Thorsen, T., Maerkl, S. J., & Quake, S. R. (2002). Microfluidic Large-Scale Integration. *Science, 298*(5593), 580-584.

Tong, L., Righini, M., Gonzalez, M. U., Quidant, R., & Kall, M. (2009). Optical aggregation of metal nanoparticles in a microfluidic channel for surface-enhanced Raman scattering analysis. *Lab on a Chip, 9*(2), 193-195.

Ueno, K., Takabatake, S., Nishijima, Y., Mizeikis, V., Yokota, Y., & Misawa, H. (2010), *The Journal of Physical Chemistry Letters, 1*(3), 657-662

Unger, A., & Kreiter, M. (2009). Analyzing the Performance of Plasmonic Resonators for Dielectric Sensing. *The Journal of Physical Chemistry C, 113*(28), 12243-12251.

Unger, M. A., Chou, H.-P., Thorsen, T., Scherer, A., & Quake, S. R. (2000). Monolithic Microfabricated Valves and Pumps by Multilayer Soft Lithography. *Science, 288*(5463), 113-116.

van Dam, R. M. (2006). *Solvent-resistant elastomeric microfluidic devices and applications.* California Institute of Technology.

Vecchi, G., Giannini, V., & Gómez Rivas, J. (2009). Shaping the Fluorescent Emission by Lattice Resonances in Plasmonic Crystals of Nanoantennas. *Physical Review Letters, 102*(14), 146807.

Verellen, N., Van Dorpe, P., Huang, C., Lodewijks, K., Vandenbosch, G. A. E., Lagae, L., & Moshchalkov, V. V. (2011). Plasmon Line Shaping Using Nanocrosses for High Sensitivity Localized Surface Plasmon Resonance Sensing. *Nano Letters, 11*(2), 391-397.

Vijayendran, R. A., & Leckband, D. E. (2000). A Quantitative Assessment of Heterogeneity for Surface-Immobilized Proteins. *Analytical Chemistry, 73*(3), 471-480.

Volpe, G., Cherukulappurath, S., Juanola Parramon, R., Molina-Terriza, G., & Quidant, R. (2009). Controlling the Optical Near Field of Nanoantennas with Spatial Phase-Shaped Beams. *Nano Letters, 9*(10), 3608-3611.

Wang, H., Chen, S., Li, L., & Jiang, S. (2005). Improved Method for the Preparation of Carboxylic Acid and Amine Terminated Self-Assembled Monolayers of Alkanethiolates. *Langmuir, 21*(7), 2633-2636.

Whitesides, G. M. (2006). The origins and the future of microfluidics. [10.1038/nature05058]. *Nature, 442*(7101), 368-373.

Whitney, A. V., Elam, J. W., Zou, S., Zinovev, A. V., Stair, P. C., Schatz, G. C., & Van Duyne, R. P. (2005). Localized Surface Plasmon Resonance Nanosensor: A High-Resolution Distance-Dependence Study Using Atomic Layer Deposition. *The Journal of Physical Chemistry B, 109*(43), 20522-20528.

Wong, H. M. K., Righini, M., Gates, J. C., Smith, P. G. R., Pruneri, V., & Quidant, R. (2011). On-a-chip surface plasmon tweezers. *Applied Physics Letters, 99*(6), 061107-061103.

Wu, C., Khanikaev, A. B., Adato, R., Arju, N., Yanik, A. A., Altug, H., & Shvets, G. (2012). Fano-resonant asymmetric metamaterials for ultrasensitive spectroscopy and identification of molecular monolayers. [10.1038/nmat3161]. *Nat Mater, 11*(1), 69-75.

Wu, H., Odom, T. W., Chiu, D. T., & Whitesides, G. M. (2002). Fabrication of Complex Three-Dimensional Microchannel Systems in PDMS. *Journal of the American Chemical Society, 125*(2), 554-559.

Xia, Y., & Whitesides, G. M. (1998). Soft Lithography. *Angewandte Chemie International Edition, 37*(5), 550-575.

Xu, H., Aizpurua, J., Käll, M., & Apell, P. (2000). Electromagnetic contributions to single-molecule sensitivity in surface-enhanced Raman scattering. *Physical Review E, 62*(3), 4318-4324.

Yang, Y., & Altermatt, P. P. (2008). *Simulation of Optical Properties of the Si/SiO2/Al Interface at the Rear of Industrially Fabricated Si Solar Cells.* Paper presented at the COMSOL Conference, Hannover.

Yannopapas, V., & Stefanou, N. (2004). Optical excitation of coupled waveguide-particle plasmon modes: A theoretical analysis. *Physical Review B, 69*(1), 012408.

Yonzon, C. R., Jeoung, E., Zou, S., Schatz, G. C., Mrksich, M., & Van Duyne, R. P. (2004). A Comparative Analysis of Localized and Propagating Surface Plasmon Resonance Sensors: The Binding of

Concanavalin A to a Monosaccharide Functionalized Self-Assembled Monolayer. *Journal of the American Chemical Society, 126*(39), 12669-12676.

Yoshimoto, K., Nishio, M., Sugasawa, H., & Nagasaki, Y. (2010). Direct Observation of Adsorption-Induced Inactivation of Antibody Fragments Surrounded by Mixed-PEG Layer on a Gold Surface. *Journal of the American Chemical Society, 132*(23), 7982-7989.

Zhang, J., Fu, Y., Chowdhury, M. H., & Lakowicz, J. R. (2007). Metal-Enhanced Single-Molecule Fluorescence on Silver Particle Monomer and Dimer: Coupling Effect between Metal Particles. *Nano Letters, 7*(7), 2101-2107.

Zhang, W., Fischer, H., Schmid, T., Zenobi, R., & Martin, O. J. F. (2009). Mode-Selective Surface-Enhanced Raman Spectroscopy Using Nanofabricated Plasmonic Dipole Antennas. *The Journal of Physical Chemistry C, 113*(33), 14672-14675.

Zhao, J., Frank, B., Burger, S., & Giessen, H. (2011). Large-Area High-Quality Plasmonic Oligomers Fabricated by Angle-Controlled Colloidal Nanolithography. *ACS Nano, 5*(11), 9009-9016.

Zhao, J., Pinchuk, A. O., McMahon, J. M., Li, S., Ausman, L. K., Atkinson, A. L., & Schatz, G. C. (2008). Methods for Describing the Electromagnetic Properties of Silver and Gold Nanoparticles. *Accounts of Chemical Research, 41*(12), 1710-1720.

Zhao, L., Kelly, K. L., & Schatz, G. C. (2003). The Extinction Spectra of Silver Nanoparticle Arrays: Influence of Array Structure on Plasmon Resonance Wavelength and Width. *The Journal of Physical Chemistry B, 107*(30), 7343-7350.

Zou, S., Janel, N., & Schatz, G. C. (2004). Silver nanoparticle array structures that produce remarkably narrow plasmon lineshapes. *The Journal of Chemical Physics, 120*(23), 10871-10875.

Zou, S., & Schatz, G. C. (2004). Narrow plasmonic/photonic extinction and scattering line shapes for one and two dimensional silver nanoparticle arrays. *The Journal of Chemical Physics, 121*(24), 12606-12612.

Zou, S., & Schatz, G. C. (2005). Silver nanoparticle array structures that produce giant enhancements in electromagnetic fields. *Chemical Physics Letters, 403*(1–3), 62-67.

Zuloaga, J., Prodan, E., & Nordlander, P. (2009). Quantum Description of the Plasmon Resonances of a Nanoparticle Dimer. *Nano Letters, 9*(2), 887-891.

List of publications

Related to thesis:

Aćimović, S.S., Kreuzer, M.P., González, Quidant, R., *Plasmon Near-Field Coupling in Metal Dimers as a Step toward Single-Molecule Sensing.* ACS Nano, 2009. **3**(5): p. 1231-1237.

Aćimović, S.S., Kreuzer, M.P., Quidant, R., *Engineering Through Mode Shaping and Lithographical Nanofabrication of Ultrasensitive Nano-plasmonic Sensors for Molecular Detection*

Nanoplasmonic Sensors, A. Dmitriev, Editor. 2012, Springer New York. p. 267-287.

Others:

Armelles, G., González-Díaz, J. B., García-Martín, A., García-Martín, J.M., Cebollada, A., González, M.U., **Acimovic, S.**, Cesario, J., Quidant, R., Badenes, G., *Localized surface plasmon resonance effects on the magneto-optical activity of continuous Au/Co/Au trilayers.* Optics Express, 2008. **16**(20): p. 16104-16112.

Renger, J., Kadic, M., Dupont, G., **Aćimović, S. S.**, Guenneau, S., Quidant, R., Enoch, S., *Hidden progress: broadband plasmonic invisibility.* Opt. Express, 2010. **18**(15): p. 15757-15768.

Graells, S., **Aćimović, S.**, Volpe, G., Quidant, R., *Direct Growth of Optical Antennas Using E-Beam-Induced Gold Deposition.* Plasmonics, 2010. **5**(2): p. 135-139.

Volpe, G., Noack, M., **Aćimović, S. S.**, Reinhardt, C., Quidant, R., et al., *Near-Field Mapping of Plasmonic Antennas by Multiphoton Absorption in Poly(methyl methacrylate).* Nano Letters, 2012.

Ciappina, M.F., **Aćimović, S. S.**, Shaaran, T., Biegert, J., Quidant, R., Lewenstein, M., *High order harmonic generation enhancement by confining electron in plasmonic spatially sculptured fields,* submitted to Physical Review A*,* 2012.